

TURKISH JOURNAL OF SCIENCE AND TECHNOLOGY (TJST)

Year: 2017 Vol: 12 Number: 2

Address:

Fırat Universitesi
Fen Bilimleri Enstitüsü
23119, Elazig - TURKEY

Tel: 0 424 212 27 07

Fax: 0 424 236 99 55

e-mail: fenbilimdergi@firat.edu.tr

New ISSN

Online: 1308-9099

Printed: 1308-9080

Old ISSN

Online: 1306 – 8555

Printed: 1306 – 8547

Refereed journal. Published twice a year

<http://web.firat.edu.tr/fenbilimleri/Dergiler/TJST/index.html>

TURKISH JOURNAL OF SCIENCE & TECHNOLOGY (TJST)

Published by Firat University

Owner

Prof. Dr. Kutbeddin DEMİRDAĞ

Rector of the Firat University

Editor

Assoc.Prof. Dr. Erkan TANYILDIZI

Firat University, Technology Faculty
Department of Electrical and Electronics Engineering

Responsible Director

Prof. Dr. Soner ÖZGEN

Director of the Graduate School of Natural and
Applied Sciences of Firat University

Editor

Assis. Prof. Dr. Sencer ÜNAL

Firat University, Engineering Faculty
Department of Electrical-Electronics Engineering

ADVISORY BOARD

Eyüp BAĞCI

Firat University, Department of Biology,
Elazig-Turkey

Metin BALCI

Middle East Technical University,
Department of Chemistry, Ankara-Turkey

Coskun BAYRAK

UALR Donaghey Collage of Eng. and
Information Tech.Dept. of Computer
Science,
Little Rock, AR, USA

Siqing XIA

Tongji Univ, State Key Lab Pollut Control
& Resource Reuse, Coll Environm Sci &
Engn, Shanghai 200092, R China

Metin CALTA

Firat University, Fisheries Faculty,
Elazig-Turkey

Zihni DEMIRBAG

Karadeniz Technical University,
Department of Biology, Trabzon-Turkey

Mustafa DORUCU

Firat University, Fisheries Faculty,
Elazig-Turkey

Abdulkadir ŞENGÜR

Firat University, Department of
Electronics and Computer Education,
Elazig-Turkey

Ali DEMİR

Istanbul Technical University, Department
of Textile Engineering, İstanbul-Turkey

Saleem HASHMI

International College of Technology,
Dublin, Ireland

Yanhui GUO

St. Thomas University, School of Science
and Technology, Miami, FL, USA

Farid El-TANTAWY

Suez Canal University, Faculty of
Science, Department of Physics, Ismailia,
Egypt

Deniz UNER

Middle East Technical University,
Department of Chemical Engineering,
Ankara-Turkey

Orhan ERMAN

Firat University, Department of Biology,
Elazig-Turkey

Rusen GECIT

Middle East Technical University, Department of
Engineering Science, Ankara-Turkey

Hikmet GECKIL

Inonu University, Department of Biology,
Malatya-Turkey

Ertan GOKALP

Karadeniz Technical University, Department of
Geodesy and Photogrametry Engineering,
Trabzon-Turkey

Hanefi GULDEMİR

Firat University, Department of Electronics and
Computer Education, Elazig-Turkey

Nilgun GULEC

Middle East Technical University, Department of
Geology Engineering, Ankara-Turkey

Erdogan GUNEL

West Virginia University, Department of
Statistics, Morgontown, USA

Sedigheh GHOFRANI

Islamic Azad University, Electrical Engineering
Department, Tehran South Branch, Iran

Wang XIBAO

Tianjin University, The School of Materials
Science and Engineering, China

İbrahim TURKMEN

Balıkesir University, Department of Geology
Engineering, Balıkesir-Turkey

Brain WOERNER

West Virginia University, Department of
Computer Sciences & Electrical Engineering,
Morgontown, WV, USA

A. Kadri CEİİN

Firat University, Department of Biology,
Elazig-Turkey

Eres SOYLEMEZ

Middle East Technical University,
Department of Engineering Science,
Ankara-Turkey

Tuncay ÖREN

Ottawa Univ, Fac Eng, Inform Technol,
McLeod Inst Sim.t Sci, Ottawa, ON KIN
6N5 Canada

Halil ONDER

Middle East Technical University,
Department of Civil Engineering,
Ankara-Turkey

Nazmi POLAT

Ondokuz Mayıs University, Department
of Biology, Samsun-Turkey

M. Polat SAKA

Middle East Technical University,
Department of Engineering Science,
Ankara-Turkey

Serdar SALMAN

Marmara University, Department of
Metal Education, İstanbul-Turkey

Binod Chandra TRIPATHY

Mathematical Sciences Division, Institute
of Advanced Study Science and
Technology Paschim Boragaon; Garchuk;
Guwahati, India

İbrahim TURKMEN

Balıkesir University, Department of
Geology Engineering, Balıkesir-Turkey

Hasan EFEOGLU

Ataturk University, Department of
Electrical-Electronics Engineering,
Erzurum-Turkey

Sakir ERDOĞDU

Karadeniz Technical University,
Department of Civil Engineering,
Trabzon-Turkey

Eoin CASEY

University College Dublin, Chemical and
Bioprocess Engineering, Dublin, Ireland

Muhsin Tunay GENÇOĞLU

Firat University, Engineering Faculty
Department of Electrical-Electronics
Engineering

Fırat Üniversitesi Turkish Journal of Science & Technology (TJST)
12-2, 2017

İÇİNDEKİLER / CONTENTS

1. Fractal Analysis of Shear-thinning Fluid Flow through Porous Media <i>Gözenekli Ortamda Kayma İnceltmeli Akışkan Akışının Fraktal Analizi</i> Fethi KAMIŞLI	1-21
2. Study of Fuzzy Logic Control of Dc-Dc Buck Converter <i>Dc-Dc Düşürücü Dönüştürücünün Bulanık Mantık Denetimi Üzerine Çalışma</i> Zeynep Bala DURANAY, Hanifi GULDEMİR	23-31
3. Optimization for Next Generation Wireless System Using Radio Over Fiber in Terms of Topology <i>Yeni Nesil Kablosuz Sistemlerin Fiber Üzerinde RF Kullanılarak Topoloji Açısından Optimizasyonu</i> Shwan Asaad OTHMAN, İbrahim TÜRKOĞLU	33-41
4. Effect of Heat Input on Microstructure, Friction and Wear Properties of Fe-Cr-B-C Coating on AISI 1020 Surface Coated by PTA Method <i>Soyafasulyesi Küspesiyle Reaktif Boya giderimi</i> Turan GÜRGENÇ, Cihan ÖZEL	43-52
5. LSE Channel Estimation and Performance Analysis of OFDM Systems <i>OFDM Sistemlerinde LSE Kanal Tahmini ve Performans Analizi</i> Bircan KAMIŞLIOĞLU, Ayhan AKBAL	53-57
6. PI and Fuzzy Logic Control of Photovoltaic Panel Powered Synchronous Boost Converter <i>Fotovoltaik Panel Beslemeli Senkron Artran Çeviricinin PI ve Bulanık Mantık Denetimi</i> Ahmet YÜKSEL, Adnan CORA	59-63
7. Performance Analysis of 20 Gb/s QPSK Modulated Dual Polarization Coherent Optical OFDM Systems <i>20 Gb/s QPSK Modülasyonlu Çift Polarizasyon Eşevreli Optik OFDM Sistemlerinin Performans Analiz</i> Ahmet GÜNER	65-69
8. Handwriting Character Recognition by using Fuzzy Logic <i>Bulanık Mantık ile El Yazısı Tanıma</i> Enes VARDAR, Kaplan KAPLAN, H. Metin ERTUNÇ	71-77
9. TiO₂ Memristor Modelling with LabVIEW <i>LabVIEW ile TiO₂ Memristör Modellemesi</i> Muhammet Emin ŞAHİN, Hasan GÜLER	79-83
10. PWM Control of AC Chopper Fed by Unbalanced 3-Phase Voltage Source <i>Dengesiz 3-Fazlı Gerilim Kaynağı ile Beslenen AA Kıyıcısının PWM Kontrolü</i> Nurbanu MACİT, Sedat SÜNER	85-90
11. A Comparative Study between Matrix Converter Fed Induction Motor Drive and Dual-Matrix Converter Fed Open-End Winding Induction Motor Drive <i>Açık-Uçlu Sargılı Asenkron Motoru Besleyen Çift-Matris Dönüştürücü Sürücüsü ile Asenkron Motoru Besleyen Matris Dönüştürücü Sürücüsünün Bir Karşılaştırması</i> A. BELADEL, A. KOUZOU, A. HAFIFA, S. SUNTER, D. MAHIA	91-99

12. Elliptic Filter Based Noninvasive Blood Pressure Analyze with LabVIEW <i>LabVIEW ile Eliptik Filtre Tabanlı Noninvaziv Kan Basıncı Analizi</i> Duygu KAYA, Mustafa TÜRK, Turgay KAYA.....	101-105
13. Development of Smart Security System for Remote Control Using Small Computer <i>Küçük Bilgisayar Kullanarak Uzaktan Kumanda için Akıllı Güvenlik Sisteminin Geliştirilmesi</i> Huda AL-SAFFAR, Ergun ERÇELEBİ.....	107-112
14. FPGA Implementation of a Chaotic Quadratic Map for Cryptographic Applications <i>Kriptografik Uygulamalar için Kaotik Kuadratik bir Haritanın FPGA Gerçekleştirilmesi</i> Hidayet OĞRAŞ, Mustafa TÜRK.....	113-119

TURKISTAN

Fractal Analysis of Shear-thinning Fluid Flow through Porous Media

Fethi KAMIŞLI

Department of Chemical Engineering, Firat University, Elazığ, Turkey.
fkamisli@firat.edu.tr

(Received: 17. 01. 2017; Accepted: 10. 05. 2017)

Abstract

The fractal capillary models for calculating the volumetric flow rates and permeabilities for Newtonian, power-law, Ellis and Bingham fluids in packed beds are developed by considering fractal nature of the tortuous capillary. The fractal permeability models for Newtonian and non-Newtonian fluids are found to be a function of the tortuosity fractal dimension, the pore-area fractal dimension, sizes of particles and clusters, the effective porosity and the flow behavior of a non-Newtonian fluid. The volumetric flow rate of each fluid as a function of pressure drop are calculated from both the converging-diverging duct approach and the derived expressions in order to compare two models with one another. In addition, hydraulic conductivity is also obtained in terms of the fractal scaling parameters. The volumetric flow rates of shear-thinning fluids, including power-law and Ellis fluids decrease with increasing the tortuosity fractal dimension. It is found that the fractal capillary model for the Newtonian and the Ellis fluids is in good agreement with the converging-diverging duct approach for the considered values of the tortuosity fractal dimension.

Keywords: Shear-thinning fluid, Porous media, Packed bed, Permeability, Fractal modeling.

Gözenekli Ortamda Kayma İnceltmeli Akışkan Akışının Fraktal Analizi

Özet

Newtonian, üs kanunu, Ellis ve Bingham akışkanlarının dolgulu yataklarda hacimsel debilerinin ve geçirgenliklerinin hesaplanması için fraktal modeller, kıvrımlı kanalların fraktal doğası göz önünde bulundurularak geliştirilmiştir. Newtonian ve Newtonian olmayan akışkanlar için fraktal geçirgenlik modeller, kıvrımlılığın fraktal boyutuna, gözenek alanının fraktal boyutuna, taneciklerin ve kümelerin büyüklüğüne, etkin gözenekliliğe ve Newtonian olmayan akış davranışına bağlı olduğu bulunmuştur. Basıncın fonksiyonu olarak herbir akışkanın hacimsel debisi hem yakınsaklık-ırsaklık yaklaşımından hem de modellerin birbiriyle kıyaslanması için geliştirilen ifadeden hesaplanmıştır. Dahası, hidrolik temaslılık fraktal ölçeklendirme parametresi cinsinden ayrıca elde edilmiştir. Üs kanunu ve Ellis akışkanlarını da içine alan kayma inceltmeli akışkanların hacimsel debileri kıvrımlılık fraktal boyutunun artmasıyla azalmaktadır. Newtonian ve Ellis akışkanları için fraktal kılcal model, incelenen kıvrımlılık fraktal boyut değerleri için, yakınsaklık-ırsaklık kanal yaklaşımı ile uyumlu olduğu bulunmuştur.

Anahtar kelimeler: Kayma inceltmeli akışkan, Gözenekli ortamlar, Dolgulu yatak, Geçirgenlik, Fraktal modelleme.

1. Introduction

The flow of fluids through porous media is of great practical importance in many diverse applications, including the production of oil and gas from geological structures, the gasification of coal, the retorting of shale oil, filtration, ground water movement, regenerative heat exchange, surface catalysis of chemical reactions, adsorption, coalescence, dying ion exchange, and

chromatography. Some applications mentioned above involve two or even three fluids, and multidimensional and unsteady flows. Attention here will be confined to steady one-dimensional flow of a single fluid relative to a fixed solid phase. In some applications, the details of volumetric flow rate and thus velocity field are of concern.

In recent years there has been considerable interest shown in the flow of a non-Newtonian fluid in porous media. A lot of liquids encountered in daily life such as most of polymeric liquids, milk, blood and some oil products and their derivative are non-Newtonian. Therefore, the flows of non-Newtonian fluids in porous media are important and have several applications including oil recovery, composite material processing and polymer processing. The creeping flows of Newtonian fluids in porous media such as granular media or packed bed have been studied for several years and have good constitutive equations namely Darcy's law, the Ergun equation and Blake-Kozeny equation. However, the mentioned constitutive equations are not applicable for non-Newtonian fluids or do not give as good results for non-Newtonian fluid as Newtonian ones.

Darcy's law was modified by Bird et al. [1] and Sabiri and Comiti [2] to obtain an equation valid for non-Newtonian fluid flows in porous media. The majority of these models have been derived using the bundle-of-tube approximation employed in the Blake-Kozeny model.

The Saffman-Taylor instability of air invasion into a non-Newtonian fluid in a rectangular Hele-Shaw cell was experimentally studied by Eslami and Taghavi [3]. The non-Newtonian fluid used in the experiments exhibited yield stress, shear-thinning as well as elastic behaviors. They observed that the Bingham number (Ba), the capillary number (Ca), the Weber number (We), the Weissenberg number (Wi), the power-law index and channel aspect ratio ($\delta \gg 1$) are important parameters on viscous flow regimes.

Rheological characterization of biologically immobilized aggregates under non-Newtonian flow was studied by Tijani et al. [4]. They concluded that the scaling relationships based on fractal geometry are vital for quantifying the effects of different laminar conditions on the aggregates' morphology and characteristics such as density, porosity and projected surface area.

The viscous fingering instability of miscible displacement involving a viscoelastic fluid was investigated by Shokri et al. [5] using both linear stability analysis and computational fluid dynamics. They observed that the elasticity has a

significant effect on the fingering instability and the flow was more stabilized when elasticity (Weissenberg number) of the displaced or displacing viscoelastic fluid was increased.

As stated previously, flows of non-Newtonian fluids in porous media have been studied for several years. Balhoff and Thompson [6] developed a macroscopic model for the flow of power-law and Ellis fluids in packed beds using results from the network model based on the functionality of flow in capillary tubes. The model is in general similar to those developed using the bundle-of-tubes approach. They claimed that a developed bundle-of-tubes model cannot be properly used for a wide variety of shear-thinning fluids.

Chhabra et al. [7] published a review paper on the flow of rheologically complex fluids through unconsolidated fixed beds and fluidized beds. They critically evaluated the prediction of macro-scale phenomena of flow regimes, pressure drop in fixed and fluidized beds, minimum fluidization velocity, dispersion and liquid-solid mass transfer.

On the other hand, Yu and Liu [8] developed the fractal-phase permeability and the relative permeability based on the fractal nature of pores in the media. Both the fractal-phase permeability and the relative permeability were found to be a function of the tortuosity fractal dimension, the pore-area fractal dimension, the phase fractal dimension and microstructural parameters. In another study a fractal permeability model based on the fractal characteristics of pores was developed for bi-dispersed porous media by Yu and Cheng [9].

The flowrate of non-Newtonian fluids depends on the pressure drop, rheological properties of the fluid, and geometry of the duct. It may be possible to develop complicated empirical correlations using these variables and data obtained from CFD modeling. Shear-thinning behavior, viscoelasticity, yield stress, time-dependency etc. are features for the most of non-Newtonian materials. However, some of these features such as time-dependent viscosity, yields stress etc. are seldom measured. The development of simple and reliable methods for predicting flowrates of power-law, Ellis and

Bingham fluids flowing through packed beds has been subject for many researchers.

As expressed earlier, Balhoff and Thompson [6] developed approximate equations specific to the flow of shear-thinning fluids in ducts that are representative of throats in the network. They also indicated that some drawbacks exist in the approach of the capillary networks. In theory each throat could be transformed into a unique capillary tube and the resulting capillary network could be used to properly model flow for that specific power-law fluid although this may seem like a reasonable approach, several problems exist with method proposed by Balhoff and Thompson [6].

There is no guarantee that the same capillary network could be used for another power-law fluid with different rheological properties.

An entirely new capillary network would have to be developed to model the flow of other non-Newtonian fluids since the capillary network could not be used for non-Newtonian fluid models such as Bingham and Herschel-Bulkly models and others.

In many situations, it is highly desirable to obtain closed-form equations analogous to Darcy's law to predict the volumetric flow rate of non-Newtonian fluids in porous media.

Therefore, the goal in this study is to develop closed-form equations analogous to Darcy's law to predict the flow rates and permeabilities for non-Newtonian fluids in porous media. The fractal capillary expressions are developed based on the fractal nature of tortuous capillaries for the volumetric flow rates and permeabilities for Newtonian, power-law and Ellis fluids. The computed flow rates from the present model for the considered fluids are compared to theoretical work and data available in the literature and a good agreement for some fluid models is found.

2. Theoretical

Many polymers and suspensions are non-Newtonian, exhibiting shear-dependent viscosity. Therefore, in this subsection it will be given some information regarding models of non-Newtonian fluids that are commonly used in the porous media or any other engineering field. The most successful attempts at describing the steady

stress-shear rate behavior of non-Newtonian fluids have been largely empirical. It would be much more satisfying if one could derive these functions from theories based on molecular structure, but most of the materials of greatest interest are extremely complex and generally inadequate for describing real behavior. Hence, at present observations represent the most reliable source of rheological information. The following represents some of the more common empirical models which have been utilized to represent the various classes of observed non-Newtonian behavior.

Power-law model

The relationship between shear stress-shear rate for a power-law fluid is given by

$$\tau = -m|\dot{\gamma}|^{n-1} \dot{\gamma} \quad \text{and} \quad \eta = m|\dot{\gamma}|^{n-1}$$

where n is power-law index, m consistency index and η shear dependent viscosity of power-law fluid. The power-law model is the most widely used of any model, since it is relatively easy to incorporate into analytical solutions to flow problems, and it can be made to fit almost any data over a limited range of shear rate. In the model the viscosity is also given above. The model predicts that τ vs $\dot{\gamma}$ is straight line on the double logarithmic plot. If the shear rate does not vary widely over a particular flow field, the power-law may provide an adequate description of shear behavior. However, it has two serious drawbacks. For constant values of n and m , it predicts unlimited increasing or decreasing apparent viscosity with shear rate; and it predicts either zero or infinite values in the limit of vanishing shear rate for n greater or less than 1, respectively. This, of course, is not observed in real fluids.

The volumetric flow rate for the power-law fluid can be obtained by integrating the velocity expression the z -direction with respect to r on the cross-sectional area of the capillary as follows:

$$q = \left[\frac{(n\pi)^n R^{3n+1}}{(3n+1)^n 2m} \left(-\frac{dp}{dz} \right) \right]^{1/n} \quad (1)$$

The volumetric flow rate equation for the flow of a power-law fluid through a tortuous capillary tube can be written in the form of Eq. (1). As can be seen from the above equation the flow rate of a power-law fluid must be proportional to the pressure gradient to the power of $1/n$ ($q \propto (dp/dz)^{1/n}$) for a capillary tube. Eq. (1) has to be valid for any capillary tube with slowly-varying radius along the axial direction. In this connection Pearson and Tardy [10] stated that for any geometry the flow rate of power-law fluid must be proportional with the pressure drop to the power of $1/n$ ($q \propto \Delta p^{1/n}$). Therefore, it can be said that a capillary tube must exist that produces some flow rate versus pressure drop as in the original porous medium for a fluid with rheological properties n and m .

Ellis model

The Ellis model uses three parameters. At low shear rates this model approaches Newtonian behavior with a zero shear viscosity, η_0 . At high shear rates power-law behavior is approached with n corresponding to the flow index. In comparison to the power-law the Ellis model is slightly more complicated algebraically, and requires the measurement of an additional parameter. It fits data over a wider range of shear rate than the power-law does, and does not suffer from the *zero shear failure*, the prediction of infinite viscosity at zero shear rates. The Ellis model has been widely used in attempts to describe complex flow of shear-thinning fluids. The shear thinning fluid is defined as of the viscosity decreases with increasing shear rate.

The volumetric flow rate for a non-Newtonian fluid described by Ellis model can be obtained by integrating the velocity expression in the z -direction on the cross-sectional area of a capillary tube as follows:

$$q = \frac{\pi R^4}{8\eta_0} \left(-\frac{dp}{dz} \right) \left[1 + \frac{4}{(\alpha+3)} \left(-\frac{R}{2\tau_{1/2}} \frac{dp}{dz} \right)^{\alpha-1} \right] \quad (2)$$

where η_0 is the low shear viscosity, α flow (power) index in the Ellis model and $\tau_{1/2}$ rheological parameter in the model, respectively. Eq. (2) gives the volumetric flow rate of the Ellis

fluid as a function of the pressure drop, flow index, viscosity of fluid and radius of the capillary tube. As can be seen from Eq. (2) an increase in the pressure gradient in the sufficient level which is equivalent to the sufficiently high shear rate will make the second term in the parenthesis much lower as comparing to the first term, unity. Therefore, the first term in the parenthesis can be neglected and thus the equation becomes equal to the volumetric flow rate of power-law fluid. On the other hand, the low pressure gradient which is equivalent to the low shear rate will make the second term in the parenthesis much lower as comparing to the first term, unity. Hence the second term in the parenthesis can be dropped and thus the equation reduces to the volumetric flow rate of a Newtonian fluid in a capillary tube.

Bingham plastic model

One class fluids, including toothpastes, oil-well drilling mud, sewage sludge, oil paints, margarines, plastic melts, aqueous suspensions of clay, grain and paper pulps, chocolate syrups, aqueous slurries of coal, peat, sand and cement require a finite shear stress to produce any motion. Such fluids are known as Bingham plastics.

The constitutive equation for Bingham plastic model is given by

$$\begin{aligned} \tau_{rz} &= \pm \tau_0 - \mu \frac{dv_z}{dr} \quad |\tau_{rz}| > \tau_0 \\ \frac{dv_z}{dr} &= 0 \quad \text{for } 0 \leq |\tau_{rz}| \leq \tau_0 \end{aligned} \quad (3)$$

Where τ_0 is yield stress and μ is effective viscosity for absolute values of the shear stress in excess of the yield stress. The arbitrary sign preceding τ_0 in Eq. (3) is chosen to be the same as the actual sign of τ_{rz} . Thus if $\tau_{rz} > 0$, the plus sign is chosen, and vice versa. A Bingham plastic does not flow below a certain yield stress τ_0 . When this stress is exceeded, the structure disintegrates and the material behaves like a Newtonian fluid.

The volumetric flow rate for Bingham fluid in a capillary tube consists of the volumetric flow rate obtained by integrating the r -dependent velocity expression with respect to r over the

cross-sectional area between r_0 and R plus the flow rate obtained by use of the constant velocity multiplied with the corresponding cross-sectional

$$q = \frac{\pi}{8\mu} \left(-\frac{dp}{dz} \right) R^4 \left[1 - \frac{8}{3R} \frac{\tau_0}{(-dp/dz)} + \frac{1}{3} \left(\frac{2\tau_0}{R(-dp/dz)} \right)^4 \right] \quad (4)$$

The obtained volumetric flow rate equations for Newtonian and non-Newtonian fluid flows through a straight capillary tube can be expressed in terms of the fractal scaling parameters. In order to express volumetric flow rate equations in terms of the fractal scaling parameters, the brief information regarding to the fractal scaling law is necessary to be given here. Hence the fractal scaling law is briefly explained in the following section.

3. Fractal Theory for Porous Media

A porous medium having various pore sizes can be considered as a bundle of tortuous capillary tubes with variable cross-sectional areas. Let the diameter of a capillary in the medium be λ and its tortuous length along flow direction be $L(\lambda)$. The tortuous nature of capillary requires that $L(\lambda) > L_0$, with L_0 being straight length. For a straight capillary, $L(\lambda) = L_0$. The relationship between the diameter and length of capillaries is given by [9]

$$L = L_0^{D_r} \lambda^{1-D_r} \quad (5)$$

where D_r is the tortuosity fractal dimension, with $1 < D_r < 2$, representing the extent of convolutedness of capillary pathways for fluid flow through a medium. The limiting case of $D_r = 2$, corresponds to a highly tortuous line that fills a plane and Eq. (5) diverges as $\lambda \rightarrow 0$, which is one of the properties of fractal line [8,9].

Since the pores in porous media are analogous to the islands or lakes on earth or spots on engineering surfaces, the cumulative size-distribution of pores or islands should also follow the same fractal scaling law. Therefore, a number

area. Therefore, the volumetric flow rate for a non-Newtonian fluid described by Bingham plastic model is obtained as follows:

of islands or pores whose size is larger than λ is given [6 and references therein] by

$$N(L > \lambda) = \left(\frac{\lambda_{\max}}{\lambda} \right)^{D_f} \quad (6)$$

and derivative of Eq. (6) is

$$-dN = D_f \lambda_{\max}^{D_f} \lambda^{-(D_f+1)} d\lambda \quad (7)$$

where D_f is the pore-area fractal dimension having values between 1 and 2 in two dimensional space. The negative sign in Eq. (7) implies that the island or pore population decreases with the increase of island or pore size and $-dN > 0$. The number of pores from Eq. (6) becomes infinity as $\lambda \rightarrow 0$, which is one of the properties of fractal objects. The total number of pores, islands or spots, from the smallest diameter λ_{\min} to the largest diameter λ_{\max} , can be obtained from Eq. (6) as

$$N_t(L > \lambda) = \left(\frac{\lambda_{\max}}{\lambda_{\min}} \right)^{D_f} \quad (8)$$

Dividing Eq.(7) by (8) yields

$$-\frac{dN}{N_t} = D_f \lambda_{\min}^{D_f} \lambda^{-(D_f+1)} d\lambda = f(\lambda) d\lambda \quad (9)$$

where $f(\lambda) = D_f \lambda_{\min}^{D_f} \lambda^{-(D_f+1)}$ is the probability density function which satisfies following condition

$$f(\lambda) \geq 0 \quad (10)$$

As in the probability theory, the probability density function $f(\lambda)$, should also satisfies the following relationship.

$$\int_{-\infty}^{\infty} f(\lambda) d\lambda = \int_{\lambda_{\min}}^{\lambda_{\max}} f(\lambda) d\lambda = 1 \quad (11)$$

However, substituting the probability density function into Eq. (11) and performing integration yields

$$\int_{\lambda_{\min}}^{\lambda_{\max}} D_f \lambda_{\min}^{D_f} \lambda^{-(D_f+1)} d\lambda = 1 - \left(\frac{\lambda_{\min}}{\lambda_{\max}} \right)^{D_f} \quad (12)$$

Therefore, Eq. (11) satisfies if and only if

$$\left(\frac{\lambda_{\min}}{\lambda_{\max}} \right)^{D_f} \cong 0 \quad (13)$$

Eq. (13) implies that $\lambda_{\min} \ll \lambda_{\max}$ must be satisfied for fractal analysis of a porous medium; otherwise the porous medium is a non-fractal medium. Thus, Eq. (13) can be considered as a criterion whether a porous medium can be characterized by fractal theory and technique. In general $\lambda_{\min} / \lambda_{\max} < 10^{-2}$ in porous media and Eq. (13) holds approximately. Therefore, the fractal theory and technique can be used to analyze properties of porous media in which the condition of $\lambda_{\min} / \lambda_{\max} < 10^{-2}$ is satisfied.

4. Fractal Permeability for non-Newtonian Fluid Flowing in Capillary Tube

Consider a unit cell consisting of a bundle of tortuous capillary tubes with variable cross-

$$Q = \int_{\lambda_{\min}}^{\lambda_{\max}} q(\lambda) (-dN(\lambda)) = \left[\left(\frac{n\pi}{3n+1} \right)^n \frac{\Delta P}{2^{3n+2} m L_0^{D_f}} \right]^{1/n} D_f \lambda_{\max}^{D_f} \int_{\lambda_{\min}}^{\lambda_{\max}} \lambda^{2+D_f/n-D_f} d\lambda \quad (16)$$

Integrating Eq.(16) yields the total volumetric flow rate of a power-law fluid in a unit cell as follows:

sectional areas. The volumetric flow rate, Q , through the unit cell is a sum of the flow rates through all the individual capillaries. The volumetric flow rate of a power-law fluid flowing through a single capillary tube is given by Eq. (1) that can be modified by taking $-dp = \Delta p$, $dz = L(\lambda)$ and $2R = \lambda$ for a single tortuous capillary tube as follows:

$$q(\lambda) = \left[\left(\frac{n\pi}{3n+1} \right)^n \frac{\lambda^{3n+1}}{2^{3n+2} m} \frac{\Delta P}{L(\lambda)} \right]^{1/n} \quad (14)$$

where \square is the hydraulic diameter of a single capillary tube, m is consistency index in power-law model, $\square P$ is the pressure drop and $L(\square)$ is the length of the tortuous capillary tube.

The volumetric flow rate of a Newtonian fluid flowing through a single tortuous capillary tube is recovered from Eq. (14) by taking $n=1$ and $m = \mu$ as follows:

$$q(\lambda) = \frac{\pi \Delta P}{128 \mu} \frac{\lambda^4}{L(\lambda)} \quad (15)$$

The total volumetric flow rate, Q , for either a non-Newtonian fluid or a Newtonian fluid can be obtained by integrating the individual volumetric flow rate, $q(\lambda)$, over the entire range of pore sizes from the minimum pore λ_{\min} to the maximum pore λ_{\max} in a unit cell. The total volumetric flow rate equation for a power-law fluid in a unit cell can be obtained from Eqs. (5), (7) and (14) as follows:

$$Q = \left[\left(\frac{n\pi}{3n+1} \right)^n \frac{\Delta P}{2^{3n+2} m L_0^{D_T}} \right]^{1/n} \frac{D_f}{3 + D_T/n - D_f} \lambda_{\max}^{3+D_T/n} \left[1 - \left(\frac{\lambda_{\min}}{\lambda_{\max}} \right)^{3+D_T/n - D_f} \right] \quad (17)$$

Since $1 < D_T < 2$, $1 < D_f < 2$ and $0 < n < 1$, in any case exponent $3 + D_T/n - D_f > 0$ and $\lambda_{\min}/\lambda_{\max} \approx 10^{-2}$ is criterion for typical fractal

geometry. Therefore, the inside of the second bracket is approximately equal to 1. Consequently, the total volumetric flow rate of a power-law fluid become

$$Q = \left[\left(\frac{n\pi}{3n+1} \right)^n \frac{\Delta P}{2^{3n+2} m L_0^{D_T}} \right]^{1/n} \frac{D_f}{3 + D_T/n - D_f} \lambda_{\max}^{3+D_T/n} \quad (18)$$

Note that the total volumetric flow rate of a Newtonian fluid is recovered from Eq. (18) by taking $n=1$ and $m=\lambda$ as follows:

$$Q = \frac{\pi \Delta P}{128 \mu L_0^{D_T}} \frac{D_f}{3 + D_T - D_f} \lambda_{\max}^{3+D_T} \quad (19)$$

The permeability expressions for a power-law fluid and a Newtonian in the porous medium are obtained using Darcy's law as follows:

$$K_M = \frac{Q}{(\Delta P A / (L_0 m))^{1/n}} = \left[\left(\frac{n\pi}{3n+1} \right)^n \frac{1}{2^{3n+2} L_0^{D_T-1} A} \right]^{1/n} \frac{D_f}{3 + D_T/n - D_f} \lambda_{\max}^{3+D_T/n} \quad (20)$$

In this equation K_M is the permeability for a power-law fluid that is a function of the pore-area fractal dimension, D_f , the tortuosity fractal dimension, D_T , the power-law index, n , and the

structural parameters, A , L_0 and λ_{\max} . The permeability expression for a Newtonian fluid flowing through porous medium is again recovered from Eq. (20) by taking $n=1$ and $m=\lambda$ as follows:

$$K = \frac{Q}{(\Delta P A / (L_0 m))} = \frac{\pi}{128 A L_0^{D_T-1}} \frac{D_f}{3 + D_T - D_f} \lambda_{\max}^{3+D_T} \quad (21)$$

Eq. (21) had been derived by Yu and Cheng [8, 9] for a Newtonian in a porous unit cell. Eq. (21) points out that the permeability for a Newtonian fluid is a function of the pore-area fractal dimension, D_f , the tortuosity fractal dimension, D_T and the structural parameters, A , L_0 and λ_{\max} . If the tortuous capillary tube is considered to be a straight capillary tube ($D_T=1$),

the Eqs. (18) and (20) reduce to the following equations, respectively.

$$Q = \left[\left(\frac{n\pi}{3n+1} \right)^n \frac{\Delta P}{2^{3n+2} m L_0} \right]^{1/n} \frac{D_f}{3 + 1/n - D_f} \lambda_{\max}^{3+1/n} \quad (22)$$

$$K_M = \left[\left(\frac{n\pi}{3n+1} \right)^n \frac{1}{2^{3n+2} A} \right]^{1/n} \frac{D_f}{3 + 1/n - D_f} \lambda_{\max}^{3+1/n} \quad (23)$$

The above equations for the Newtonian case become

$$Q = \frac{\pi \Delta P}{128 \mu L_0} \frac{D_f}{4 - D_f} \lambda_{\max}^4 \quad (24)$$

$$K = \frac{\pi}{128 A} \frac{D_f}{4 - D_f} \lambda_{\max}^4 \quad (25)$$

Eqs.(18)-(25) indicate that the volumetric flow rate and permeability for power-law fluids and Newtonian fluids are very sensitive to the maximum pore size λ_{\max} . Eqs. (22) and (23) point out that the effects of process variables on the volumetric flow rate and permeability for a power-law fluid. The larger pore diameter and pore-area fractal dimension D_f , the larger volumetric flow rate and permeability value. If it is assumed that the consistency index, m , is constant while the power-law index changes, the larger power-law index having value between 0

and 1, the larger volumetric flow rate and permeability value. From Eqs. (22)–(25) it can be seen that the volumetric flow rate and permeability for power-law and Newtonian fluids will reach possible maximum values as the pore-area fractal dimension approaches its possible maximum value of 2 since those quantities, as stated earlier, increase with increasing pore diameter. The pore-area fractal dimension

$D_f = 2$ corresponds to a smooth surface or plane or compact cluster [9]. This means that if it is considered a smooth surface or compact cluster or a circle or a square to be the cross-sectional area of a pore, the pore-area fractal dimension of the cross-section is 2 and the pore volume fraction of the cross-section is 1. Under such a condition the volumetric flow rate and permeability for both fluid cases take their maximum values. Hence, the maximum volumetric flow rate and permeability for a power-law fluid flowing through the unit cell with a single capillary tube or pore are obtained from Eqs. (22) and (23) as the pore-area fractal dimension, D_f , takes its maximum value of 2.

$$Q = \left[\left(\frac{n\pi}{3n+1} \right)^n \frac{\Delta P}{2^{3n+2} m L_0} \right]^{1/n} \frac{2}{3+1/n-2} \lambda_{\max}^{3+1/n} = \left[\left(\frac{n\pi}{3n+1} \right)^n \frac{\Delta P}{2^{3n+2} m L_0} \right]^{1/n} \frac{2}{3+1/n-2} De^{3+1/n} \quad (26)$$

$$K_M = \left[\left(\frac{n\pi}{3n+1} \right)^n \frac{1}{2^{3n+2} A} \right]^{1/n} \frac{2}{3+1/n-2} \lambda_{\max}^{3+1/n} = \left[\left(\frac{n\pi}{3n+1} \right)^n \frac{1}{2^{3n} \pi} \right]^{1/n} \frac{2}{3+1/n-2} De^{(3n-1)/n} \quad (27)$$

For the case of Newtonian fluids, the above equations reduce to the following equations.

$$Q = \frac{\pi \Delta P}{128 \mu L_0} De^4 = \frac{A \Delta P}{32 \mu L_0} De^2 \quad (28)$$

where De can be called equivalent diameter of a unit cell and is taken to be equal to λ_{\max} .

$$K = \frac{\pi}{128 A} \lambda_{\max}^4 = \frac{De^2}{32} \quad (29)$$

Eq. (28) indicates that the present model for power-law and Newtonian fluids is consistent with the physical situation since it is exactly the Hagen-Poiseuille equation for a Newtonian fluid flow through a tube. Therefore, besides Eqs. (28)-(29), Eq. (15) with $D_T = 1$ (and thus $L = L_0$) can be used for obtaining the volumetric flow rate and permeability for a Newtonian fluid flow through the unit cell with a straight capillary tube. However, the volumetric flow rate equation (Eq. 14) developed for a power-law fluid flow through a tube can't be used for obtaining volumetric flow rate of that fluid flow through the unit cell with a

straight capillary tube since Eq. (14) with $D_T = 1$ (and thus $L = L_0$) isn't entirely equal to Eq. (26).

The volumetric flow rate, Q , through the unit cell is a sum of the flow rates through all the individual capillaries. The volumetric flow rate of an Ellis fluid flowing through a single capillary tube is given by Eq. (2) that can be modified by taking $-dp = \Delta P$, $dz = L(\lambda)$ and $2R = \lambda$ for a single tortuous capillary tube as follows:

$$q(\lambda) = \frac{\pi \lambda^4}{128 \eta_0} \frac{\Delta P}{L(\lambda)} \left[1 + \frac{4}{(\alpha + 3)} \left(\frac{\lambda}{4 \tau_{1/2}} \frac{\Delta P}{L(\lambda)} \right)^{\alpha-1} \right] \quad (30)$$

where λ is the hydraulic diameter of a single capillary tube, η_0 is the low shear viscosity of

$$Q = \int_{\lambda_{\min}}^{\lambda_{\max}} q(\lambda) (-dN(\lambda)) = \frac{\pi \Delta P}{128 \eta_0 L_0^{D_T}} D_f \lambda_{\max}^{D_f} \int_{\lambda_{\min}}^{\lambda_{\max}} \left[\lambda^{2+D_T-D_f} + 4 \left(\frac{\Delta P}{4 \tau_{1/2} L_0^{D_T}} \right)^{\alpha-1} \frac{\lambda^{2+\alpha D_T-D_f}}{\alpha+3} \right] d\lambda \quad (31)$$

Integrating Eq.(31) yields the total volumetric flow rate of an Ellis fluid in a unit cell as follows:

$$Q = \frac{\pi \Delta P}{128 \eta_0 L_0^{D_T}} D_f \lambda_{\max}^{D_f} \left[\frac{\lambda_{\max}^{3+D_T}}{3+D_T-D_f} \left(1 - \left(\frac{\lambda_{\min}}{\lambda_{\max}} \right)^{3+D_T-D_f} \right) + \frac{4 \lambda_{\max}^{3+\alpha D_T}}{(\alpha+3)(3+\alpha D_T-D_f)} \left(\frac{\Delta P}{4 \tau_{1/2} L_0^{D_T}} \right)^{\alpha-1} \left(1 - \left(\frac{\lambda_{\min}}{\lambda_{\max}} \right)^{3+\alpha D_T-D_f} \right) \right] \quad (32)$$

Since $1 < D_T < 2$ and $1 < D_f < 2$, in any case exponent $3+D_T-D_f > 0$ and $3+\alpha D_T-D_f > 0$ and $\lambda_{\min} / \lambda_{\max} \approx 10^{-2}$ is criterion for typical fractal geometry. Therefore,

Ellis Fluid, $\tau_{1/2}$ is the rheological parameter, ΔP is the pressure drop and $L(\lambda)$ is the length of the tortuous capillary tube.

The total volumetric flow rate, Q , for either a non-Newtonian fluid or a Newtonian fluid can be obtained by integrating the individual volumetric flow rate, $q(\lambda)$, over the entire range of pore sizes from the minimum pore λ_{\min} to the maximum pore λ_{\max} in a unit cell. The total volumetric flow rate equation for an Ellis fluid in a unit cell can be obtained from Eqs. (5), (7) and (30) as follows:

the ratio of $\lambda_{\min} / \lambda_{\max}$ is negligible in the above equation. In other words, the insides of the parentheses are approximately equal to 1. Consequently, the total volumetric flow rate of an Ellis fluid becomes

$$Q = \frac{\pi \Delta P \lambda_{\max}^{3+D_T}}{128 \eta_0 L_0^{D_T}} \frac{D_f}{3+D_T-D_f} \left[1 + \frac{4(3+D_T-D_f)}{(\alpha+3)(3+\alpha D_T-D_f)} \left(\frac{\lambda_{\max}^{D_T} \Delta P}{4 \tau_{1/2} L_0^{D_T}} \right)^{\alpha-1} \right] \quad (33)$$

The permeability expressions for an Ellis fluid in the porous medium are obtained using Darcy's law as follows:

$$K = \frac{Q}{(\Delta P A / (L_0 \eta_0))} = \frac{\pi \lambda_{\max}^{3+D_T}}{128 A L_0^{D_T-1}} \frac{D_f}{3 + D_T - D_f} \left[1 + \frac{4(3 + D_T - D_f)}{(\alpha + 3)(3 + \alpha D_T - D_f)} \left(\frac{\lambda_{\max}^{D_T} \Delta P}{4 \tau_{1/2} L_0^{D_T}} \right)^{\alpha-1} \right] \quad (34)$$

K is the permeability for an Ellis fluid that is a function of the pore-area fractal dimension, D_f , the tortuosity fractal dimension, D_T , the flow index, α , rheological parameter, $\tau_{1/2}$, and

the structural parameters, A, L_0 and λ_{\max} . If the tortuous capillary tube is considered to be a straight capillary tube ($D_T = 1$), the Eqs. (33) and (34) reduce to the following equations, respectively.

$$Q = \frac{\pi \Delta P \lambda_{\max}^4}{128 \eta_0 L_0} \frac{D_f}{4 - D_f} \left[1 + \frac{4(4 - D_f)}{(\alpha + 3)(3 + \alpha - D_f)} \left(\frac{\lambda_{\max} \Delta P}{4 \tau_{1/2} L_0} \right)^{\alpha-1} \right] \quad (35)$$

$$K = \frac{\pi \lambda_{\max}^4}{128 A} \frac{D_f}{4 - D_f} \left[1 + \frac{4(4 - D_f)}{(\alpha + 3)(3 + \alpha - D_f)} \left(\frac{\lambda_{\max} \Delta P}{4 \tau_{1/2} L_0} \right)^{\alpha-1} \right] \quad (36)$$

Eqs.(33)-(36) indicate that the volumetric flow rate and permeability for an Ellis fluid are very sensitive to the maximum pore size λ_{\max} as in the power-law and Newtonian fluids. Eqs. (35) and (36) show that the effects of process variables on the volumetric flow rate and permeability for an Ellis fluid. The larger pore diameter and pore-area fractal dimension D_f , the larger volumetric flow rate and permeability value. Furthermore, the larger flow index, the larger volumetric flow rate and permeability value. Eqs. (35)–(36) indicate that the volumetric flow rate and permeability for an Ellis fluid will reach possible maximum values as the pore-area fractal dimension approaches its possible maximum value of 2 since those quantities, as stated earlier, increase with increasing pore diameter. The pore-area fractal dimension $D_f = 2$ corresponds to a smooth surface or plane or compact cluster [9]. This means that if it is considered a smooth surface or compact cluster or a circle or a square to be the cross-sectional area of a pore, the pore-area fractal dimension of the cross-section is 2 and the pore volume fraction of the cross-section is 1.

Under such a condition the volumetric flow rate and permeability for Ellis model take their maximum values. Hence, the maximum volumetric flow rate and permeability for an Ellis fluid flowing through the unit cell with a single capillary tube or pore are obtained from Eqs. (35) and (36) as the pore-area fractal dimension, D_f , takes its maximum value of 2.

$$Q = \frac{\pi \Delta P \lambda_{\max}^4}{128 \eta_0 L_0} \left[1 + \frac{8}{(\alpha + 3)(1 + \alpha)} \left(\frac{\lambda_{\max} \Delta P}{4 \tau_{1/2} L_0} \right)^{\alpha-1} \right] \quad (37)$$

$$K = \frac{\pi \lambda_{\max}^4}{128 A} \left[1 + \frac{8}{(\alpha + 3)(1 + \alpha)} \left(\frac{\lambda_{\max} \Delta P}{4 \tau_{1/2} L_0} \right)^{\alpha-1} \right] \quad (38)$$

Eq. (37) is exactly the same as Eq. (30) with $D_T = 1$ (and thus $L = L_0$) for the limiting values of $\alpha = 0, 1$ and 2. Therefore, the present model is consistent with the physical situation. Hence, besides Eqs. (37)-(38), Eq. (30) with $D_T = 1$ (and consequently $L = L_0$) can be used for obtaining the volumetric flow rate and permeability for an

Ellis fluid flow through the unit cell with a straight capillary tube as α takes the values of 0, 1 and 2. Eq. (30) can't be used for obtaining volumetric flow rate of an Ellis fluid flow through the unit cell with a straight capillary tube when α takes a value other than the values of 0, 1 and 2. As stated previously, the volumetric flow rate, Q , through the unit cell is a sum of the flow rates

$$q(\lambda) = \frac{\pi \lambda^4}{128 \mu L(\lambda)} \frac{\Delta P}{L(\lambda)} \left[1 - \frac{16 \tau_0}{3 \lambda (\Delta P / L(\lambda))} + \frac{1}{3} \left(\frac{4 \tau_0}{\lambda \Delta P / L(\lambda)} \right)^4 \right] \quad (39)$$

where λ is the hydraulic diameter of a single capillary tube, μ is the effective viscosity for absolute values of the shear stress in excess of the yield stress, τ_0 is the yield stress, ΔP is the pressure drop and $L(\lambda)$ is the length of the tortuous capillary tube. The total volumetric flow rate, Q , for either a non-Newtonian fluid or a

$$Q = \int_{\lambda_{\min}}^{\lambda_{\max}} q(\lambda) (-dN(\lambda))$$

$$= \frac{\pi \Delta P}{128 \mu L_0^{D_T}} D_f \lambda_{\max}^{D_f} \int_{\lambda_{\min}}^{\lambda_{\max}} \left[\lambda^{2+D_T-D_f} - \frac{16 \tau_0 L_0^{D_T}}{3 \Delta P} \lambda^{2-D_f} + \frac{1}{3} \left(\frac{4 \tau_0 L_0^{D_T}}{\Delta P} \right)^4 \lambda^{2-3D_T-D_f} \right] d\lambda \quad (40)$$

Integrating Eq. (40) gives the total volumetric flow rate of a Bingham fluid versus pressure drop in a unit cell as follows:

$$Q = \frac{\pi \Delta P}{128 \mu L_0^{D_T}} \frac{D_f \lambda_{\max}^{3+D_T}}{3+D_T-D_f} \left[1 - \left(\frac{\lambda_{\min}}{\lambda_{\max}} \right)^{3+D_T-D_f} - \frac{16 \tau_0 L_0^{D_T}}{3 \Delta P \lambda_{\max}^{D_T}} \frac{3+D_T-D_f}{3-D_f} \left(1 - \left(\frac{\lambda_{\min}}{\lambda_{\max}} \right)^{3-D_f} \right) + \frac{1}{3} \frac{3+D_T-D_f}{(3-3D_T-D_f)} \left(\frac{4 \tau_0 L_0^{D_T}}{\Delta P \lambda_{\max}^{D_T}} \right)^4 \left(1 - \left(\frac{\lambda_{\min}}{\lambda_{\max}} \right)^{3-3D_T-D_f} \right) \right] \quad (41)$$

Since $1 < D_T < 2$ and $1 < D_f < 2$, in any case exponent $3+D_T-D_f > 0$ and $3-D_f > 0$ and $3-3D_T-D_f < 0$. By considering the criterion, $\lambda_{\min} / \lambda_{\max} \approx 10^{-2}$, for a typical fractal

through all the individual capillaries. The volumetric flow rate of a Bingham fluid flowing through a single capillary tube is given by Eq. (4) that can be modified by taking $-dp = \Delta p$, $dz = L(\lambda)$ and $2R = \lambda$ for a single tortuous capillary tube as follows:

Newtonian fluid can be obtained by integrating the individual volumetric flow rate, $q(\lambda)$, over the entire range of pore sizes from the minimum pore λ_{\min} to the maximum pore λ_{\max} in a unit cell. The total volumetric flow rate equation for a Bingham fluid in a unit cell can be obtained from Eqs. (5), (7) and (39) as follows:

geometry the terms $\lambda_{\min} / \lambda_{\max}$ with the exponents $3+D_T-D_f > 0$ and $3-D_f > 0$ is negligible in the above equation. However, as $\lambda_{\min} / \lambda_{\max}$ is equal to 10⁻², the term $\lambda_{\min} / \lambda_{\max}$ with the

exponents $3-3D_T-D_f < 0$ goes to an unacceptable large value that can be considered as an unrealistic physical situation. Under the light

of above arguments, the total volumetric flow rate of a Bingham fluid becomes

$$Q = \frac{\pi \Delta P}{128 \mu L_0^{D_r}} \frac{D_f \lambda_{\max}^{3+D_r}}{3+D_T-D_f} \left[1 - \frac{16 \tau_0 L_0^{D_r}}{3 \Delta P \lambda_{\max}^{D_r}} \frac{3+D_T-D_f}{3-D_f} + \frac{1}{3} \frac{3+D_T-D_f}{(3-3D_T-D_f)} \left(\frac{4 \tau_0 L_0^{D_r}}{\Delta P \lambda_{\max}^{D_r}} \right)^4 \left(1 - \left(\frac{\lambda_{\min}}{\lambda_{\max}} \right)^{3-3D_T-D_f} \right) \right] \quad (42)$$

The permeability expressions for a Bingham fluid in the porous medium are obtained using Darcy's law as follows

$$K = \frac{Q}{(\Delta P A / (L_0 \mu))} = \frac{\pi \lambda_{\max}^{3+D_r}}{128 A L_0^{D_r-1}} \frac{D_f}{3+D_T-D_f} \left[1 - \frac{16 L_0^{D_r} \tau_0 (3+D_T-D_f)}{3(3-D_f) \lambda_{\max}^{D_r} \Delta P} + \frac{1}{3} \frac{(3+D_T-D_f)}{(3-3D_T-D_f)} \left(\frac{4 \tau_0 L_0^{D_r}}{\lambda_{\max}^{D_r} \Delta P} \right)^4 \left(1 - \left(\frac{\lambda_{\min}}{\lambda_{\max}} \right)^{3-3D_T-D_f} \right) \right] \quad (43)$$

K is the permeability for a Bingham that is a function of the pore-area fractal dimension, D_f , the tortuosity fractal dimension, D_T , the yield stress, τ_0 , and the structural parameters, A, L_0, λ_{\min} and λ_{\max} .

If the tortuous capillary tube is considered being a straight capillary tube ($D_T = 1$), the Eqs. (42) and (43) reduce to the following equations, respectively.

$$Q = \frac{\pi \Delta P}{128 \mu L_0} \frac{D_f \lambda_{\max}^4}{4-D_f} \left[1 - \frac{16 \tau_0 L_0}{3 \Delta P \lambda_{\max}} \frac{4-D_f}{3-D_f} - \frac{4-D_f}{3 D_f} \left(\frac{4 \tau_0 L_0}{\Delta P \lambda_{\max}} \right)^4 \left(1 - \left(\frac{\lambda_{\min}}{\lambda_{\max}} \right)^{-D_f} \right) \right] \quad (44)$$

$$K = \frac{\pi}{128 A \mu} \frac{D_f \lambda_{\max}^4}{4-D_f} \left[1 - \frac{16 \tau_0 L_0}{3 \Delta P \lambda_{\max}} \frac{4-D_f}{3-D_f} - \frac{4-D_f}{3 D_f} \left(\frac{4 \tau_0 L_0}{\Delta P \lambda_{\max}} \right)^4 \left(1 - \left(\frac{\lambda_{\min}}{\lambda_{\max}} \right)^{-D_f} \right) \right] \quad (45)$$

Eqs.(44)-(45) indicate that the volumetric flow rate and permeability for a Bingham fluid are very sensitive to the maximum pore size λ_{\max} as in the other fluid models such as the Ellis, the power-law and the Newtonian. Eqs. (44) and (45) show that the effects of process variables on the volumetric flow rate and permeability for a

Bingham fluid. The larger pore diameter and pore fractal dimension D_f , the larger volumetric flow rate and permeability value. Eqs. (44) –(45) indicate that the volumetric flow rate and permeability for a Bingham fluid will reach possible maximum values as the pore area fractal

dimension approaches its possible maximum value of 2 since those quantities, as stated earlier, increase with increasing pore diameter. The pore area fractal dimension $D_f = 2$ corresponds to a smooth surface or plane or compact cluster [9]. This means that if it is considered a smooth surface or compact cluster or a circle or a square to be the cross-sectional area of a pore, the pore fractal dimension of the cross-section is 2 and the

$$Q = \frac{\pi \Delta P \lambda_{\max}^4}{128 \mu L_0} \left[1 - \frac{32 \tau_0 L_0}{3 \Delta P \lambda_{\max}} - \frac{1}{3} \left(\frac{4 \tau_0 L_0}{\Delta P \lambda_{\max}} \right)^4 \left(1 - \left(\frac{\lambda_{\min}}{\lambda_{\max}} \right)^{-2} \right) \right] \quad (46)$$

$$K = \frac{\pi \lambda_{\max}^4}{128 A \mu} \left[1 - \frac{32 \tau_0 L_0}{3 \Delta P \lambda_{\max}} - \frac{1}{3} \left(\frac{4 \tau_0 L_0}{\Delta P \lambda_{\max}} \right)^4 \left(1 - \left(\frac{\lambda_{\min}}{\lambda_{\max}} \right)^{-2} \right) \right] \quad (47)$$

Eq. (46) gives totally different result from Eq. (39) with $D_T = 1$ (and consequently $L = L_0$) although identical equations for other fluid models give approximately similar results. As mentioned previously, the flow rate equation obtained for a Newtonian fluid flow through the unit cell with a straight capillary tube is the same as that obtained for a Newtonian fluid flow through a tube. For other fluid models namely the power-law and the Ellis models the flow rate equations obtained for flow through the unit cell with a straight capillary tube are approximately similar to those obtained for flow through a tube. Unfortunately the similar agreement between the two flow rate equations for flow of a Bingham fluid through the unit cell with a straight capillary tube (Eq. 46) and through a tube (Eq. 39) is not observed, which is clearly seen in the comparison of Eq. (46) and Eq. (39) with $D_T = 1$ (and thus $L = L_0$). As can be seen from Eq. (46) the term of $(\lambda_{\min} / \lambda_{\max})^{-2}$ takes a value of 104 as the ratio of $\lambda_{\min} / \lambda_{\max}$ takes a value of 10-2 that is used as a criterion whether a porous medium can be characterized by fractal theory and technique. Therefore, it can be said that the equations of the volumetric flow rate (Eq. 46) and permeability (Eq. 47) for a Bingham fluid flow through the unit

pore volume fraction of the cross-section is 1. Under such a condition the volumetric flow rate and permeability for the Bingham model take their maximum values. Hence, the maximum volumetric flow rate and permeability for a Bingham fluid flowing through the unit cell with a single capillary tube or pore are obtained from Eqs. (44) and (45) as the pore-area fractal dimension, D_f , takes its maximum value of 2.

cell with a straight capillary tube will not give the correct results since the term of $\lambda_{\min} / \lambda_{\max}$ could not be dropped from those equations completely. In other words, the present approach based on the fractal characteristics of pores in the media is not valid for obtaining the volumetric flow rate of the Bingham fluid and thus permeability.

5. Volumetric Flow Rates with Hydraulic Conductivity in a Single Tortuous Capillary Tube

Eq. (19) expressed in terms of the fractal scaling parameters can be used for obtaining volumetric flow rate of a Newtonian fluid flow in a single tortuous capillary tube. As expressed earlier the tortuosity influences the volumetric flow rates of non-Newtonian and Newtonian fluids as evidenced in Eqs. (18), (19), (33) and (42). On the other hands, the volumetric flow rate of a Newtonian fluid in a converging-diverging duct (see Fig. 1) is given by Balhoff and Thompson [6].

$$q = \frac{g}{\mu} \Delta P \quad (48)$$

where ΔP stands for the pressure drop along the converging-diverging duct, μ the viscosity of the Newtonian fluid and g hydraulic conductivity. The hydraulic conductivity for the converging-diverging duct is given by

$$g = \frac{\pi R_d^4}{8l_0} \quad (49)$$

where R_d is the duct geometric constant and given by

$$R_d = \left(\frac{8lg}{\pi} \right) (0.47\gamma_R^3 - 1.34\gamma_R^2 + 1.19\gamma_R + 0.68) \quad (50)$$

which was numerically determined by Balhoff and Thompson [6] where l is the pore-to-pore distance and γ_R is the aspect ratio and taken to be 0.3. R_d is also equals to the radius of capillary, R for a straight capillary tube. The converging-diverging duct is schematically shown in Fig. 1. As can be seen from the figure the aspect ratio is 0.3, the pore-to-pore distance is 1 cm, the outside diameter is 0.5 cm and hydraulic conductivity is $6.83 \times 10^{-5} \text{ cm}^3$ [6].

One can obtain the hydraulic conductivity in terms of the fractal scaling parameters by comparing Eq. (19) with Eq. (48) as follows:

$$Q = \left(\left(\frac{n}{3n+1} \right)^n \frac{4\pi^{n-1} R^{3(n-1)} D_f^{n-1} (3+D_T-D_f) g \Delta p}{m(3+D_T/n-D_f)} \right)^{1/n} = \left(\frac{g}{\mu_F} \Delta p \right)^{1/n} \quad (52)$$

where

$$\mu_F = m \frac{\pi}{4} \left(\frac{3n+1}{n\pi} \right)^n \frac{(3+D_T/n-D_f)^n}{D_f^{n-1} (3+D_T-D_f)} R^{3-3n}$$

and g is given by Eq. (51).

$$Q = \frac{g \Delta P}{\eta_0} \left[1 + \frac{4(3+D_T-D_f)}{(\alpha+1)(3+\alpha D_T-D_f)} \left(\frac{4(3+D_T-D_f)}{\pi D_f R^3 \tau_{1/2}} g \Delta P \right)^{\alpha-1} \right] = \frac{g \Delta P}{\eta_0} \left[1 + \left(\frac{g}{\mu_E} \Delta P \right)^{\alpha-1} \right] \quad (53)$$

where g is given by Eq. (51) and μ_E is equal to

$$g = \frac{D_f}{3+D_T-D_f} \left(\frac{\pi R^{3+D_T}}{2^{4-D_T} L_0^{D_T}} \right) \quad (51)$$

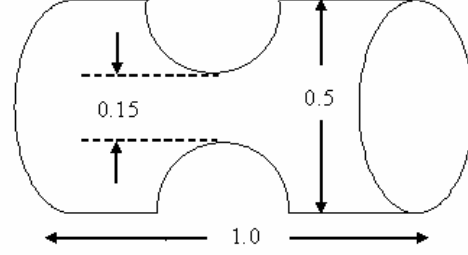


Figure 1. Schematic of axis-symmetric converging-diverging duct

As can be seen from Eq. (51) the hydraulic conductivity is independent of the fluid properties but dependent on the structural parameters (R, L_0, D_T and D_f) of a capillary tube or duct. The volumetric flow rate of a power-law fluid flow through the unit cell with a straight capillary tube, in terms of the fractal scaling parameters, is given by Eq. (18) and can be expressed in terms of the hydraulic conductivity as follows:

Eq. (48) is recovered from the above equation by setting $n = 1$ and $m = \square$ with the g given by Eq. (51). The volumetric flow rate of an Ellis fluid flow through the unit cell with a straight capillary tube, in terms of the fractal scaling parameters, is given by (33) and can be expressed in terms of the hydraulic conductivity as follows:

$$\mu_E = \frac{\pi}{4} \tau_{1/2} D_f R^3 \left(\frac{(\alpha+3)}{4} \right)^{1/(\alpha-1)} \left(\frac{3 + \alpha D_T - D_f}{(3 + D_T - D_f)^\alpha} \right)^{1/(\alpha-1)}$$

tube, in terms of the fractal scaling parameters, is given by (42) and can be expressed in terms of the hydraulic conductivity as follows:

The volumetric flow rate of a Bingham fluid flow through the unit cell with a straight capillary

$$Q = \frac{g \Delta P}{\mu} \left[1 - \frac{D_f}{3 - D_f} \frac{\pi R^3 \tau_0}{3 g \Delta P} + \frac{1}{3} \frac{(3 + D_T - D_f)}{(3 - 3D_T - D_f)} \left(\frac{\pi D_f R^3 \tau_0}{4 g \Delta P (3 + D_T - D_f)} \right)^4 \left(1 - \left(\frac{\lambda_{\min}}{\lambda_{\max}} \right)^{3-3D_T-D_f} \right) \right]$$

The above equation can be rearranged as follows:

$$Q = \frac{g \Delta P}{\mu} \left[1 - \frac{1}{3} \frac{\mu_{B1}}{g \Delta P} + \frac{1}{3} \left(\frac{\mu_{B2}}{4 g \Delta P} \right)^4 \left(1 - \left(\frac{\lambda_{\min}}{\lambda_{\max}} \right)^{3-3D_T-D_f} \right) \right] \quad (54)$$

where $\mu_{B1} = \pi R^3 \tau_0 \left(\frac{D_f}{3 - D_f} \right)$ and

$$\mu_{B2} = \pi R^3 \tau_0 \left(\frac{D_f}{(3 + D_T - D_f)^3 (3 - 3D_T - D_f)} \right)^{1/4}$$

As stated previously, the term of $(\lambda_{\min}/\lambda_{\max})^{3-3D_T-D_f}$ in Eq. (54) takes a value of 10^4 as the ratio of $\lambda_{\min}/\lambda_{\max}$ takes the value of 10^{-2} . Therefore, it can be said that the equation of the volumetric flow rate (Eq. 54) for a Bingham fluid flow through the unit cell with a straight capillary tube will not give the correct results since the term of $\lambda_{\min}/\lambda_{\max}$ could not be dropped from the equation completely.

Here τ_0 is yield stress and g (hydraulic conductivity) is given by Eq. (51). Yield stress fluids require a minimum stress to initiate flow. In order to correctly model flow of these fluids, the equation for flow must accurately predict the applied pressure drop that yields the flow.

After obtaining the volumetric flow rates for the considered fluid models in terms of the fractal scaling parameters, we can also obtain an equation for apparent viscosity of power-law fluids in terms of the fractal scaling parameters easily. In order to obtain the apparent viscosity of the power-law fluid in the unit cell with a straight capillary tube, the strain tensor has to be

determined. Therefore, one has to examine the flow of the power-law fluid flow through the unit cell with a straight capillary tube. The only non-vanishing velocity gradient in the tubular flow is dv_z/dr . The rate of strain tensor reduces to following expression [11].

$$\dot{\gamma} = \sqrt{\frac{1}{2}(\dot{\gamma} : \dot{\gamma})} = \sqrt{\left(\frac{dv_z}{dr} \right)^2} = \left| \frac{dv_z}{dr} \right| \quad (55)$$

In tubular flow for all r , $dv_z/dr < 0$; therefore the absolute value of the strain rate has to be equal to $-dv_z/dr$. Thus, from Eqs. (55) and (18) the strain rate in terms of the fractal scaling parameters for the power-law fluid can be written as follows:

$$\dot{\gamma} = \left(-\frac{R}{2m} \frac{dp}{dz} \right)^{1/n} = \frac{3 + D_T/n - D_f}{D_f} \left(\frac{3n+1}{n\pi} \right) \frac{Q}{R^3} \quad (56)$$

and the apparent viscosity for a power-law fluid is given by

$$\eta_{app} = m \dot{\gamma}^{n-1} \quad (57)$$

where m is the consistency index and n the power-law index. Combining Eqs. (56) and (57) yields the apparent viscosity in terms of the fractal scaling parameters.

$$\eta_{app} = m \left(\frac{\Delta P R^{D_T}}{2^{2-D_T} m L_0^{D_T}} \right)^{\frac{n-1}{n}} = m \left(\frac{3 + D_T/n - D_f}{D_f} \left(\frac{3n+1}{n\pi} \right) \frac{Q}{R^3} \right)^{n-1} \quad (58)$$

Eq. (58) represents the fractal expression for apparent viscosity of power-law fluids. This expression shows the influences of parameters on the viscosity. As can be seen from Eq. (57) the apparent viscosity of power-law fluids depends on the velocity gradient and power-law index and decreases with increasing the velocity gradient since the values of power-law index vary between 0 and less than 1 for pseudo plastic fluids. Furthermore, it is well-known that the velocity gradient depends very much on the pressure gradient and size of geometry. Therefore, every parameter that increases the velocity gradient will cause the viscosity of fluid to decrease. Thus, it can be said that the apparent viscosity of power-law fluids decreases with increasing the pressure gradient and radius of pore as seen from Eq. (58). On the other hand, an increase in the value of the tortuosity fractal dimension, D_T and the length of pore, L_0 will decrease the flow velocity in the pore and thus affects the viscosity of power-law fluid in affirmative way. In other words, a decrease in viscosity of a power-law fluid by increasing shear rate will be hindered by increasing the tortuosity fractal dimension and the length of pore.

6. Results and Discussion

Tortuosity factor can be calculated from the empirical equations that relate tortuosity to porosity in porous media. The tortuosity fractal dimension D_T can be calculated from a relationship between the tortuosity and structural parameters such as R and L_0 . There are the number of relationships between tortuosity and porosity as indicated by Chhabra et al. [7]. The tortuosity factor, T , defined as L/L_0 . Chhabra et al. [7] reported that the considerable confusion exists in the literature regarding the value and the meaning of tortuosity factor T . Some discussion and equations ($T = \sqrt{2}$, $T = 1/\varepsilon$ and $T = 1/\sqrt{\varepsilon}$) regarding tortuosity factor are given in their

paper. The following equation was given by Comiti and Renaud [12].

$$T = 1 + B \ln(1/\varepsilon) \quad (59)$$

where ε is the porosity and the value of constant B depends on the shape of packing and of flow particle configuration (for example, $B = 0.41$ for tightly packed spheres, $B = 3.2$ for square based parallelepipedal particles of height-to-size ratio equal to 0.1 tightly packed in cylindrical column). Furthermore, Dharamadhikari and Kale [13] claimed that the tortuosity factor is function of the flow rate for polymer solutions.

The relationship between the tortuosity fractal dimension and tortuosity in porous media is given by Yu [14].

$$D_T = 1 + \frac{\ln T}{\ln(L_0/2R)} \quad (60)$$

In two-dimensional space the porosity for Fig. 1 can be obtained as follows:

$$\varepsilon = \frac{V_t - V_p}{V_t} = \frac{0.5 \times 0.1 - \pi \times 0.35^2 / 4}{0.5 \times 0.1} = 0.8076$$

where V_t is the total volume of the cylindrical cell and V_p is the volume of spherical particle in the two-dimensional space. The tortuosity can be calculated from Eq. (59) with the use of the obtained porosity and taking $B = 0.41$, and then the tortuosity fractal dimension can be obtained from Eq. (60). However, in order to obtain the tortuosity fractal dimension one needs the radius and straight length of the tortuous capillary. Balhoff and Thompson [6] performed the FEM simulations on the power-law fluid in a converging-diverging duct. They obtained different dimensions for the structural parameters (length and radius of capillary) at each value of power-law index n . For instance, the structural parameters R and L were respectively obtained to

be 0.106 cm and 0.731 cm for a value of $n = 0.30$ while those parameters were found to be 0.097 cm and 0.501 cm for a value of $n = 0.80$, respectively. Note that in their study the structural parameters vary with power-law index to match the FEM data which shows the weakness of their network model.

In order to compare the present model to the converging-diverging duct approach, the average values of radii and lengths used in that study are taken to be the radius and straight distance of tortuous capillary tube in the present investigation. Therefore, R , L_0 are taken to be 0.102 cm and 0.620 and thus the tortuosity fractal dimension D_T is found to be 1.0752 from Eqs. (59) and (60).

A determined value of the tortuosity fractal dimension from relationships among porosity, tortuosity and the tortuosity fractal dimension can be used in Eq. (52) with $n = 1$ and $D_f = 2$, Eq. (52) with $D_f = 2$ and Eq. (53) with $D_f = 2$ to obtain the volumetric flow rates versus pressure drops for a Newtonian fluid, a power-law fluid and an Ellis fluid, respectively. The converging-diverging duct can be transformed into a single fractal capillary with the structural parameters, $R = 0.102$ cm, $L_0 = 0.620$ cm and $D_T = 1.0752$ that do not vary with n for the power-law model and \square for the Ellis model. The determined value for the tortuosity fractal dimension ($D_T = 1.0752$) is used in the flow rate equations to determine an agreement or a disagreement between the fractal capillary model and the converging-diverging duct approach. Furthermore, values of the tortuosity fractal dimension are varied around the determined value to examine how the volumetric flow rates for the considered fluid models change.

In the converging-diverging duct approach the equation which gives the volumetric flow rate of power-law fluid is given as follows [6].

$$q = \left[\frac{4g}{m\pi R_d^{3-3n}} \left(\frac{n\pi}{3n+1} \right)^n \Delta p \right]^{1/n} \quad (61)$$

where g is hydraulic conductivity and equal to 6.83×10^{-5} cm³ and m is consistency index and R_d is duct geometric constant given by Eq. (50).

In the converging-diverging duct approach the volumetric flow rate of a power-law fluid as a function of pressure drop is calculated using Eq. (61) with $g = 6.83 \times 10^{-5}$, $m = 1$ and Eq. (50).

On the other hand, the fractal expressions are developed based on the fractal nature of tortuous capillaries in a porous media. In other words, it is assumed that the converging-diverging duct can be transformed into a single fractal capillary.

Fig. 2 shows the volumetric flow rate of a Newtonian fluid versus pressure drop for various values of the tortuosity fractal dimension, D_T . Fig. 2 is depicted using Eq. (52) with $n = 1$, $m = 1$ and $D_f = 2$ and Eq. (61) with $n = 1$ for the fractal capillary model and the converging-diverging duct approach, respectively. As can be seen in Fig. 2 the fractal capillary model and converging-diverging duct approach are in good agreement as the tortuosity fractal dimension has a value around the determined value of 1.0752. The deviation between the two models for flow rate of a Newtonian fluid increases with increasing the tortuosity fractal dimension. Moreover, the deviation slightly increases with increasing pressure drop. In whole computations the hydraulic conductivity is taken to be equal to Eq. (51) in the fractal capillary model equations and 6.83×10^{-5} in the converging-diverging duct approach. In other words, the constant value of $g = 6.83 \times 10^{-5}$ is not used in none of the fractal capillary model equations but the converging-diverging duct approach. In order to compare the converging-diverging duct approach with the fractal capillary model, the volumetric flow rates of power-law fluids obtained from both models (Eq. (61) for the converging-diverging duct approach, and Eqs. (14) and (52) for the fractal capillary model) are drawn in Fig. 3, Figs. 4a and 4b as a function of pressure drop.

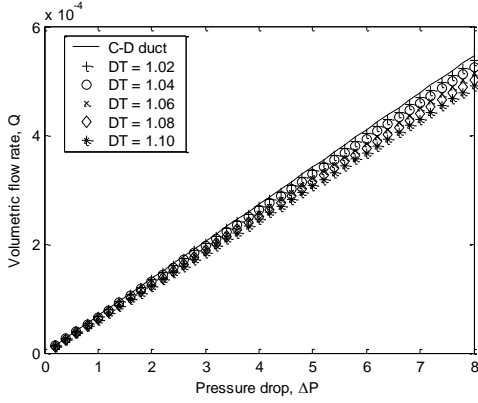


Figure 2. Variation of the volumetric flow rate of Newtonian fluids as a function of pressure drop

The volumetric flow rate for a power-law fluid with $n = 0.8$ as a function of pressure drop is illustrated in Fig. 3. The figure is depicted using Eq. (52) with $D_f = 2$ and Eq. (71) for the fractal capillary model and the converging-diverging duct approach, respectively. As can be seen in the figure the agreement between the fractal capillary model and the converging-diverging duct becomes better when values of the tortuosity fractal dimension approaches 1.0. In other words, the deviation between the two models becomes worst as values of the tortuosity fractal dimension go away from 1.0. Furthermore, the deviation between the two models is dependent on the pressure drop and increases with increasing pressure drop. Fig. 4a is sketched using Eq. (14) with the equivalent parameters of $L(\lambda)$ (Eq. 5) for obtaining the volumetric flow rate of a power-law fluid ($n = 0.3$) flow through a single tortuous capillary tube as a function of pressure drop. Fig. 4b is depicted using Eq. (52) with $D_f = 2$ for the volumetric flow rate of a power-law fluid ($n = 0.3$) through the unit cell with a straight capillary tube as a function of pressure drop. In both figures volumetric flow rates of power-law fluids versus pressure drop for the converging-diverging duct approach are computed from Eq. (61) with appropriate values of L and R . From the comparison of Figs. 4a and 4b it is clearly seen that the agreement between Eq. (14) and Eq. (61) is much better than that between Eq. (52) and Eq. (61).

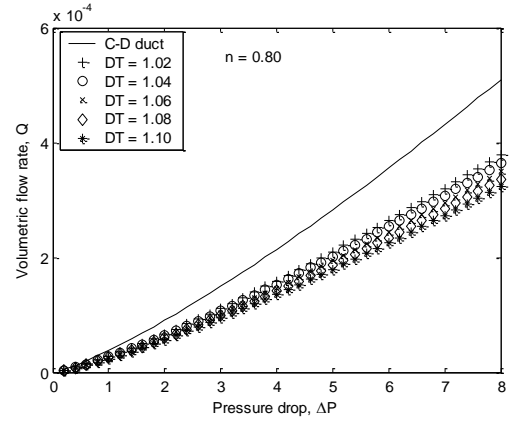


Figure 3. Variation of the volumetric flow rate of a power-law fluid ($n = 0.8$) as a function of pressure drop

Consequently, the model equations developed for volumetric flow rates of non-Newtonian fluid flows in the unit cell with straight capillary tube can't be correctly used for obtaining volumetric flow rates of those fluid flows through a single tortuous capillary.

The difference between Eq. (14) with equivalent parameters of $L(\lambda)$ and Eq. (52) with substituting Eq. (51) comes from the term of $D_f / (3 + D_f/n - D_f)$. Therefore, the farther a value of power-law index from the unity, the larger disagreement between Eq. (14) and Eq. (52) at each constant value of D_f (D_f is set to be 2 in the present study).

As mentioned previously those equations for Newtonian fluid case can be used for one another for obtaining flow rate as a function of pressure drop.

As can be seen in the figures (Figs. 4a and 4b) the deviation between the two models increases with increasing the tortuosity fractal dimension D_T . From the comparison of Fig. 3 and Figs. 4a and 4b it can be concluded that the deviation, in the volumetric flow rate of power-law fluids obtained from the fractal expression (Eq. 52) and converging-diverging duct (Eq. 61), for the lower power-law index ($n = 0.3$) is larger than that for the higher power-law index ($n = 0.8$). Therefore, it can be said that the deviation between the two models increases with decreasing power-law index, which can be evidenced by considering Figs. 2, 3 and 4. Fig. 4b indicates that at low

pressure drops the flow rate of power-law fluid with $n = 0.3$ is very low relative to that of power-law fluid with $n = 0.8$ at corresponding pressure drop.

Ellis fluids are also examined in terms of the volumetric flow rates as a function of pressure drop to check an agreement or a disagreement between the two models. The volumetric flow rate for an Ellis fluid in the converging-diverging duct approach is calculated from the following equation.

$$q = \frac{g}{\eta_0} \Delta p \left[1 + \frac{4}{\alpha + 3} \left(\frac{4 g \Delta p}{\tau_{1/2} \pi R_d^3} \right)^{\alpha-1} \right] \quad (62)$$

In this equation g , $\tau_{1/2}$, η_0 and α are taken to be $6.83 \times 10^{-5} \text{ cm}^3$, 0.719 Pa , 4.35 Pa.s and 2.47 , respectively. These data were experimentally determined by Park (see paper by Balhoff and Thompson, [6]) for 0.5 % polyacrylamid (separan) solution.

In the fractal capillary model the volumetric flow rate of Ellis fluids is calculated from Eq. (53) with $D_f = 2$ and Eq. (51). For various values of flow (power) index, α in the Ellis model, the volumetric flow rate of Ellis fluids as a function of pressure drop are computed and shown graphically in Figs. 5, 6 and 7 in attempt to see an agreement or a disagreement between the two models.

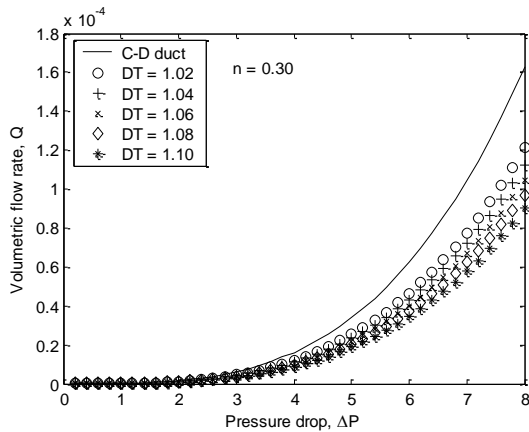


Figure 4a. Variation of the volumetric flow rate of a power-law fluid ($n = 0.3$) flow through a tortuous capillary tube as a function of pressure drop

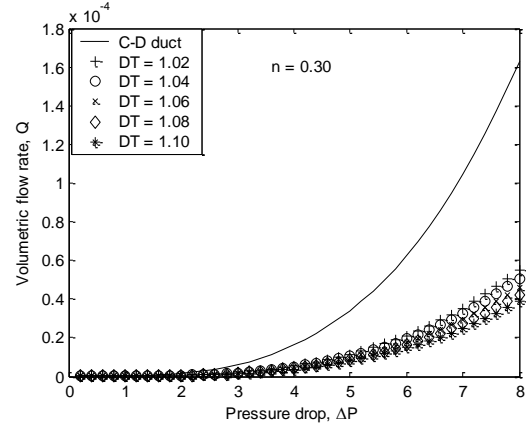


Figure 4b. Variation of the volumetric flow rate of a power-law fluid ($n = 0.3$) flow through the unit cell with a straight capillary tube as a function of pressure drop

Fig. 5 is depicted for the volumetric flow rate of an Ellis fluid with $\alpha = 2.0$ versus pressure drop. The figure is drawn using Eqs. (53) and (62) for the fractal capillary model and the converging-diverging duct approach, respectively. As can be seen in the figure the good agreement between the two models is observed for values of D_T around the determined value of 1.0752. The deviation between the fractal capillary model and the converging-diverging duct approach for an Ellis fluid with $\alpha = 2.0$ increases with a value of D_T going away from unity. As can be seen in the figure the volumetric flow rate of Ellis fluids calculated from the fractal expression is higher than that calculated from the converging-diverging duct approach for all considered values of D_T . Note that flow rate equation developed for the unit cell with a straight capillary tube (Eq. 53) reduces to the flow rate equation for a single tortuous capillary tube (Eq. 40 with equivalent parameters of $L(\lambda)$ as flow index takes the value of 2.

The volumetric flow rates of Ellis fluids obtained from the converging-diverging duct approach and the fractal capillary model with various values of the tortuosity fractal dimension, as a function of pressure drop, are depicted in Fig. 6 for $\alpha = 2.47$ and in Fig. 7 for $\alpha = 3.0$. The identical trend for volumetric flow rates versus pressure drops is observed in the three figures (Figs. 5, 6 and 7). Only difference between

these figures is magnitude of the volumetric flow rates of Ellis fluids at the corresponding value of the pressure drop. In other words, the volumetric flow rate of Ellis fluids slightly decreases with increasing flow (power) index, α , in the Ellis model at a constant value of D_T .

As a result, the agreement between the model predictions for volumetric flow rate of a Newtonian fluid flow through a single tortuous capillary tube by the proposed model and those in converging-diverging duct by the FEM is found to be good. Although not comparing to experimental studies, the present fractal capillary model developed for different fluid behaviors is compared with the theoretical studies that have already been compared to the experimental studies.

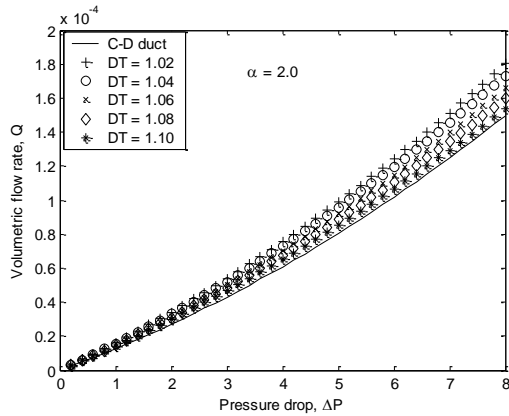


Figure 5. Variation of the volumetric flow rate of an Ellis fluid ($\alpha = 2.0$) as a function of pressure drop

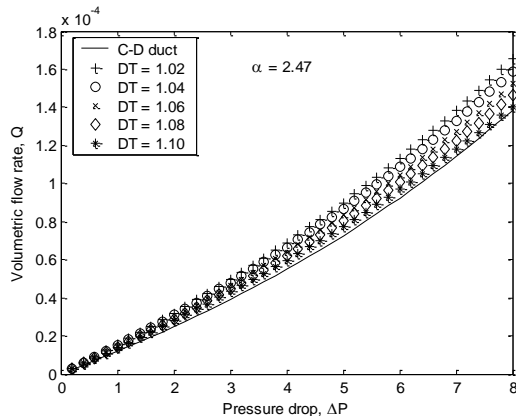


Figure 6. Variation of the volumetric flow rate of an Ellis fluid ($\alpha = 2.47$) as a function of pressure drop

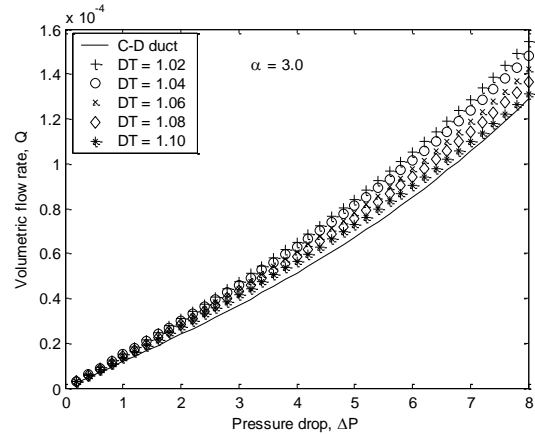


Figure 7. Variation of the volumetric flow rate of an Ellis fluid ($\alpha = 3.0$) as a function of pressure drop

7. Conclusions

To derive flowrate expression for each fluid as a function of pressure gradient is desirable to easily predict amount of fluid passing through porous media. The fractal capillary expressions for calculating volumetric flow rates and permeabilities for Newtonian, power-law and Ellis fluids are developed based on the fractal nature of tortuous capillary. In addition, hydraulic conductivity has also been expressed in terms of fractal scaling parameters. The fractal capillary model is used to model the shear-thinning fluids, including power-law and Ellis fluids. For each fluid the flow rates obtained from both the proposed model and the converging-diverging duct approach supported by FEM are compared to one another to check the accuracy of the developed model. Good agreement between the proposed model and the converging-diverging duct approach is observed at the considered values of the tortuosity fractal dimension for Newtonian fluids. It is also observed that the volumetric flow rate and permeability for Newtonian, power-law and Ellis fluids are very sensitive to the maximum pore size. The flow rates and permeabilities for power-law and Ellis fluids depend on values of the pore-area fractal dimension, the tortuosity fractal dimension and flow indices. The flow rates of power-law fluids increase with increasing power-law index having values between 0 and less than 1.0 but decreases

with increasing the tortuosity fractal dimension. On the other hand, the flow rate of Ellis fluid decreases with increasing both flow (power) index in the Ellis model and the tortuosity fractal dimension. It can also be concluded that the volumetric flow rate and permeability increase with increasing both pore diameter and pore-area fractal dimension. The good agreement between

the developed model and the converging-diverging duct approach for flow rates of Ellis fluids is obtained at the values of DT around the determined value for all flow indices considered here. It can be concluded that the fractal capillary model can be used to model shear-thinning fluids, including power-law and Ellis fluids with different rheological properties.

8. References

1. Bird, R.B., Stewart, W.E. and Lightfoot, E.N. (2008). Transport phenomena, Revised 2nd Edition, Wiley, New York.
2. Sabiri, N. and Comiti, J. (1995). Pressure drop in non-Newtonian purely viscous fluid flow through porous media. *Chem. Eng. Sci.*, **50**: 1193-1201.
3. Eslami, A. and Taghavi, S.M. (2017). Viscous fingering regimes in elasto-visco-plastic fluids. *J. Non-Newt. Fluid Mech.*, **243**: 79–94.
4. Tijani, H.I., Abdullah, N., Yuzir, A. and Ujang, Z. (2015). Rheological and fractal hydrodynamics of aerobic granules. *Bioresource Techn.*, **186**: 276–285.
5. Shokri, H., Kayhani, M. H. and Norouzi, M. (2017). Nonlinear simulation and linear stability analysis of viscous fingering instability of viscoelastic liquids. *Physics of Fluids*, **29**: 033101 <http://dx.doi.org/10.1063/1.4977443>
6. Balhoff, M.T. and Thompson, K.E. (2006). A macroscopic model for shear-thinning flow in packed beds based on network modeling. *Chem. Eng. Sci.*, **61**: 698-719.
7. Chhabra, R.P., Comiti, J. and Machac, I. (2001). Flow of non-Newtonian fluids in fixed and fluidized beds. *Chem. Eng. Sci.*, **56**: 1-27.
8. Yu, B. and Liu, W. (2004). Fractal analysis of permeability for porous media. *AIChE J.*, **50**: 46-57.
9. Yu, B. and Cheng, P. (2002). A fractal permeability model for bi-dispersed porous media. *Int. J. Heat Mass Transfer*, **45**: 2983-2993.
10. Pearson, J.R.A. and Tardy, P.M.J. (2002). Models for flow of non-Newtonian and complex fluids through porous media. *J. Non-Newt. Fluid Mech.*, **102**: 447-473.
11. Bird, R.B., Armstrong, R.C. and Hassager, O. (1987). Dynamics of polymeric liquids, Wiley, New York.
12. Comiti, J. and Renaud, M. (1989). A new model for determining mean structure parameters of fixed beds from pressure drop measurements: Application to beds packed with parallel pipedal particles. *Chem. Eng. Sci.*, **44**: 1539-1545.
13. Dharamadhikari, R.V. and Kale, D.D. (1985). Flows of non-Newtonian fluids through porous media, *Chem. Eng. Sci.*, **40**: 527-529.
14. Yu, B.M. (2005). Fractal character for tortuous stream tubes in porous media. *Chinese Physics Letters*, **22**:158-160.

Study of Fuzzy Logic Control of Dc-Dc Buck Converter

Zeynep Bala DURANAY, Hanifi GULDEMİR

Firat University, Technology Faculty, Department of Electrical-Electronics Eng., 23119 Elazig/Turkey
zbduranay@firat.edu.tr

(Geliş/Received:02.02.2017; Kabul/Accepted: 10.05.2017)

Abstract

Because of unspecified transfer function of dc-dc converters fuzzy controllers can be used instead of classical controllers. The design of fuzzy controllers does not require an exact mathematical model. Instead they are designed based on general knowledge of the plant. In this paper, a fuzzy logic controller for a dc-dc buck converter is designed. The designed controlled system is simulated in MATLAB/Simulink software. Different parameters such as input voltage and output load are varied and the responses of fuzzy controller to these variations have been studied and investigated in order to evaluate the designed controller performance. The simulation results are presented. Fast dynamic response of the output voltage and robustness to load and input voltage variations are obtained.

Keywords: Fuzzy logic controller, Dc-dc converter, Buck converter.

Dc-Dc Düşürücü Dönüştürücünün Bulanık Mantık Denetimi Üzerine Çalışma

Özet

Dc-dc dönüştürücülerin transfer fonksiyonunun tam olarak belirlenemediği durumda, klasik denetleyiciler yerine bulanık denetleyiciler kullanılabilir. Bulanık denetleyicilerin tasarımı tam bir matematiksel model gerektirmez. Bunun yerine denetlenecek sistemin genel bilgisine dayanarak tasarlanırlar. Bu çalışmada, dc-dc düşürücü dönüştürücü için bulanık mantık denetleyicisi tasarlanmıştır. Tasarlanan kontrollü sistemin MATLAB/Simulink ortamında benzetimi yapılmıştır. Giriş gerilimi ve çıkış yükü gibi farklı parametreler değiştirilerek bulanık denetleyicinin bu değişikliklere olan tepkisi incelenmiş ve tasarlanan kontrolörün performansını değerlendirilmiştir. Elde edilen benzetim sonuçları sunulmuştur. Çıkış geriliminin hızlı dinamik cevabı ve yük değişiklikleri ile giriş gerilimi değişimlerine karşı dayanıklılığı görülmüştür.

Anahtar Kelimeler: Bulanık mantık denetleyici, Dc-dc çevirici, Düşürücü çevirici.

1. Introduction

In some applications, it is necessary to convert the constant dc voltage value to a variable dc voltage. In power electronics, the circuits that perform this operation are called dc-dc converters. The dc-dc converters can also be called as a dc-chopper. A converter can be thought of as a dc equivalent circuit of a transformer with a continuously adjustable winding ratio. As transformers can reduce or increase AC voltage, dc-dc converters can also reduce or increase the voltage value of the dc source. Dc-dc converters are widely used in many office appliances, personal computer power supplies, spacecraft power systems,

laptops, communication devices, speed control and braking in dc motors, mine hammers, freight elevators, trolleys and electric automobiles. The block diagram of a converter can be given as shown in Figure 1.

At the inputs of these converters, there is the constant dc voltage obtained by rectifying the mains voltage. Therefore, fluctuations in input voltage occur due to change of line voltage. That is, the input voltage at the dc-dc converters is an unregulated dc voltage. The inverter output is a regulated DC voltage whose amplitude and polarity are different from the input voltage.

Switched dc-dc converters are used to convert an unregulated dc input to a controlled

dc output at the desired voltage range.

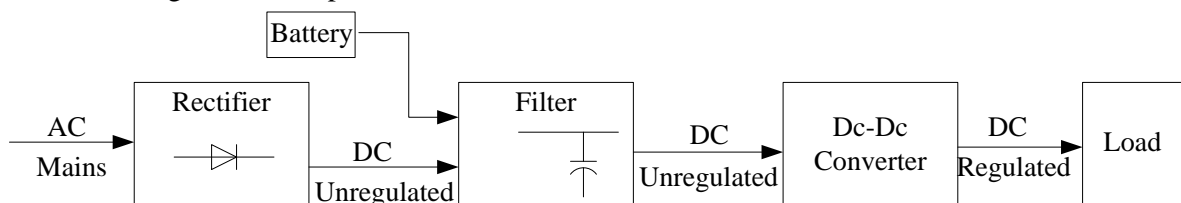


Figure 1. Converter block diagram

In practice, the efficiency of dc-dc converters is about 70-95%. High efficiency can be achieved by the use of switching elements which consume less power and are controlled at higher frequencies. Parallel to the developments in electronics, BJT, MOSFET and IGBT are used as switching elements in dc-dc converters in recent years. However, igbt and MOSFETs are preferred in high-power converter applications [1].

The basic energy required for the operation of the electronic circuits is provided by dc power supplies which convert the AC input signal to the dc output signal. There are basically two types of DC power supply.

- Linear power supplies
- Switched dc power supplies

The basic operating principle of the switched-mode voltage regulator is based on transferring the high frequency switching of the DC voltage applied to the input to the output. For this operation, the input voltage is chopped and the pulse duty ratio is changed. In short, pulse width modulation (PWM) is performed. This process makes the regulator output independent of changes in load and input voltage.

Advantages and disadvantages:

- The structure is complex and high costs.
- There is a need to filter the output due to noise and distortion.
- The efficiencies are quite high.
- Since the operating frequencies are very high, the dimensions of the circuit elements such as coil and transformer are smaller.
- Multiple outputs can be obtained and the poles of the output voltage can be changed.

The most important feature in power electronic systems is efficiency. So, as a rule, power electronic systems do not use resistances as a power electronics circuit element. Voltage drop and current flow are realized with the help of switches.

There is no voltage drop when an ideal switch is in the on state, and no current through when it is in the off state. Thus a switch can be thought of as an effective loss-free resistor depending on duty ratio.

Conversion of the power dc to dc is done with switched-mode power converters. It consists of reactive and switching elements. The operating principle is based on by setting the on and off times of the switching elements used in the circuit. If the frequency of the load-supplying voltage is large, practically dc power transmission is possible without interruption to the load. Thus, the design of the converters can be designed depending on the proper configuration of the reactive elements and the switching methods.

Switched dc-dc converters are nonlinear and time-varying systems due to the inductance behavior of their structures. Dc-dc Converters can be classified in many different ways. However, in terms of the functions performed by the converters, the dc-dc converters can be classified as follows;

- Step-Down converter, (Buck)
- Step-Up converter (Boost)
- Step-Down/ Up converter (Buck-Boost)
- Cuk converter
- Full Bridge converter

Buck and boost converters are basic converters. The buck-boost and cuk converters are formed by the use of basic converters. Full bridge converters are a different application of step down converter. The converter variants are also referred to as switched DC power supplies in certain applications [2].

The buck type dc-dc converters are used when a lower voltage than the source voltage is needed. Different control algorithms are applied to control the output voltage of dc-dc converters. Voltage-Mode Control and Current-Mode Control are two traditional methods to control dc-dc converters [3]. The transient responses of voltage-mode control is robust to disturbances, but are slow. Current-mode control improves the speed of transient responses. The disadvantages with this method are its instability when the duty-cycle is greater than one half and the need for a ramp compensation circuit to avoid this problem [4]. Current-Mode Control has more complex and expensive circuit structures to be implemented when compared Voltage-Mode Control.

If classical linear control techniques are used, the small signal model is derived by linearization around an operating point from the state space average model [1]. The classical controllers are simple to implement however, it is difficult to account the variation of system parameters, because of the dependence of small signal model parameters on the converter operating point [2]. Large signal and system parameter variations cannot be easily dealt with these techniques. The intrinsic nonlinearity and wide input voltage and load variations must be cope with the control technique, while ensuring stability and providing fast transient response in any operating condition. To achieve the desired performance, the classical control methods for dc-dc converters require the transfer function of the converter which is usually a complicated task.

Another method for control of converters is fuzzy controller which has an acceptable level of efficiency regarding the nonlinear model of converters. In fuzzy control method, the control action is based on some linguistic rules which can decrease the complexity of the nonlinear model and does not require an accurate

mathematical modeling of the systems and computational complexity [5, 6]

Its design philosophy deviates from all the previous methods by accommodating expert knowledge in controller design. This control technique is based on the human ability to understand the system behavior and it is also based on controlling qualitative rules. This control technique can extend the ability to control large signals since each operating point will have a specific driver without changing the circuit structure.

The use of fuzzy logic control enables to improve and overcome the deficiency of the control method based on small signal models. Fuzzy logic control improves the dynamic behavior of the system, and becomes very useful when the system mathematical model is difficult to obtain. Unlike other robust schemes, which are computationally intensive linear methods, implementation of fuzzy logic is simple.

In this study, a fuzzy logic controller is used to control a Buck converter which will have a constant output voltage under load and input voltage variations. For this topology, the tests on load regulation and line regulation are carried out to evaluate the controller's performance.

2. The Mathematical Model of Dc-Dc Buck Converter

The buck converter is shown in Figure 2. When the switch is on the circuit is connected to the dc input source resulting an output voltage across the load resistor.

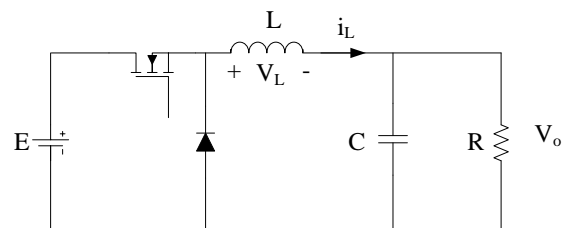


Figure 2. Buck converter

If the switch changes to off position, the capacitor voltage will discharge through the load. Controlling switch position the output voltage can be maintained at a desired level lower than

the input source voltage. The buck converter can be described by the following set of equations

$$L \frac{di_L}{dt} = uE - V_o \quad (1)$$

$$C \frac{dv_o}{dt} = i_L - i_o \quad (2)$$

Where i_L is the inductor current, V_o is the output capacitor voltage, E is the constant external input voltage source, L is the inductance, C is the capacitance of the output filter and R is the output load resistance. u is the control input taking discrete values of 0 and 1 which represents the switch position.

$$u = \begin{cases} 0 & \text{if switch is off} \\ 1 & \text{if switch is on} \end{cases} \quad (3)$$

It is assumed here that the inductor current will have a nonzero value due to load variations which is known as the continuous conduction mode (CCM). Figure 3 shows the current and voltage in continuous conduction mode.

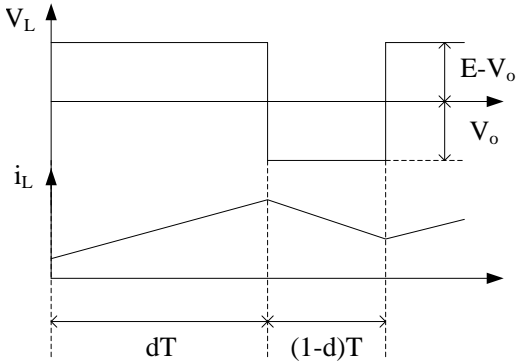


Figure 3. Current in buck converter

If taking the inductor current and capacitor voltage as the states of the system and rewriting equations (1) and (2) in the form of state equations, the following state equations in matrix form can be obtained.

$$\begin{bmatrix} \frac{di_L}{dt} \\ \frac{dv_o}{dt} \end{bmatrix} = \begin{bmatrix} 0 & -\frac{1}{L} \\ \frac{1}{C} & -\frac{1}{RC} \end{bmatrix} \begin{bmatrix} i_L \\ v_o \end{bmatrix} + \begin{bmatrix} \frac{E}{L} \\ 0 \end{bmatrix} u \quad (4)$$

where

$$i_o = \frac{V_o}{R} \quad (5)$$

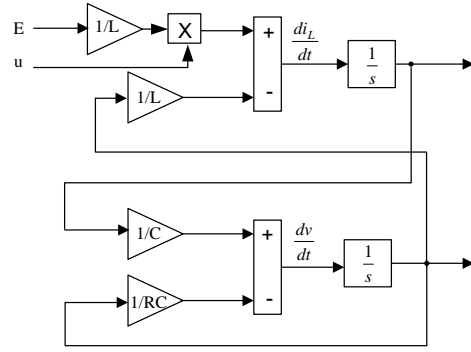


Figure 4. Simulink block diagram of a buck converter

Figure 4 shows the Simulink block diagram implementation of the buck converter using state equations (4).

3. Fuzzy Logic Control

The fuzzy logic control is an important application of the fuzzy set theory first introduced by L. A. Zadeh in 1965. The most important feature that distinguishes the concept of fuzzy set from the classical set concept is that fuzzy set uses linguistic variables rather than numerical variables [7].

Linguistic variables, defined as variables whose values are sentences in a natural language (such as small and large), may be represented by fuzzy sets. The application of fuzzy logic does not require accurate mathematical formulations. A block diagram of a fuzzy logic controller is shown in Figure 5. and the implementation involves the processes of fuzzification, inference and defuzzification.

The fuzzification interface converts input data into suitable linguistic values using the membership functions. During the phase of inference, the fuzzy if-then rules are evaluated using an inference engine and the controller action is inferred from the knowledge of the fuzzy rules and the linguistic variables definition. The conversion of the inferred fuzzy result to a crisp control action is performed through the defuzzification [8].

Because its control algorithm is described by if-then rules instead of intensive mathematical equations or large look-up tables, the design of fuzzy logic non-linear controller is easier. It reduces the development cost and time and needs less data storage in the form of membership

functions and rules. It is also highly reliable and robust to change in circuit parameters and external disturbances [9].

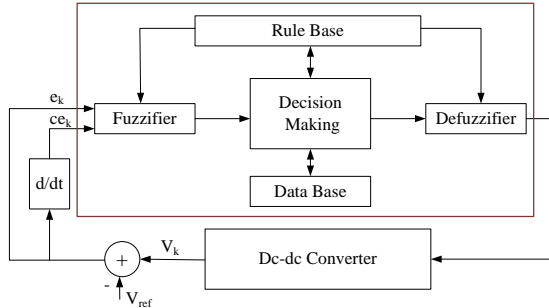


Figure 5. Basic configuration of fuzzy logic controller

4. Fuzzy Logic Controller Design

Fuzzy set is an extension of crisp set, where the element belongs or does not belong to the set with 0 or 100%. That is in a fuzzy set, the element may partially belong to the set, that is an element can belong to more than one set. This set is characterized by a membership function that applies a membership degree for the set with a range of 0 to 1 to each element in a given class.

Design of fuzzy controllers is based on expert knowledge of the system to be controlled instead of accurate mathematical model. There are two inputs in the fuzzy controller. The first is the error $e(k)$ between the output voltage $V[k]$ and the reference value V_{ref} and the second is the difference between successive errors i.e. change of error $ce(k)$ and are given by

$$e(k) = V_{ref} - V(k) \quad (6)$$

$$ce(k) = e(k) - e(k-1) \quad (7)$$

The output of the fuzzy controller is the change in duty cycle $\Delta d[k]$, which is fed to PWM block and the PWM output is fed as switching signal to the converter [10]. In Figure 5, the voltage at the output of the buck converter is compared with reference voltage and the output of the comparator is the error signal which is the input of the Fuzzy controller together with the change in error signal. The output of the controller is duty cycle which is fed to PWM block and the PWM output is fed as switching signal to the converter.

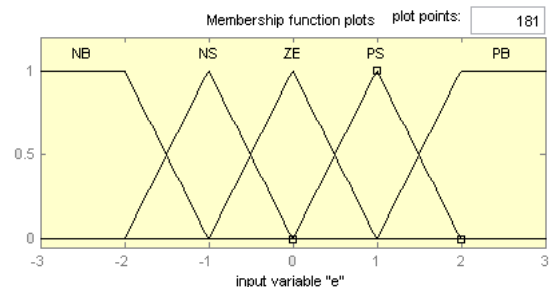
A Mamdani based control system architecture has been realized. Max–min composition techniques and center of gravity methods have been used in the inference engine and defuzzification. The max–min inference method is used to obtain the control decision. It is based on the minimum function to describe the AND operator present in each control rule and the maximum function to describe the OR operator. The output of the fuzzy controller structure is crisp, and thus, a combined output fuzzy set must be defuzzified. The sum–product composition method has been used to express the qualitative action in a quantitative action. It calculates the crisp output as the weighted average of the centroids of all output membership functions.

Fuzzy logic controller consists of three components fuzzification, fuzzy inference system and defuzzification. In general a fuzzy set is issued to express a fuzzy variable which is defined by a membership function. The values of membership function vary between 0 and 1. The fuzzy rule base are the IF-THEN rules.

4.1 Fuzzification

Fuzzification is the process of converting input data into suitable linguistic values. The first step in the design of a fuzzy logic controller is to define membership functions for the inputs. Five fuzzy levels are chosen and defined by the following fuzzy-set values for the error e and change in error ce :

- NB negative big;
- NS negative small;
- ZE zero;
- PS positive small;
- PB positive big.



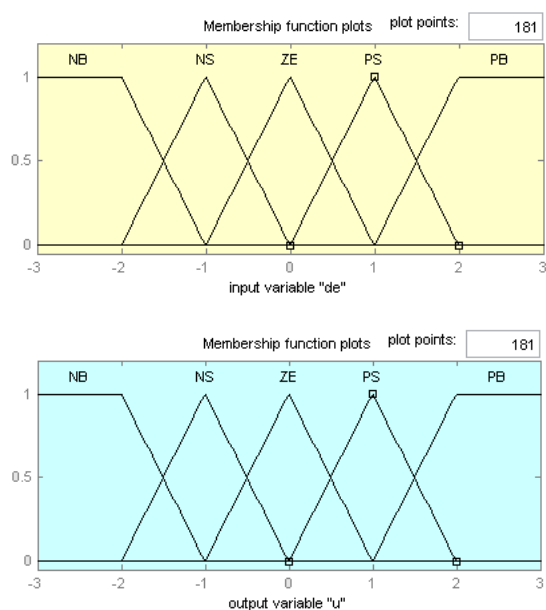


Figure 6. Membership functions for e, ce and u

The number of fuzzy levels depends on the input resolution. Increasing the number of fuzzy levels, increases the input resolution. Due to its simplicity, the triangular membership function is chosen for the controller input. Fuzzifier determines the degree of membership in every linguistic variable for given inputs. All linguistic variables other than two will have zero membership because there are only two overlapping memberships.

4.2 Rule base or decision-making

The heuristic control rules that correspond the fuzzy output to the fuzzy inputs are obtained from analysis of the system behavior. Sometimes the control actions in the rule table might also be developed using “trial and error” and from an “intuitive” feel of the system to be controlled. The control rules listed in Table 1 for the dc–dc converter are determined from converter behavior. A typical rule can be written as follows.

If e is NB and ce is PS then output is ZE
 Error (e), change of error (ce) and output represent degree of membership.

		E				
		NB	NS	ZE	PS	PB
CE	NB	NB	NB	NB	NS	ZE
	NS	NB	NB	NS	ZE	PS
	ZE	NB	NS	ZE	PS	PB
	PS	ZE	ZE	PS	PB	PB
	PB	NS	PS	PB	PB	PB

The fuzzy IF-THEN rule expresses a fuzzy implication relation between the fuzzy sets of the premise and the fuzzy sets of the conclusion. The rules IF part describes situation for which rules are designed and THEN part describes the response of fuzzy system. For example, IF the Error is NB and Change of Error is PS THEN Duty Cycle is ZE.

If the membership functions of the input variables provide a linear mapping between the inputs and the output of the controller, any control law can be directly implemented by choosing the output as the desired control law because the output is a function of the input variables.

The derivation of the fuzzy control rules is heuristic in nature and based on the following criteria [11-13]:

- 1) If the output of the converter is far from the reference point, the change of duty cycle must be large so as to bring the output to the reference point quickly.
- 2) If the output of the converter is approaching the reference point, a small change of duty cycle is necessary.
- 3) If the reference point is reached and the output is steady, the duty cycle remains unchanged.
- 4) If the output is above the reference point, the sign of the change of duty cycle must be negative.
- 5) If the output of the converter is far from the reference point, the sign of the change of duty cycle must be negative and large in order to bring the output to the reference point quickly.

Figure 7 represents the surface view of the rules for the proposed fuzzy logic control. The rules are represented as the combinations of the two inputs error and change in error for a function of output

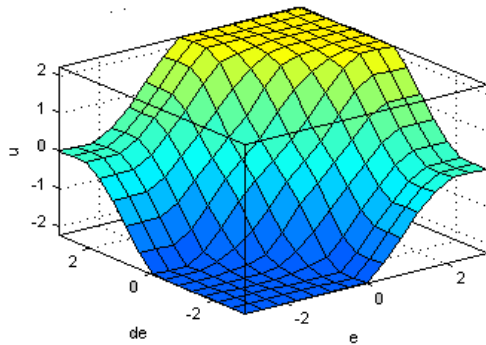


Figure 7. Rules in 3D surface

4.3 Inference mechanism

The max-min inference method is used to obtain the control decision. It is based on the minimum function to describe the AND operator present in each control rule and the maximum function to describe the OR operator.

4.4 Defuzzification

Conversion of the fuzzy to crisp or non-fuzzy output is defined as De-fuzzification. That is defuzzification unit transforms the fuzzy control actions to continuous (crisp) signals, which is applied to the physical plant.

5. Simulations

The steady-state output voltage of a dc-dc converter is controlled by the duty ratio. To account for changes in load current, input voltage, losses, and nonidealities in the converter, a closed loop control is required to obtain a desired output voltage and to maintain it. Figure 8 shows a block diagram of output voltage control for a buck converter.

The goal here is to implement a robust fuzzy controller that can achieve robustness around the operating point (e.g. in the case of a load change), good dynamic performance (i.e. rise time, overshoot, settling time and limited output ripple) in the presence of input voltage variations (and load changes); and invariant dynamic performance in presence of varying operating conditions. Therefore the system performance is checked under four different conditions namely start-up transient, line variation, load variation, and also circuit components variations.

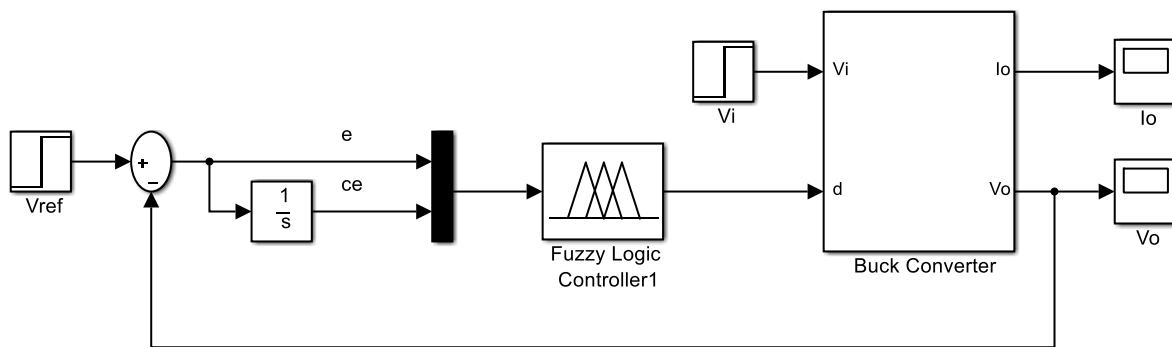


Figure 8. Simulink block of the fuzzy controlled buck converter

Simulations were performed on a typical ‘buck’ converter circuit, whose parameters are shown in Table 2.

Table 2. Buck converter parameters			
E (V)	L (mH)	C (μF)	R (Ω)
20	40	4	40

Figure 9 shows the output voltage and current when a change in the reference voltage from 10V to 12V occurs at 5ms.

The robustness is tested against the load variation. Figure 10 shows the recovering features of the fuzzy controlled buck converter to the imposed load variation. The load resistance

was subject to a sudden change from $R = 40 \Omega$ to $R = 60 \Omega$ at time $t = 5\text{ms}$, while the system was already stabilized to the desired voltage value of 10 V .

Figure 11 shows the waveforms, when the input voltage E is changed from 20 V to 18V at the time $t=5\text{ ms}$ with a desired steady state output voltage of 10 V . Figure 10 and 11 proves the robustness of the fuzzy logic control against changes in the load and variations in the input voltage.

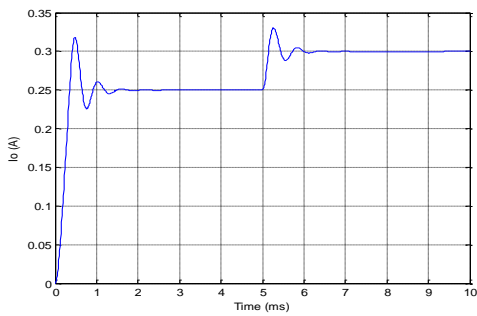


Figure 9. Output voltage and current waveforms for step change in reference voltage

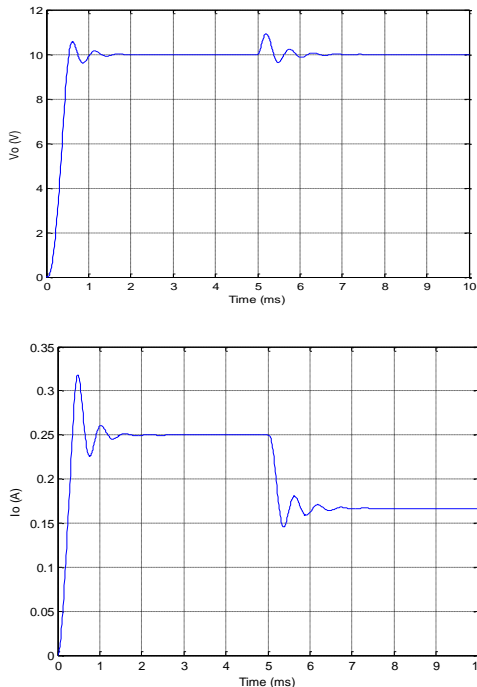


Figure 10. Output voltage and input current waveforms for 50% step load variations

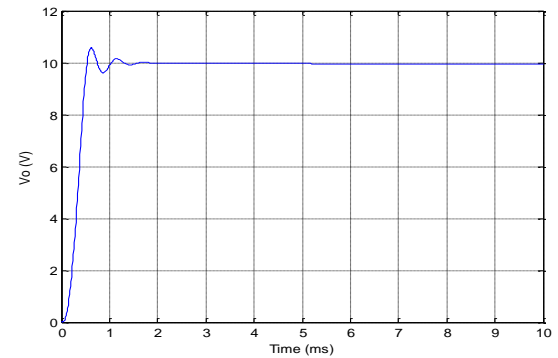
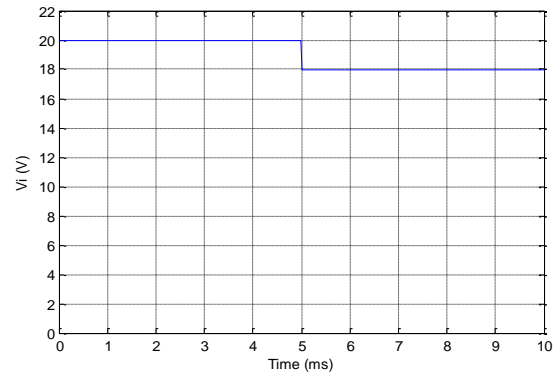


Figure 11. Input and output voltage waveforms for step changes in input voltage

6. Conclusions

A fuzzy logic controller designed and simulated for a dc-dc buck converter. The control feedback error computed as the difference between the output and the reference voltage, and its rate of change, are used as inputs for the fuzzy block which in turn determines the duty ratio of signal driving the switching element. The results of the simulations demonstrate that with the use of fuzzy logic controller the robustness of the output voltage and good dynamic behavior is achieved even for large supply and load variations. The simulation results illustrate that the fuzzy logic control can be an alternative to conventional control techniques and can provide considerable control performances as tracking the desired output voltage.

7. References

1. Forsyth, A.J. (1998). Modeling and control of dc-dc converters. *Power Engineering Journal*, 229-236.
2. Mattavelli, P., Rosetto, L. and Spiazzi, G. (1997). Small-signal analysis of dc-dc converters with sliding

- mode control. *IEEE Transactions on Power Electronics*, **12**: 96-102.
3. Dixon, L.H. (1990). Average current-mode control of switching power supplies. in *Unitrode Power Supply Design Seminar Handbook*.
 4. Gomes, E., Serra, G. and Gomes, J. (2011). A Fuzzy PI controller application in boost converter. *Robotics and Automotive Mechanics Conference*, 216-221.
 5. Mattavelli, P., Rosetto, L., Spiazzi, G. and Tenti, P. (1997). General purpose fuzzy controller for dc-dc converters. *IEEE Transaction on Power Electronics*. **12**: 79-89.
 6. Al-Odienat, A.I., Al-Lawama, A.A. (2008). The advantages of PID fuzzy controllers over the conventional types. *American Journal of Applied Sciences*, 653-658.
 7. Zadeh, L.A. (1965). Fuzzy sets. *Information and Control*, **8**: 338-353.
 8. Raviraj, V.S.C. and Sen, P.C. (1997). Comparative study of proportional–integral, sliding mode, and fuzzy logic controllers for power converters. *IEEE Transactions on Industry Applications*, **33**(2): 518-524.
 9. Govindaraj, T. and Rasila, R. (2011). Development of fuzzy logic controller for DC–DC buck converters. *Int J Engg TechSci.*, **2**(2): 192-198.
 10. Liping, G., Hung, J.Y. and Nelms, R.M. (2009). Evaluation of dsp-based pid and fuzzy controllers for dc–dc converters. *IEEE Transactions on Industrial Electronics*, **56**(6): 2237-2247.
 11. So, W. C. and Tse, C.K. (1996). Development of a fuzzy logic controller for dc-dc converters: design, computer simulation and experimental evaluation. *IEEE Trans. on Power Electronics*, **11**: 24-32.
 12. Rubaai, A. and Chouikha, M.F. (2004). Design and analysis of fuzzy controllers for dc-dc converters. *First Int. Symposium on Control Communication and Signal Processing*, 479-482.
 13. Prasad, K.V.H.M., Rao, CH.U. and Hari, A.S. (2012). Design and simulation of a fuzzy logic controller for buck & boost converters. *International Journal of Advanced Technology & Engineering Research (IJATER)*, **2**(3): 218-224.

Optimization for Next Generation Wireless System Using Radio Over Fiber in Terms of Topology

Shwan Asaad OTHMAN, İbrahim TÜRKOĞLU

Firat University, Faculty of Technology, Department of Software Engineering, 23119, Elazig/Turkey
shwan.asaad1985@gmail.com, iturkoglu@firat.edu.tr

(Geliş/Received:08.06.2017; Kabul/Accepted: 06.09.2017)

Abstract

This dynamic execution of Radio over Fiber (RoF) joins utilizing minimal effort optoelectronic parts are evaluated for dispersed receiving wire applications in cutting edge remote frameworks. Vital configuration issues are examined and an illustrated the outline is exhibited for a remote framework requiring the transmission of four radio channels for every connection course. Each of these channels has 100 MHz transmission capacity, balance many-sided quality of 256-QAM and 2048 OFDM subcarriers. The Radio Access Network (RAN) is using for all types of mobile system, each of this RAN have a different topology such as star, circle, tree, etc. On the other hand, to creating and using a new RAN is better to use mesh topology which is suitable for the new system. In the same way, in the field of using new RAN, topology can be apply as a mesh, which includes RoF. It also call as next generation mobile system for the new system, instead of using microwave it can use fiber optic that is why microwave are ignored. This type of use is more useful in terms of quality and system optimization for 4G and similar systems.

Keywords: Next generation, New Radio Access Network (RAN), Radio over Fiber (RoF), Mesh topology, Dispersion of fiber optic.

Yeni Nesil Kablosuz Sistemlerin Fiber Üzerinde RF Kullanılarak Topoloji Açısından Optimizasyonu

Özet

Bu çalışmada, minimum maliyete sahip optoelektronik elemanlar kullanılarak oluşturulan fiber üzerinden radyo (RoF) dalgalarının dinamik iletiminde uzak sistemlerdeki zayıflama dağıtık kablolu alıcı uygulamaları için değerlendirildi. Önemli gruplama sorunları incelendi ve bir örnek ile açıklandı. Sonuçlar, her bir bağlantı yolu için dört radyo kanallı iletime gereksinim duyan uzak sistemle sunuldu. Bu kanalların her biri, 100 Mhz iletim kapasitesine, 256-QAM çok yönlü kalite dengeleyicisine ve 2048-OFDM ara taşıyıcılarına sahiptir. Radyo Erişim Ağı (RAN) mobil sistemlerin tüm türleri için kullanılıyorken, bu RAN sistemlerinin her biri ise farklı bir topolojiye sahiptir: yıldız, halka, ağaç, vb. Diğer yandan, yeni bir RAN tasarlamak ve kullanmak için örgü ağ topolojisinin kullanımı, yeni sistemler için daha uygundur. Benzer şekilde, yeni RAN kullanımında, örgü ağ topoloji RoF yapısına dahil olabilmesi nedeniyle daha uygulanabilir. Bu yeni sistemler için, mikro dalga kullanımı yerine mikrodalganın göz ardı edilerek doğrudan fiber optik hattın kullanımı yeni nesil mobil sistem olarak da adlandırılır. Bu tarz kullanım, 4G ve benzer sistemler için kalite ve sistem optimizasyonu açısından daha kullanışlıdır.

Anahtar Kelimeler: Yeni nesil, Yeni Radyo Erişim Ağı (RAN), Radyo Üzerinden Fiber (RoF), Örgü ağ topolojisi, Fiber optik dağılım.

1. Introduction

Change in the nature of the service, new frequency bands and non-backwards compatible transmission technology is generally called the next generation. New generations have risen again in every 10 years from 1981, analog 1st G

to analog 2nd G network, then the 3th G multimedia support followed the two previous generations. And finally, the 4th G comes, in last years a great growth in the industry of wireless, both subscribers, and mobile technology. A dramatic change from fixed to mobile cellular telephony. Together, the vendors and mobile

network operators have important role of effective networks with the equally effective anning coming into focus. The 5th G is multi Technology Core as given in Table 1. The assemblage of new technologies such as Nano-technology, Cognitive Radio, Cloud Compute, and based on all IP Platform form a core [1]. Table 1 is the mobile generation evolution from 1G to 5G.

Table 1. Evolution of mobile radio standards [1]

N.G	1G	2G	3G	4G	5G
Year	1970	1980	1990	2000	2012
Standards	AMPS, NMT, HICAP	GSM, I-DEN, D-AMPS	CDMA 2000, WCDMA	Signal Standard LTE, Advance	Single Unified Standard
Data Bandwidth	1.9 Kbps	14.4 Kbps	2 Mbps	200 Mbps	1 Gbps & Higher
Core Network	PSTN	PSTN	Packet Network	INTERNET	INTERNET
Multiplex	FDMA	CDMA, TDMA	CDMA	OFDMA	CDMA, BDMA
Service	Analog Voice	Digital Voice	Higher capacity, Broadband Data	Broadband Data With High Speed	Dynamic Information Access

RoF systems use optical fiber, which has minimum lack and wide band width transmission area that allow the spreading of broadband data or high frequency signals into many Base Station (BS) is easy. [2]

The benefits of Radio over Fiber technology makes it an important for the future of wireless communication and makes the companies race to know that technology and implement it to obtain a system that more efficient and has better performance. The technology of Fiber optic gives technical works advantage over commercial.

2. Materials and Method

2.1. Radio over fiber

RoF indicates to a technology that using light to tone radio signal and transfer it over an optical fiber connected to divide radio signals of a centric place to remote stations as shown in Figure 1. The radio signals frequencies are divided into RoF systems cover a great range (often in the GHz region), which rely on the kind of the apps. The electrical signal may be baseband the current modulated RF signal,

design. This development leads to optimization related services and Network PI modulated IF (Intermediate Frequency), or data to be distributed. RoF conveyance systems are divided into 2 general categories (RF Fiber; IF-over-Fiber) rely on the range of frequency of the radio signal to be transmitted In RF-over-Fiber design, a data (usually more than 10 GHz) is imposed on a light signal wave prior to transported over the optical link. In IF-over-Fiber architecture, an IF radio signal together with less frequency (Less than 10 GHz) is utilized for tone light before being transported over the optical link [4].

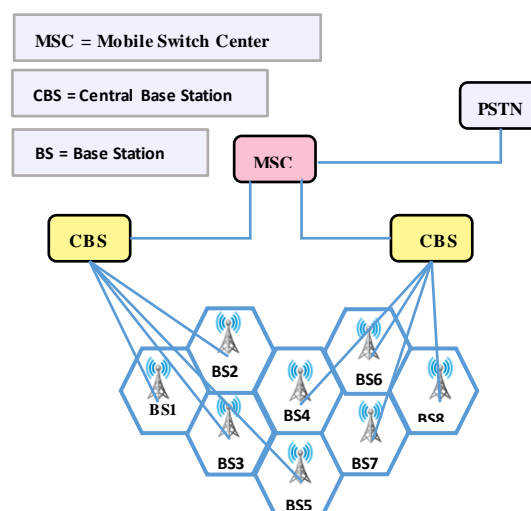


Figure 1. Remote network antenna for micro-cell for RoF system

RoF, is composed of a CS (Control Station) with BS joined by an optical fiber network or link as shown in Figure 2.

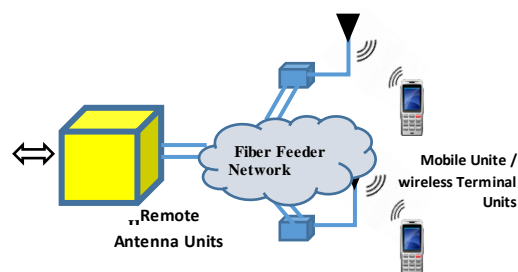


Figure 2. The radio over fiber system concept

The transmitting of peak frequency signals is more affronts due to the requirement of peak frequency part and bigger bandwidth link. This

refers to larger frequency signals are more sensitive to the transmission, transmitter and receiver link signal failure [5].

Transmitting of the constant frequency of RF signal, it is not important. For example, an LO signal, if present, may be utilized to down-convert the uplink holder to an IF in the RAU (Radio Access Unit). Performing it would permit the use of low-frequency components for the up-link way in the RAU – directing to a system for reducing cost. By putting a different LO in the RAU, it can transmit from the head end to the RAU by the RoF system. As it available at the RAU, the LO can be used to tone down conversion of the uplink signals [6].

RoF technology advantages are compares with electronic signal distribution are mentioned as follow;

- Low Attenuation Loss
- Large Bandwidth
- Radio Frequency Interference Immunity
- Reduced Power Consumption

2.2. Cell planning

Therefore, RAN in the mobile system Next generation contains a group of BTS (Base Transceiver Station) that all of them are designed next together. Each BTS contains cell that called six dimensions or squib. Also, each cell contains three Antennas. When we want to send the frequency for all of the BTS we have to make them as a group because it is easier to send the frequency for each group. So, BTS groups are arranging like (3,7,9,12,...) and they called cluster size. However, it has a special rule to make them. Cluster size rule is (i, j) to finding (N) it can be use this rule ($N = i^2 + ij + j^2$). For distance of the (i, j) rule and it can be use $D = \sqrt{3N}$, in the picture below will illustrate how we classify BTS over the groups as shown in Figure 3 [7].

Where is $i =$ blue line, $j =$ black line, $D =$ red line, $i =$ vertical, $j =$ horizontal, $D =$ distance between two cell.

Table 2 is the cluster size calculation for the cell planning procedure.

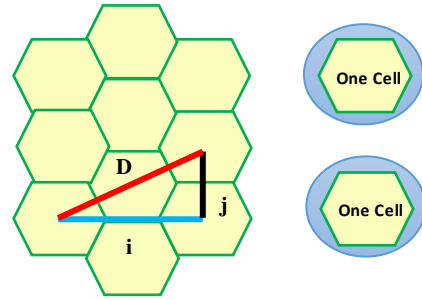


Figure 3. Cell planning in cluster size

Table 2. Cell planning in cluster size [7]

i	j	$N = i^2 + ij + j^2$	$D = \sqrt{3N}$	Radius Cells
0	0	0	$D = \sqrt{3 * 0}$	0
0	1	1	$D = \sqrt{3 * 1}$	$1.73 \cong 2$
1	0	1	$D = \sqrt{3 * 1}$	$1.73 \cong 2$
1	1	3	$D = \sqrt{3 * 3}$	3
0	2	4	$D = \sqrt{3 * 4}$	3.46
2	0	4	$D = \sqrt{3 * 4}$	3.46
1	2	7	$D = \sqrt{3 * 7}$	4.58
2	1	7	$D = \sqrt{3 * 7}$	4.58
2	2	12	$D = \sqrt{3 * 12}$	6
0	3	9	$D = \sqrt{3 * 9}$	5.19
3	0	9	$D = \sqrt{3 * 9}$	5.19
3	1	13	$D = \sqrt{3 * 13}$	6.24
1	3	13	$D = \sqrt{3 * 13}$	6.24
3	2	19	$D = \sqrt{3 * 19}$	7.54
2	3	19	$D = \sqrt{3 * 19}$	7.54
3	3	27	$D = \sqrt{3 * 27}$	9

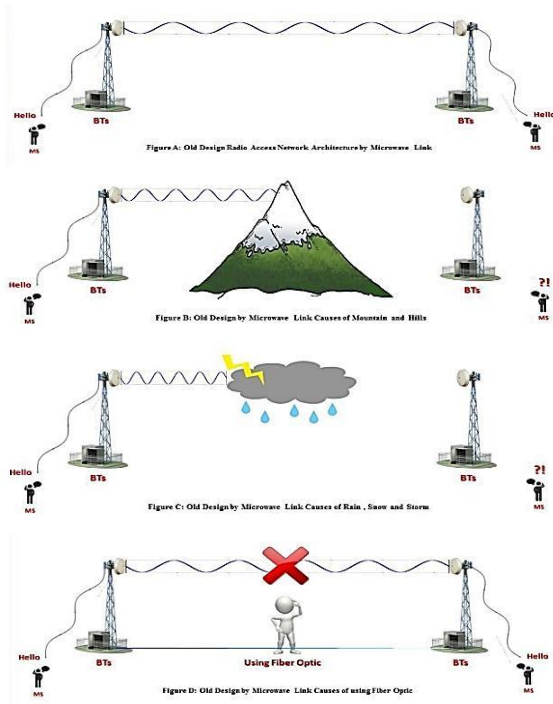
2.3. Problem of statement

To reduce and increase all of the problems that mentioned above and to solve the disconnection between BTS and BSC (Base Station Central), it is better to use fiber optic instead of using microwave, because by using fiber optic in the case of calling those problems are an increase.

Same challenge between two Base Stations (BSs) or between BSs and BSC as shown in Figure 4.

- a. In old RAN Communication was done Directly between Two BTS by Microwave Link as shown in figure (a).

- b. The problems that rise between two BTS during sending a signal to occur because of Mountain and Hills as shown in figure (b).
- c. Or because of Rain, Snow, Storm, and Airplane in Airport as shown in figure (c).
- d. The aim from this topic is design a new RAN to solving this problem by removing of Microwave Link between two BTS in place of it, using Fiber optic between all BTS then a group of BTS connected to one BSC then Connected to Core Network after connected to the Internet as shown in figure (d).



2.4. Method

2.4.1. Design and optimization for new RAN by matlab environment

Dispersion is divided into two main parts (Intramodal and Intermodal dispersion) and (Intermodal). Also (Intermodal) is divided into two parts: Step and Graded Index; all of the parts will make the Total Dispersion (σ_T) [8].

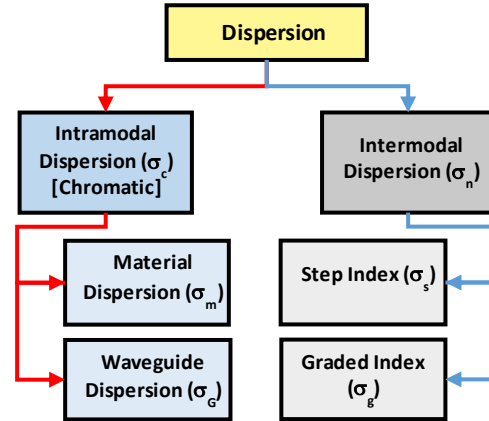


Figure 5. Design and optimization for the challenges of optical fiber

First dispersion, material dispersion (σ_m) in intramodal dispersion (σ_c), also (σ_m) = (σ_c) because waveguide dispersion (σ_G) near of zero therefor (σ_m) = (σ_c) [8].

First dispersion, material dispersion (σ_m) in intramodal dispersion (σ_c), also (σ_m) = (σ_c) because waveguide dispersion (σ_G) near of zero therefor (σ_m) = (σ_c) [8].

$$\sigma_m = \frac{\sigma_\lambda L}{c} \left| \lambda \frac{d^2 n_1}{d\lambda^2} \right| \quad (1)$$

Where σ_m = material dispersion, σ_λ = constant, $c = 2.998 \times 10^8$ constant, L = length of the fiber optic, n_1 =constant, λ = wavelength of the light.

Second dispersion, step index (σ_s) in intermodal dispersion (σ_n), has been explained dispersion by Δ or NA. [9]

$$\sigma_s = \frac{Ln_1\Delta}{2\sqrt{3}c} = \frac{L(NA)^2}{4\sqrt{3}n_1c} \quad (2)$$

Where σ_s = step index, L = length of the fiber optic, n_1 = constant, Δ = relative refractive index difference, relative with (NA) Numerical Aperture n_1 and n_2 , c = constant.

Total dispersion (σ_T) is the result of intermodal and intramodal; dispersion, by finding the total dispersion we can calculate the data bit rate by dividing total dispersion by (0.2). [10]

$$\sigma_T = \sqrt{\sigma_c^2 + \sigma_n^2} \quad (3)$$

Where σ_T = Total dispersion, σ_c = intramodal dispersion, σ_n = intermodal dispersion.

The Total Dispersion (σ_T) has been measured, because of the find out Data rate by this equation as follow:

$$BT_{Max} = \text{maximum bit rate} = \frac{0.2}{\sigma_c} \quad (4)$$

2.4.2. Designing topology with optisystem software

Furthermore, in terms of creating new design for next generation mobile system that topology is a mesh, after we create Matlab code by using optimization, then using the process of Optisystem for creating new design in the shape of software, then we use (1 km) or (2 km) fiber optic cable for this system, so some information are collecting before using the system. As shown in Figure 6 [11].

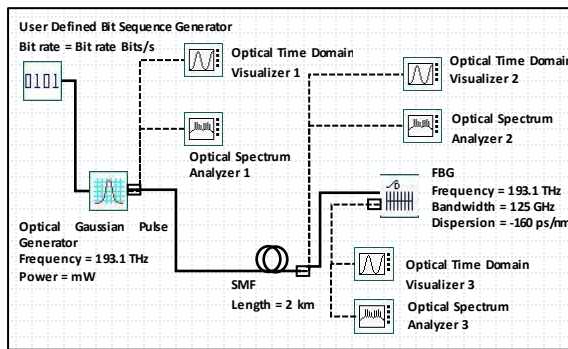


Figure 6. Compensation of dispersion ideal dispersion compensation

2.4.3. Hardware implementation using optical components

The simulation of the proposed design with optisystem software, which is a new RAN design for the system, it is topology well be in a mesh topology, for next generation mobile system of 4th generation or above. The aim from this topic is to design a new RAN to solving this problem by removing of microwave link between two BTS in place of it, using fiber optic between all BTS. After, the practically work included a few instrument connected in sequence as (RF Generator, Attenuator, RoF Transmitter, Fiber

Optic Cable, RoF Receiver, Spectrum Analyzer, Optical Spectrum Analyzer), presented in Figure 7.

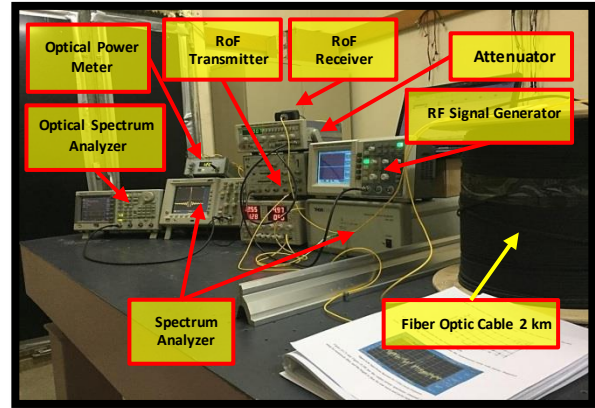


Figure 7. Spectrum analyzer and optical spectrum analyzer

The mentioned instruments practically have been connected to gain the results which came to those achieved by optisystem simulation, shown in Figure 8.

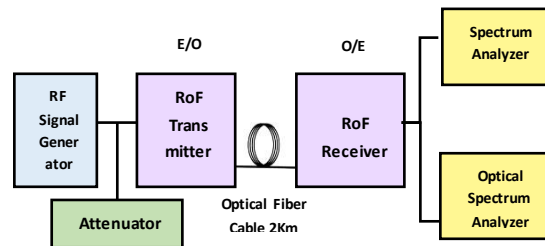


Figure 8. Connected between all parts

First, RF signal Generator has been used as a laser source, then connecting to attenuator part, that used the increasing and decreasing of power during reading the results. After the connection to RoF transmitter part, which is composed of (E/O and light source), and 2 km fiber optic cable has been connected, after that the RoF receiver connected as comprised in (O/E and detector), finally connected to the both parts of spectrum analyzer and optical spectrum analyzer.

3. Result and Discussion

The proposed RAN architecture employs grouping the overall coverage base stations into a number equal to the cluster size. For example,

for cluster size $N = 3$, there will be three groups, and seven groups when $N = 7$, etc. The contribution of this work is that the 4G mobile system will have central base stations (CBSs) for each group connected to these central base stations, unlike the GSM system which has many base transceivers (BTS). In the GSM system, each group of these BTSs is connected to a base switching control (BSC), and these BSCs are connected to the Mobile Switching Center (MSC), with all of these connections between BTSs, BSCs, and the MSC made via a microwave link.

In this work, each group of base stations will be connected directly to CBSs through the use of the RoF technique, using a fiber optic channel instead of a microwave link. Figure 9 shows the connection of one group of base stations to their central base station (the black nodes represent base stations and the red lines are fiber optic links using RoF technique). A practical view for the proposed RAN is shown in Figure 10.

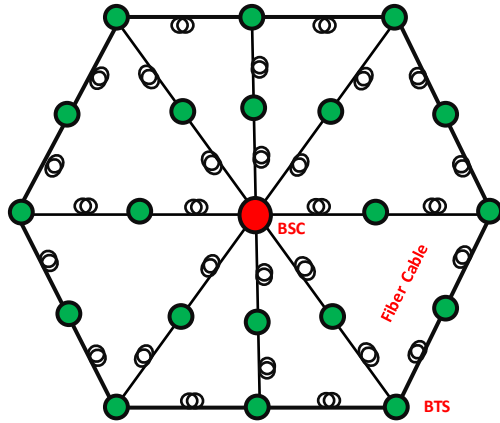


Figure 9. Proposed base station mesh topology to each group

The length of the fiber optic cable between two adjacent base stations BS must be greater than twice the reuse distance D of each base station for cluster size N , therefore, the length of the fiber for different cluster sizes can be obtained as given in Table 3.

For the proposed RAN, for each group of base stations and additional central base station, the first tier base station number = 6, second tier = 12, third tier = 18, i.e. 6 base stations will be added for each subsequent tier. Now the total number of base stations needed for a certain coverage area and cluster size can be obtained,

after calculation for each group as shown in Table 4.

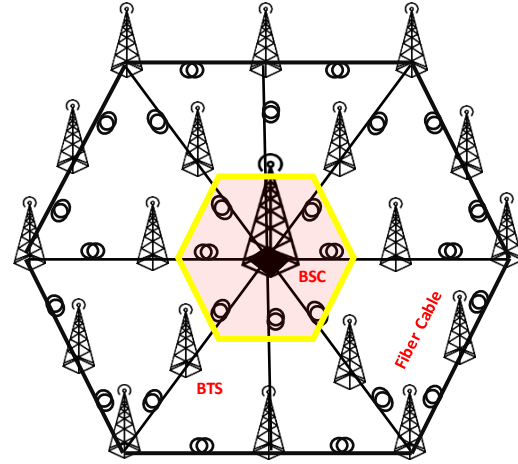


Figure 10. Proposed practical view mesh topology to each group

Table 3. The fiber length radius cells and cluster size calculation

Cluster Size (N)	L (Fiber Length, km)
0	$0 \Rightarrow R$
1	$1.73 \cong 2 \Rightarrow R$
3	$3 \Rightarrow R$
4	$3.46 \Rightarrow R$
7	$4.58 \Rightarrow R$
9	$5.19 \Rightarrow R$
12	$6 \Rightarrow R$
13	$6.24 \Rightarrow R$
19	$7.54 \Rightarrow R$
27	$9 \Rightarrow R$

Table 4. Fiber length (radius cells) and (N) cluster size calculation

No. of (N)	No. of Tiers	BSs	Radius Cells	Coverage Area
0	1	0	0	$(2.6 \times R^2) \times 1$
1	7	127	2	$(2.6 \times R^2) \times 127$
3	7	381	3	$(2.6 \times R^2) \times 381$
4	7	508	3.46	$(2.6 \times R^2) \times 508$
7	7	889	4.58	$(2.6 \times R^2) \times 889$
9	7	1143	5.19	$(2.6 \times R^2) \times 1143$
12	7	1524	6	$(2.6 \times R^2) \times 1524$
13	7	1651	6.24	$(2.6 \times R^2) \times 1651$
19	7	2413	7.54	$(2.6 \times R^2) \times 2413$
27	7	3429	9	$(2.6 \times R^2) \times 3429$

If, Cluster Size $N = 7$ seven groups, BTS radius cell = 4.58 km, the number of Base Transmission Station BTS = 889 and the commonly coverage area = 48,484.85 km².

3.1. Proposed design and optimization results using matlab environment

Figure 11 shows the relation between data rate and the fiber length using multimode graded index fiber optics with different relative refractive index differences (Delta). It is shown that fiber length is about 2 km. Thus, relative refractive index difference must be less than 0.04 for a higher data rate.

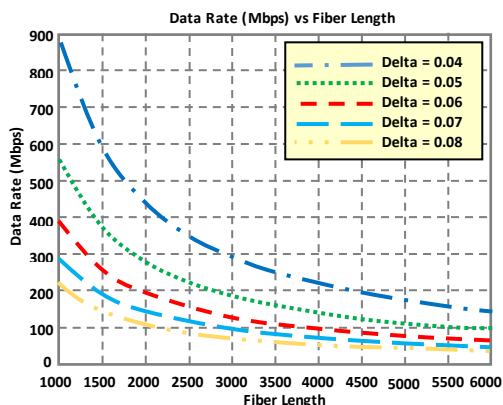


Figure 11. Experimental setup components and connection

Figure 12 shows the relationship between fiber length and data rate with different Numerical Apertures (NA), using multimode step index fiber optics, it is found that for higher data rate and fiber length about 2 km, the numerical aperture must be less than 0.028.

Figure 13 shows the relationship between data rate and relative refractive index difference for different cluster sizes (N) using multimode step index fiber optics. It is shown that without clustering (N=1), the data rate is higher, but this causes higher CCI (Co-Channel Interference) and ACI (Adjacent Channel Interference), and hence SIR (Signal-to-Interference Ratio) will be decreased. Therefore, N=3 and N=7 clustering would be more optimal.

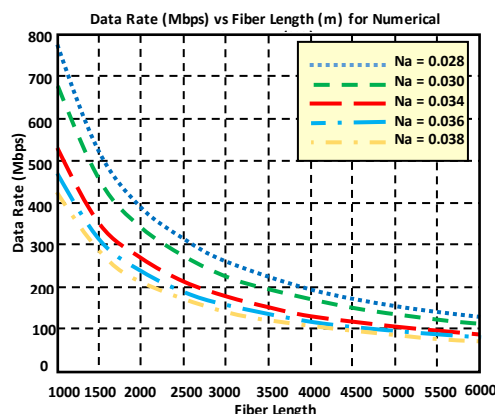


Figure 12. Data rate versus fiber length for step index fiber

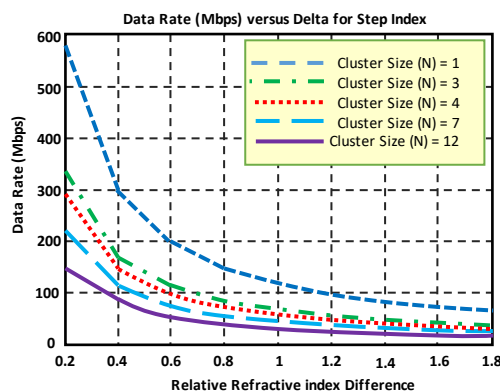


Figure 13. Data rate versus relative refractive index difference for step index

3.2. Proposed design results in design using optisystem software

The optimization to obtain best values of dispersion and then data rate, using OptiSystem software the RAN design using RoF done, the designed system whereas Figure 14 is the transmitted pulse, Figure 15 is the received pulse at the end of the fiber, Figure 16 is the output pulse after minimization of the pulse broadening and dispersion using Fiber Bragg Grating (FBG) technique for dispersion minimization.

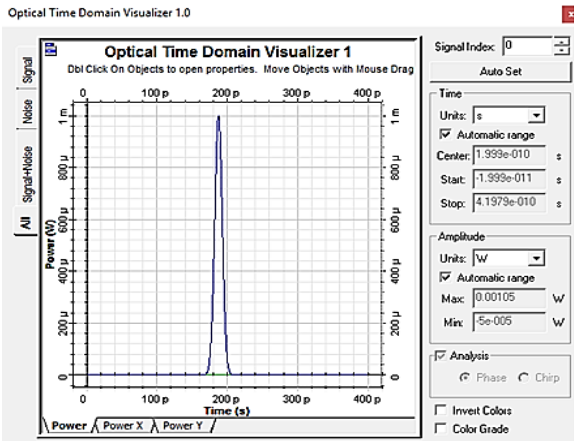


Figure 14. The transmitted pulse launched top the fiber optic

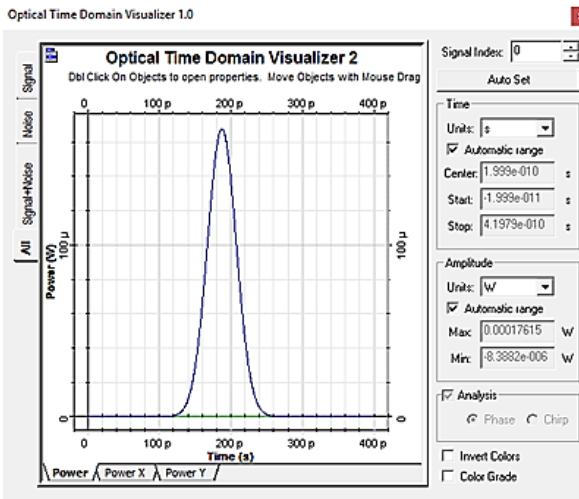


Figure 15. The output pulse from the fiber optic

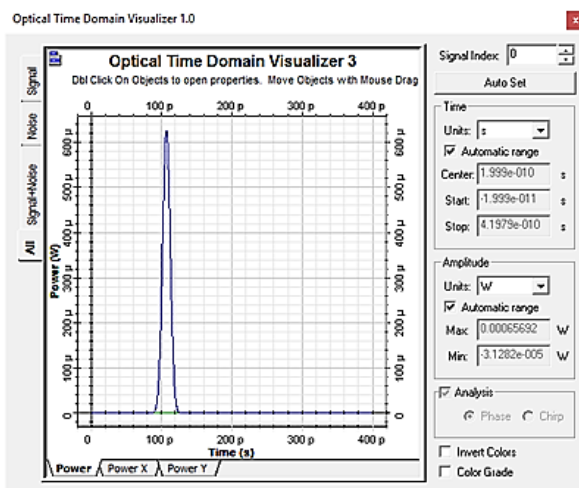


Figure 16. The output pulse from FBG

3.3. Proposed design results for the practical parts

Figure 17 is the input power spectrum from the experimental setup with carrier frequency 2GHz.

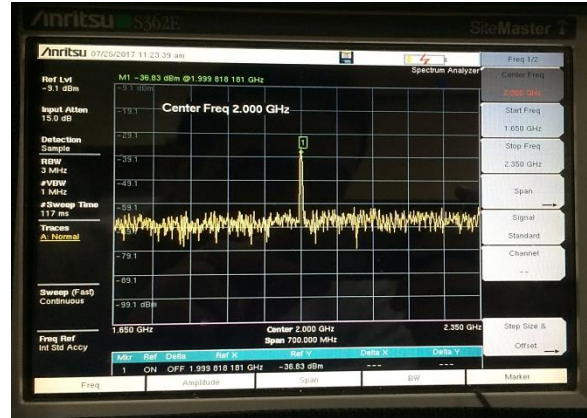


Figure 17. Input power spectrum for 2 GHz carrier frequency

Figure 18 and Figure 19 are the output power spectrums obtained in the experimental setup for multimode fiber, and the length is 2 km for sine wave and pulse inputs respectively. It is shown that the output power for sin wave input has greater (which is about -48dB) than that when the input is a pulse (which is about -75 dB) because of the optical fiber will affect more when the input is a pulse which is by the effect of dispersion.

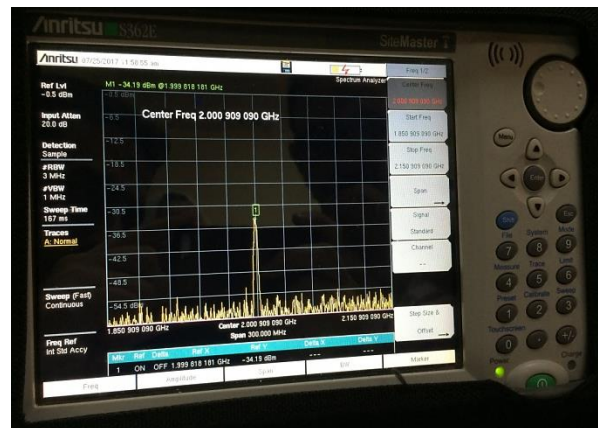


Figure 18. Output power spectrum for 2 GHz carrier frequency with sine wave input

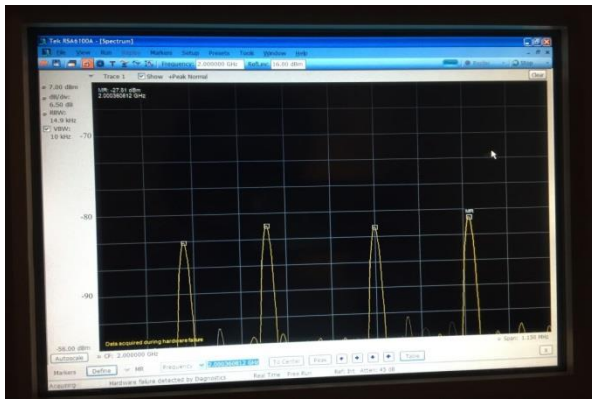


Figure 19. Output power spectrum for 2 GHz carrier frequency with sine wave input

4. Conclusions

A new RoF topology is proposed for the 4G mobile system. The topology involved grouping the coverage into N groups. Each group has many base stations connected to a central base station; thus, there are N central base stations connected to the core network through access gateways, and finally, to the Internet. The use of fiber optic channels allows for high data rate and improved signal quality. Moreover, no interference and free space losses were observed. The maintenance of the proposed topology would be easier, and the overall network would be more reliable. Thus, despite its high installation cost, the proposed RoF topology should provide low running costs.

5. References

- Gawas, A.U. (2015). An Overview on Evolution of Mobile Wireless Communication Networks: 1G-6G, *International Journal on Recent and Innovation Trends in Computing and Communication*, **3**(5): 3130 – 3133.
- Lee, D.W., Won, Y.Y. and Han, S.K. (2008). Bidirectional Gigabit Millimeter-wave Wavelength Division Multiplexed Radio over Fiber Link Using a Reflective Semiconductor Optical Amplifier. *IEICE Transaction on Communications*, **E91-B**(7): 2418-2421.
- Al-Raweshidy, H. And Komaki, S. (2002). Radio Over Fiber Technologies for Mobile Communications Networks.
- Pooja, J., Saroj, B. and Manisha, B. (2015). Advantages and Limitation of Radio over Fiber System. *International Journal of Computer Science and Mobile Computing*, **4**(5): 506-511.
- Lim, C., Nirmalathas, A., Bakaul, M., Gamage, P., Lee, K., Yang, Y., Novak, D. and Waterhouse, R. (2010). Fiber-Wireless Networks and Subsystem Technologies. *Journal of Lightwave Technology*, **28**(4): 390-405.
- Vyas, A.K. and Agrawal, N. (2012). Radio over Fiber: Future Technology of Communication, *International Journal of Emerging Trends & Technology in Computer Science (IJETTCS)*. **1**(2): 233-237.
- Hamad-Ameen J.J. (2008). Cell Planning in GSM Mobile. *WSEAS Transactions on Communication*. **5**(7): 393-398.
- Auguste, J.L., Blondy, J.M., Maury, J., Marcou, J., Dussardier, B., Monnom, G., Jindal, R., Thyagarajan, K. and Pal, B.P. (2002). Conception, Realization and Characterization of a Very High Negative Chromatic Dispersion Fiber. *Optical Fiber Technology*. **8**(1): 89-105.
- Petersen, C.R., Moller, U., Kubat, I., Zhou, B., Dupont, S., Ramsay, J., Benson, T., Sujecki, S., Abdel-Moneim, N., Tang, Z., Furniss, D., Seddon, A. and Bang, O. (2014). Mid-infrared supercontinuum covering the 1.4–13.3 μ m molecular fingerprint region using ultra-high NA chalcogenide step-index fibre, *Nature Photonics*, **8**(11): 830–834.
- Yabre, G. S. (2000). Comprehensive theory of dispersion in graded-index optical fibers. *Journal of Lightwave Technology*, **18**(2): 166-177.
- Kaur, M. and Sarangal, H. (2015). Analysis on Dispersion Compensation with Dispersion Compensation Fiber (DCF). *SSRG International Journal of Electronics and Communication Engineering (SSRG-IJECE)*, **2**(2): 56-59.

Effect of Heat Input on Microstructure, Friction and Wear Properties of Fe-Cr-B-C Coating on AISI 1020 Surface Coated by PTA Method

Turan GÜRGENÇ¹, Cihan ÖZEL²

¹Firat University Technology Faculty Automotive Engineering Department, 23119 ELAZIĞ

²Firat University Engineering Faculty Mechanical Engineering Department, 23119 ELAZIĞ
tgurgenc@firat.edu.tr

(Geliş/Received:23.06.2017; Kabul/Accepted:06.09.2017)

Abstract

In this study, low carbon steel AISI 1020 surface was coated in different heat inputs with (%-wt.) 70FeCr-30FeB ferro alloy powder mixture by using plasma transferred arc (PTA) welding method. The microstructure of the coating layers were investigated by using optical microscope (OM), scanning electron microscope (SEM), X-ray diffraction (XRD) and energy dispersive X-ray (EDS). The dry sliding wear and friction properties were determined using a block-on-disc type wear test device. Wear tests were performed at 19.62 N, 39.24 N, 58.86 N load and the sliding distance of 900 m. The results were show that coated samples were consisted of mostly M₇C₃ (M=Cr, Fe) carbide, (Cr, Fe)B, FeB and Fe₂B boride. It was seen that the dendrites were growth with increasing heat input. The highest average microhardness value was measured 1096 HV on sample coated with low heat input. It was determined that the sample with the highest wear resistance was the sample coated by the low heat input.

Keywords: PTA welding, AISI1020, Fe-Cr-B-C coating, Wear, Friction.

PTA Yöntemiyle Kaplanan AISI 1020 Yüzeyine Fe-Cr-B-C Kaplamanın Mikroyapı, Sürtünme ve Aşınma Özelliklerine Isı Girdisinin Etkisi

Özet

Bu çalışmada, düşük karbonlu AISI 1020 çeliğinin yüzeyi farklı ısı girdilerinde (% ağırlık) 70FeCr-30FeB ferro alaşım tozu karışımıyla plazma transfer ark (PTA) kaynak yöntemi kullanılarak kaplandı. Kaplama tabakalarının mikro yapıları optik mikroskop (OM), taramalı elektron mikroskobu (SEM), X ışını kırınımı (XRD) ve enerji dağılımlı X-ray (EDS) kullanılarak incelendi. Kuru kaymalı aşınma ve sürtünme özellikleri blok-on-disk tip aşınma test cihazı kullanılarak belirlendi. Aşınma testleri 19.62 N, 39.24 N, 58.86 N yükte ve 900 m kayma mesafesinde gerçekleştirildi. Sonuçlar, kaplanmış numunelerin genelde M₇C₃ (M=Cr, Fe) karbürü, (Cr, Fe)B, FeB ve Fe₂B borüründen oluştuğunu gösterdi. Dendritlerin artan ısı girdisiyle büyüdüğü görüldü. En yüksek ortalama mikro sertlik değeri düşük ısı girdisiyle kaplanan numunede 1096 HV olarak ölçüldü. En yüksek aşınma direncine sahip numunenin düşük ısı girdisi ile kaplanan numune olduğu tespit edildi.

Anahtar Kelimeler: PTA kaynak, AISI 1020, Fe-Cr-B-C kaplama, Aşınma, Sürtünme.

1. Introduction

Metallic machine parts expose to wear under working conditions, this causes significant loss of material per year [1]. Surface coating is the one of the most frequently used method for improving the wear of metal surfaces [2]. Welding is a method that use for depositing wear resistance materials on surface of metallic parts [3, 4]. The deposition of wear resistance materials on the surface with different welding methods such as plasma transferred arc (PTA) welding, gas

tungsten arc welding (GTA) welding, oxyacetylene welding and laser welding have been widely used in industry to protect the metallic parts surfaces from wear [5-8]. High carbon and chromium content alloys are widely used in wear resistance required applications, such as mining, minerals, cement and paper industries [9]. Fe-Cr-C alloys are generally used as coating material, because of low price and high mechanical properties [10]. Fe-Cr-C alloys coating have excellent wear and corrosion resistance, because of comprising high hardness

carbides in the microstructure, such as M_3C , M_7C_3 and $M_{23}C_6$ [11]. Also Fe-Cr-B and Fe-Cr-B-C alloys coatings are known as high wear and corrosion resistance coatings [12-14].

In this study, 70FeCrC-30FeB ferro alloy powder mixture was coated on AISI 1020 steel in different heat inputs by using PTA welding method. The microstructure of the coating layers were analyzed with using OM, SEM, EDS and XRD. The microhardness, wear and friction coefficient properties of the coatings were determined. Finally worn surfaces were examined by using SEM microscope.

2. Material and Method

In this study, commercially provided AISI 1020 low carbon steel was used as substrate material. The substrate was prepared in dimensions as shown in Figure 1. High carbon content FeCrC and FeB ferro alloy powders were used as coating materials. The powders sizes are approximately 38 μm . In Table 1, the chemical composition of AISI 1020 steel and ferro alloy powders are given.

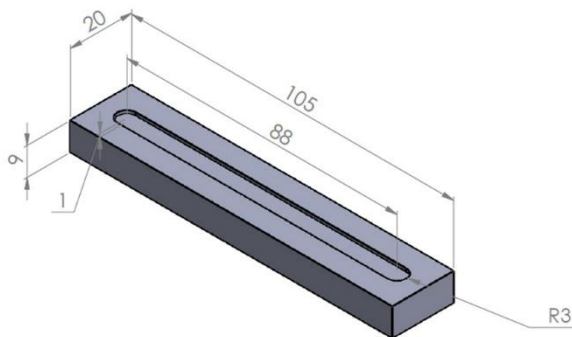


Figure 1. The dimensions of AISI 1020 (mm).

Table 1. Chemical compositions of AISI 1020 and ferroalloys (wt.-%).

Material	Cr	B	C	Mn	Fe	Other
AISI1020	-	-	0.2	0.356	Bal.	0.306
FeCrC	66.77	-	7.95	-	Bal.	0.557
FeB	-	18.22	0.3	-	Bal.	0.55

The surface of the substrate material was cleaned before coating with acetone after spraying the compressed air to clean the surface from oil and dirt. After that substrate was dried in the furnace at 60°C for 30 minutes in order to remove the moisture. The powders were dried in the furnace at 110 °C for 1 hour to remove the moisture of the coating powders. These powders, containing (%-wt.) 70FeCrC-30FeB, were weighed with a precision scale and a total of 30 g powder mixture was obtained for surface coating. This mixture was stirred for 1 hour at 150 rpm/min in a mechanical stirrer and it was placed in the opened channel on the substrate material. It was stuck to the surface with alcohol to prevent alloy powders from flying during welding. After this process, experimental samples were placed in the furnace to remove moisture and kept there at 100 °C for 1 hour for drying. After the samples had been removed from the furnace, they were kept until the room temperature was reached and the surface coating processes were carried out at different coating speeds and heat inputs using the Thermal Dynamics WC100B PTA welding device with the parameters given in Table 2. Argon was used as the plasma gas and shielding gas. After the coating process, the samples were put on to cool at room temperature.

Table 2. PTA coating parameters

Sample	S1	S2	S3	S4	S5	S6
Current (A)	120	140	160	120	140	160
Coating speed (m/min)	0.15	0.15	0.15	0.1	0.1	0.1
Voltage (V)				18-20		
Plasma gas flow rate (l/min)				0.5		
Shielding gas flow rate (l/min)				8		
Coating length (mm)				2		
Heat input (kJ/mm)	0.475	0.585	0.704	0.713	0.878	1.056

Then, these samples were sanded with 60, 120, 180, 240, 400, 600, 800, 1000 and 1200 mesh SiC sandpaper, respectively, and then polished with using 3µm size of diamond paste. The polished samples were washed with alcohol and dried. After this process, the samples were etched for 2 minutes with a mixture of 15 g of FeCl₃, 15 ml of HCl and 100 ml of distilled water. The etched samples were cleaned with alcohol and dried with hot air after being washed with soap.

The etched coating surfaces were examined using an optical microscope (OM) and scanning electron microscope (SEM). The chemical composition of the compounds comprising the coating was determined by the energy-dispersive X-ray analysis (EDS) and the type of the compounds was determined by the X-ray diffraction (XRD) analysis. The hardness of the coating was measured by applying a force of 200 gf from the midpoint of the top surface of the coating to the main material at 0.25 mm intervals with a microhardness test device.

The samples required for the adhesive wear test were cut at 6x9x6 mm³ from near the midpoint of the coated samples. Before the wear test, the coated surfaces of the samples were sanded with 400 mesh sandpaper and then cleaned with alcohol. Wear tests were carried out

in a "block-on-disc" adhesive wear tester at a normal load of 19.62 N, 39.24 N and 58.86 N. AISI 52100 bearing steel 15 mm in diameter was used as the abrasive and the samples were worn at a total of 900 m sliding distance at each load. Weight losses were measured with a precision scale of 10⁻⁵ g precision at every 300 m. During the wear test, the change in friction force dependent on the sliding distance was recorded and transferred to the computer via a data logger. Finally, the worn coating surfaces were analyzed using a SEM microscope.

3. Results and Discussion

3.1. Microstructure

In Figure 2 and Figure 3 the macro photographs and interface images of the Fe-Cr-B-C coated samples were shown respectively. As seen from the test specimens there is no crack or porosity on the coated surfaces, interfaces and coating layers.

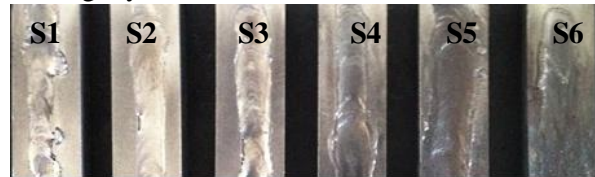


Figure 2. Macro photographs of the coated surfaces.

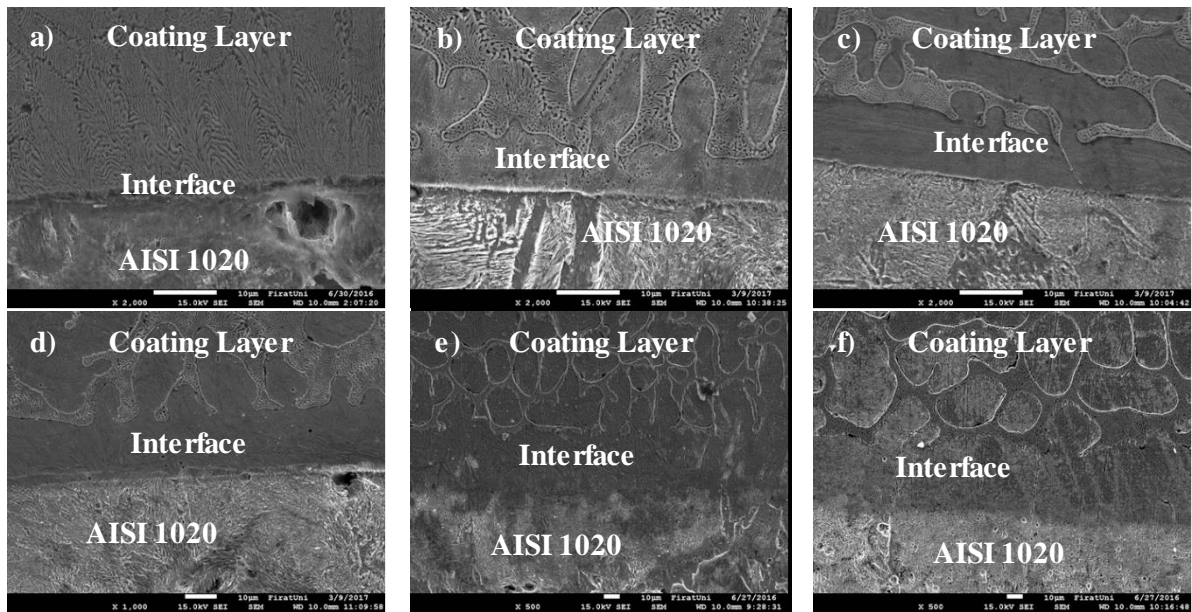


Figure 3. SEM images of coating interfaces a) S1 (x2000), b) S2 (x2000), c) S3 (x2000), d) S4 (x1000), e) S5 (x500) and f) S6 (x500).

The coating layers some properties were given in Table 3. As seen from the Table 3 coating layers depths and interface regions heights were increase with increasing heat input. The percentages of dendrites increased with increasing heat input because of intensive melting. Also with increasing heat input dendrites were growth.

Table 3. General properties of coating layers.

Sample	H	H _I	Dendrite	%P	A.av.	W.av.
S1	1410 μm	1.875 μm	-	-	-	-
S2	1470 μm	7.295 μm	Dendrite	31.5	75.2 μm ²	6.2 μm
S3	1560 μm	9.975 μm	Dendrite	42	364.2 μm ²	9 μm
S4	2170 μm	17.8 μm	Dendrite	45.6	486.6 μm ²	16.8 μm
S5	3490 μm	38.31 μm	Dendrite	54.5	2561.7 μm ²	31.1 μm
S6	4610 μm	42.33 μm	Dendrite	70.2	2621 μm ²	34.2 μm

H: Coating maximum depth; **H_I:** Average interface height taken from five different points; **%P:** Percante of the dendrites; **A.av.:** Average area of the phases; **W.av.:** Average width of the phases

The boron and carbon ratios in the coating areas could not be determined by EDS analysis because of the atomic numbers were low. The boron containing compounds in the coatings were determined by the XRD analysis given in Figure 4. According to the XRD analysis results, all of the coating layers were generally composed of M_7C_3 ($M=Cr, Fe$) carbide, $(Cr, Fe)B$, FeB and Fe_2B borides. In addition to these phases a little amount of $\alpha-Fe$ and $FeCr$ were detected. These structures were also observed in similar studies [15, 16].

The OM photographs of the coating layers are shown in Figures 5-10. As seen from the Figures, different microstructures appeared in the coating layers with the change of heat input. This can be explained by the change of the melting amount of the substrate material with the change of heat input and therefore the change of the chemical composition of the coating. As it seen from Figure 5a, borides and carbides in the coating layer are solidified as a colony because of the solidification time is short due to low heat input. The other samples (S2-S6) microstructures were consists of dendrites and interdendritic eutectic structures (Figure 6-10).

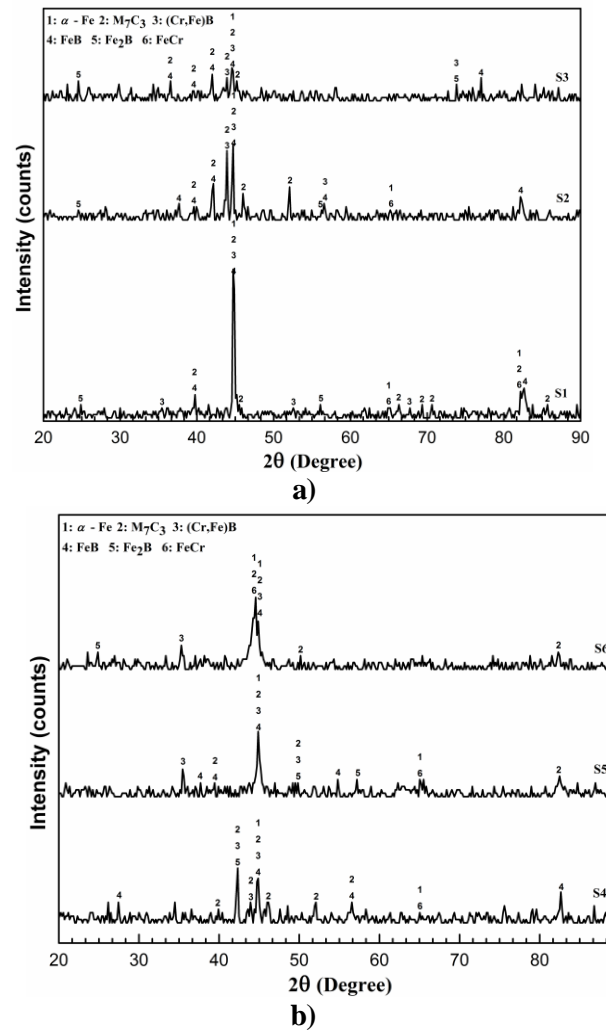


Figure 4. XRD results a) S1-S3 and b) S4-S6.

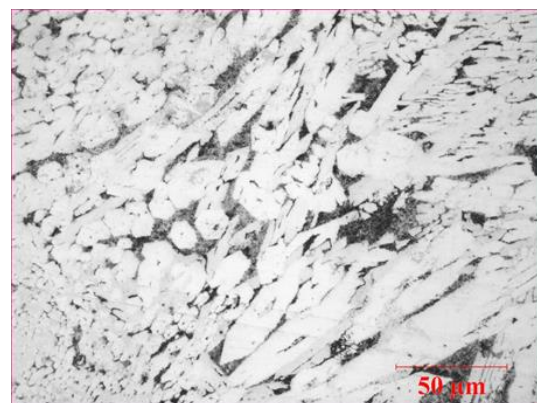


Figure 5. OM photograph of S1 x500.

The dendrite arms expand and stretch as the heat input increases. In addition, parallel to the increase of the heat input the dendrites occupy a

larger area due to the transition of the Fe element to the structure.

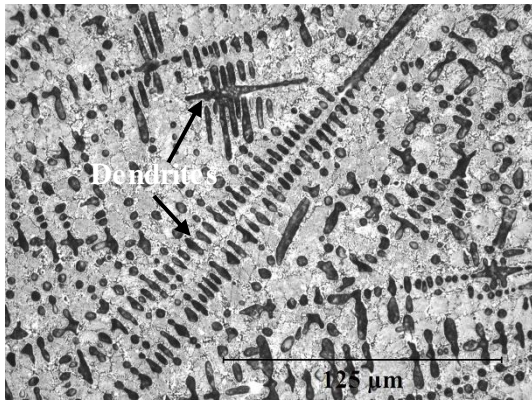


Figure 6. OM photograph of S2 x500.

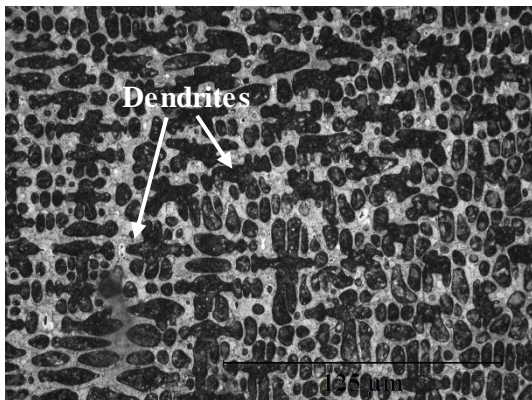


Figure 7. OM photograph of S3 x500.



Figure 8. OM photograph of S4 x500.

Figure 11 shows the SEM photographs and EDS analyzes taken from different points of the coating areas. According to the EDS results taken from point 1 in Figure 11a, this point contains (%-wt.) 32.82Fe-31.23Cr-35.95C elements.

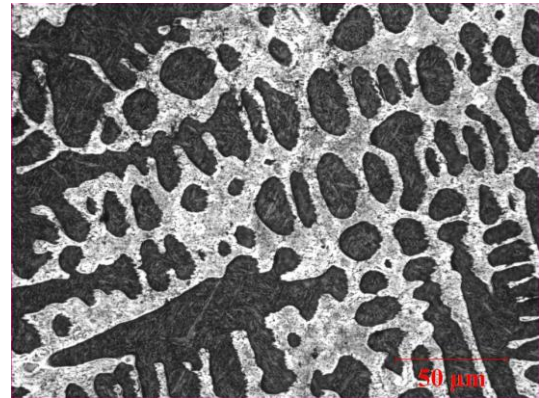


Figure 9. OM photograph of S5 x500.

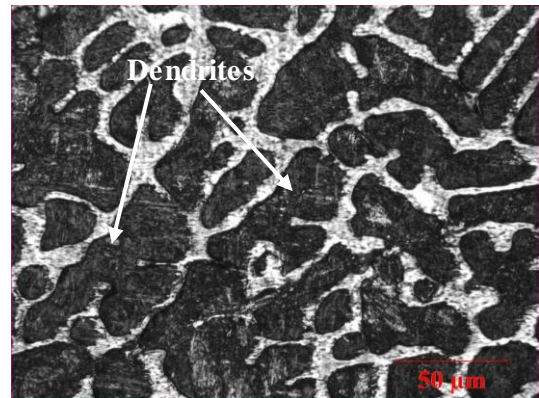


Figure 10. OM photograph of S6 x500.

According to the Cr/Fe ratio, this phase is M_7C_3 (M=Fe, Cr) carbide. The phase at point 2 contains (%-wt.) 38.43Fe-20.82Cr-40.75C elements.

It is thought that from EDS and XRD results, this phase is (Cr, Fe)B boride. According to the EDS results taken from dendrites, point 3 in Figure 11b contains (%-wt.) 73.24Fe-8.54Cr-18.22C elements, point 5 in Figure 11c contains (%-wt.) 65.84Fe-4.76Cr-29.4C elements, point 7 in Figure 11d contains (%-wt.) 66.52Fe-5.08Cr-28.4C elements, point 9 in Figure 11e contains (% wt.) 58.92Fe-4.72Cr-36.36C elements and point 11 in Figure 11f contains (%-wt.) 67.15Fe-3.13Cr-29.71C elements. Also according to the EDS results taken from eutectics, area 4 in Figure 11b contains (%-wt.) 63.50Fe-16.51Cr-19.99C elements, area 6 in Figure 11c contains (%-wt.) 68.79Fe-10.49Cr-20.72C elements, area 8 in Figure 11d contains (%-wt.) 64.69Fe-9.37Cr-25.94C elements, area 10 in Figure 11e contains

(%-wt.) 59.77Fe-10.16Cr-30.08C elements and area 12 in Figure 12f contains (%-wt.) 68.09Fe-9.87Cr-22.04C elements. As can be seen from the

EDS analysis results, similar structures are in different chemical compositions due to different melting intensities with the change of heat input.

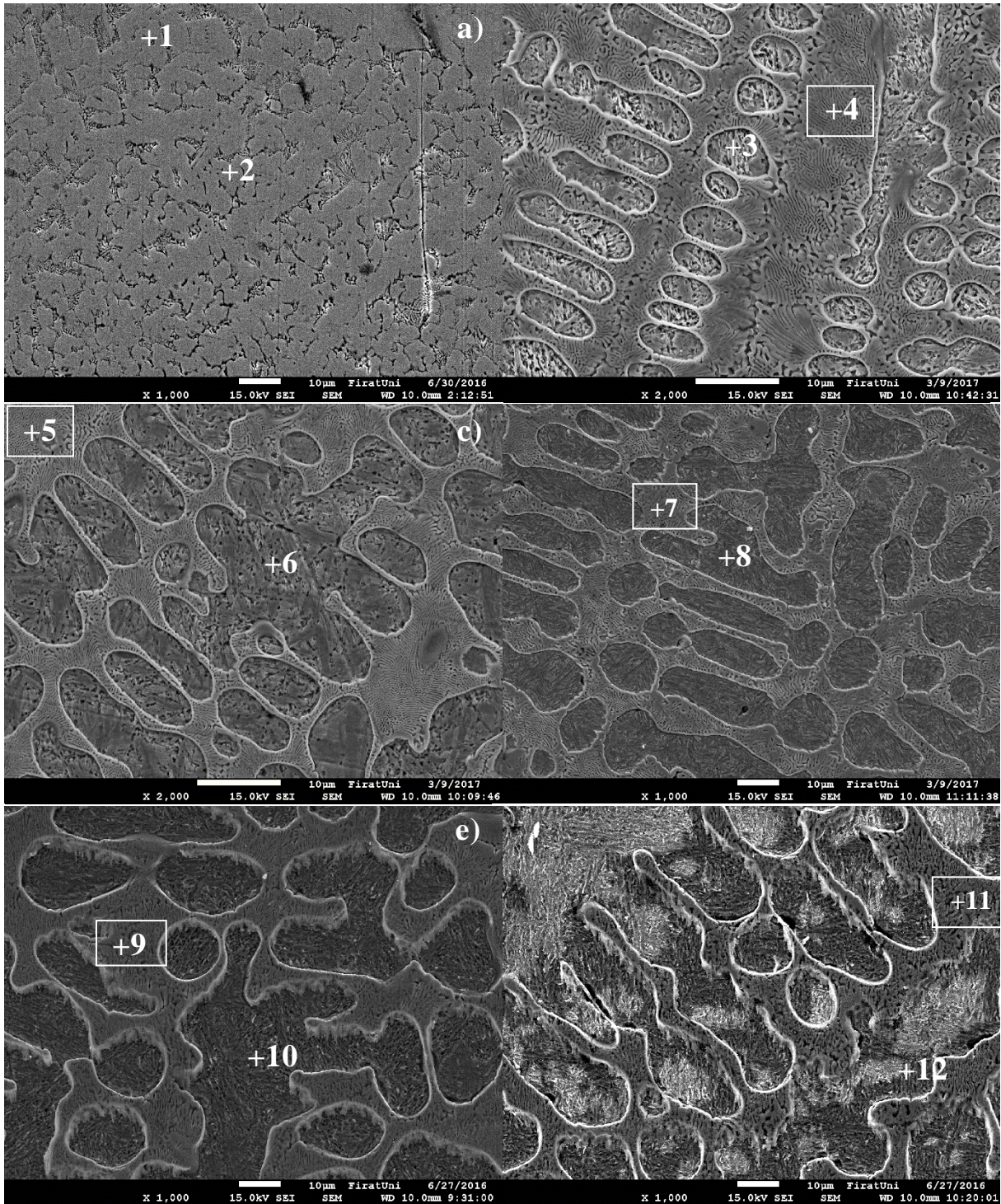


Figure 11. SEM photographs of the coating layers a) S1 (x1000), b) S2 (x2000), c) S3 (x2000), d) S4 (x1000), e) S5 (x1000) and f) S6 (x1000).

3.2 Microhardness

The microhardness distribution of the coating layers are given in Figure 12. It was seen that the microhardness of the coating layers are higher than the substrate material due to the hard borides and carbides in their structures. It was seen that the average microhardness of the coating layers

varied from 621 to 1096 HV and decreased with increasing heat input. The highest microhardness value was measured as 1254 HV in sample S1, which was coated with the lowest heat input. The average microhardness values of the coating layers are 1096 HV, 991 HV, 858 HV, 812 HV, 703 HV and 621 HV for samples S1, S2, S3, S4, S5, S6 respectively

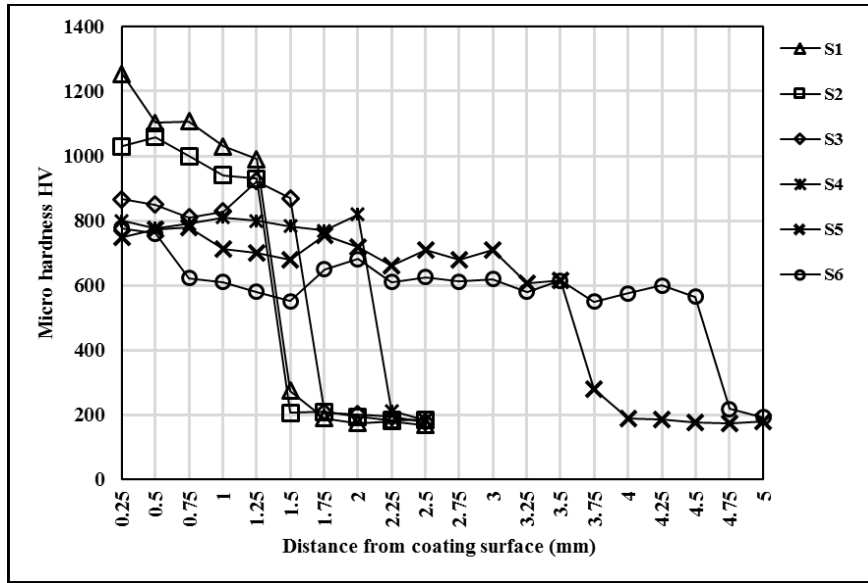


Figure 12. Microhardness distribution of coating layers

3.3. Wear and Friction

At 19.62 N, 39.24 N and 58.86 N normal load the change in wear losses according to the sliding distance are given in Figures 13-15 respectively. It was found that the wear losses of coated samples are less than the substrate material at all load values. As the average microhardness of the coating layers decreased, wear losses increased. The sample with the best wear resistance at all load values is the sample S1, which is coated with the lowest heat input and has the highest average hardness. The sample with the lowest wear resistance is the sample S6, which is coated with highest heat input and is the softest sample. At 19.62 N load, the wear resistances of the other specimens except the specimens coated with high heat input (S5 and S6), tending to increase according to the sliding distance (Figure 13).

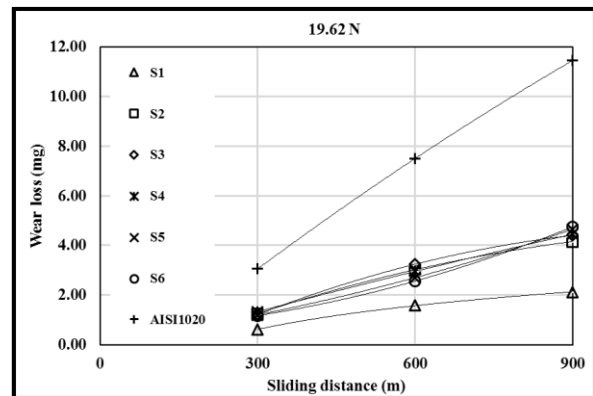


Figure 13. Wear losses at 19.62 N load.

At 39.24 N load, the wear resistances of all samples decreased when the sliding distance increased to 600 m and increased when the sliding distance increased to 900 m (Figure 14).

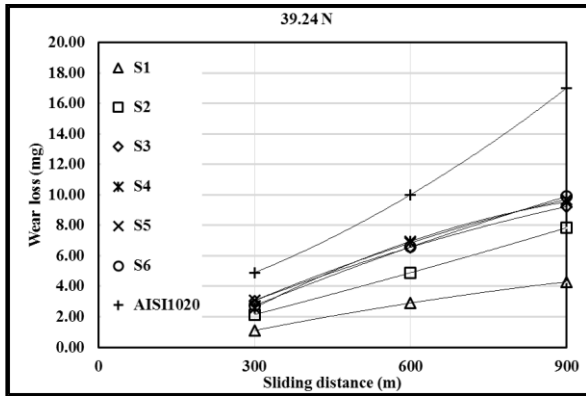


Figure 14. Wear losses at 39.24 N load.

At 58.86 N load (Figure 15), the wear resistance of the S6, which is coated by the highest heat input, is increased according to the sliding distance. The wear resistances of the S1-S5 decreased with the increase of the sliding distance to 600 m and increased when the sliding distance increased to 900 m.

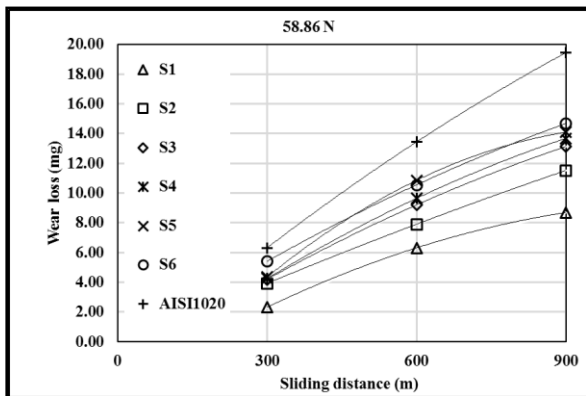


Figure 15. Wear losses at 58.86 N load.

The change in wear losses according to the normal load is given in Figure 16. As it seen, the wear resistance of the S1, which has the highest average microhardness, decreases as the load increases. The wear loss of the S2, which has an average micro hardness close to this sample, increases with increasing load. The wear resistances of the other samples decreased when the load increased to 39.24 N and increased when the load increased to 58.86 N.

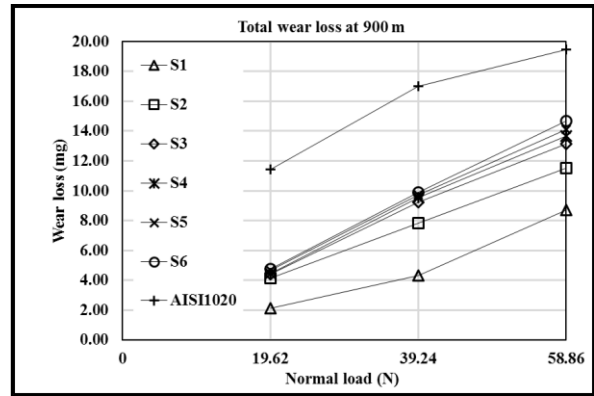


Figure 16. Wear losses according to normal load.

In Figure 17, the variation of average friction coefficients (μ_{ave}) according to the load is shown. The samples with high average microhardness have higher μ_{ave} values and as the heat input increases, the μ_{ave} values decrease at all load. The μ_{ave} values of the samples vary between 0.619 - 0.806 at 19.62 N load, 0.665 - 0.78 at 39.24 N load and 0.601 - 0.74 at 58.86 N load.

At 19.62 and 39.24 N load, the average coefficient of frictions of all samples are lower than the AISI 1020. The average friction coefficients of S1-S5 at 58.86 N load are higher than the AISI 1020. Also S6's average friction coefficient is close but higher than the AISI 1020 at 58.86 N load.

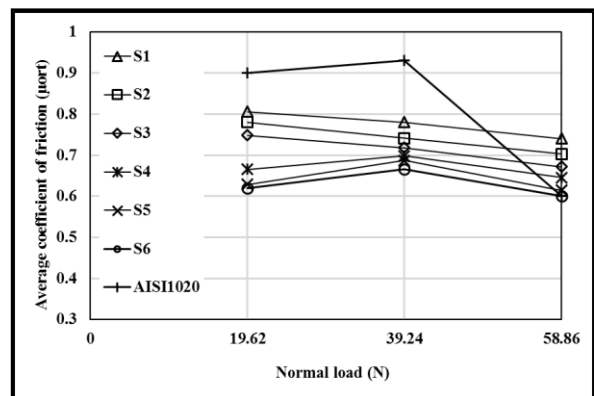


Figure 17. The variation of average friction coefficients according to load.

The wear surface SEM photographs of the samples worn at most (S6), at least (S1) and the substrate material at each load are shown in Figure 17. Significant amounts of the material were lost at all loads from substrate (Figure 17a-

c). In the substrate material, it was determined that the particles broken from the surface were removed from the surface at 19.62 N and 39.24 N load while the broken particles were plastered to the grooves formed on the surface at 58.86 N load due to the high temperature. Peeling and craters were observed on the worn surface of the substrate material at low load. Again, the roughness of the surface at this load is much higher because the broken particles did not plaster to the surface due to the low load (Figure 17a). Wide and deep craters were observed on the worn surfaces at medium and high loads. Wear was usually in the form of scraping. According to the EDS results taken from the wear surfaces of the

substrate material, oxidation occurred on the worn surfaces and these oxides were plastered to the surface at a high load and reduced the friction coefficient. If S1's worn surfaces investigated, it is seen that grooves formed on the surface at 19.62 and 39.24 N load (Figure 17d and e). At 58.86 N load, the abrasion is more of a scrape, and scraping pits formed on the surface (Figure 17f). As it seen from S6's worn surface photographs, grooves and spalling formed at 19.62 N load (Figure 17g). At 39.24 N load, it is seen that the particles have been stripped off from the surface and scraping pits and spalling formed on worn surface (Figure 17h). At 58.86 N load, the grooves flattened with increasing wear (Figure 17i).

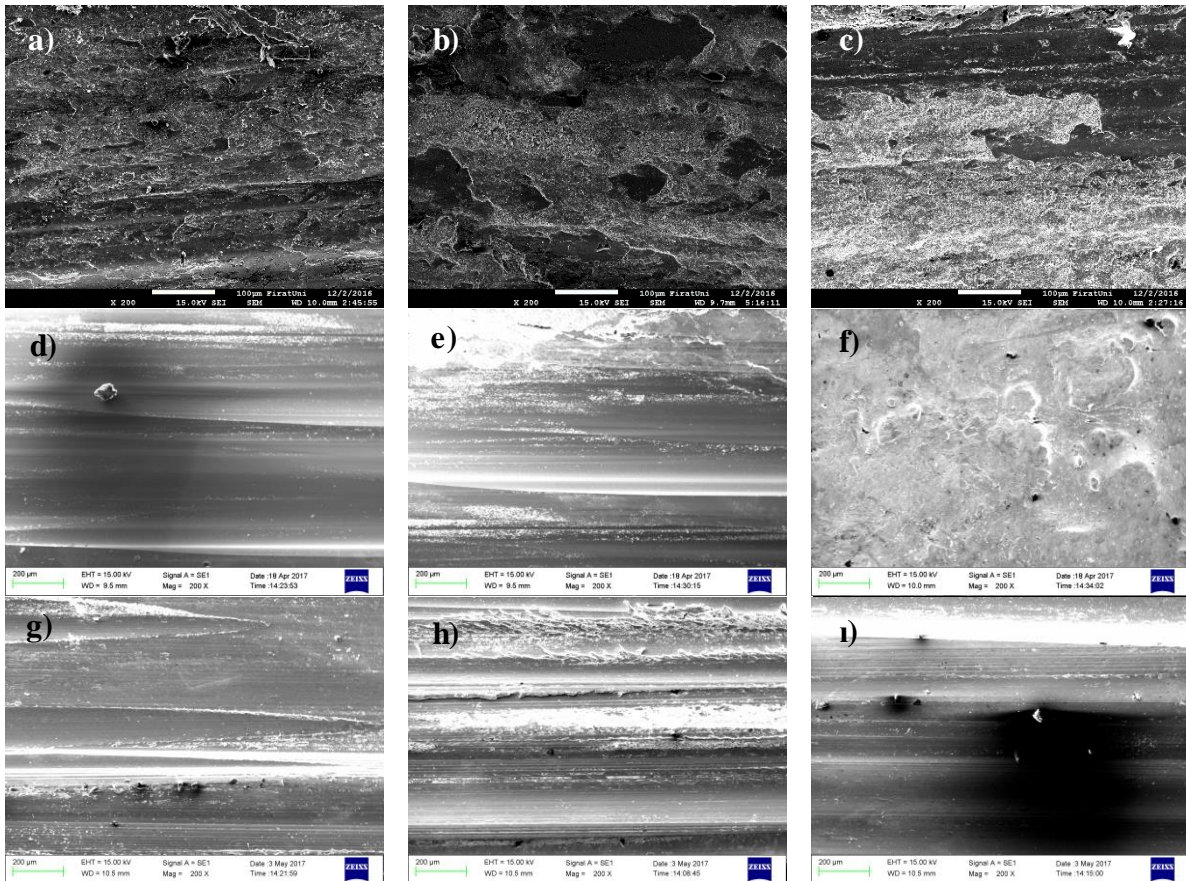


Figure 18. SEM photographs of the wear surface **a)** AISI 1020 19.62 N, **b)** AISI 1020 39.24 N, **c)** AISI 1020 58.86 N, **d)** S1 19.62 N, **e)** S1 39.24 N, **f)** S1 58.86 N, **g)** S6 19.62 N, **h)** S6 39.24 N and **i)** S6 58.86 N.

Acknowledgment

The authors thanks to the Firat University Research Fund (FUBAP-MF.15.09) for their financial contribution to this research.

4. Conclusions

- The surface of AISI 1020 was successfully modified with Fe-Cr-B-C elements by using the PTA welding method.

- Coating layers depths and interface regions heights were increase with increasing heat input.
- No porosity or cracks were found on the coating layers and interfaces.
- Coating layers were generally composed of M_7C_3 (M=Cr, Fe) carbide, (Cr, Fe)B, FeB and Fe_2B borides.
- The dendrite arms expand and stretch as the heat input increases.
- The average microhardness of the coating layers varies from 621 to 1096 HV and decreases as the heat input increases. The highest microhardness value was measured at 1254 HV in sample, which was coated with the lowest heat input.
- The total wear loss of the coated samples was observed to be lower when compared to AISI 1020 steel at 19.62 N, 39.24 N and 58.86 N load. As the average microhardness of the coating layers decreased, wear losses increased.
- The samples with high average microhardness have higher μ_{ave} values and as the heat input increases, the μ_{ave} values decrease.

5. References

1. Gou, J., Lu, P., Wang, Y., Liu, S., and Zou, Z. (2016). Effect of nano-additives on microstructure, mechanical properties and wear behaviour of Fe-Cr-B hardfacing alloy. *Applied Surface Science*, **360**: 849-857.
2. Buchely, M., Gutierrez, J., Leon, L., and Toro, A. (2005). The effect of microstructure on abrasive wear of hardfacing alloys. *Wear*, **259**(1): 52-61.
3. Tamg, Y., Juang, S., and Chang, C. (2002). The use of grey-based Taguchi methods to determine submerged arc welding process parameters in hardfacing. *Journal of Materials Processing Technology*, **128**(1): 1-6.
4. Chatterjee, S. and Pal, T. (2003). Wear behaviour of hardfacing deposits on cast iron. *Wear*, **255**(1): 417-425.
5. Saha, A. and Mondal, S.C. (2016). Multi-objective optimization in WEDM process of nanostructured hardfacing materials through hybrid techniques. *Measurement*, **94**: 46-59.
6. Korkut, M., Yilmaz, O., and Buytoz, S. (2002). Effect of aging on the microstructure and toughness of the interface zone of a gas tungsten arc (GTA) synthesized Fe-Cr-Si-Mo-C coated low carbon steel. *Surface and Coatings Technology*, **157**(1): 5-13.
7. Wang, Z.-T., Zhou, X.-H., and Zhao, G.-G. (2008). Microstructure and formation mechanism of in-situ TiC-TiB₂/Fe composite coating. *Transactions of Nonferrous Metals Society of China*, **18**(4): 831-835.
8. Wu, Q., Li, W., Zhong, N., Gang, W., and Haishan, W. (2013). Microstructure and wear behavior of laser cladding VC-Cr₇C₃ ceramic coating on steel substrate. *Materials & design*, **49**: 10-18.
9. Wiczerzak, K., Bala, P., Stepień, M., Cios, G., and Kozieł, T. (2016). Formation of eutectic carbides in Fe-Cr-Mo-C alloy during non-equilibrium crystallization. *Materials & design*, **94**: 61-68.
10. Yang, J., Hou, X., Zhang, P., Zhou, Y., Yang, Y., Ren, X., and Yang, Q. (2016). Mechanical properties of the hypereutectoid Fe-Cr-C hardfacing coatings with different nano-Y₂O₃ additives and the mechanism analysis. *Materials Science and Engineering: A*, **655**: 346-354.
11. Buytoz, S., Yildirim, M.M., and Eren, H. (2005). Microstructural and microhardness characteristics of gas tungsten arc synthesized Fe-Cr-C coating on AISI 4340. *Materials Letters*, **59**(6): 607-614.
12. Jin, H., Rhyim, Y., Park, C., and Kim, M. (1997). Microstructure and wear-resistance of Fe-Cr-B base metamorphic alloys. *Metals and Materials*, **3**(1): 60-64.
13. Jin, H., Park, C., and Kim, M. (2001). In situ TEM heating studies on the phase transformation of metastable phases in Fe-Cr-B alloy spray coatings. *Materials Science and Engineering: A*, **304**: 321-326.
14. Jin, H., Rhyim, Y., Hong, S., and Park, C. (2001). Microstructural evolution of the rapidly quenched Fe-Cr-B alloy thermal spray coatings. *Materials Science and Engineering: A*, **304**: 1069-1074.
15. Manna, I., Chattopadhyay, P., Banhart, F., Croopnick, J., and Fecht, H.-J. (2008). Microstructural evolution of wear-resistant FeCrB and FeCrNiCoB coating alloys during high-energy mechanical attrition. *Wear*, **264**(11): 940-946.
16. Yüksel, N. and Şahin, S. (2014). Wear behavior-hardness-microstructure relation of Fe-Cr-C and Fe-Cr-C-B based hardfacing alloys. *Materials & design*, **58**: 491-498.

LSE Channel Estimation and Performance Analysis of OFDM Systems

Bircan KAMIŞLIOĞLU, Ayhan AKBAL

Fırat Üniversitesi, Mühendislik Fakültesi, Elektrik Elektronik Mühendisliği Bölümü, Elazığ
bkamislioglu@firat.edu.tr

(Geliş/Received: 15.02.2017; Kabul/Accepted: 11.04.2017)

Abstract

Orthogonal frequency division multiplex (OFDM) is one of the best approaches to overcome frequency selectivity of channels. In multiple-input multiple-output (MIMO) orthogonal frequency division multiplexing (OFDM) systems, we purposed channel estimation with least squares (LS) estimation method in this paper. To improve channel estimation achievement a LS algorithm is developed, so we obtain Bit Error Rate (BER) performance of channel. Mean Square Error (MSE) of LS estimation calculated and depicted with figures. Signal to noise ratio (SNR) indicated notable efficacy in this paper that obtained by using the LS algorithm, in particular channels with variation in time.

Keywords : Channel Estimation, LSE, MIMO System, OFDM.

OFDM Sistemlerinde LSE Kanal Tahmini ve Performans Analizi

Özet

Dikgen frekans bölmeli çoğullama (Orthogonal frequency division multiplex-OFDM) kanalların frekas seçiciliğiyle baş etmek için kullanılan en iyi yöntemlerden biridir. Bu çalışmada çok girişli çok çıkışlı (Multiple-Input Multiple-Output-MIMO) OFDM sistemlerinde kanal tahmini için en küçük kareler (Least Squares-LS) yöntemi önerilmiştir. Kanal tahmininin başarısını ilerletmek için bir en küçük kareler algoritması geliştirilmiştir bunun sonucunda kanalın bit hata oranı (Bit Error Rate-BER) performansı elde edilmiştir. LS tahmin edicinin ortalama karesel hatası hesaplanmış ve şekillerle gösterilmiştir. LS algoritması kullanılan bu çalışmada sinyal gürültü oranı özellikle zamanla değişen kanallarda önemli bir etki göstermiştir.

Anahtar Kelimeler: Kanal Tahmini, LSE, MIMO Sistemler, OFDM.

1. Introduction

In recent years in communication systems data rate is getting high and researchers have notable interest on rapid modulation techniques. As a multicarrier modulation technique OFDM is fairly interested by researchers. Because of its basic application and stability, frequency-fading channels are transformed the channel into flat-fading sub channels. OFDM has been performed for a lot of applications, such as high speed telephone line communication, digital audio broadcasting, wireless local area network digital television broadcasting and lines of digital subscriber. In recent communication systems we can realize a remarkable increased capacity OFDM and multiple antennas together and this enhancement obtained due to diversity of

transmit and receive sides. [1]. Adding training pilot symbols at the transmitter in practice implementations, CSI is effective estimated at the receiver. Channel estimation with pilot symbol is especially attractive for wireless communication systems in the channel with varying time [2].

Meanwhile a lot channel estimators use for OFDM, error probability examination availability of channel estimation errors has taken notionally less care. In recent days phase shift keying and quadrature amplitude modulation approximations were progressive about BER performance for channel estimation errors of OFDM [3, 4].

OFDM systems consist completely of pilot symbols because of identifying the multiple training channels. This approach for single input

and single output (SISO) systems is showed in [5-7], whereas MIMO systems is detailed described in [8]. Like this application firstly any transmission of data we compute estimation of the CSI. When remarkably changes exist for CSI, reobtaining pilot symbols is transmitted. To estimate the CSI in fast time varying surroundings, we must continuously retrain for such systems. About retraining, these systems are experienced an incremented BER because of their antiquated channel estimates. Wiener filter method as based on a known channel correlation function can be used to advance the estimation of channel parameters [9, 10].

MSE of the channel estimation with LS technique is recommended the pilot symbols have an optimum location for SISO OFDM systems. If this channel estimation technique wanted to length to MIMO OFDM systems, seeing that either the location of the pilot symbol or the pilot sequence must be optimized to enhance the MSE value minimum with channel estimation method with LS [11].

In this paper, based on pilot tones MIMO OFDM system is described with a LS channel estimation scheme. MSE of the channel estimation with LS technique is computed, optimum pilot tones of the pilot subcarriers are supplied. LS channel estimation design for multiple OFDM symbols is debated. LS channel estimation algorithm is proposed to advance estimation application.

The organization of this paper is regulated as trace. In chapter II OFDM technique is explained, LSE channel estimation steps are given in chapter III. Analysis of channel estimation is introduced in chapter IV and conclusions are offered in chapter V.

2. OFDM Technique

Transmission system of the OFDM about account is depicted in Figure 1. High data rate streams of the random input signal are transformed into low data rate streams. The low data rate streams are modulated in parallel subcarriers in the OFDM. This parallel stream is dedicated input to the IFFT block structure. The data is transformed from frequency to time before the data accessed the channel by the IFFT block

structure. The data is encoded with adding the cyclic prefix as the guard interval and transmission is succesfull at receiver [12]. Binary source generator produced the digital input data like as BPSK, QPSK and QAM modulation approach are used to modulate the binary data with several different constellations. The data is transformed frequency domain to time domain by the IFFT block in Figure 2. To insert guard interval known as CP succeed the problems like ICI/ISI with acquiring the delay connected problems at the channel. Before the symbols transmitting to the channel, firstly the symbols of OFDM are in the time domain available length. After that all the operations enforced in the inverse direction and obtained OFDM signal as the output of receiver block. CP insertion in the OFDM modulation is the most extensive technique among all the multicarrier modulations because of its facility and its stability across to multipath fading using the cyclic prefix. Even so this technique caused a decrement of spectral efficiency owing to the CP. Also the OFDM spectrum is not dense because of the large side lobe levels resulting from the rectangular pulse [13].

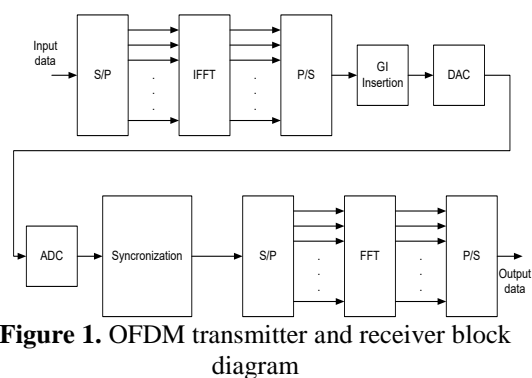


Figure 1. OFDM transmitter and receiver block diagram

OFDM is a typical multiple channel modulation technique that used to separate to the channel numerous of parallel sub channels and the parallel channels transmit multiple symbols. OFDM has an attractive feature that is considered efficient spectral and also applications of OFDM cope with equalization of dispersive slowly fading channels which is a perfect way. OFDM is used by multiuser systems that exhibited perfect schemes for multiple accesses such as transmission systems with single carrier. When we compared to carrier systems with each other,

as a variable modulation technique for multiple access systems OFDM is in that case intrinsically make easy multiple access both time domain and frequency domain.

OFDM also has some imperfections properties. OFDM is sensitive errors of carrier frequency, because a given spectral assignment divides into many narrow subcarriers by OFDM structure with small spacing for subcarriers inherently. Furthermore, to obtain the orthogonality about subcarriers, it needs linear amplifiers. Because of OFDM systems own a high peak to average power ratio the systems require a large amplifier power back off and a many of bits in the analog to digital (A/D) and digital to analog (D/A) designs. So high requirement is available transmitter and receiver sides in OFDM [14].

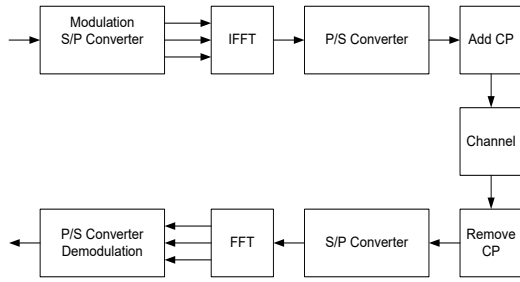


Figure 2. OFDM block diagram

OFDM modulation and demodulation block diagram is given in Figure 2. Guard interval is transformed CP in this figure.

3. Channel Estimation With Least Square Method

In this part, channel estimation with LS design is clarified. Data vector is formulated as $X_r(n)$ in Equation 1.

$$X_r(n) = S_r(n) + B_r(n) \quad (1)$$

In Equation 1, $S_r(n)$ is some optional $K \times 1$ data vector, $B_r(n)$ is some optional $K \times 1$ pilot sequence vector and demodulated signal is described in Equation (2).

$$Y_q(n) = \sum_{r=1}^{N_r} \text{diag}\{X_r(n)\} Fh_{q,r} + \Xi_q(n) \quad (2)$$

$$= \sum_{r=1}^{N_r} (\text{diag}\{S_r(n)\} + \text{diag}\{B_r(n)\}) * Fh_{q,r} + \Xi_q(n) \quad (3)$$

Taking to FFT of $Y_q(n)$ in Equation (3) we obtained finally as Equation (4).

$$Y_q(n) = \sum_{r=1}^{N_r} S_{r,\text{diag}}(n) Fh_{q,r} + \sum_{r=1}^{N_r} B_{r,\text{diag}}(n) Fh_{q,r} + \Xi_q(n) \quad (4)$$

We consider the data model as Equation (5).

$$Y_q = Th_q + Ah_q + \Xi_q \quad (5)$$

LS estimate of h_q can obtained as \hat{h}_q and formulated in Equation (6).

$$\hat{h}_q = A^T Y_q \quad (6)$$

Note that equation (6) shows that \hat{h}_q is a composition of the true channel vector h_q and noise vector in the system. We can see whether or not the pilot tones are the same for each ofdm symbol. Namely, same set of pilot tones in ofdm structure is not compulsory.

4. Channel Estimation Performance And Simulations

This section presents enhancement of the MSE of the channel estimation with LS. Results of applications are provided to have optimal pilot sequences and optimal placement of the pilot tones in point of the MSE. In Equation 7, L describes the maximum channel length. MSE calculation of the channel estimation with LS is formulated in Equation 7.

$$MSE = \frac{1}{LNt} \mathcal{E} \left\{ \left\| \hat{h}_q - h_q \right\|^2 \right\} \quad (7)$$

Because of obtaining the minimum MSE of the channel estimation with LS linked to a fixed power ρ given for training and zero mean white noise is σ_n^2 in Equation 8.

$$MSE_{\min} = \frac{\sigma_n^2}{\rho} \quad (8)$$

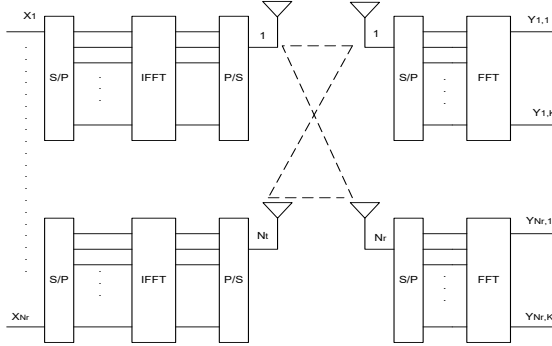


Figure 3. MIMO-OFDM block diagram

Figure 3 is depicted block diagram of MIMO-OFDM. In Figure 3 number of transmit antennas is N_t , number of receive antennas is N_r and number of subcarriers is K . Each transmit or receive antenna which is common practice in wireless communications. Since we extracted the cyclic prefix from the q th receive antenna, $Y_q(n)$ is obtained as $K \times 1$ vector length.

To channel estimation in OFDM is used is utilized in conventional OFDM modulator or demodulator. Take for the OFDM symbol that is transmitted from the r th antenna at time index n is denoted by $K \times 1$ the vector $X_r(n)$. Before transmission, IFFT is processed to this vector, and v lengthed a cyclic prefix is added. If all channels maximum length is L we obtain that $v \geq L-1$,

pilot symbols. OFDM is directly practicable to techniques from single carrier flat fading systems when each subcarrier is flat fading. The sparse insertion of known pilot symbols is found in pilot symbol assisted modulation (PSAM) on channels with flat fading that is in a stream of data symbols in such systems. When the pilot symbols attenuation is calculated the data symbols attenuations among the pilot symbols are characteristically predicted with the fading channel on time correlation features.

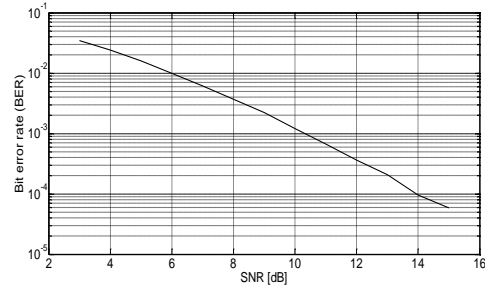


Figure 4. BER versus SNR in LS channel estimation for MIMO OFDM

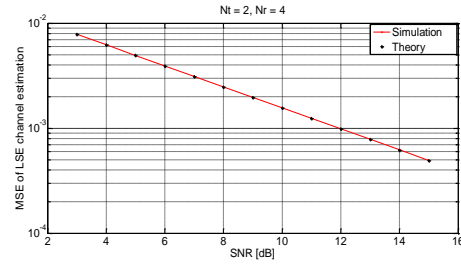


Figure 5. MSE of LSE channel estimation for MIMO OFDM

BER versus SNR in LS channel estimation for MIMO OFDM system application is shown in Figure 4. MSE of LS channel estimation in simulation and theory for MIMO OFDM system is depicted in Figure 5. In application we selected that $N_t=2$, $N_r=4$, number of subcarriers is 128 and percentage of guard interval is 0.25. Number of pilot symbols is 64 plus number of the data symbols is 64 we get all of subcarriers. In literature most of document explains that channel estimation impressions consist of two steps using the channel correlation property. First, correlation of channel technique is attenuations of the data symbols is estimated used to measure and smooth the attenuations at the pilot positions. Then complex valued by these measurements in the second step. Channel correlation properties are used in this second step by filters interpolation technique or a decision directed technique. [15].

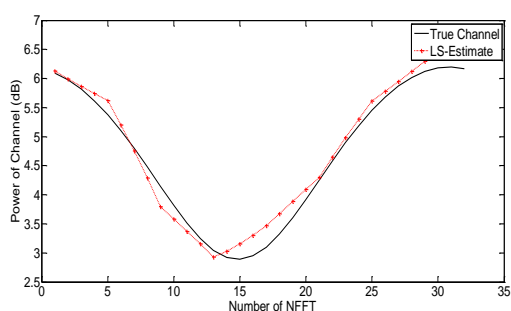


Figure 6. Power of channel with LSE channel estimation and true channel.

In Figure 6 power of estimated channel and true channel with LSE is depicted. Estimated channel power is fairly close to true channel. So this result shows that LS estimation is appropriate for MIMO OFDM channel estimate.

5. Conclusion

This study focused channel estimation with LS method based on pilot tones approach has been evaluated for application of MIMO OFDM systems. The pilot sequences must be equal powered, equal spaced, and obtained orthogonal phase shift to enhance the channel estimation with the minimum MSE. Our results indicates that purposed method about pilot tones the number of transmit antennas are increased so pilot tones for training require more and decreases the efficiency of application. When the channel is slowly time-varying, estimating the channel parameters can reduce this effect over multiple OFDM symbols. Also in next organizations, BER performance will be improve with different from LS estimation method about of MMSE estimation method.

6. References

1. Bölcskei, H., Gesbert, D., Paulraj, A. J., (2002). On the capacity of OFDMbased spatial multiplexing systems. *IEEE Trans. Commun.*, 50, 225–234.
2. Cavers, J.K., (1991). An analysis of pilot symbol assisted modulation for Rayleigh fading channels. *IEEE Trans. Veh. Technol.*, 40, 686–693.
3. Chang, M.X. Su, Y.T., (2002). Performance analysis of equalized OFDM system in Rayleigh fading. *IEEE Trans. Wireless Commun.*, 1, 721–732.
4. Cheon, H., Hong, D., (2002). Effect of channel estimation error in OFDMbased WLAN. *IEEE Commun. Lett.*, 6, 190–192.
5. Deneire, L., Vandenameele, P., Van der Perre, L., Gyselinckx, B., Engels, M., (2001). A low complexity ML channel estimator for OFDM. *Proc. IEEE Int. Conf. Commun.*, Helsinki, Finland, 11–14.
6. Edfors, O., Sandell, M., Van de Beek, J.J., Wilson, S.K., Borjesson, P.O., (1998). OFDM channel estimation by singular value decomposition. *IEEE Trans. Commun.*, 46, 931–939.
7. Van de Beek, J.J., Edfors, O., Sandell, M., Wilson, S. K., Brjesson, P. O., (1995). On channel estimation in OFDM systems. *Proc. IEEE Vehic. Technol. Conf.*, 2, 815–819.
8. Jeon, W. G., Paik, K. H., Cho, Y. S., (2000). An efficient channel estimation technique for OFDM systems with transmitter diversity. *Proc. IEEE Int. Symp. Pers., Indoor Mobile*, 2, 1246–1250.
9. Li, Y., Seshadri, N., Ariyavisitakul, S., (1999). Channel estimation for OFDM systems with transmitter diversity in mobile wireless channels. *IEEE J. Select. Areas Commun.*, 17, 461–471.
10. Li, Y.G., Cimini, L.J., Sollenberger, N.R., (1998). Robust channel estimation for OFDM systems with rapid dispersive fading channels. *IEEE Trans. Commun.*, 46, 902–915.
11. Ohno, S., Giannakis, G. B., (2001). Optimal training and redundant precoding for block transmissions with applications to wireless OFDM. *Proc. IEEE ICASSP*, Salt Lake City, UT, 2389–2392.
12. Veerananarayanareddy, C., Prabhakar, K., (2015). A Novel BER Analytical Performance of DWT based ofdm using various channel over dft based OFDM. *International journal of engineering and computer science* 4(9), 14313.
13. Le Floch, B., Alard, M., Berrou, C., (1995). Coded orthogonal frequency division multiplex. *Proc. IEEE*, 83(6), 982–996.
14. Beek, J.J., (1998). Channel Estimation in OFDM Systems. Lulea University of Technology, 1402-1544.
15. Van de Beek, J.J., (1998). Synchronization and Channel Estimation in OFDM Systems. Lulea University of Technology, Division of Signal Processing.

PI and Fuzzy Logic Control of Photovoltaic Panel Powered Synchronous Boost Converter

Ahmet YÜKSEL, Adnan CORA

Karadeniz Teknik Üniversitesi, Mühendislik Fakültesi, Elektrik Elektronik Mühendisliği Bölümü, Trabzon
ahmetyuksel@ktu.edu.tr

(Geliş/Received: 26.02.2017; Kabul/Accepted: 19.04.2017)

Abstract

In this paper, control of DC/DC synchronous boost converter for photovoltaic panels with different controllers is simulated in the Matlab/SIMULINK software. Firstly, synchronous boost converter is simulated, and then regarding to the changes in reference and source voltages traditional PI and Fuzzy Logic control is achieved. Results obtained are analyzed and compared.

Keywords : Synchronous; Boost Converter; PI; Fuzzy Logic

Fotovoltaik Panel Beslemeli Senkron Artıran Çeviricinin PI ve Bulanık Mantık Denetimi

Özet

Bu çalışmada fotovoltaik paneller için DC/DC senkron artıran çeviricinin farklı denetleyicilerle denetimi Matlab/SİMULİNK ortamında benzetim yapılarak yapılmıştır. İlk olarak senkron artıran çevirici benzetimi yapılmıştır ve sonrasında çeviricinin referans gerilim değişimi ve kaynak gerilim değişim durumları altında, geleneksel PI ve Bulanık Mantıkla denetimi yapılmıştır. Denetim sonuçları analiz edilerek sonuçlar karşılaştırılmıştır.

Anahtar Kelimeler: Senkron; Artıran Çevirici; PI; Bulanık Mantık

1. Introduction

As the usage of electrical energy continuously increasing this also brings so many problems in together. Problems in providing fossil energy resources, environmental disasters, increasing in energy consumption, in order to stay away from nuclear energy disputes are being the reason of global disagreements and even the wars. Therefore in recent years financial losses as the result of not to providing energy demand properly, regional electricity cut-offs directed people to the renewable energy sources for their clean and reliable energy needs [1].

Approximately 20 % of the energy needs is being provided from renewable energy sources in the world, in Turkey this figure is almost in the rate of 9 % only [2-3]. Electrical energy generated from sun as one of those energy sources is usually obtained by using photovoltaic (PV) panels. While total generated energy from this type of energy was 177 GW in 2014, at the

beginning of 2016 this figure reached 227 GW. As in January 2017 in Turkey, this figure has exceeded 860 MW [3]. With regard to the installed power, respectively China, Germany and Japan are the leader countries in this sector [2]. According to the load or systems energy to be provided, whether they are DC or AC, power electronic circuits differ from one to another[4-5].

In order to meet the needs of DC sources, PV systems are in need of boost, buck or buck-boost converters. According to their circuit structures these converters increase or decrease input voltages, at the same time if they include a diode in their circuit, they are called asynchronous converter, or if they include a switch instead of a diode are called synchronous converters (Figure 1-a and -b).

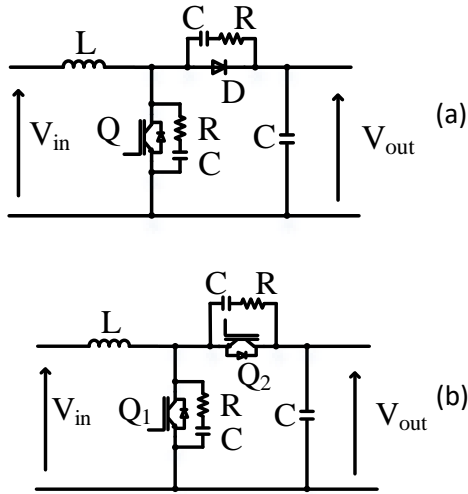


Figure 1. (a) Asynchronous Boost Converter
(b) Synchronous Boost Converter

In the synchronous converters using a switch instead of diode, as there will not be a voltage drop in forward direction their efficiencies are higher than asynchronous converters[5,6]. Another advantage of synchronous converters output voltage is constant when it is controlled even in no load case. Output voltage in both converter types will be changed with the solar irradiance, temperature and load. In order to fix this output voltage it must be controlled. In the literature there are papers in controlling of synchronous converter [6,7]. Beside these works, in [8] maximum power point tracking in distributed grids, cost and efficiency analysis are verified for asynchronous and synchronous converters. Efficiency of synchronous type converters reached up to 98 %.

In the controlling of converters are implemented in different ways based on current or voltage. Aims of controlling can be sequenced as maximum power transfer, reactive power control, bus voltage stability and providing load with the quality power supply[9,10]. In [11] fuzzy logic control of buck converter is done for water electrolysis. Beside this in [12], radiant control of synchronous converter is done in case of changing LEDs' status ON or OFF.

In this study, design of a PV panel powered synchronous boost converter is made and then fuzzy logic and PI control under varying source and reference voltage cases, the results obtained

are compared and proper control method is proposed.

2. General Description of The System

General block diagram of a PV panel powered converter is in Figure 2. System structure includes a PV panel, a synchronous converter, a filter and a control unit.

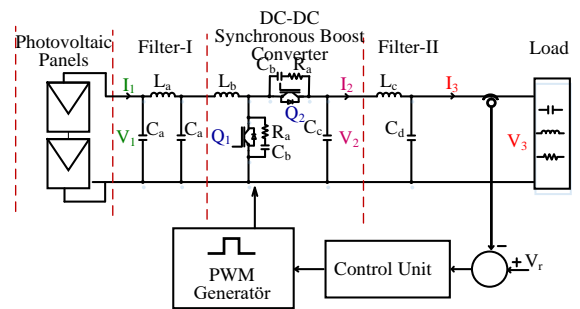


Figure.2. Systems' General Diagram

2.1. Synchronous Boost Converter

Synchronous boost converter transfer D.C. voltages applied to their inputs by boosting to their outputs according to duty-cycle of switches (Figure 1-b). DC voltage that is generated PV panel will be boosted by synchronous boost converter. Then filtering output filter, this voltage will supply to load

$$\frac{V_{out}}{V_{in}} = \frac{1}{1-D} \tag{1}$$

Where, V_{out} : output voltage, V_{in} : input voltage and D is the duty-cycle.

Output voltage of a synchronous boost converter is basically determined by the duty-cycle of Q_1 switch. Q_1 and Q_2 are opposite switches. When one is ON, the other is OFF. Switching frequencies are 100-1000 times higher than asynchronous converter. Despite in such higher frequencies switching causes to be smaller passive circuit components in greater power systems causes more losses. Therefore faster semiconductor materials and better switching actions are needed.

2.2. Controller Structure

System controlling depends on synchronous converter control. Classical PI controller and fuzzy logic controllers will be used to stabilize the voltage at the output of converter. Output voltage readings will be compared with reference voltage, the difference between those is the error. In both controllers to decrease the error, to the Q₁ and Q₂ switches of converter, Pulse Width Modulation (PWM) signal will be produced.

$$e(k) = r(k) - y(k) \tag{2}$$

Where, e(k): error signal, r(k): reference signal and y(k): output signal.

2.2.1. Fuzzy Logic

Fuzzy logic controller without being in need of a mathematical model adjusts the input signal according to the output signal. System variables is designed for system control. Output voltage of boost converter can be controlled by changing the duty-cycle of the switch used. The error in equation (2) and the changing error in equation (3) are inputs of fuzzy logic controller

$$de(k) = e(k) - e(k - 1) \tag{3}$$

Where, de(k) change in error is obtained from subtracting previous value of error.

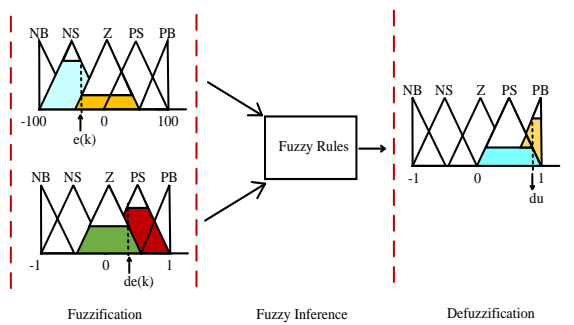


Figure.3. Fuzzy Main Diagram

Fuzzy Logic Controller as it is seen in Figure 3 becomes combination of three parts as fuzzification, rule base and defuzzification. Input and output membership functions chosen as a triangle. Two inputs signals, five membership

functions converted fuzzy membership by using Positive Greater (PG), Positive Smaller (PS), Zero (Z), Negative Smaller (NS) and Negative Greater (NG).

After the fuzzification process, rules in Table.1 is applied to determine fuzzy memberships of equalized output signal. Finally, by using the max-min method definite results is obtained. In order to confirm Fuzzy Logic Parameters a better control can be provided by the trial and error method.

Table.1. Rule Base

		de				
		NB	NS	ZZ	PS	PB
e	NB	NB	NB	NS	NS	ZZ
	NS	NB	NS	NS	ZZ	PS
	ZZ	NS	NS	ZZ	PS	PS
	PS	NS	ZZ	PS	ZZ	NS
	PB	ZZ	PS	PS	PB	PB

These definite values will be given PWM generator, and according to the duty cycle values PWM will generate two signals inverse of each other, at high frequencies that will be applied to the switches by this mean error will approach to zero.

Fuzzy Logic can be applied to different control systems with fundamental alterations, for detailed information refer to [13,14].

2.2.1. PI Controller

A PI controller is designed to approach to zero the error between the output voltage and the reference voltage such as fuzzy logic controller. In figure 4, a PI controller block diagram is seen.

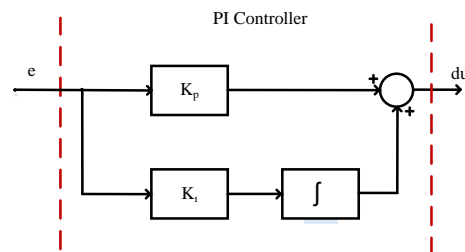


Figure.4. PI Controller Block Diagram

Output of the PI controller like fuzzy logic controller generates PWM signal according to du signal at its output, so the error becomes zero.

3. Simulation Work

In this section, system simulation of a PV panel powered synchronous boost converter with DC loads is done in Matlab/SIMULINK software. Simulation works are accomplished under variable reference and source voltages. Output voltage is controlled by PI and Fuzzy Logic Controllers. Used system parameters are given in Table.II.

Table.2. Parameters of the System

Photovoltaic Panel		Synchronous Boost Converter	
$V_{open-circuit}$	37.6 V	L_b	2.55 uH
$I_{short-circuit}$	8.55 A	R_a	33 Ohm
N_{serial}	1	C_b	300 pF
$N_{parallel}$	2	C_c	1 mF
$T_{ambient}$	25 °C	f_s	100 kHz
$S_{ambient}$	1000W/m ²		
Filter-I		Filter-II	
L_a	16.2 uH	L_c	0.338 uH
C_a	33 uF	C_d	10 mF
Load			
P	0.5kW		

Control results of a PV powered high frequency switching synchronous boost converters' PI and Fuzzy Logic controls are shown in Figure 5 and 6 respectively. In the case of synchronous boost converter output voltage changes with a defined reference voltage and changing of source voltage with the light intensity. Therefore, indirectly changing in the source voltage, output voltage did not change are shown. In Figure 6 similar situations for Fuzzy Logic controller are valid.

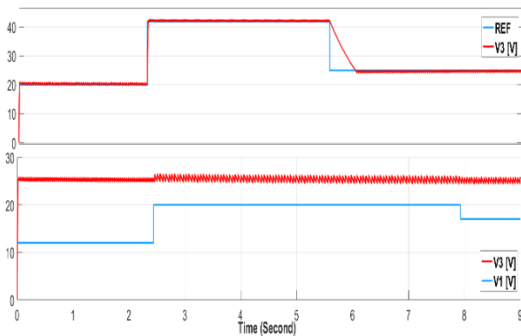


Figure.5. PI Control Results of the System

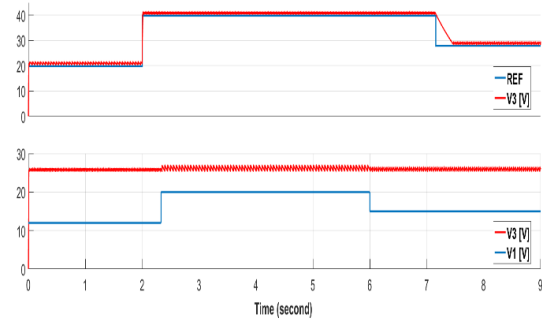


Figure.6. Results of Fuzzy Logic Control of the System

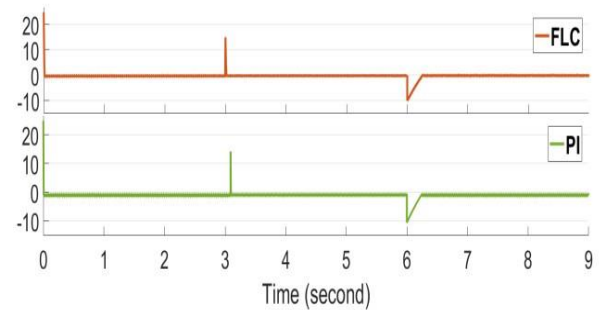


Figure.7. the Change of the Error in Variable Reference Voltage for Both Controller

Where, V1: PV output voltage, V3: Synchronous boost converter output voltage, REF: Reference Voltage. FLC: Fuzzy Logic Controller.

4. Results

In this study, output voltage of a PV panel powered synchronous boost converter PI and Fuzzy logic control is done. In the simulation work, in case of changing in source voltage and reference voltage, PI and Fuzzy Logic control of output voltage show that it is precisely stabilized. When Fuzzy Logic controller gives faster response to the changings in reference voltage, lesser overshoot rate with respect to PI controller are observed. Both control methods give faster response to any increases in reference voltage but in case of any decreases in reference voltage both methods give slow response. In accordance with these results it is observed that fuzzy logic control is better than PI control.

Because of the developments in power electronics in recent years when switches working at high frequencies will be commercially available, it is expected that usage of high power synchronous converters will increase, also their efficiencies are higher.

5. References

1. Tsengenes G. and Adamidis G., "Investigation of The Behavior of a Three phase Grid-Connected Photovoltaic System to control active and Reactive Power", *Electric Power Systems Research*, Vol. 81, pp. 177-184, 2011.
2. Renewables 2016: Global Status Report, REN21, 2016, ISBN 978-3-9815934-7-1-4.
3. Karagol E.T. ve Kavaz İ. "Dünyada ve Türkiyede Yenilenebilir Enerji", pp 18-26, Sayı197, Nisan 2017
4. Li Q. and Wolfs P., "A Review of the Single Phase Photovoltaic Module Integrated Converter Topologies with Three Different DC Link Configurations", *IEEE Transactions on Power Electronics*, Vol. 23, No. 3, pp. 1320-1333, May 2008.
5. Bansal, Sudha, Lalit Mohan Saini, and Dheeraj Joshi. "Design of a DC-DC converter for photovoltaic solar system." *Power Electronics (IICPE)*, 2012 IEEE 5th India International Conference on. IEEE, 2012.
6. C. G. Wilson, J. Y. Hung and R. N. Dean, "A sliding mode controller two-phase synchronous buck converters," *IECON 2012 - 38th Annual Conference on IEEE Industrial Electronics Society*, Montreal, QC, 2012, pp. 2150-2155.
7. Y. Yuan, Y. Lv and G. Tong, "Study on the digitally controlled system of ZCS-QRC synchronous buck converter," *Control Conference (CCC)*, 2011 30th Chinese, Yantai, 2011, pp. 4486-4491.
8. Graditi, G., et al. "Comparative analysis of synchronous rectification boost and diode rectification boost converter for DMPPT applications." *Industrial Electronics (ISIE)*, 2011 IEEE International Symposium on. IEEE, 2011.
9. Yu W., Lai J. S. J., Qian H. and Hutchens C., "High-Efficiency MOSFET Inverter with H6-Type Configuration for Photovoltaic Nonisolated AC-Module Applications", *IEEE Transactions on Power Electronics*, Vol. 26, No. 4, pp. 1253-1260, April 2011
10. Altas, Ismail H., Ozkop E, Adel M. Sharaf. "A Novel PV-Powered Standalone Village Electricity Utilization Fuzzy Logic Dynamic Controller Strategy." *INISTA 2009* 5: 47.
11. Sahin, Mustafa Ergin, and Halil Ibrahim Okumus. "Fuzzy logic controlled parallel connected synchronous buck DC-DC converter for water electrolysis." *IETE Journal of Research* 59.3 (2013): 280-288.
12. Pirci Baris, Bilgin M. Zeki, Erfidan Tarık " Seri Bağlı Led Armatürlerin Senkron DC-DC Dönüştürücü Kullanarak Işık Şiddeti Kontrolü ", *Elektrik - Elektronik ve Biyomedikal Mühendisliği Konferansı(ELECO2014)*, BURSA, TÜRKİYE, 27-29 Kasım 2014, ss.288-292
13. Altas, I. H., and A. M. Sharaf. "A novel maximum power fuzzy logic controller for photovoltaic solar energy systems." *Renewable Energy* 33.3 (2008): 388-399.
14. Altas, Ismail H., and Adel M. Sharaf. "A generalized direct approach for designing fuzzy logic controllers in Matlab/Simulink GUI environment." *International journal of information technology and intelligent computing* 1.4 (2007): 1

Performance Analysis of 20 Gb/s QPSK Modulated Dual Polarization Coherent Optical OFDM Systems

Ahmet GÜNER

Bingöl University Department of Electrical and Electronics Engineering, Bingöl
aguner@bingol.edu.tr

(Geliş/Received:10.02.2017; Kabul/Accepted:09.04.2017)

Abstract

In this study, 20 Gb/s Dual Polarization Coherent Optical Orthogonal Frequency Division Multiplexing (DP-CO-OFDM) system is studied to obtain the relation between the Bit Error Rate (BER) and launch power for different transmission length and polarization mode dispersion (PMD) coefficient. DP-CO-OFDM system is simulated by designing a Monte Carlo simulation. In this simulation, the effects of chromatic dispersion, launch power and PMD coefficient on received signals are demonstrated with constellation diagrams and results are given in form of BER-Launch Power variations.

Keywords: Coherent Optical OFDM, optical communication, dual polarization, polarization mode dispersion

20 Gb/s QPSK Modülasyonlu Çift Polarizasyon Eşevreli Optik OFDM Sistemlerinin Performans Analiz

Özet

Bu çalışmada, farklı iletim uzunluğu ve polarizasyon mod dağılımı (PMD) katsayısı için Bit Hata Oranı (BER) ve başlatma gücü arasındaki ilişkiyi elde etmek için 20 Gb/s Çift Polarizasyon Eşevreli Optik Ortogonal Frekans Bölmeli Çoklama (DP-CO-OFDM) sistemi incelenmiştir. DP-CO-OFDM sistemi bir Monte Carlo simülasyonu ile benzetimi yapılmaktadır. Bu benzetimde, kromatik dağılım, başlatma gücü ve PMD katsayısının alınan sinyaller üzerindeki etkileri takımyıldız diyagramları ile gösterilmiş ve sonuçlar BER-başlatma gücü değişimleri biçiminde verilmiştir.

Anahtar Kelimeler: Eşevreli optik OFDM, optik haberleşme, çift polarizasyon, polarizasyon mod dağılımı

1. Introduction

In 2005, the demonstration of the coherent receivers has been caused the increase of interest in coherent optical communications [1]. The main point of coherent communications is to improve sensitivity of the receiver. In addition, it allows the detection of both amplitude and phase increasing the detection capabilities, and combined with advance modulations formats [2].

Recently, the coherent optical communication and OFDM method are combined to obtain both advantages in a communication link. CO-OFDM technique is proposed for long haul transmission to remove inter-symbol interference (ISI) caused by chromatic dispersion in optical communication [3]. CO-OFDM systems allow for equalization of dispersive effects of optical channel.

The first CO-OFDM transmission was reported in 2006 [4, 5]. Dual polarization CO-OFDM has been experimentally demonstrated at 1 Tb/s over 600 km transmission [6]. In conventional coherent optical OFDM systems, training symbols (TSs) are added at the transmitter to facilitate channel estimation, which provides crucial channel information and enables efficient digital compensation of linear fiber impairments such as chromatic dispersion (CD) and polarization mode dispersion (PMD) [7].

In this study, the bit error rate (BER) performance of DP-CO-OFDM system is investigated for different launch powers with the increase in the transmission length under the effect of CD, PMD and the fiber nonlinearity. Also it is shown in constellation diagram the effect of CD, PMD and the higher launch power

on optical signals before or after the conventional TS based channel equalization. In section 2, a general dual polarization coherent optical OFDM system is described. In section 3, the TS based channel equalization is described. In section 4, the results of simulated system are reported and finally in section 5, the conclusion is made.

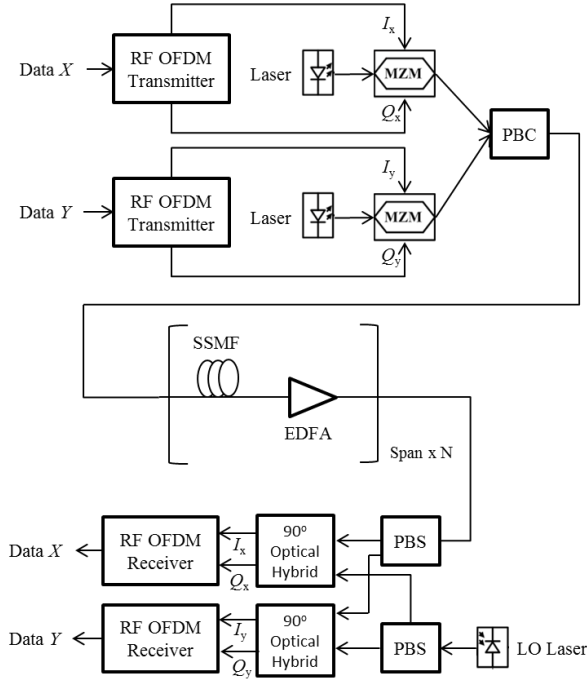


Fig. 1. Block diagram of a DP-CO-OFDM system. PBC : polarization beam combiner, PBS : polarization beam splitter, LO : local oscillator.

2. Dual Polarization Coherent Optical OFDM System

In Fig. 1, it is shown a general dual polarization coherent optical OFDM system. At the transmitter, the data sets are first mapped to QPSK symbols. Then, training symbols are added into OFDM symbol before IFFT. Two optical IQ modulators are used to convert the electrical signals to the optical signals and a polarization beam combiner combines the two optical signals.

The optical channel consists of many standard single mode fiber (SSMF) spans with CD, PMD, fiber nonlinearity and attenuation. In optical channel, the erbium-doped fiber amplifier

(EDFA) for gain is used in line amplification of signal.

In the receiver, two polarization beam splitters are used for mapping X polarization and Y polarization of the optical signal onto optical carrier. The polarized optical signals are passed through 90° optical hybrids that converting the optical signals to electrical signals along with light of LO laser. Then, the data symbols on each subcarrier are obtained by FFT. The channel estimation is implemented to compensate for the inter-subcarrier interference caused by CD and PMD.

3. Channel Estimation and Equalization

The linear fiber impairments in DP-CO-OFDM system can be described by a 2×2 multiple-input multiple-output (MIMO)-OFDM model in frequency domain on subcarrier basis as follows [7]:

$$\begin{bmatrix} R_x^i \\ R_y^i \end{bmatrix} = \begin{bmatrix} H_{xx}^i & H_{xy}^i \\ H_{yx}^i & H_{yy}^i \end{bmatrix} \begin{bmatrix} T_x^i \\ T_y^i \end{bmatrix} \quad (1)$$

Where T and R are the transmitted data and the received data. i is subcarrier index, x and y are polarization indexes. H_{xy}^i is channel frequency response of the i th subcarrier from X polarization to Y polarization. In (1), the noise term is omitted for simplicity.

In CO-OFDM systems, the training symbols (TS) using for estimation of the channel are added at the transmitter. Thanks to the training symbols are orthogonal, all coefficient of H matrix are estimated as follows,

$$H_{xx}^i = \frac{R_x^i}{TS_x^i}, H_{xy}^i = \frac{R_x^i}{TS_y^i}, H_{yx}^i = \frac{R_y^i}{TS_x^i}, H_{yy}^i = \frac{R_y^i}{TS_y^i}, \quad (2)$$

In TS based channel equalizer, the value of \hat{H}_{xy}^i can be obtained by the inverse of H_{xy}^i in (2). Then the signal at the i th subcarrier can be recovered by,

$$\begin{bmatrix} T_x^i \\ T_y^i \end{bmatrix} = \begin{bmatrix} H_{xx}^i & H_{xy}^i \\ H_{yx}^i & H_{yy}^i \end{bmatrix}^{-1} \begin{bmatrix} R_x^i \\ R_y^i \end{bmatrix} = \begin{bmatrix} \hat{H}_{xx}^i & \hat{H}_{xy}^i \\ \hat{H}_{yx}^i & \hat{H}_{yy}^i \end{bmatrix} \begin{bmatrix} R_x^i \\ R_y^i \end{bmatrix} \quad (3)$$

4. Simulations Results

In order to get the results of performance analysis, a simulation of DP-CO-OFDM systems was developed by using MATLAB. Optical fiber parameters and basic OFDM parameters are given Table 1 and Table 2 respectively. The data transmission bit rate is 10 Gp/s on each polarization.

Table 1. Fiber optical parameters

Parameter	Value
Wavelength	1550 nm
Velocity of light	200000 km/s
Fiber optical cable length	100 – 1000 km
Chromatic dispersion parameter	16 ps/(nm.km)
PMD coefficient	0.1 – 0.6 ps/km
Nonlinearity coefficient	1.32 (W.km)^{-1}
Attenuation	0.2 dB/km
Gain of EDFA	12 dB
Noise figure of EDFA	5 dB
Length of spans	100 km

Table 2. OFDM parameters

Parameter	Value
FFT/IFFT length (N_{FFT})	256
Number of subcarriers	128
Cyclic prefix	% 6.25
Modulation	QPSK
OFDM symbol rate	39.06 MHz

In Fig. 2, it is shown output signal constellation diagram before the channel equalization after transmission length 10 km, 50 km, 200 km and 500 km respectively for 0.1 ps/km PMD coefficient. The constellation points increase as the circumference and scatter due to the chromatic dispersion as a function of the transmission length.

In Fig. 3, it is shown output signal constellation diagram after the channel equalization by keeping launch power -6 dBm, -2 dBm, 0 dBm and 2 dBm respectively for 0.1 ps/km PMD coefficient after 900 km transmission length. As the launch power increases, the constellation points scatter as a function of the launch power because a higher launch powers lead to a larger nonlinear distortion.

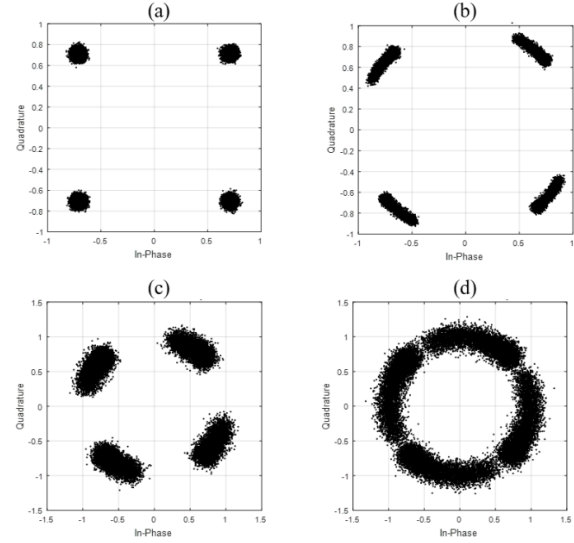


Fig. 2. Output signal constellation of X polarization of QPSK OFDM systems with Launch power -2 dBm for different transmission length, (a) L = 10 km, (b) L = 50 km, (c) L = 200 km (d) L = 500 km

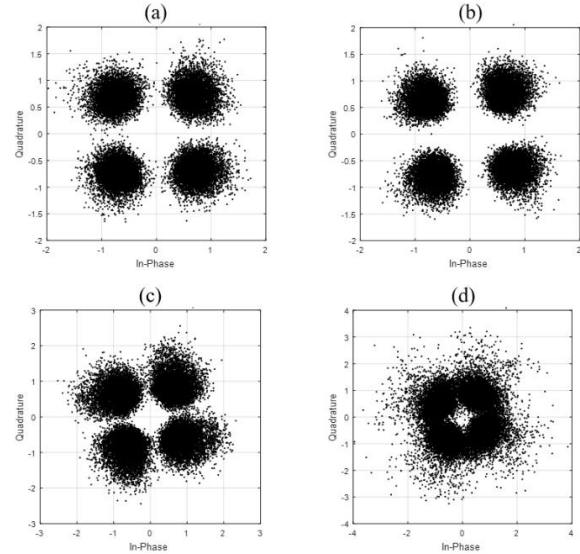


Fig. 3. Output signal constellation of X polarization of QPSK OFDM systems after 900 km transmission for different launch power, (a) -6 dBm (b) -2 dBm (c) 0 dBm (d) 2 dBm

As shown in Fig. 4, the bit error rate (BER) as a function of the launch power decreases initially up to -1 dBm after 800 km transmission length as the launch power increases. However, at higher launch powers, BER increases due to distortions caused by the fiber nonlinearity.

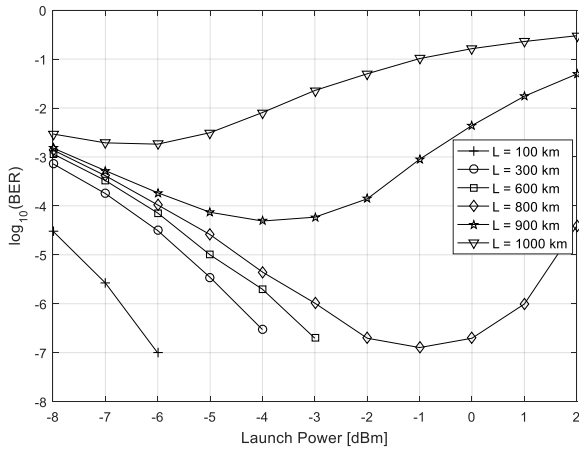


Fig. 4. BER of DP-CO-OFDM systems versus launch power for different transmission length

As also shown in Fig. 4, as the transmission length increases, value of the launch power at which BER begins to increase varies as a function of the transmission length.

In Fig. 5, it is shown output signal constellation diagram before the channel equalization by keeping PMD coefficient 0.1 ps/km and 0.3 ps/km respectively after 100 km transmission length. The circumference of the constellation points increase due to PMD as shown with red line in Fig. 5

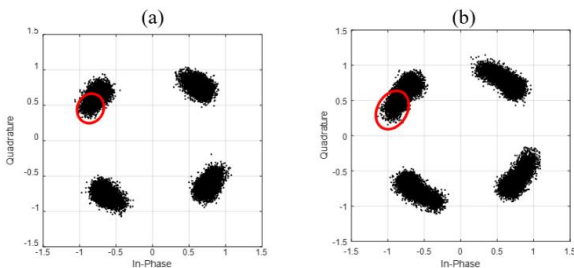


Fig. 5. Output signal constellation of X polarization of QPSK OFDM systems with Launch Power -2 dBm after 100 km transmission for (a) PMD = 0.1 ps/km (b) PMD = 0.3 ps/km

As shown in Fig. 6, the PMD coefficient changes from 0 ps/km to 0.6 ps/km at a step of 0.2 ps/km and BER as a function of the PMD coefficient increases due to the degradation caused by PMD.

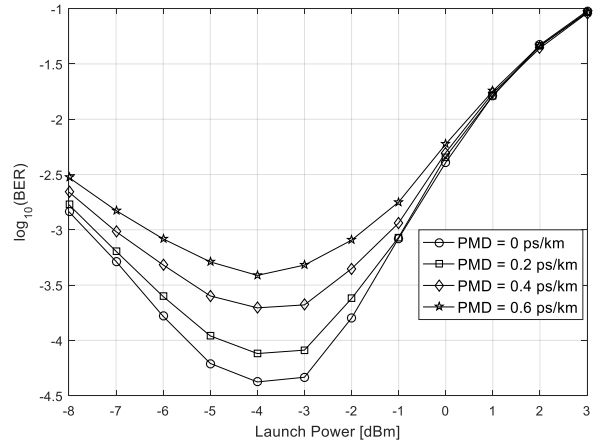


Fig. 6. BER of DP-CO-OFDM systems versus launch power after 900 km transmission for different PMD coefficient

5. Conclusions

We have analyzed performance of DP-CO-OFDM system against transmission impairments such as CD, PMD and fiber nonlinearity through simulations. The simulations are designed by QPSK modulated OFDM signals with dual polarization each with 10 Gb/s. The results of simulation show that at higher launch powers, BER increases due to the fiber nonlinearity and distortions caused by CD and PMD with the increase of the transmission length. Also the results of simulation are supported by constellation diagrams at fixed launch power and fixed transmission length.

6. References

1. Kikuchi, K. (2016). Fundamentals of coherent optical fiber communications, *J. Lightw. Technol.* 34(1), pp. 157-179.
2. Torres-Zugaide, J., Aldaya, I., Campuzano, G. and Castano, G. (2016). Hammerstein-based equalizer for nonlinear compensation in coherent OFDM long-reach PONs, *International Conference on Transparent Optical Networks (ICTON)*, pp. 1-3.
3. Yazgan, A. and Cavdar, İ.H. (2014). Optimum link distance determination for a constant signal to noise ratio in M-ary PSK modulated coherent optical OFDM systems, *Telecommunication Systems*, vol.55, pp.461-470.
4. Djordjevic, I.B. and Vasic, B. (2006). Orthogonal frequency division multiplexing for high-speed optical transmission, *Optics Express*, 14, 3767–3775.

5. Shieh, W. and Athaudage, C. (2006). Coherent optical orthogonal frequency division multiplexing, *Electronics Letters*, 42, 5–589.
6. Ma, Y., Yang, Q., Chen, S. and Shieh, W. (2010). 1-Tb/s single-channel coherent optical OFDM transmission with orthogonal-band multiplexing and subwavelength bandwidth access, *J. Lightw. Technol.*, vol. 28, no. 4, pp. 308–315.
7. Li, X., Zhong, W.D., Alphones, A., Yu, C. and Xu, Z. (2014). Channel Equalization in Optical OFDM Systems Using Independent Component Analysis, *IEEE/OSA Journal of Lightwave Technology*, vol. 32, no. 18, pp. 3206-3214.

Handwriting Character Recognition by using Fuzzy Logic

Enes VARDAR, Kaplan KAPLAN, H. Metin ERTUNÇ

Department of Mechatronic Engineering, Kocaeli University, Izmit / Kocaeli
kaplan.kaplan@kocaeli.edu.tr

(Received: 19.02.2017; Accepted: 05.04.2017)

Abstract

In Handwriting character recognition can be used to seek texts in big documents, take notes on tablet or decide whether or not internet user is a human or a computer in terms of Web security. In this study, a handwriting recognition system is studied by using fuzzy rules. The system includes 4 parts, namely image processing, feature extraction, fuzzification of the inputs, and defuzzification. In the first stage, image processing based on morphological operations are used to perform the handwriting recognition under the same conditions. The feature extraction process is employed to find the total number of white pixels in each column. Then these pixel numbers are assigned to arrays. The next step is to find the local maximum and minimum values by considering this arrays as an increasing-decreasing mathematical function. Therefore, it is observed that the handwritten letters of these values are divided into various groups. In the next operation, fuzzy classification membership functions and rule tables of text groups are generated by using extracted feature data. For a better recognition performance, the letters group have to be known in order to use image fuzzy logic algorithm. Consequently, this group of letters was successfully classified with fuzzy logic rules.

Keywords: Handwriting recognition, character recognition, fuzzy logic approach, image processing algorithms.

Bulanık Mantık ile El Yazısı Tanıma

Özet

El yazısı karakter tanıma, büyük bel gelerde metinleri araştırmak, tablet üzerinde not almak veya İnternet kullanıcısının bir insan veya bir bilgisayar olup olmadığını Web güvenliği açısından karar vermek için kullanılabilir. Bu çalışmada, el yazısının tanınmasında bulanık kuralların kullanıldığı bir sistem incelenmektedir. Sistem görüntü işleme, özellik çıkarma, verilerin bulanıklaştırılması ve bulanık çıkarım olmak üzere 4 bölüme içermektedir. İlk aşamada, morfolojik işlemlere dayalı görüntü işleme, aynı koşullar altında el yazısı tanımayı gerçekleştirmek için kullanılmaktadır. Özellik çıkarma işlemi ise her sütunundaki toplam beyaz piksel sayısını bulmak için kullanılmıştır. Bulunan toplam piksel sayıları okunan sütun sırası ile dizilerde saklanır. Sonraki işlem ise bu diziyi artan-azalan bir matematiksel fonksiyon olarak göz önünden bulundurup, yerel maksimum ve minimum değerlerini bulmaktır. Böylece, bulunan bu değerlerden oluşan el yazısı harflerinin çeşitli gruplara ayrıldığı görülmüştür. Sonraki adımda çıkarılan özellik verileri kullanılarak harf gruplarının bulanık kümeleri üyelik fonksiyonları ve kural tabloları oluşturulmuştur. Daha iyi bir tanıma işlemi için, görüntüye bulanık mantık algoritması uygulanmadan önce hangi harf grubunda olduğu bulunması gerekmektedir. Daha sonra bu harf grupları bulanık mantık kuralları ile başarıyla sınıflandırılmıştır.

Anahtar Kelimeler: El yazısı tanıma, karakter tanıma, bulanık mantık yaklaşımı, görüntü işleme algoritmaları

1. Introduction

Nowadays, studies on handwriting recognition have found numerous application area in technological development. Handwriting recognition systems can greatly facilitate human life by speeding up many operations such as reading tax statements, directing mail, reading bank checks and so on and so forth. On the other hands, these systems may reduce the need for human interaction. Therefore, the academics

and commercial studies about handwriting characters have recently become an important research topic in pattern recognition. The human handwritings have been tried to be recognized by many artificial intelligence methods such as Artificial Neural Networks (ANN) [1], K-Nearest Neighbors (KNN) [2], and Linear Differential Analysis (LDA) [3]. One of the methods in application is Fuzzy Logic approach. Fuzzy logic is very suitable for handwriting recognition systems because of its capability for

processing of uncertain data. The difficulty in handwriting recognition systems is that handwriting characteristic varies greatly from person to person. For this reason, handwriting recognition systems are quite complex.

In this study, we have studied on the set of images containing big handwritten letters with straight lines. Image processing and feature extraction algorithms in the system were coded in C++ environment. Fuzzy logic algorithms have been constructed and tested in MATLAB environment for handwritten letters. Once the fuzzy logic algorithms were tested in MATLAB to check the recognition performance, then they are written in C++. In the final stage, all the algorithms are combined in a single software, and, therefore handwritten characters are recognized with a reliable performance.

2. Materyal ve Metot

2.1. Image processing

Most of the images require preliminary image processing algorithms before applying any recognition technique. In order to increase the accuracy of the classification, it is very important to include descriptive features when extracting features. The steps of image processing algorithms used in this study are explained as in the following subsections.

2.1.1. Convert the image into a binary image

The image to be classified in this section is converted from RGB space to gray space by using *OpenCV* in C++ environment. The grayscale histogram density is automatically calculated and converted to a binary image with the applied threshold value. In the obtained binary image, all the pixel values above the threshold value are assigned to 1 (white) value and all the pixel values below the threshold value are assigned to 0 (black) value. Thus, the image to be classified is divided into two parts that are 1 and 0 with the threshold value. Since feature extraction is related to the number of pixels that have value of 1, the division of parts must be done properly. For this, the Otsu Method, which has a library on *OpenCV* that automatically calculates the threshold value, is used. This

method assumes that the image is composed of only two color classes, namely, the background and the foreground. The variance values for all threshold values for these two color class is calculated. The threshold value, which has the smallest variance value, is determined as the optimum threshold value

2.1.2. Finding more than one character in the image

In this section, binary image applied with threshold value is used as input. The binary image can have more than one character. Firstly, the characters must be separated from the whole image and considered as single image, and each process referred to in this work must be applied. As a first step, the boundary lines is found by the *findContours* function in *OpenCV* library [7]. The boundary lines are stored in a array with two memory files. The first memory of the array is the object and the second is the point of the object boundary line. The object boundaries are dropped to an array by using a simple for loop. Then, the smallest rectangles surrounding these boundary lines are found with the help of *OpenCV* rectangle as in Fig. 1 [7]. This rectangular image is cropped sequentially from the left of the image, and each cropped rectangle is regarded as an image to be classified.



Figure 1. The handwriting image divided into character groups

2.1.3. Image standardization

The last step of image processing procedure is the size standardization of the image characters. Since character images are in different sizes from each other, they need to be reduced to the same size for comparison and recognition of images adequately. By means of this algorithm, the images to be classified in different sizes are standardized to (40×30) pixel dimensions.

2.1.4. Feature extraction

In feature extraction stage, the approach is to scan all the columns of the digitized imager respectively and keep the total number of white pixels in each column in a string form. Then classification of the characters is performed by comparing the total number of white pixels in this column. Figure 2 shows the A letters drawn with different handwriting and Table 1 lists the column pixel data after image processing procedure is applied to these characters. Note that the pixel values of the characters are different according to each column in Table 1. The main reason of the characters' difference is that they are written by different handwritings.

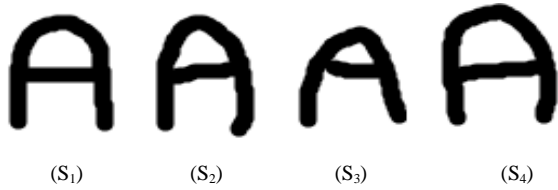


Figure 2. The characters 'A' written by different handwriting

As the columns are observed carefully, even if the characters looks like in the form of a different character, the Table 1 gives a hint about classification scheme. In all four cases, the coloumn data shows that the values of pixels increase to nearly 21, decrease to nearly 11, increase nearly 39 again, and finally decrease to 0, respectively. For this reason, a mathematical function can be evaluated according to the local maximum and local minimum values of the data in Table 1. The difference between the current local maximum (or minimum) and the previous local minimum (or maximum) gives us the transition values. These transition values will form the inputs of the fuzzy system. It is possible to verbalize these pixel values in the column with fuzzy logic. Then, the characters can be defined by these verbal statements with fuzzy rules. It is important to determine transition values correctly in terms of accuracy of system.

Step 1 (Finding extreme values): In this process, the program takes into account the data in the column and compares it with the previous data set in order to see whether or not it extracts a local maximum or local minimum point. Figure 3 shows the flow diagram of the algorithm for

computing the extremum (transition) values written in C++. In Table 2, the transition values are listed for the letter 'A' with this block diagram. In the diagram, CD is the current state data and PD is the data in the previous column. Outputs of this algorithm is a transition number and a transition value associated with it. For instance, the parameters $T_1 = 23$ indicates that the transition number is 1 and the transition size is 23. The algorithm also includes determining directional change. When a directional change (transition value) is determined, there must be more difference than ± 3 value between CD and PD. Negative DIT (-DIT) (Direction of transition) means incrementation and positive DIT (+DIT) means the decrementation. If there is a difference equal to 2 or less between CD and PD, the big one is selected. If CD is big, the direction sign is considered. If the direction sign is positive, then L_max is equal to CD, otherwise the algorithm will search the next column. If PD is big and the direction sign is negative, then L_min becomes as CD. If the direction sign is positive, the other column is passed.

Table 1. S_1, S_2, S_3 and S_4 pixel data

Coloumn	S_1	S_2	S_3	S_4
1	5	8	0	0
2	14	14	9	11
3	20	19	14	17
4	23	16	17	24
5	22	16	20	19
6	15	16	17	15
7	13	14	14	13
8	11	13	12	12
9	12	14	13	13
10	13	14	14	13
11	13	14	15	12
12	14	15	32	12
13	14	32	32	11
14	14	38	30	12
15	38	39	29	13
16	39	22	25	38
17	39	16	13	40
18	14	13	13	40
19	14	14	13	27
20	14	14	13	13
21	14	14	14	13
22	14	14	14	12
23	14	14	13	12
24	14	14	13	12
25	14	14	13	12
26	14	13	12	13
27	14	13	12	12
28	12	10	10	11
29	8	5	5	9
30	0	0	0	0

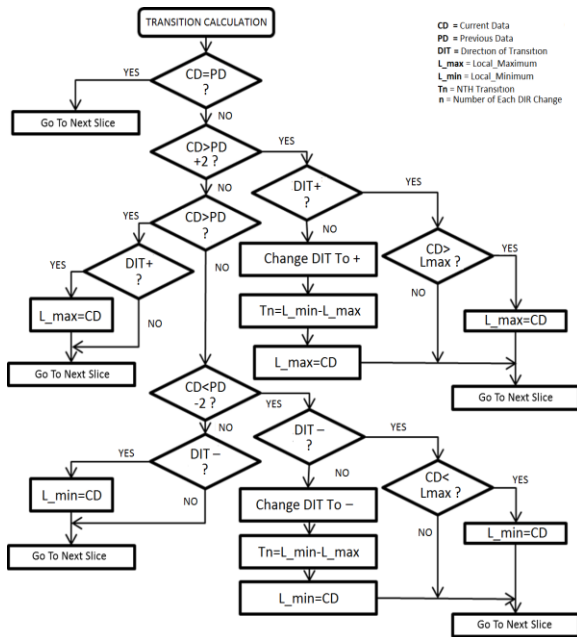


Figure 3. Transition value calculation algorithm

The transition values of the character A (S_1) found using the algorithm in Fig. 3 are shown in Table 2. As shown in Table 2, there are 4 transition points of character A ($T_1 = 23$, $T_2 = -12$, $T_3 = 28$, $T_4 = -39$). The feature extraction in order to characterize each character is applied to all the letters. In feature extraction operations, characters are divided into 3 character sets with 2, 4, or 6 transition values. B, E, G, S have six transition values; A, C, F, J, O, P, R, Z, D have four transition values and H, I, K, L, M, N, T, U, V, Y letters have two transition values character sets, respectively. Firstly, the character to be recognized is determined by which of these letter class, and so this operation facilitates decision of classes with and also flow of the system. These transition values can not provide sufficient accuracy in each character set in order to recognize the characters. For this reason, the total number of pixels, the first maximum and minimum column number, and the characteristic length specific for the character set are extracted by the software to increase the accuracy of the program.

Step 2 (Finding total pixel data): In this process, the pixel of images that are standardized and considered to be drawn in certain dimensions are scanned in C++ in order to find the total number of white pixels. The total number of pixels is not used because it does not

vary much in the class which has only 4 transition values. The total number of pixels found is written in the fuzzy logic rule table and in the membership functions with TPS abbreviation.

Step 3 (Finding the first maximum and minimum points): It was observed that the column numbers in which the first and maximum transition values were found during the observation of the data differ between the letters and that the same letter has close values even in different handwritten letters. The first maximum and minimum column numbers found differ in letter sets with 2 transition and 4 transition values. They are not used since these values do not vary sufficiently in the 6-pass value set.

Table 2. Display of transition variables

Coloumn	CR	PR	DIR	T	L_min	L_max	Tn
0	0	0	+		0	0	0
1	5	0	+		0	5	0
2	14	5	+		0	14	0
3	20	14	+		0	20	0
4	23	20	+		0	23	0
5	22	23	+		0	23	0
6	15	22	-	T_1	15	23	23
7	13	15	-		13	23	0
8	11	13	-		11	23	0
9	12	11	-		11	23	0
10	13	12	-		11	23	0
11	13	13	-		11	23	0
12	14	13	-		11	23	0
13	14	14	-		11	23	0
14	14	14	-		11	23	0
15	38	14	+	T_2	11	23	-12
16	39	38	+		11	39	0
17	39	39	+		11	39	0
18	14	39	-	T_3	11	39	28
19	14	14	-		14	39	0
20	14	14	-		14	39	0
21	14	14	-		14	39	0
22	14	14	-		14	39	0
23	14	14	-		14	39	0
24	14	14	-		14	39	0
25	14	14	-		14	39	0
26	14	14	-		14	39	0
27	14	14	-		14	39	0
27	12	14	-		14	39	0
29	8	12	-		8	39	0
30	0	8	-	T_4	0	39	-39

Step 3 (Feature extraction of a set of letters with four transition values): In this process, the character lengths of this set of letters shown in Fig. 4 are determined to increase the accuracy of the system. The logic of the written algorithm is to count the number of black pixels remaining between the first white pixel and the next white

pixel. To find the length between the vertical and horizontal red lines, the scan operation is performed from (20,0) to (20,30), and from (0,28) to (40,28), respectively. The accuracy of recognizing letters has been increased thanks to differences in letters (C, F, J, P, Z) that do not have horizontal length (HU), and the letters (C, F, J, P, Z) do not have vertical length (VU).

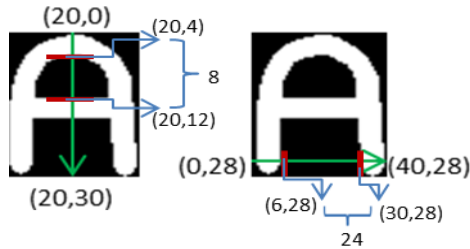


Figure 4. The characteristic length extraction

Step 4 (Feature extraction of a set of letters with two transition values): Characteristic length extraction in the case of two transition values is to determine the length between the horizontal and vertical red lines shown in Fig. 5. The reason for obtaining these lengths is the same as in the previous feature extraction process. The difference only in the scanning process is that the scanning direction is from (33,0) to (33,30) for the vertical lengths, from (12,3) to (28,3) for horizontal lengths. In this letter set, only the letter K is recognized by using fuzzy logic with the length of the letter K in the vertical direction, the differences in the horizontal length between the letters with the transition values, the first maximum column number, and the total pixel values.

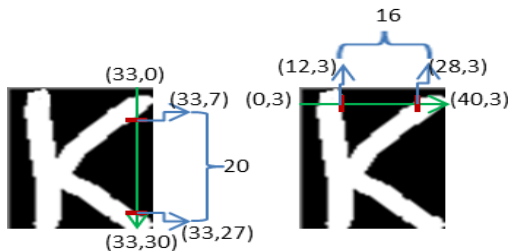


Figure 5. The characteristic length extraction

2.1.5. Fuzzification of data

Fuzzification is the process of converting information received from the system into symbolic values, which are linguistic qualifiers. By taking advantage of the membership process,

it determines the fuzzy set and membership level to which the input information belongs, and assigns numerical values to the entered numerical values such as “small, smallest”. In order to determine each verbal expression, firstly the intervals where the values of the data change must be found. In this study, many different handwritten characters have been evaluated for each character; feature data were examined, and variation intervals of values were found. Each variable interval is divided into sub-regions and each sub-region is labeled with verbal expression. The rule tables of each character group are determined via the MATLAB FIS Editor interface by using the variable data found in C++ software in order to find the membership level of these verbal expressions. Then the variable data are labeled as verbal expressions; fuzzy clusters and membership functions are created in the most accurate way by trial and error method. The fuzzy clusters and membership functions that have been verified by MATLAB program are created in C++ and integrated into image processing and fuzzy logic software. The fuzzy sets in the system consist of 3 membership functions that are small (S), medium (M) and large (L). These membership functions are defined as triangular and trapezoidal functions as shown in Fig. 6. The trapezoid membership function consists of 4 points, n_1, n_2, n_3 and n_4 , and the triangular membership function consists of 3 points, n_1, n_2 ve n_3 . Points of triangular and trapezoidal functions of all letter sets are given in Table 3, Table 4 and Table 5.

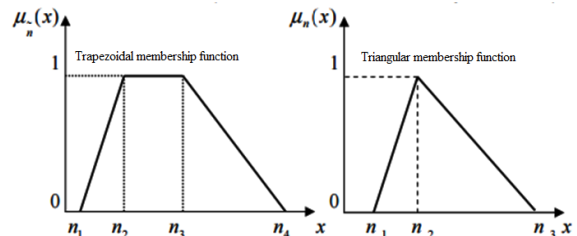


Figure 6. Trapezoidal and triangular membership functions

Table 3. Membership functions of letters with 6 transition values

	T ₁	T ₂	T ₃	T ₄	T ₅	T ₆	TPS
S	[0 0 23 30]	[0 0 17 23]	[0 0 15 22]	[0 0 15 22]	[0 0 15 22]	[0 0 20 30]	[0,300,449,500]
M	[23 30 40 40]	[17 23 30]	[15 22 25 30]	[15 22 25 30]	[15 22 27 30]	[20 30 40 40]	[449 500 536 600]
L	[23 30 40 40]	[25 30 40 40]	[25 30 40 40]	[27 30 40 40]	[536 600 775 800]

Table 4. Membership functions of letters with 4 transition values

	T ₁	T ₂	T ₃	T ₄	HU	VU	Min ₁
S	[0 0 20 31]	[0 0 15 20]	[0 0 14 23,5]	[0 0 22 33]	[0 0 2 3]	[0 0 18 20]	[0 0 10 18]
M	[20 31 40 40]	15 20 25 30]	[14 23,5 25 30]	[22 33 40 40]	[2 3 40 40]	[18 20 40 40]	[10 18 30 30]
L	-----	25 30 40 40]	[25 30 40 40]	-----	-----	-----	-----

Table 5. Membership functions of letters with 2 transition values

	T ₁	T ₂	VU	HU	Max ₁	TPS
S	[0 0 15 20]	[0 0 14 20]	[0 0 2 5]	[0 0 15 20]	[0 0 5 10]	[0 0 300 400]
M	[15 20 24 30]	[14 20 24 30]	[2 5 25 40]	[15 20 40 40]	[5 10 13 21]	[300 400 500 600]
L	[24 30 40 40]	[24 30 40 40]	[25 30 40 40]	-----	[13 21 25 40]	[500 600 700 800]

Table 6. Fuzzy rule tables of letters with 6 transition values

Letter	T ₁	T ₂	T ₃	T ₄	T ₅	T ₆	TPS
S	Medium	Medium	Small	Small	Medium	Medium	Small
B	Medium	Small	Small	Small	Medium	Medium	Large
G	Medium	Medium	Large	Medium	Small	Medium	Medium
E	Medium	Medium	Medium	Medium	Large	Medium	Medium

Table 7. Fuzzy rule tables of letters with 4 transition values

Letter	T ₁	T ₂	T ₃	T ₄	HU	VU	Min ₁
A	Medium	Small	Medium	Large	Medium	Small	Small
J	Large	Large	Medium	Medium	Small	Medium	Medium
F	Large	Large	Medium	Large	Small	Small	Small
O	Medium	Small	Small	Medium	Medium	Medium	Medium
P	Large	Small	Small	Large	Small	Small	Small
R	Medium	Small	Small	Large	Medium	Small	Small
Z	Large	Medium	Large	Large	Small	Small	Medium
C	Medium	Medium	Medium	Medium	Small	Medium	Medium
D	Medium	Small	Small	Medium	Small	Medium	Medium

Table 8. Fuzzy rule tables of letters with 2 transition values

Letter	T ₁	T ₂	VU	HU	Max ₁	TPS
H	Large	Large	Small	Medium	Medium	Medium
I	Large	Large	Small	Small	Large	Large
K	Medium	Medium	Medium	Small	Medium	Medium
M	Large	Large	Small	Small	Medium	Large
N	Medium	Medium	Small	Medium	Large	Medium
T	Large	Large	Small	Small	Small	Small
U	Large	Large	Small	Medium	Large	Medium
V	Small	Small	Small	Medium	Large	Small
Y	Small	Small	Small	Medium	Medium	Small
L	Large	Large	Small	Small	Large	Small

2.1.6. Fuzzy inference

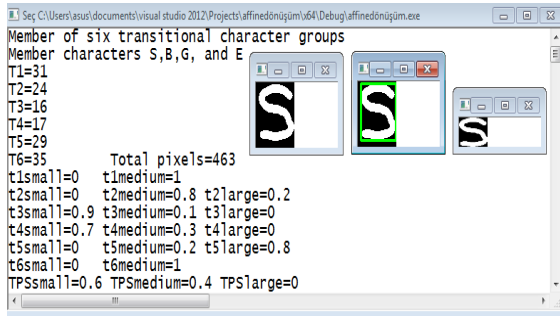
Fuzzy inference is the process and inference of the fuzzy concepts in a way similar to the ability of people to make decisions and make inference. In fuzzy inference, there are several methods such as min-max, max-prod and

Tsukamoto. Min-max was used in this study. The number of transition values of the letter and the letter set given above will be evaluated according to in the rule table. In the rule table, the number of the transition values of the image to be recognized and the character set of letters given above is found. For each letter rule in the rule table, the membership function value of the fuzzy set which the letter is the member is found, respectively. The minimum values of the membership degree of each rule found are stored in an array. The maximum value obtained between these minimum ratings specifies which letter is the image.

3. Testing of Handwriting Recognition System

Figure 7 shows the output of the program with the image of the letter *S* handwritten to be classified. The letter *S* image was first converted to binary image by thresholding method, and then the boundary points were found in the OpenCV library. The character to be recognized is regarded as a separate image by the smallest rectangle formed by these boundary points, and this image has been translated into (40 × 30) pixel dimensions for standardization data in the program. As shown in the program output, this character is a member of a set of letters with 6 transition value. The fuzzy logic inputs in this set of letters are the transition values and the total number of pixels. The total pixel values and transition values found and the membership degree of the fuzzy clusters are calculated. In the next step, the membership degrees as shown in Figure 8 are placed in each letter rule table as in Table 6. The minimum membership degree between the membership degrees listed in rule table is found. As shown in Figure 8, *S* character has 0.2, *B* character has 0, the character *G* has 0 and the character *E* has a membership rate of 0.1. based on taking into account the maximum membership level between these minimum membership degree, it can be determined which letter rule is the Max degree member of the image to be classified. As seen from the Min values, this character belongs to two rules. The letter *E* is a member with a membership level of 0.14 and the letter *S* is also a member with a membership level of 0.2. As mentioned before,

the maximum value (0,2) between these two membership levels indicate the letter S.

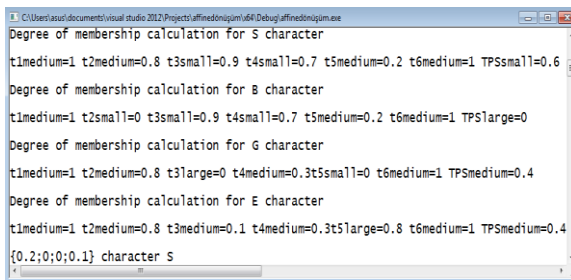


```

Member of six transitional character groups
Member characters S,B,G, and E
T1=31
T2=24
T3=16
T4=17
T5=29
T6=35      Total pixels=463
t1small=0   t1medium=1
t2small=0   t2medium=0.8   t2large=0.2
t3small=0.9   t3medium=0.1   t3large=0
t4small=0.7   t4medium=0.3   t4large=0
t5small=0   t5medium=0.2   t5large=0.8
t6small=0   t6medium=1
TPSsmall=0.6   TPSmedium=0.4   TPSlarge=0

```

Figure 7. C ++ program output



```

Degree of membership calculation for S character
t1medium=1 t2medium=0.8 t3small=0.9 t4small=0.7 t5medium=0.2 t6medium=1 TPSsmall=0.6
Degree of membership calculation for B character
t1medium=1 t2small=0 t3small=0.9 t4small=0.7 t5medium=0.2 t6medium=1 TPSlarge=0
Degree of membership calculation for G character
t1medium=1 t2medium=0.8 t3large=0 t4medium=0.3 t5small=0 t6medium=1 TPSmedium=0.4
Degree of membership calculation for E character
t1medium=1 t2medium=0.8 t3medium=0.1 t4medium=0.3 t5large=0.8 t6medium=1 TPSmedium=0.4
{0.2;0;0.1} character s

```

Figure 8. C ++ program output

4. Conclusion

In this study, a handwriting recognition system is realized by using image processing, feature extraction and fuzzy logic algorithms in C++ environment. Character images written in different handwriting, image processing algorithms, feature extraction are examined. The accuracy of the system has been increased by examining more than one samples for each letter. As a result of this examination, it is found that the same data in each letter does not vary, that each letter does not have the same number of

variable data numbers, and that each letter does not contain the same variable data. Therefore, letters are separated into character groups and fuzzy logic algorithm is created by using variable data of each group of letters. Handwritten letters are successfully classified by using fuzzy logic algorithm. In this study, the dotted letters (ö, ü, i) were not classified due to the uncertainties of the data. In future work, the authors will be concentrated on a recognition system based on more advanced intelligent algorithms such as artificial neural networks, neuro-fuzzy inference system and support vector machines.

5. References

1. Erdem O. A., Uzun E. (2005). Turkish Times New Roman, Arial, And Handwriting Characters Recognition By Neural Network: Journal of the Faculty of Engineering and Architecture of Gazi University, Ankara, 20: 13-19.
2. Weijie S., Jin X. (2011). Hidden Markov Model with Parameter-Optimized K-Means Clustering for Handwriting Recognition. IEE E2011 International Conference on Internet Computing & Information Services (ICICIS), Hong Kong, 235-438.
3. Prasad, M. M., Sukumar M. (2013). 2D-LDA based online handwritten kannada character recognition. Int. JI. of Computer Science and Telecommunications **4**(1): 14-18.
4. Jasim M. K., Al-Saleh A. M., Aljanaby A. (2013). A Fuzzy Based Feature Extraction Approach for Handwritten Characters. International Journal of Computer Science Issues (IJCSI). **10**: 208-2015.
5. Gowan W. A. (1995). Optical character recognition using fuzzy logic. Microprocessors and Microsystems, **19**: 423-434.

TiO₂ Memristor Modelling with LabVIEW

Muhammet Emin ŞAHİN*, Hasan GÜLER

Fırat University, Electrical – Electronics Engineering, Faculty of Engineering, 23119 Elazığ, Turkey

*mesahin@firat.edu.tr

(Geliş/Received: 25.01.2017; Kabul/Accepted: 22.02.2017)

Abstract

The fourth fundamental circuit element-Memristor, was mathematically modelled by Prof. Leon Chua in 1971. After about four decades, researchers at the Hewlett–Packard (HP) laboratories submitted the development of a new basic circuit element that completes the missing link between charge and flux linkage, which was suggested by Chua. Though a physical memristor device was not discovered then, many unique simulation applications are executed to take advantage of memristor feature which is different from other circuit elements by many researchers. In this paper, we use TiO₂ memristor model on account of its simplified expressions and the same ideal physical behaviors. Firstly, we obtained the mathematical equations of TiO₂ memristor. Then, these equations are created with LabVIEW and results are submitted. Finally, results of this system's behavior and stability analysis of are submitted.

Keywords: LabVIEW, Memristor, modelling and simulation, physical behavior.

LabVIEW ile TiO₂ Memristör Modellemesi

Özet

Dördüncü temel devre elemanı olan memristor, 1971'de Prof. Leon Chua tarafından matematiksel olarak modellendi Yaklaşık kırk yıl sonra. Hewlett-Packard (HP) laboratuvarlarındaki araştırmacılar, Chua tarafından keşfedilen, akı ve yük arasındaki eksik bağlantıyı tamamlayan yeni devre elemanını geliştirdi. Fiziksel memristör keşfedilmemiş olmasına rağmen, birçok araştırmacı tarafından diğer devre elemanlarından farklı olan memristor özelliklerinden yararlanmak için birçok benzersiz simülasyon uygulaması gerçekleştirilir. Bu makalede, basitleştirilmiş ifadeler ve aynı ideal fiziksel davranışlar nedeniyle TiO₂ memristor modelini kullanıyoruz. Öncelikle, TiO₂ memristorun matematik denklemlerini elde ettik. Ardından, bu denklemler LabVIEW platformunda oluşturulmakta ve sonuçlar sunulmaktadır. Son olarak, bu sistemin davranış ve kararlılık analizinin sonuçları sunulmaktadır.

Anahtar Kelimeler: LabVIEW, Memristör, modelleme ve benzetim, fiziksel davranış.

1. Introduction

Leon O. Chua published his work where the fourth passive two-terminal electrical component memristor was described in 1970s [1]. Current, voltage and magnetic flux are the basic elements in circuit theory. There is a relationship between them. Three of them define the three basic devices which are resistor, capacitor, inductor. They showed that memristor should represent the relation between electric, charge (q) and magnetic flux (φ),

$$d\phi = Mdq \quad (1)$$

Herewith Memristor was developed for several times, but the scientists did not realised,

that they developed a new component–memristor [2]. R. S. Williams who is leader of HP team invented this item, while they have been searching for a device which is a resistor with a state and not for a device, which has charge – magnetic flux relation. This work was published and it include the first relations for memristor modeling [3].

Memristor has drawn the worldwide attention after HP released its invention. After then many researchers focus on this element. Owing to different properties, memristors are being found out for many potential applications in the areas of nonvolatile memory very-large-scale integrated (VLSI) circuit, digital image processing, artificial neural networks, and pattern recognition and signal processing [4].

In this paper, we focalize the memristor modeling with LabVIEW. We submitted memristor model with different mathematical statement. Similar works have not founds up to, thus we assume that this is a different publications of the models and simulations described below. In methods, our nonlinear model of the memristor is presented and a formula is given in order to infer model parameters used physical parameters. In methods, measurements of simulation are defined. Final part of methods contributions of this paper are summarized.

2. The Memristor

In 2008, R. Stanley Williams of Hewlett Packard was submitted an experimental solid state version. It has TiO₂ and TiO_{2-x} sandwiched in between platinum electrodes. TiO₂ is resistive and TiO_{2-x} conductive and the ratio of these two layer varies with the application of current. They had designed a cross-bar structure with a layer of platinum dioxide, a layer of switching molecules and a thin film of titanium sandwiched between two platinum electrodes.

A semi-conductor device was either use magmatic field as flux or keeps charge as capacitor, memristor which has memory feature used chemical mechanism. One of the film slide depletion of oxygen atoms. The absence oxygen act as carriers it mean that the depleted layer has lower resistance than the non-depleted layer. Meanwhile the resistance of the film is dependent on how much charge has been went through it, in a particular direction, which is convertible by changing the direction of current [5-8].

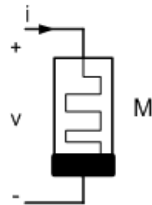


Figure 1. The memristor.

A memristor device is essentially a two-terminal passive electronic element with memory capacity. Its memristance state is affected from

amplitude, polarity, and duration of the external applied power. The physical model of the HP memristor from [7], shown in Figure 1, consists of a two layer thin film (thickness $D \approx 10\text{nm}$) of TiO₂ sandwiched between two platinum electrodes. One of the layers, which is described as TiO_{2-x}, is doped with oxygen vacancies and thus it exhibits high conductivity. The width w of the doped region is modulated depending on the amount of electric charge passing through the memristor.

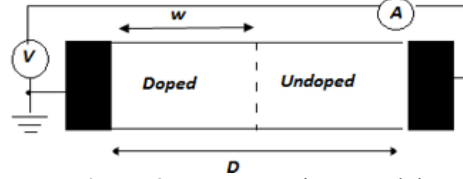


Figure 2. HP's memristor model.

Fig. 2 exhibits HP's memristor model. We see that total memristance is made of w and D regions. The total resistance of the memristor, M , is a sum of the resistances of the doped and undoped regions:

$$M(t) = R_{on} \left(\frac{w(t)}{D} \right) + R_{off} \left(1 - \frac{w(t)}{D} \right) \quad (2)$$

where R_{on} and R_{off} are the limited values of memristance for $w=D$ and $w=0$. We selected internal state as $x = w/D$ [0,1] then we rewritten as

$$M(t) = R_{off} + (R_{on} - R_{off})x(t) \quad (3)$$

when $t=0$, the initial memristance is

$$M_0 = R_{off} + (R_{on} - R_{off})x_0 \quad (4)$$

resistance of doped area affects the movement speed of the boundary between the doped and undoped regions

$$\frac{dx}{dt} = ki(t)f(x), \quad k = \mu_V R_{on} / D^2 \quad (5)$$

where $\mu_V \approx 10^{-14} \text{ m}^2 \text{ s}^{-1} \text{ V}^{-1}$ is the average ionic mobility parameter. As for a memristive device, these nonlinearities are manifested particularly at the thin film edges, especially at the two boundaries. This phenomenon, called nonlinear dopant drift, can be simulated by multiplying a

proper window function (x) on the right side of (5).

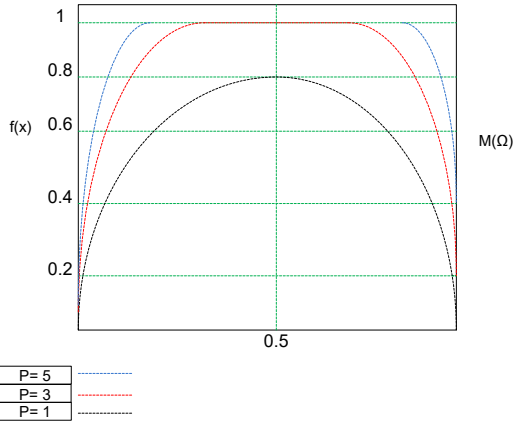


Figure 3. Joglekar window function for $P = 1$, $P = 3$ and $P = 5$.

$$f(x) = 1 - (2x - 1)^{2P} \quad (6)$$

where P is a positive integer called the control parameter. Fig. 3 shows the behaviour of the Joglekar window function for different values. Nonlinearity changes with value of P integer. As the integer P increases, the model tends to the linear. Based upon this, we selected $P=1$.

$$f(x) = 4x - 4x^2 \quad (7)$$

Substituting (7) into (5),

$$\int_x^{x(t)} \left(\frac{1}{x(\tau)} - \frac{1}{1-x(\tau)} \right) dx(\tau) = \int_0^t 4ki(\tau) d\tau \quad (8)$$

where the internal state variable satisfies $x(\tau) \in [x_0, x(t)]$ and the integration time is $0 \leq \tau \leq t$.

Assume $q_0=0$; we can get

$$\frac{x(t)}{1-x(t)} = \frac{x_0}{1-x_0} * e^{4kq(t)} \quad (9)$$

then the expression of $x(t)$ can be calculated as

$$x_0 = \frac{R_{off} - R_0}{\Delta R} \quad (10)$$

then, the expression of $x(t)$ can be calculated as

$$x(t) = 1 - \frac{1}{Ae^{4kq(t)} + 1} \quad (11)$$

where A is a constant and its value is determined by R_{off} , R_{on} , and R_0 :

$$A = \frac{R_{off} - R_0}{R_0 - R_{on}} \quad (12)$$

This mathematical statements are used for modelling memristor. They are made control and simulation block in LabVIEW.

3. Memristor Modelling with LabVIEW

We developed a behavioral model of a memristor at device level using the LabVIEW programme by following the mathematical equations presented before. The reason of preferring the LabVIEW program is its graphic based structure and the ease provided to user in constituting interface [10].

We examined TiO₂ memristor model to make it easy to comprehend and ready to be used in memristive systems.

We used labVIEW programme which is a graphics-based software platform. The usage of program is going up in engineering applications for making this model [11]. We used mathematical equations which are given previous part. Model depicted control and simulation block in labVIEW. Fig.4 shows the memristor model of LabVIEW front panel.

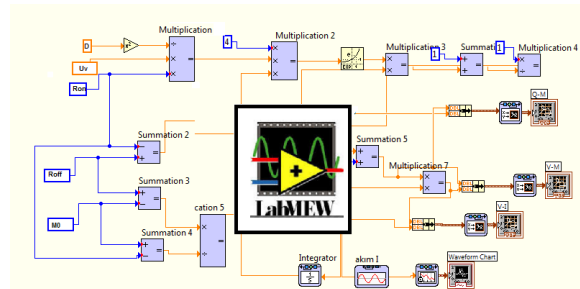


Figure 4. Memristor model of LabVIEW.

The parameters of the model are $R_{on} = 100\Omega$, $R_{off} = 20k\Omega$, $M_0 = 10k\Omega$, $D = 10nm$ and $\mu v \approx 10^{-14} m^2 s^{-1} V^{-1}$ [7]. Moreover, the simulation results in Figure 6.

(8)

In order to show memristor characteristics, values of passive elements, and, are chosen to work firstly 0.5mA input current at 5 Hz. Memristor model was simulated to examine the behavior via using LabVIEW program.

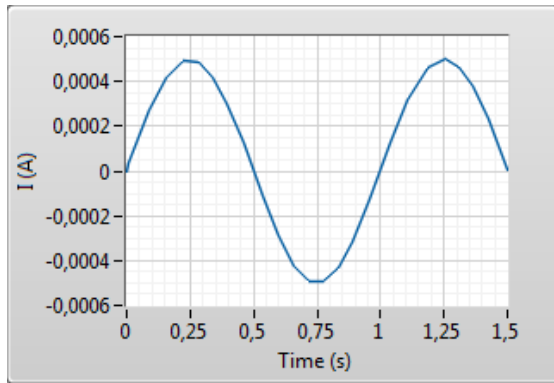


Figure 5. Memristor's current graph.

Fig. 5 shows that input current graph to time. The value of this is 0.5 mA sinus flowing through the memristor in this model.

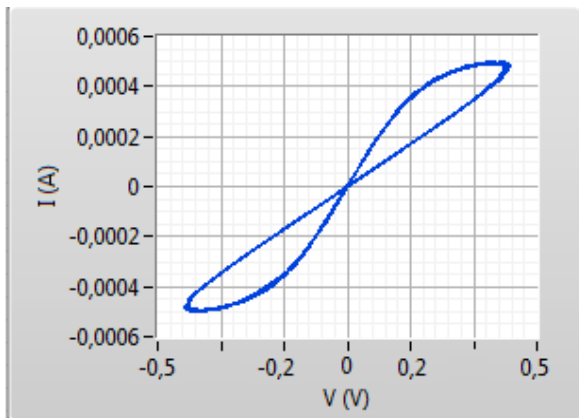


Figure 6. Relationship between memristor's current (I) and voltage (V).

The typical hysteresis loop in figure 6 shows its switching characteristic; that is, the memristance can switch between low resistance and high resistance.

One of the most important memristors' observed specialty is the existence of a pinched hysteresis that effect could be represented by the $i-v$ pinched hysteresis loop characteristic, as Chua highlighted that 'If it's pinched, it's a memristor' [12].

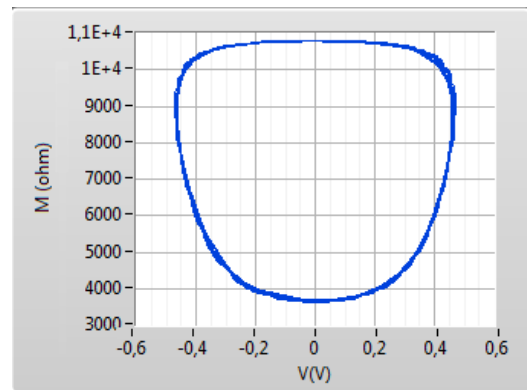


Figure 7. Relationship between memristor's voltage and memristance.

Figure 7 illustrates that the memristance is a nonlinear function of the flow of charge. Figure 8 shows the relationship between the memristance M and the charge q . Especially, in the part of the higher memristance state, the change ratio of the memristance is low, while, in the part of the lower memristance state, the change ratio of the memristance is high.

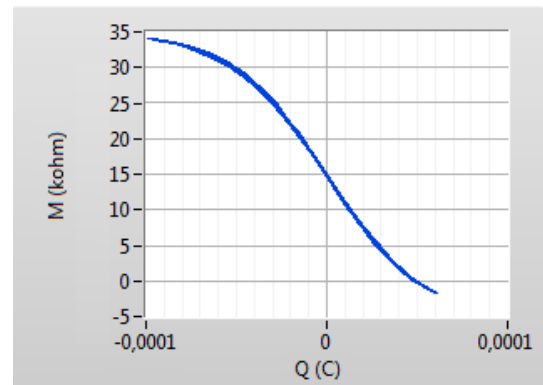


Figure 8. Relationship between memristor's charge and memristance.

If we increase input signal frequency, memristor behave as linear resistor. Fig.9 shows signal frequency is at 20Hz and fig.10 shows that memristor's loop turns the line chart at 200 Hz.

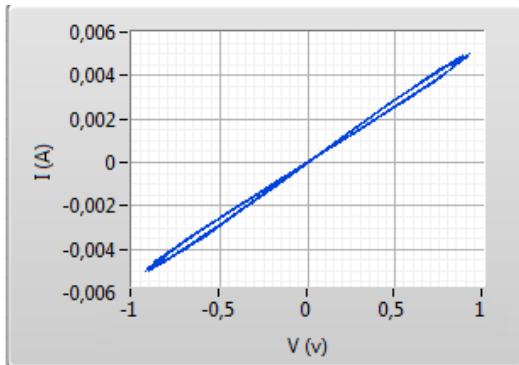


Figure 9. Relationship between memristor's current (I) and voltage (V).

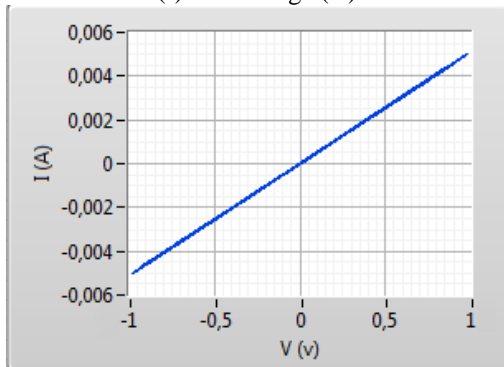


Figure 10. Relationship between memristor's current (I) and voltage (V).

4. Conclusion

Although HP workers has inveted to memristor physically, it is not submitted to the market yet and it will be probably not available for at least some years. Hence, memristor studies are still going on theoretically and based simulation. This paper is one of them. Since memristors have a natural nonlinear behaviour, they can be used in chaotic circuit systems and other different systems such as secure communication and cryptology. The main aim of this study is to show the possibility of application of memristor based circuits.

LabVIEW environments were used to achieve simulation and real time application.

5. References

1. L. Chua, "Memristor-the missing circuit element," *Circuit Theory*, IEEE
2. G. Dearnaley, A. M. Stoneham, and D. V. Morgan, "Electrical phenomena in amorphous oxide films," *Reports on Progress in Physics*, vol. 33, no. 3, p. 1129, 1970. [Online]. Available: <http://stacks.iop.org/0034-4885/33/i=3/a=306>
3. D. B. Strukov, G. S. Snider, D. R. Stewart, and R. S. Williams, "The missing memristor found," *Nature*, vol. 453, pp. 80–83, 2008.
4. ME Sahin, H Guler, T Kaya, LabVIEW Model Of Memristor With Nonlinear Dopant Drift, *European Journal of Technic* 6 (2), 124-130,2016
5. Mazumder, P., Kang, S. M., & Waser, R. (2012). Memristors: devices, models, and applications. *Proceedings of the IEEE*, 100(6), 1911-1919.
6. Biolek, Z., Biolek, D., & Biolkova, V. (2009). SPICE Model of Memristor with Nonlinear Dopant Drift. *Radioengineering*(18), 210-214.
7. Zhang, Y., Xuliang, Z., & Juebang, Y. (2009). Approximated SPICE model for memristor. In *Communications, Circuits and Systems, ICCAS 2009. International Conference* (pp. 928-931). IEEE.
8. R. Williams, How we found the missing memristor, *Spectrum*, IEEE 45 (2008), no. 12, 28 –35. 2, 7, 9, 24, 28
9. Guler, H., & Ata, F. (2014). The Comparison of Manual and LabVIEW Based-Fuzzy Control on Mechanical Ventilation. *Journal of Engineering in Medicine*, 916-925.
10. Aydin, S. G., Turgay , K., & Hasan , G. (2016). Wavelet-based study of valence–arousal model of emotions on EEG signals with LabVIEW. *Brain Informatics*, 3(2), 109-117.
11. Chua, L. (2011). Resistance switching memories are memristors. *Applied Physics A*, 102(4), 765-783.

PWM Control of AC Chopper Fed by Unbalanced 3-Phase Voltage Source

Nurbanu MACİT, Sedat SÜNTER

Firat University, Electrical and Electronic Engineering, Elazığ, Turkey

nmacit@firat.edu.tr

(Geliş/Received: 23.01.2017; Kabul/Accepted: 12.02.2017)

Abstract

In recent years, power electronic has become even more popular with the development of semiconductor switching devices. Power electronics applications can be found almost in all systems related to electrical and electronic fields. With the power electronic circuits, AC or DC voltages at various amplitudes can be obtained from constant voltage sources. AC voltage with constant frequency and variable amplitude with high power factor can be provided by an AC chopper. Purpose of these power electronic circuits is to make the system more efficient, provide output waveforms with higher quality (less harmonics) and prevent power loss in large power systems. In this study, a three-phase PWM controlled AC chopper circuit has been modelled and simulated in MATLAB / Simulink package program. In this simulation, the output statements obtained for the switching devices by a different control method are discussed. Various operating conditions have been examined where a three-phase unbalanced voltage source without and with having the 5th and 7th harmonics was applied to the input side of the chopper. As a result, superiority of the control system used in the PWM controlled AC chopper has been demonstrated by the simulation results.

Keywords: Three-Phase PWM AC Chopper, Hysteresis Band Current Controller (HBCC), Harmonic Analysis, Pulse width Modulation (PWM).

Dengesiz 3-Fazlı Gerilim Kaynağı ile Beslenen AA Kıyıcısının PWM Kontrolü

Özet

Son yıllarda, güç elektroniği, yarıiletken anahtarlama araçlarının da gelişimiyle birlikte daha popüler hale gelmiştir. Neredeyse elektrik ve elektronik ile ilgili tüm sistemlerde güç elektroniği uygulamaları bulunmaktadır. Güç elektroniği devreleri ile farklı genliklerdeki AA veya DA gerilimleri sabit gerilim kaynaklarından elde edilebilir. Bir AC kıyıcı ile sabit frekanslı, yüksek güç faktörlü ve değişken genlikli AA gerilimi elde edilebilir. Bu güç elektroniği devrelerinin amacı, sistemi daha verimli hale getirmek, daha yüksek kalitede (daha az harmonik) çıkış dalga formları sağlamak ve büyük güç sistemlerinde güç kaybını önlemektir. Bu çalışmada, üç fazlı PWM kontrollü AA kıyıcı devresi, MATLAB / Simulink paket programı ile modellenmiştir ve benzetimi yapılmıştır. Bu simülasyonda, farklı bir kontrol metodu ile anahtarlanan yarıiletken anahtarlar için elde edilen sonuçlar tartışılmıştır. 5. ve 7. harmoniklerin olduğu ve olmadığı üç fazlı dengesiz gerilim kaynağının kıyıcının giriş tarafına uygulandığı çeşitli çalışma koşulları incelenmiştir. Sonuç olarak, PWM kontrollü AA kıyıcıda kullanılan kontrol sisteminin üstünlüğü simülasyon sonuçları ile gösterilmiştir.

Anahtar Kelimeler: 3-Fazlı PWM AA Kıyıcı, Histerezis Bant Akım Kontrolörü (HBCC), Harmonik Analizi, Darbe Genişlik Modülasyonu (PWM).

1. Introduction

Along with the developing technology, the amount of energy consumed all over the world has also increased. Due to the amount of energy consumed, new ways have been sought to meet this energy demand. More efficient systems with smaller structures and circuits designed to consume less power loss despite adverse

conditions are required. The most popular circuit is the power electronics circuits, which are still being developed. Power electronic circuits reduce energy loss on the earth with renewable energy processing and create efficient systems for it. Power electronic circuits transform electrical power by using the switching characteristics of semiconductor elements.

AC chopper circuits of the power electronic family are the basic concept of this study. AC choppers are, at its most basic definition, a power circuit which can convert a constant frequency AC voltage to another voltage at a desired amplitude [1,2]. Single-phase and three-phase versions of the AC chopper are available. AC choppers with natural commutation have negative features such as high harmonics on the mains or load sides. AC choppers are used in many industrial areas. Frequent use of such power electronic circuits has led to poor quality in energy systems [2]. It is possible to further improve AC choppers by eliminating these undesirable features. With the use of power electronic devices which can operate at high switching frequencies, the PWM method has begun to be used in the chopper circuits [3]. PWM AC chopping circuits have reduced side effects of the natural commutated ones as well as have become a special application of these circuits [3,4].

In this study, it is aimed to obtain load current with less harmonics by applying Hysteresis Band Current Controller (HBCC) technique for three-phase PWM AC chopper. The HBCC technique is preferred because of its dynamic response and simplicity [5]. Thanks to this controller, whatever the input voltage of the system is, a load current with very low harmonics at the output is obtained. The results will be quite advantageous for all power electronics-based systems.

2. Hysteresis Band Current Controller for a Three Phase AC Chopper

Fig.1 shows the circuit schema of the three-phase AC chopper [6]. The simulation model of this circuit using MATLAB / Simulink is shown in Fig. 2 [6]. IGBTs are used as switching semiconductor devices and a three-phase $R-L$ load is used at the output. Depending on the nature of the load used, there will be a load phase angle between the voltage and current space vectors of the source. The reference currents in the AC chopper must have the same frequency as the source voltage and the same phase angle as that of the load [6]. With the

HBCC technique, the reference currents are obtained and the continuity of the load current paths is ensured [6].

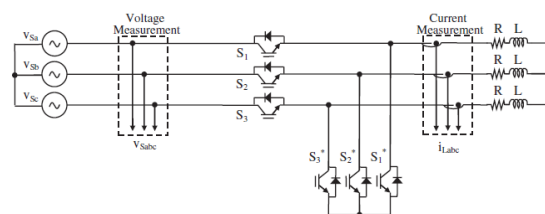


Fig. 1. The power scheme of the three-phase PWM AC chopper [6]

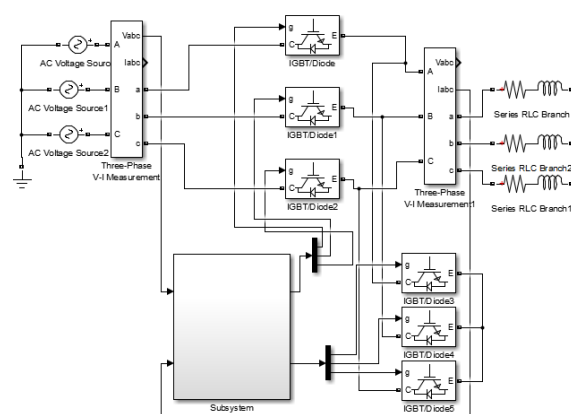


Fig. 2. The Simulink model of the three-phase PWM AC chopper

The reference currents can be obtained using phase locked loop (PLL) or using abc/dq transformations called Park Transform. The continuity of the load current conduction paths is also provided using the technique called the minimum voltage algorithm [3,6]. The minimum voltage algorithm ensures the continuity of the resulting current paths by triggering the correct switch according to the instantaneous values of the source voltage [3,6].

In the proposed model, the on and off states of the switches are provided using specific switching states. The goal is to obtain high quality waveforms at the output whatever the input voltage source is. In order to demonstrate the superiority of the control system, three-phase voltage source having harmonics or unbalanced input. Undesirable changes in the source voltage (such as noise or harmonic distortion) will directly affect the output voltage and hence the

amplitude of the output current. To analyze this situation, the fifth and seventh harmonics of the input voltage source are added to the input with certain amplitude ratios [7].

2.1. Analysis of HBCC technique applied to AC chopper

Any kind of load can be controlled with the PWM AC chopper connected to the three-phase source. The PLL block shown in Fig. 3 is used to set the source frequency [6]. The *abc / dq* transform block is also used to set the load phase. Only the amplitudes of the generated reference currents are input to the control system depending on the demand.

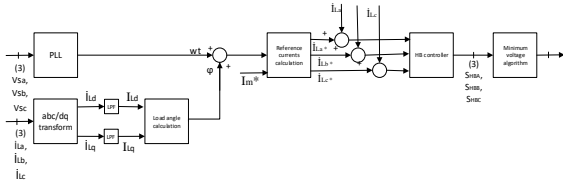


Fig. 3. The application of the HBCC theory [6]

The minimum voltage algorithm can be used in various systems. For instance, in a 3-phase inverter as the 3-phase chopping operation is made independent of each other, the current flow is continuous. In the proposed topology, the chopping procedures depend on each other and the flow paths are separated from each other during the phase chopping operation. The minimum voltage algorithm is used to prevent such undesirable situations. Depending on the instance, the switch with the minimum voltage is kept off while the chopper continues to operate in the other two phases and the sum of these currents returns from the phase with the minimum voltage.

2.2. Switching states

Besides the values in Table 1, four different switching states have been performed.

Table 1. System parameters used in simulation

Parameters	Values
Source	$V_{sA} = 220 \text{ V}$ (rms)
	$f = 50 \text{ Hz}$
Load	$L = 20 \text{ mH}$
	$R = 10 \text{ } \Omega$

By referring to Fig.1, the following switching situations exist:

Table 2. Switching situations

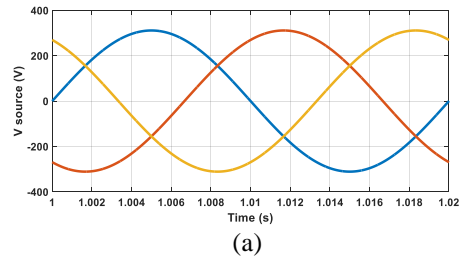
Switching States	ON	OFF
1	S_1, S_1^*, S_2^* and S_3^*	S_2 and S_3
2	S_1, S_3, S_1^* and S_2^*	S_2 and S_3^*
3	S_1, S_2, S_1^* and S_3^*	S_3 and S_2^*
4	S_1, S_2, S_3 and S_1^*	-

3. Analyses

In the simulation, two different conditions were performed. The first condition is used to observe the effect of the distorted three-phase input supply on a three-phase *R-L* load where no power electronic circuit was used and the load is directly connected to the input supply as shown in Fig. 4. The second condition is to observe the effect of the same source voltage on *R-L* load using HBCC technique applied to PWM AC chopper.

3.1. Analysis of the proposed system fed by 3-phase input supply

In this application, a balanced and undistorted three phase voltage set is applied to the system input. In this case, the wave form of the load current of the system is observed to be smooth. The waveforms obtained are as follows for a complete period:



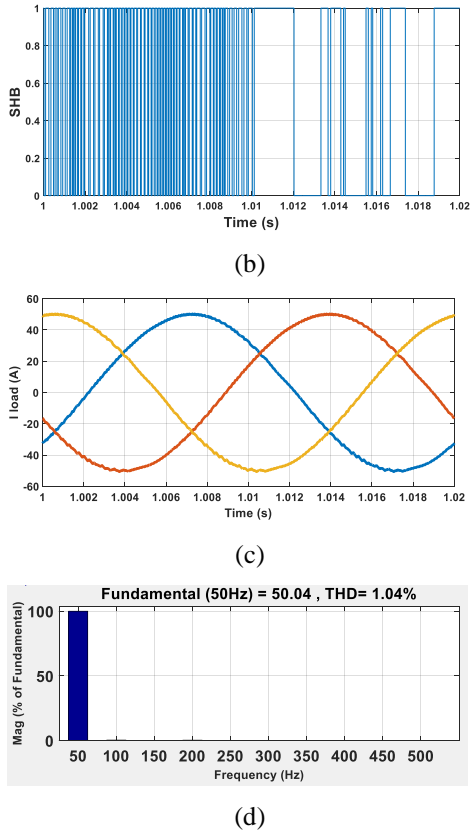


Fig.4. Simulation results of the PWM AC chopper fed by a distorted 3-phase supply and feeding a three-phase star connected R-L load. (a) Voltage source, (b) Switching signal, (c) Load current, (d) The harmonic spectrum of the load current.

In the Fig.4, 1-1.02 s is selected as a full period interval to see more clearly the waveform and harmonic analysis of the load current. Since the circuit is still in transient state at 0-0.02 s, the waveforms are harmonic. Therefore, the period of 1-1.02 s reached the permanent status has been taken into account. In this range, reference current is $I=50 A$. With the obtained waveforms and FFT analysis, it can be said that the harmonics are at an acceptable level.

In this application, Total Harmonic Distortion (THD) of the load voltage waveform is 1.04%. These results show us how reasonable and feasible the controller proposed for the three-phase PWM chopper.

3.2. Analysis of 3-phase star-connected r-l load fed by a distorted three-phase input supply

Undesirable changes in the source voltage such as noise or harmonic distortion will directly affect the output voltage and hence amplitude of the output current. To demonstrate these effects, the fifth and seventh harmonics of the input voltage set are added at certain amplitude ratios in the simulation model.

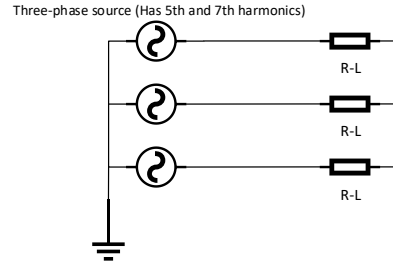


Fig. 5. A star-connected 3-phase system with harmonic voltage applied to the input

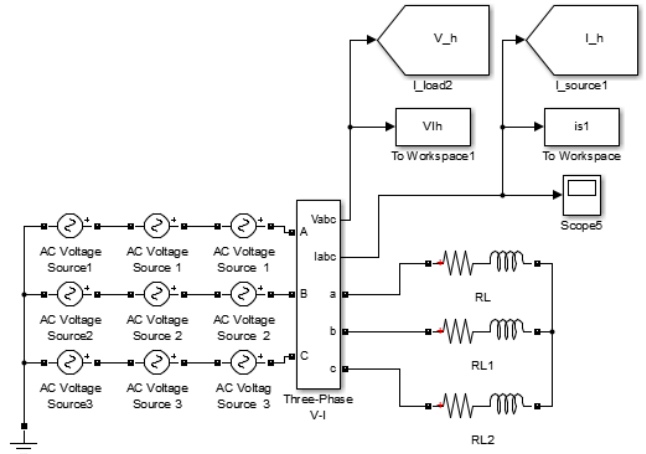


Fig. 6. Simulation Model of the star-connected 3-phase system with harmonic voltage applied to the input

In order to demonstrate the superiority of the AC chopper system used in this work, a distorted supply voltage model is created in Simulink/Matlab to be used as input to the system. The three-phase sinusoidal voltage source with harmonics is defined as follows:

$$V_{1h} = k_1 \cos(5\omega t) + k_2 \cos(7\omega t) \quad (1)$$

$$V_{2h} = k_1 \cos\left(5\omega t - \frac{2\pi}{3}\right) + k_2 \cos\left(7\omega t + \frac{2\pi}{3}\right) \quad (2)$$

$$V_{3h} = k_1 \cos\left(5\omega t + \frac{2\pi}{3}\right) + k_2 \cos\left(7\omega t - \frac{2\pi}{3}\right) \quad (3)$$

The k_1 and k_2 values in Eq.(1-3) are set to be about 10% of the supply voltages [7]. V_{1h} , V_{2h} and V_{3h} are the harmonic voltages of A, B and C phases, respectively. The resulting simulation waveforms are given in Fig. 6 for a full period.

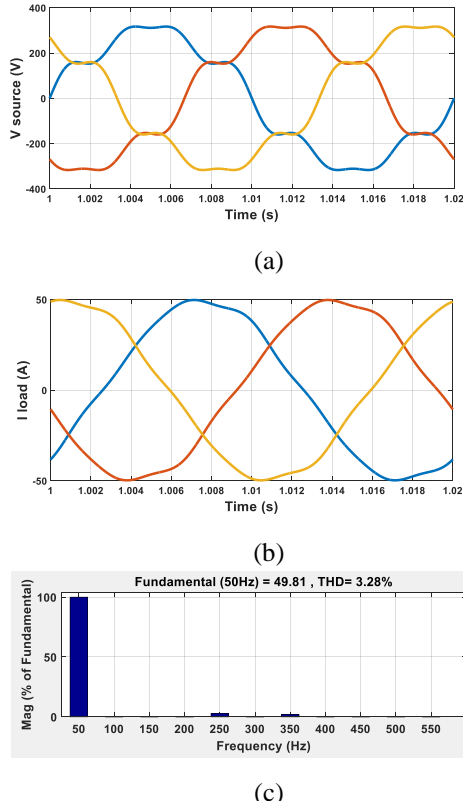


Fig.7. Simulation results of star-connected 3-phase load fed by a distorted 3-phase supply, (a) Distorted source voltages, (b) Load currents, (c) The harmonic spectrum of the load current.

As can be seen in Fig.7, when a voltage source with harmonics is applied directly to the $R-L$ load, all harmonics of the supply are reflected to the output. THD of the load current waveform is 3.28%.

3.3. Analysis of the proposed system fed by a distorted 3-phase input supply

In this case, three-phase voltage supply with 5th and 7th harmonics used in the previous system was also applied to the input of the PWM AC chopper controlled by the HBCC. The Simulink model of the system including the distorted voltage supply source is illustrated in

Fig.8. Comparing to the previous system, the superiority of the proposed method in [6] is confirmed by the simulation results in Fig.9. It is observed that the system gives successful results, that is, the waveforms of the load currents and voltages have sufficient quality. The simulation results taken for a complete period are shown in Fig. 9.

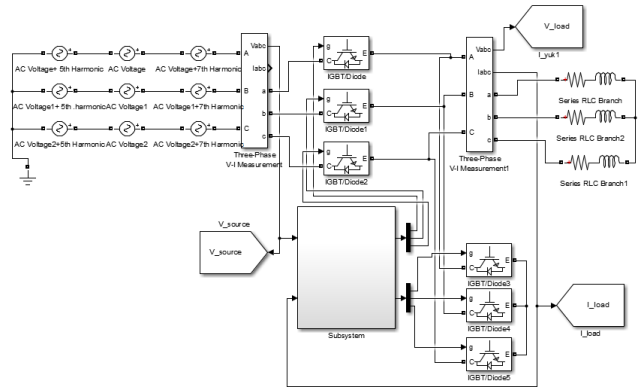


Fig. 8. Simulink model for 3-phase PWM AC chopper fed by a distorted input supply

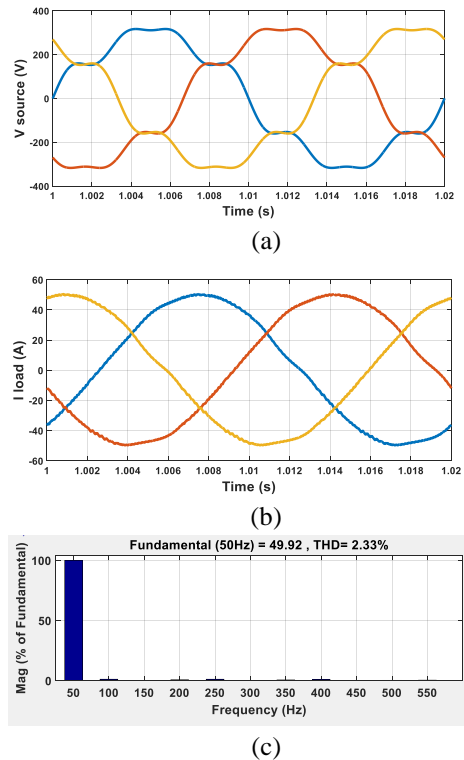


Fig.9. Simulation results of the PWM AC chopper fed by a distorted 3-phase supply and feeding a three-phase star connected $R-L$ load. (a) Voltage source, (b) Load current, (c) The harmonic spectrum of the load current.

As can be seen in the Fig.9 (b), the resulting load current waveforms have less harmonics than expected and their shapes are almost pure sinusoidal waveforms. As seen in Fig.9 (c), main harmonics are much dominant. This is why the hysteresis band controller is used in the simulation and proposed in [6]. Thanks to this controller the switches used in the chopper are controlled in a manner to have less harmonics at the output. The controller in simulation are designed for analysing the parameter of voltage and current. In general, it has features such as reducing the harmonic components and increasing the power factor of a particular circuit.

In this study, Total Harmonic Distortion (THD) of the load voltage waveform is 2.33%. These results show us how reasonable and feasible the controller proposed for the three-phase PWM chopper.

4. Conclusions

In this study, a PWM AC chopper with hysteresis band controller has been modelled and simulated with the Simulink/MATLAB package program. It is aimed to have more efficient chopper comparing to the traditional 3-phase AC chopper. Although, the traditional phase controlled AC chopper has not been simulated in this work, its waveforms are well known. Therefore, it could be easily stated that the performance of the proposed system would be much better than that of the traditional AC chopper. In addition, operating conditions of the PWM AC chopper have been made much worst by adding the 5th and 7th harmonics to the input voltage waveforms. Even so promising simulation results have been obtained. The simulation results show that the proposed control

algorithm minimizes the amount of THD at the output currents. Despite of the voltages with harmonics applied to the input, three-phase currents at the output are stable and they consist of very low amount of harmonics because of the HBCC used. As a result, the ratio of harmonics is reduced significantly with the switching control algorithm. These results have been supported by the harmonic analysis.

5. References

1. Rashid, H. M., Power Electronics Devices, Circuits and Applications (4th Edition), England.
2. Bodur, H., Güç Elektronigi I, http://afguven.com/depo/ESM312/guc_elektronigi.pdf, (Access: 16.08.2016)
3. Kwon BH, Min BD, Kim JH. 'Novel topologies of AA choppers', IEE Proc Electr Power; 143(4):323–30, Appl 1996.
4. Kim JH, Min BD, Kwon BH, Won SC. A PWM buck–boost AC chopper solving the commutation problem. IEEE Trans Ind Electron 1998;45(5):832–5.
5. Chun, T., and Choi, M., 'Development of Adaptive Hysteresis Band Current Control Strategy of PWM Inverter with Constant Switching Frequency', Conference Proceedings of Applied Power Electronics Conference and Exposition, San Jose CA, Vol. 1, pp. 194-199, 3-7 March 1996.
6. Kale, M., Karabacak, M., and Saracaoglu, B., 'A Novel Hysteresis Band Current Controller Scheme for Three Phase AA chopper', Electrical Power and Energy Systems 44, pp. 219–226, 2013.
7. Sunter, S., Altun, H., and Clare, J. C., 'A Control Technique for Compensating the Effects of Input Voltage Variations on Matrix Converter Modulation Algorithms', Electric Power Components and Systems, pp. 807-822, 2010.

A Comparative Study between Matrix Converter Fed Induction Motor Drive and Dual-Matrix Converter Fed Open-End Winding Induction Motor Drive

A. BELADEL¹, A. KOUZOU¹, A. HAFAIFA¹, S. SUNTER^{2*}, D. MAHIA³

¹ Applied Automation and Industrial Diagnostics Laboratory (LAADI), Faculty of Sciences and Technology, Djelfa University, Algeria

²Firat University, Elazig, Turkey

³University Amar Telidji of Laghouat, Algeria

*_ssunter@firat.edu.tr

(Geliş/Received: 24.02.2017; Kabul/Accepted: 12.04.2017)

Abstract

This paper deals with a comparative study between the control of three to three phase matrix converter feeding a star-connected three phase induction machine and the control of three to three phase dual matrix converter feeding an open-end winding induction machine. The control strategy used in both cases is based on a proposed direct transfer function control approach of Venturini algorithm which allows to obtain a unity power factor at the input side to boost the output phase voltage up to 150% compared to the input phase voltage, while keeping the main advantage of the matrix converter by providing a fully bidirectional power flow operation. The main objective of using the open-end winding topology is to ensure the minimization of the common mode voltage which is clearly observed in the case of star-connected winding. Simulation results are presented under both control strategies, where both matrix converters are supplied from the same three-phase power source. Whereas; the two output voltage system of the dual matrix converter are shifted with 180 degrees. Based on the obtained results the performances of the both control approaches are technically discussed.

Keywords : Matrix converter, Dual matrix converter, Direct transfer function approach, Simulation Model, Open-End Induction Machine Drive.

Açık-Uçlu Sargılı Asenkron Motoru Besleyen Çift-Matris Dönüştürücü Sürücüsü ile Asenkron Motoru Besleyen Matris Dönüştürücü Sürücüsünün Bir Karşılaştırması

Özet

Bu makale yıldız bağlı üç-fazlı asenkron motoru besleyen üç-faza üç-faz matris dönüştürücünün kontrolü ve açık-uçlu sargılı asenkron makineyi besleyen üç-faza üç-faz çift matris dönüştürücünün kontrolü ile ilgilidir. Her iki durumda kullanılan kontrol stratejisi, tam olarak çift yönlü güç akışını sağlayan matris dönüştürücünün avantajlarını koruyarak giriş faz gerilimine göre çıkış faz gerilimini %150'ye kadar yükselten ve giriş tarafında birim güç faktörü elde etmeyi sağlayan Venturini algoritmasının direkt transfer fonksiyonu kontrol yaklaşımına dayanır. Açık-uçlu sargı topolojisinin kullanılmasının ana nedeni yıldız-bağlı sargı durumunda açıkça gözlemlenen ortak mod geriliminin en aza indirilmesidir. Benzetim sonuçları her iki matris dönüştürücünün aynı üç-fazlı güç kaynağından beslendiği durumda her iki kontrol stratejisi için sunulmuştur. Çift matris dönüştürücünün iki çıkış gerilim seti 180 derece kaydırılmıştır. Elde edilen sonuçlara dayanarak her iki kontrol yaklaşımının performansları teknik olarak tartışılmıştır.

Anahtar Kelimeler : Matris dönüştürücü, Çift matris dönüştürücü, Direkt transfer fonksiyonu yaklaşımı, Benzetim modeli, Açık-uçlu asenkron makine Sürücüsü

1. Introduction

Recently, dual-matrix converter feeding open-end winding induction motor drives have

attracted great interest due to their inherent advantages compared to the standard star or delta connected induction machine drives. The main characteristics of open-end winding induction

machine are [1,2]: Since the machine is powered from both ends of the winding, each matrix converter has half of the machine power rating and therefore each stator phase current can be controlled individually. Consequently, depending on the modulation strategy, possibility of doubling the effective switching frequency is caught. The matrix converter (MC) is a forced commutated converter which can achieve varying amplitude and frequency at the output side. Indeed in recent years, significant research efforts have focused on direct matrix converter where it is increasingly used in several applications due to some implicit advantages comparing to their analogue indirect power electronics conversion using two stages power conversion, DC-AC and AC-AC. Main outstanding advantages of the matrix converter can be summarized as follows [2,3]:

1. Direct conversion (no dc link);
2. Sinusoidal input and output currents can be achieved;
3. The easiness of the input power factor control for any kind of load;
4. Bi-directional power flow capability;
5. Simple and compact design;

On the other side, due to the high integration capability of the semiconductor structures, the matrix converter topology is being recommended for several extreme and critical applications. However, the topology of the matrix converter itself has pushed the researchers to run after more favorable control strategies. In this context several modulation techniques have been developed to fulfil the requirement of the matrix converter control. Among these techniques two main control approaches are being used, the scalar approach such as; the direct transfer function approach (DTF) proposed by Venturini [4,5], and the space vector approach such as; direct and indirect space vector modulation (DSVM and ISVM) [6,7].

In this paper, the direct transfer function control approach is applied to the matrix converter for feeding an open-end three-phase load topology to overcome the main problem of the common mode voltage and to achieve a more flexible control and the operation reliability [8,9]. The both sides of the three-phase load are

supplied using dual three-phase to three-phase matrix converters. The dual matrix converter has the same topology as shown in Fig. 1. The load is an open-end winding induction machine supplied by a dual matrix converter.

In this paper, a comparison between the applications of the same induction machine supplied by a single matrix converter and a dual-matrix converter is presented. Simulation tests were performed to demonstrate the effectiveness of the used topology and control approach for both single and dual matrix converter applications for the same induction machine.

C_f limits the voltage distortion between the terminals of the converter.

L_f limits the current distortion of the supply.

R_f limits the overshoot on turn-on and avoids the resonance excitation by the supply or converter.

2. The Matrix Converter Topology

The topology of a three-phase input - three-phase output matrix converter is presented in Fig.1. The voltages V_{i1} , V_{i2} and V_{i3} are the input-voltages and V_{o1} , V_{o2} and V_{o3} are the output voltages. Each leg has three bidirectional power switches to ensure the connection between one phase of the input and one phase of the output at any instant [8].

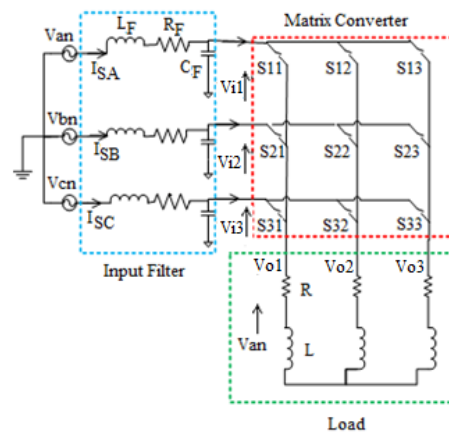


Figure 1. Three-phase matrix converter with input filter

These switches are operating under the two main constraints which are: The input side is not short-circuited and the output side cannot present an open-circuit at any instant. These are the two main important constraints that they are imposed by the normal operation of matrix converter to protect both of the matrix converter and the load [9-11].

The vector of the input voltages is given as follows:

$$\begin{bmatrix} V_{i1} \\ V_{i2} \\ V_{i3} \end{bmatrix} = V_{im} \begin{bmatrix} \cos(\omega_i t) \\ \cos(\omega_i t + 2\pi/3) \\ \cos(\omega_i t + 4\pi/3) \end{bmatrix} \quad (1)$$

The vector of the output voltages is given as follows:

$$\begin{bmatrix} V_{o1} \\ V_{o2} \\ V_{o3} \end{bmatrix} = V_{om} \begin{bmatrix} \cos(\omega_o t) \\ \cos(\omega_o t + 2\pi/3) \\ \cos(\omega_o t + 4\pi/3) \end{bmatrix} \quad (2)$$

2.1. The Switching Equations

The symbol S_{ij} represents the ideal bidirectional switches, where i ($=1, 2, 3$) represents the index of the output side and j ($=1, 2, 3$) represents the index of the input side. The relation between the output voltages and the input voltages can be achieved via an intermediate matrix M , which is known as the modulation matrix, hence the relation between the input and output voltages can be expressed as follows:

$$[V_o] = [M] \cdot [V_i] \quad (3)$$

The relation between the input current $[I_i]$ and output current $[I_o]$ can be deduced:

$$[I_i] = [M]^T \cdot [I_o] \quad (4)$$

where $[M]^T$ represents the transposed matrix of $[M]$.

Equation (3) can be presented in a developed manner as follows:

$$\begin{bmatrix} V_{o1} \\ V_{o2} \\ V_{o3} \end{bmatrix} = \begin{bmatrix} m_{11} & m_{12} & m_{13} \\ m_{21} & m_{22} & m_{23} \\ m_{31} & m_{32} & m_{33} \end{bmatrix} \begin{bmatrix} V_{i1} \\ V_{i2} \\ V_{i3} \end{bmatrix} \quad (5)$$

where the elements of the modulation matrix representing the modulation coefficients are expressed as follows:

$$m_{ij} = \frac{t_{ij}^k}{T_s} \quad (6)$$

During the switching process, the bidirectional switches can connect or disconnect the phase i of the input to the phase j of the output which is connected to the load. In general, the modulation coefficient must provide the following rules [12]:

- At any instant, only one switch S_{ij} ($i = 1, 2, 3$) conducts in order to avoid short-circuit between the input phases.

$$\sum_{i=1,2,3} S_{ij}(t) = 1; j = \{1,2,3\} \quad \forall t \quad (7)$$

- At any instant, at least two switches S_{ij} ($j = 1, 2, 3$) conduct to ensure a way to the inductive load current.
- The switching frequency $f_s = \omega_s/2\pi$ must have a higher value than the maximum of f_i, f_o ($f_s \gg \max f_i f_o$).
- During the period, T_s which is known as the sequential period, the sum of the conduction times of switches being used to synthesize the same output phase must be equal to T_s .

The time t_{ij} ; which is called the time of modulation, can be defined as:

$$t_{ij} = m_{ij} \cdot T_s \quad (8)$$

3. Modified Direct Transfer Function Approach

The modified direct transfer function approach [4,5] permits to control the switch, S_{ij} , whereas the output voltage, V_{oij} and the input current, i_{ij} are sinusoidal with the same values of the output frequency, the input amplitude, the input frequency and the displacement factor.

The maximum voltage output is obtained by the injection of the third harmonic of the output and input waveforms. The mean values of the output voltage over the sequence K^{th} are then given by:

$$\begin{aligned} v_{o1}^{(k)} &= v_{i1}^{(k)} \frac{t_{11}}{T_s} + v_{i2}^{(k)} \frac{t_{12}}{T_s} + v_{i3}^{(k)} \frac{t_{13}}{T_s} \\ v_{o2}^{(k)} &= v_{i1}^{(k)} \frac{t_{21}}{T_s} + v_{i2}^{(k)} \frac{t_{22}}{T_s} + v_{i3}^{(k)} \frac{t_{23}}{T_s} \\ v_{o2}^{(k)} &= v_{i1}^{(k)} \frac{t_{21}}{T_s} + v_{i2}^{(k)} \frac{t_{22}}{T_s} + v_{i3}^{(k)} \frac{t_{23}}{T_s} \end{aligned} \quad (9)$$

The conduction time is modulated with the ω_m while T_s is constant, such as $\omega_m = \omega_o - \omega_i$, these times are defined as follows:

1. In the first phase, we have:

$$\begin{aligned} t_{11} &= \frac{T_s}{3} (1 + 2q \cos(\omega_m t + \theta)) \\ t_{12} &= \frac{T_s}{3} \left(1 + 2q \cos(\omega_m t + \theta - \frac{2\pi}{3})\right) \\ t_{13} &= \frac{T_s}{3} \left(1 + 2q \cos(\omega_m t + \theta - \frac{4\pi}{3})\right) \end{aligned} \quad (10)$$

2. In the second phase, we have:

$$\begin{aligned} t_{21} &= \frac{T_s}{3} \left(1 + 2q \cos(\omega_m t + \theta - \frac{4\pi}{3})\right) \\ t_{22} &= \frac{T_s}{3} (1 + 2q \cos(\omega_m t + \theta)) \\ t_{23} &= \frac{T_s}{3} \left(1 + 2q \cos(\omega_m t + \theta - \frac{2\pi}{3})\right) \end{aligned} \quad (11)$$

3. In the third phase, we have:

$$\begin{aligned} t_{31} &= \frac{T_s}{3} \left(1 + 2q \cos(\omega_m t + \theta - \frac{2\pi}{3})\right) \\ t_{32} &= \frac{T_s}{3} \left(1 + 2q \cos(\omega_m t + \theta - \frac{4\pi}{3})\right) \\ t_{33} &= \frac{T_s}{3} (1 + 2q \cos(\omega_m t + \theta)) \end{aligned} \quad (12)$$

where θ is initial phase angle.

The output voltage is:

$$[V_o^{(k)}] = [M^{(k)}] \cdot [V_i^{(k)}] \quad (13)$$

$$[M^{(k)}] = \begin{bmatrix} 1 + 2q \cos(A) & 1 + 2q \cos\left(A - \frac{2\pi}{3}\right) & 1 + 2q \cos\left(A - \frac{4\pi}{3}\right) \\ 1 + 2q \cos\left(A - \frac{4\pi}{3}\right) & 1 + 2q \cos(A) & 1 + 2q \cos\left(A - \frac{2\pi}{3}\right) \\ 1 + 2q \cos\left(A - \frac{2\pi}{3}\right) & 1 + 2q \cos\left(A - \frac{4\pi}{3}\right) & 1 + 2q \cos(A) \end{bmatrix} \quad (14)$$

where

$$\begin{cases} A = \omega_m t + \theta \\ \omega_m = \omega_o - \omega_i \end{cases} \quad (15)$$

This mathematical development shows that the matrix converter with modified direct transfer function approach generates three-phase sinusoidal voltage waveforms at the output.

4. Modelling of the Open-End Winding Induction Machine

The open-end stator winding induction machine presented in Fig. 2 is supplied by two three-phase voltage systems and these systems are defined as:

The three-phase systems supplied by the first matrix converter: $[V_{s1}] = [V_{s11} \ V_{s12} \ V_{s13}]^T$;

The three-phase systems supplied by the second matrix converter: $[V_{s2}] = [V_{s21} \ V_{s22} \ V_{s23}]^T$;

Hence, the voltage vector applied on the stator winding of the machine is:

$$[V_s] = [V_{s11} - V_{s21} \ V_{s12} - V_{s22} \ V_{s13} - V_{s23}]^T$$

The mathematical flux model is defined in (d-q) reference frame, and described by the following state equations representation:

$$\frac{dX(t)}{dt} = [A(\omega, \omega_{dq})][X(t)] + [B] \cdot U(t) \quad (16)$$

$$Y(t) = [C] \cdot Y(t) \quad (17)$$

where

$X(t) = [\phi_{sd} \ \phi_{sq} \ \phi_{rd} \ \phi_{rq}]$ is the state vector;

$U(t) = U_1(t) - U_2(t) = [V_{sd1} - V_{sd2} \ V_{sq1} - V_{sq2}]$ is the control vector;

$Y(t) = [I_{sd} \ I_{sq} \ I_{rd} \ I_{rq}]$ is the output vector.

The principle diagram of the system is shown in Fig. 2:

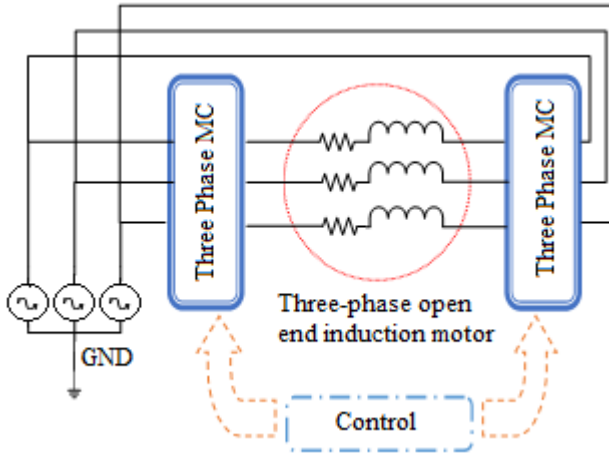


Figure 2. Three phase open-end winding induction motor fed by dual matrix converter

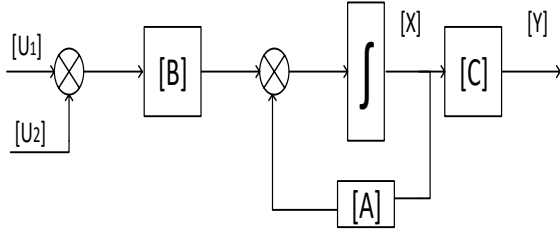


Figure 3. Block diagram of the open-end winding machine

On the other side the following parameters are taken into account:

$\tau_s = \frac{L_s}{R_s}$ is the stator constant time

$\tau_r = \frac{L_r}{R_r}$ is the rotor constant time

$\sigma = 1 - \frac{M_{sr}^2}{L_s L_r}$ is the coefficient of dispersion of Blondel

R_r is the rotor resistance, R_s is the stator resistance, L_r is the rotor inductance, L_s is the stator inductance, M_{sr} is the mutual inductance between stator and rotor.

The equation for current vector is

$$[I] = [L]^{-1}[\Phi] \quad (18)$$

The matrices [A], [B] and [C] are defined as follows:

$$[A] = \begin{bmatrix} -\frac{1}{\sigma\tau_s} & \omega_{dq} & \frac{M_{sr}}{\sigma\tau_s L_r} & 0 \\ -\omega_{dq} & -\frac{1}{\sigma\tau_s} & 0 & \frac{M_{sr}}{\sigma\tau_s L_r} \\ \frac{M_{sr}}{\sigma\tau_r L_s} & 0 & -\frac{1}{\sigma\tau_r} & \omega_{dq} - \omega \\ 0 & \frac{M_{sr}}{\sigma\tau_r L_s} & -(\omega_{dq} - \omega) & -\frac{1}{\sigma\tau_r} \end{bmatrix} \quad (19)$$

$$B = \begin{bmatrix} 1 & 0 & 0 & 0 \\ 0 & 1 & 0 & 0 \\ 0 & 0 & 1 & 0 \\ 0 & 0 & 0 & 1 \end{bmatrix}$$

$$[C] = [L]^{-1} = \begin{bmatrix} \frac{1}{\sigma L_s} & 0 & \frac{M_{sr}}{\sigma L_s L_r} & 0 \\ 0 & -\frac{1}{\sigma\tau_s} & 0 & \frac{M_{sr}}{\sigma L_s L_r} \\ -\frac{M_{sr}}{\sigma L_r L_s} & 0 & -\frac{1}{\sigma L_r} & 0 \\ 0 & -\frac{M_{sr}}{\sigma L_r L_s} & 0 & \frac{1}{\sigma L_r} \end{bmatrix} \quad (20)$$

The mechanical equation is given as follows:

$$T_{em} - T_r = j \frac{d\omega}{dt} + f\omega \quad (21)$$

$$T_{em} = \frac{3}{2}p(\Phi_{sa}I_{s\beta} - \Phi_{s\beta}I_{sa}) \quad (22)$$

where T_{em} is the electromagnetic torque; T_r is the load torque.

5. Simulation

In this work, two simulation tests were performed to prove the advantage of the use of the open-end winding induction machine fed by a dual matrix converter having the same topology and characteristic. The first simulation presents the induction machine fed by only one matrix converter, where the output voltage is characterized by a fundamental frequency of $f_0=50$ Hz and a magnitude of $V_0=350$ V. The parameters of the input voltage source and the induction machine are presented in Table 1. On the other side, due to the distortion which may occur in the input current and to avoid the propagation of this kind of harmonics pollution toward the source, an LC input filter is inserted as shown in Fig.2 where its parameters can be found in Table 1. [13-15].

5.2. Induction Motor Fed by A Three-Phase Matrix Converter

In this case, a single three-phase matrix converter is used to feed a three-phase induction motor. The output voltage and the output current of the matrix converter are presented in Fig. 4 and 6, respectively. Total Harmonic Distortion (THD) of the output voltage and current waveforms, which is defined in Eq. (23), are presented in Fig. 5 and 7, respectively. It can be concluded that the harmonic rays are around the switching frequencies ($n \times f_s$) where it is taken as $f_s=10$ kHz

$$THD = \sqrt{\frac{V_2^2 + V_3^2 + \dots + V_n^2}{V_1^2}} \quad (23)$$

The fundamental harmonic amplitude of the output voltage is 344.4 V with THD of 99.36% as shown in Fig. 5 and harmonics rays can be remarked clearly around the switching frequency. However, due to the inductive nature of the induction motor, the output current poses a low THD as 2.77%. Figs. 8 and 9 show the decoupling carried out between the flux and the electromagnetic torque. The decoupling between torque and machine speed is remarked clearly especially at the interval between 1.5 s and 2.5 s. The supply current waveform is shown in Fig.10. The result shows great effect of the input filter where the high order harmonics are eliminated by the input filter.

Table 1. Simulation parameters

V_s	Input voltage	350 V
f_s	Input frequency	50 Hz
L_f	Filter inductance	0.03 H
R_f	Filter Resistance	0.5 Ω
C_f	Filter Capacitance	25 μ F
R_s	Stator resistance	4.85 Ω
R_r	Rotor resistance	3.81 Ω
L_s	Stator inductance	0.274 H
L_r	Rotor inductance	0.274 H
L_m	Mutual inductance	0.258 H

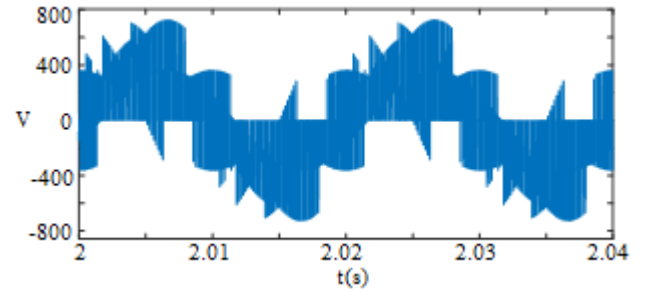


Figure 4. Output line voltage waveform of the matrix converter

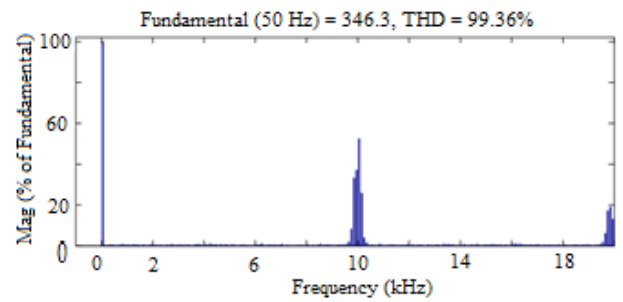


Figure 5. Harmonic spectrum of the matrix converter output voltage waveform

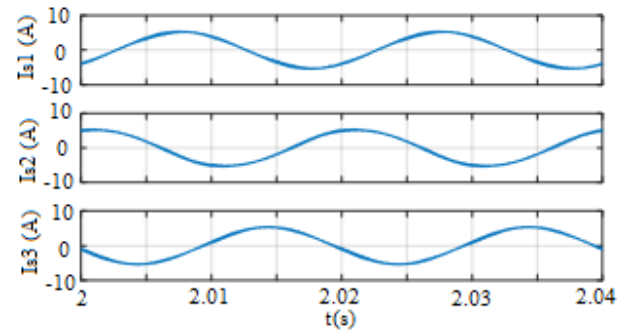


Figure 6. Three-phase motor currents

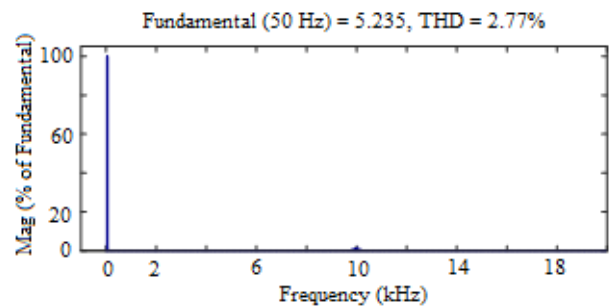


Figure 7. Harmonic spectrum of the matrix converter output current

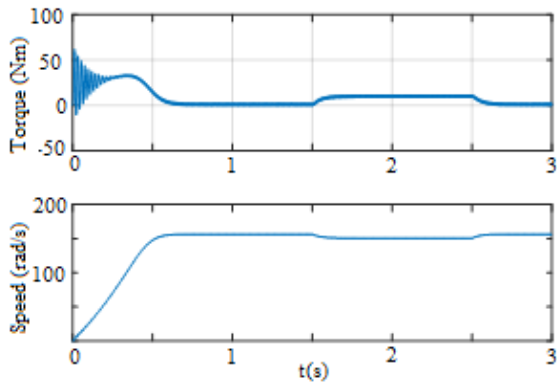


Figure 8. Torque (up) and speed (bottom) of the induction motor

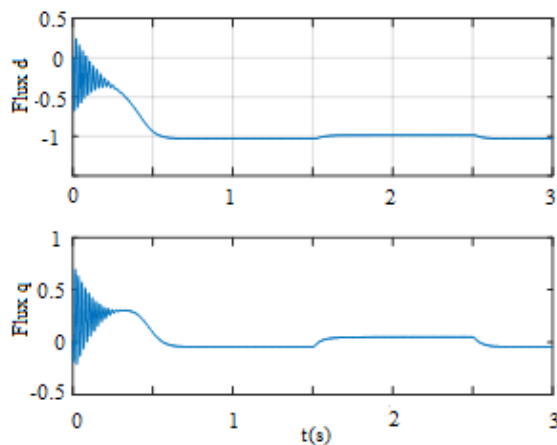


Figure 9. Flux flowing rotor axis "d" (up) and flux flowing rotor axis "q" (bottom)

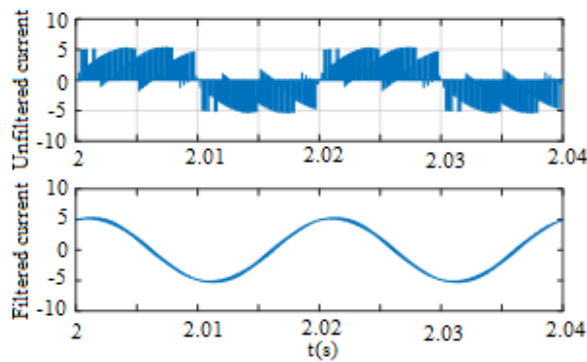


Figure 10. The supply current without and with filtering, respectively

5.2. Dual Matrix Converter Feeding Open-End Winding Induction Motor

In this case, two of three-phase matrix converter feed the both sides of the open-end winding of the same induction machine stated previously. Under this topology the common mode voltage (CMV) will be totally removed and the three-phase load can be controlled

independently. Due to the balanced nature of the load, the voltage applied at each load phase is the same except for the eventual required phase shift. Figs.11 and 12 illustrate the voltages between the two terminals of the three-phase load and the load currents, respectively. It is obvious that the fundamental magnitude of the voltage is 348.5 V with a THD of 75.12 % whereas, the fundamental current is 4.636 A with THD of 3.36 % which means that there is an improved voltage and current quality in comparison with the situation where the machine is fed by a single three-phase matrix converter (Fig. 13 and Fig. 14). In the same time a less harmonic rays can be remarked clearly near the switching frequency $f_s = 10$ kHz. The two level voltages is clearly observed and the three-level voltage at the load terminals is also obviously observed. The effect of the input filter can be seen clearly in Fig. 17., Figs.15 and 16 show the decoupling carried out between the flux and the electromagnetic torque. In the same time, the decoupling between the torque and the speed of the machine can be seen especially at the interval between 1.5 s and 2.5 s.

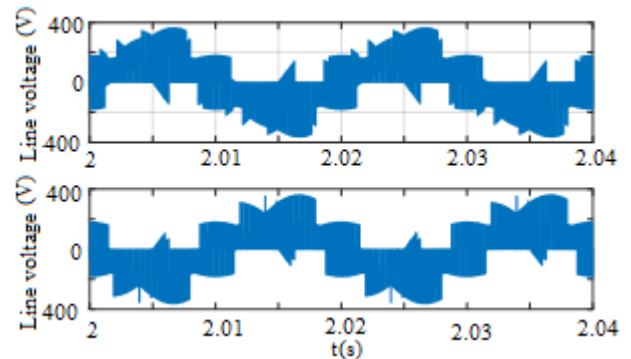


Figure 11. Output line voltage waveforms of MC1 (up) and MC2 (bottom)

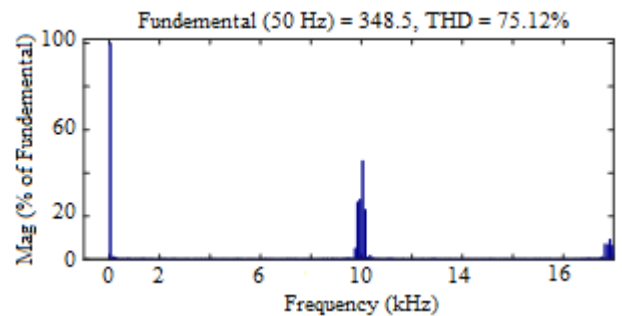


Figure 12. The Harmonic spectrum of the output voltage applied to one phase of the induction motor

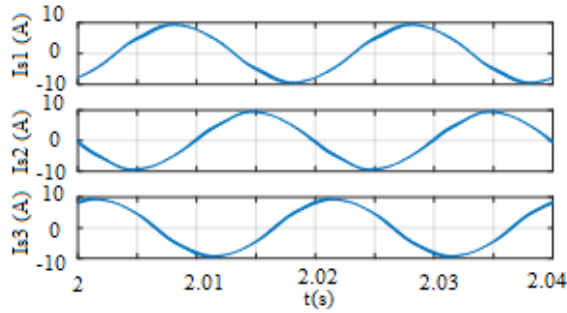


Figure 13. Three-phase motor currents

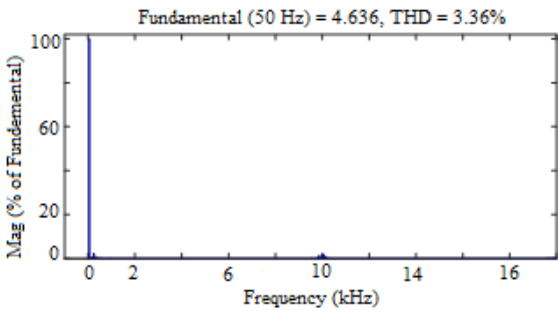


Figure 14. Harmonic spectrum of the output current

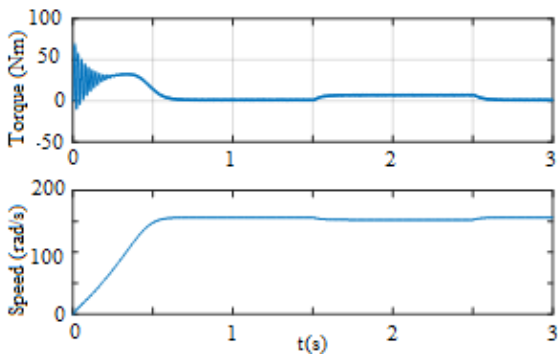


Figure 15. Torque (up) and speed (bottom) of the induction motor

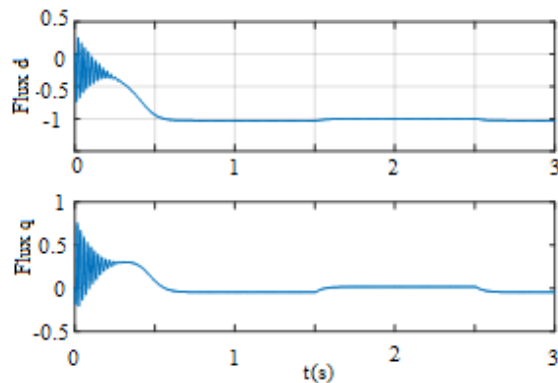


Figure 16. Flux flowing rotor axis "d" (up) and flux flowing rotor axis "q" (bottom)

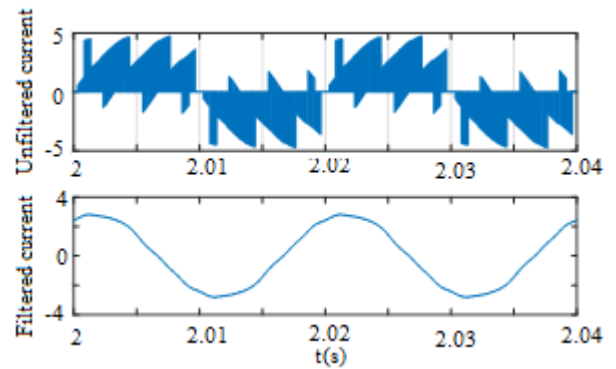


Figure 17. The supply current without and with filtering, respectively

6. Conclusions

In this paper, the main advantages of the dual matrix converter used in open-end structure are proved by simulation results. The results show clear improvement on quality of the voltages enforced to the induction machine drive and elimination of the common mode voltage which is major problem in all three-phase load applications, especially in three-phase electrical machines. On the other side, due to the multilevel nature of the voltage applied at the terminal of the open-end load, the current quality is also improved, where the THD is decreased at nearly 48% compared to the classical topology based on one matrix converter. An important issue is that the use of a dual matrix converter is more reliable in case of fault on one or more switches. This problem can be solved by easily adjusting control signals of the switches. Finally, it can be said that the presented topology can have a large use in electric machines application in industry based on the afore-mentioned advantages.

7. References

1. Riedemanna, J., Andradeb, I., Peñab, R., Blasco-Gimenezc, R., Clare J., Melin, P., Rivera, M. (2016). Modulation strategies for an open-end winding induction machine fed by a two-output indirect matrix converter, *Mathematics and Computers in Simulation*, 144-152.
2. Wheeler, P.W., Rodriguez P.W., Clare, J.C., Empringham, L., Weinstein, A., (2002). Matrix converters: A technology review. *IEEE Transactions on Industrial Electronics*, 49(2), 276-288.

3. Vargas, R., Rodríguez, J., Ammann, U., Wheeler, P.W. (2008). Predictive current control of an induction machine fed by a matrix converter with reactive power control. *IEEE Transactions on Industrial Electronics*, **55**(12), 4362-4371.
4. Venturini, M. (1980). A new sine wave in sine wave out, conversion technique which eliminates reactive elements. *POWERCON 7*, E3-1-E3-15.
5. Alesina, A., Venturini, M. (1989). Analysis and design of optimum-amplitude nine-switch direct AC-AC converters, *IEEE Transactions on Power Electronics*, **4**(1), 101-112.
6. Ahmed, S.M., Abu-Rub, H., Kouzou, A. (2013). Predictive simultaneous power and current control in a three-phase direct matrix converter. *International Conference on Power Electronics and Their Applications (ICPEA)*, Djefia-Algeria.
7. Bachir, G., Bendiabdellah, A. (2009). A comparative study between two control strategies for matrix converter. *Advances in Electrical and Computer Engineering*, **9**(2), 23-27.
8. Beladel, A., Kouzou, A., Hafaifa, A., Mahia D., (2016). Dual matrix converter feeding an open-end winding load based on modified direct transfer approach, *International Scientific Conference on Engineering, Technologies and Systems*.
9. Altun, H., Sünter, S. (2003). Matrix converter induction motor drive: modeling, simulation and control. *Electrical Engineering*, **86**(1), 25-33.
10. Rodriguez, J., Silva, E., Wheeler, P., (2013). Matrix converter controlled with the direct transfer function approach: analysis, modelling and simulation, *International Journal of Electronics*, 63-85.
11. Djahbar A., Mazari B., (2007). High performance motor drive using matrix converter, *Acta Electrotechnica et Informatica*, **2**(7).
12. Guizana, S., Ammar, F.B., (2005). Dual open-end stator winding induction machine fed by redundant voltage source inverters, *Turkish Journal of Electrical Engineering & Computer Sciences*, **92**(2), 2171-2181.
13. Riedemann, J., Clare, J.C., Wheeler, P.W., Blasco-Gimenez, R., Rivera, M., Pena, R. (2016). Open-end winding induction machine fed by a dual-output indirect matrix converter. *IEEE Transactions on Industrial Electronics*, **63**(7), 4118-4128.
14. Gopal, M., Gopakumar, K., Tekwani, P.N., Emil, L.A., (2007). Reduced-switch-count five-level inverter with common-mode voltage elimination for an open-end winding induction motor drive, *IEEE Transactions on Industrial Electronics*, **54**(4).
15. Elbar, M., Mahmoudi, M.O., Naas, B., (2010). A Carrier-Based PWM Techniques Applied to a Three-Level Four-Leg Inverter For Use as a Shunt Active Power Filter, *J. Electrical Systems*, Special Issue (2), 47-57.

Elliptic Filter Based Noninvasive Blood Pressure Analyze with LabVIEW

Duygu KAYA, Mustafa TÜRK, Turgay KAYA

Firat University, Department of Electrical and Electronics Engineering, Elazığ /Turkey
dgur@firat.edu.tr

(Geliş/Received: 20.02.2017; Kabul/Accepted: 18.04.2017)

Abstract

The blood in the vein is called blood pressure or tension. It depends on the amount of blood pumped by the heart and the resistance of the vessels to this flow and the flexibility of the arterial walls. Very low values than optimum blood pressure and very high values than normal blood pressure are important. With this aim, Noninvasive Blood Pressure Analyze with LabVIEW offers an insight into us. LabVIEW is a graphical programming language that uses a Dataflow model instead of sequential lines of text code. LabVIEW runs principle of Data flow programming that allows multiple operations to work in parallel. So, designers spend less time than a text based programming language. Application areas such as signal processing, image processing and Data analysis are available. In this paper, LabVIEW- based Noninvasive Blood Pressure Analyze (NIBP) using different Data and to obtain systolic/diastolic pressure. As a result of this, the current data are divided into optimum blood pressure, normal blood pressure and prehypertension

Key Words: Blood Pressure; Elliptic Filter; LabVIEW.

LabVIEW ile Eliptik Filtre Tabanlı Noninvaziv Kan Basıncı Analizi

Özet

Damarlardaki kan, kan basıncı ya da tansiyon olarak isimlendirilir. Kan basıncı, kalp tarafından pompalanan kan miktarına ve damarların bu akışa karşı göstermiş oldukları dirence ve arter duvarların esnekliğine bağlıdır. Optimal kan basıncından çok düşük değerler ve normal kan basıncından çok yüksek değerler önem arz etmektedir. Bu amaçla, LabVIEW ile noninvaziv kan basıncı analizi, bize bu konu hakkında fikir sunmaktadır. LabVIEW, ardışık metin kodları yerine veri akışı modelini kullanan bir grafik programlama dilidir. LabVIEW, çoklu işlemlerin paralel çalışmasına olanak tanıyan veri akışı programlama ilkesine göre çalışmaktadır. Bu nedenle, tasarımcılar metin tabanlı bir programlama dilinden daha az zaman harcamaktadırlar. Sinyal işleme, görüntü işleme ve veri analizi gibi uygulama alanlarında kullanılmaktadır. Bu çalışmada farklı veriler kullanarak sistolik / diyastolik basınç elde etmek için LabVIEW tabanlı non-invaziv kan basıncı analizi (NIBP) kullanılmıştır. Yapılan çalışma sonucunda mevcut veriler, optimum kan basıncı, normal kan basıncı ve prehipertansiyona bölünür.

1. Introduction

Blood Pressure (BP) is the pressure that the blood in the vein bed makes to the vein walls during the flow. It depends on the amount of blood pumped by the heart and the resistance of the vessels to this flow and the flexibility of the arterial walls [1]. As the heart contracts, blood is pumped into the arteries. This increases the pressure in the arteries, while the pressure decreases in the heartbeats. As a consequence of this, the BP is indicated by two values, namely systolic pressure and diastolic pressure and the unit is millimeters of mercury (mmHg) [2]. With

BP measurement, it is decided which characteristics the person exhibits from optimum, normal, hypertension, hypotension and prehypertension. The optimum BP is below 120/80 mmHg. The normal BP is below 130/85 mmHg. Hypertension is higher than normal accepted values and one of the most important health problems. The BP is above 140/90 mmHg. Hypertension can lead to headache, dizziness, and can lead to heart-kidney disorders, paralysis and visual disturbances if not noticed. Hypotension is abnormally low BP that is 90/60 mmHg below. It can occur due to

many reasons such as sadness, stress, long-term hunger and vitamin deficiency. But every low BP not indicate a health problem. Prehypertension is used to describe patients whose BP is elevated but still within normal limits. The BP is between 120-139 mmHg systolic and 80-89 mmHg diastolic [3]. BP monitors should be considered to prevent serious illnesses and situations that could cause life-threatening injuries. The aim of this paper to investigate LabVIEW- based Noninvasive Blood Pressure Analyze (NIBP) using different Data and to obtain systolic/diastolic pressure. As a result of this, the current Data are divided into optimum pressure, normal pressure and prehypertension.

The structure of this paper is as follows: Second section includes preprocessing of signals, database signals taken from LabVIEW. Third section includes evaluation of results. The last section includes conclusion and future works.

2. Material and Methods

A. Database

Signals required for paper are taken from the LabVIEW own Database. Signals of three Databases that are NIBP_Data_1, NIBP_Data_2, NIBP_Data_3 were used to examine. Each signal is sampled at intervals of 0.002 for 31, 32, 27 seconds, respectively. These signals correspond to prehypertension, normal and optimal respectively.

B. LabVIEW

LabVIEW is a graphical programming language that uses a Dataflow model instead of sequential lines of text code. Comparison of the other language, LabVIEW runs principle of Data flow programming that allows multiple operations to work in parallel [4,5]. It provides that acquires of

bioelectrical signal, preprocesses and analyzes them.

LabVIEW is a software based graphical programming language that consists of front panel and block diagram. The sections where the user interface prepares and the code is written correspond to front panel and block diagram, respectively. The block diagram of designed system is shown in Figure 1. LabVIEW is called a Virtual Instrument (VI) because it resembles the physical instruments used in the laboratory with the way it works [6]. The biomedical workbench toolkit in LabVIEW allows applications such as recording, by sensor with DAQ hardware, and viewing bioelectrical signal, heart rate variability (HRV) analysis, ECG Feature Extracture and Noninvasive Blood Pressure Analyze By file format converter, the files are converted into different types of file formats for the various applications. For instance, it supports .hea, .tdms, .mat, .rec extensions file [7]. In this paper, .tdms extensions file was used.

C. Preprocessing

Used signals are recorded with many low frequency undesired noise caused by the circulatory system. Filtering should be done to suppress them. For this, lowpass elliptic filter was chosen. An elliptic filter is a signal processing filter with equalized ripple behavior in both the passband and the stopband [8]. The level of ripple on each band is a configurable filter. As the ripple in the pass-band approaches zero, the filter becomes a Chebyshev type II filter, as the ripple in the stopband approaches zero, it becomes a Chebyshev type I filter and both band approaches zero, filter becomes a Butterworth filter. Although this filter has ripple both band, it has a rapid decline from the pass band to the stop band. With this filter, undesired signals removed then with BP analyzer systolic/diastolic and mean arterial pressure (MAP) were obtained.

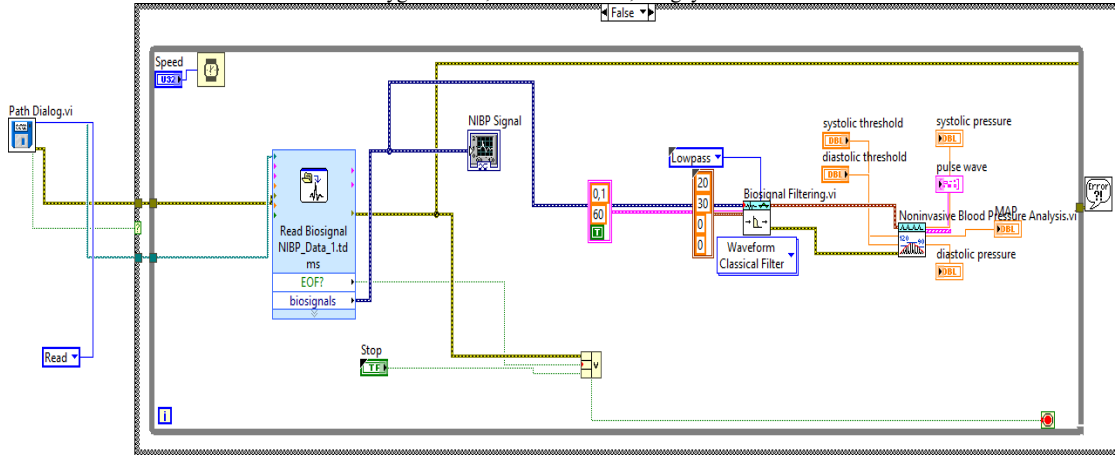


Fig.1 Block diagram of designed system

3. Results and Discussion

Mentioned techniques have been applied to BP signals to obtain systolic/diastolic BP and MAP value. In order to interpret the results obtained, the values that the World Health Organization (WHO) prescribes for BP limit values are taken as references. The classification of BP by the World Health Organization International Hypertension Committee is given in Table 1. Obtained BP results are shown in Table 2.

Figure 2 shows NIBP_Data_1, Figure 3 shows the result of the analysis, Figure 4 shows the NIBP_Data_2, Figure 5 shows the analysis result, Figure 6 shows the NIBP_Data_3, and Figure 7 shows the analysis results.

Obtained results show that NIBP_Data_1 corresponds to prehypertension, NIBP_Data_2 corresponds to normal BP and NIBP_Data_3 corresponds to optimal BP.

Table 1. Classification of BP

Category	systolic, mmHg	diastolic, mmHg
Hypotension	< 90	< 60
Normal	< 130	< 85
Optimal	< 120	< 80
Prehypertension	130-139	85-89
Stage 1 hypertension	140- 159	90-99
Stage 2 hypertension	160-169	100-109

Table 2. Obtained BP Results

Category	systolic, mmHg	diastolic, mmHg	MAP mmHg
NIBP_Data_1	131	86	93
NIBP_Data_2	122	72	83
NIBP_Data_3	107	64	72

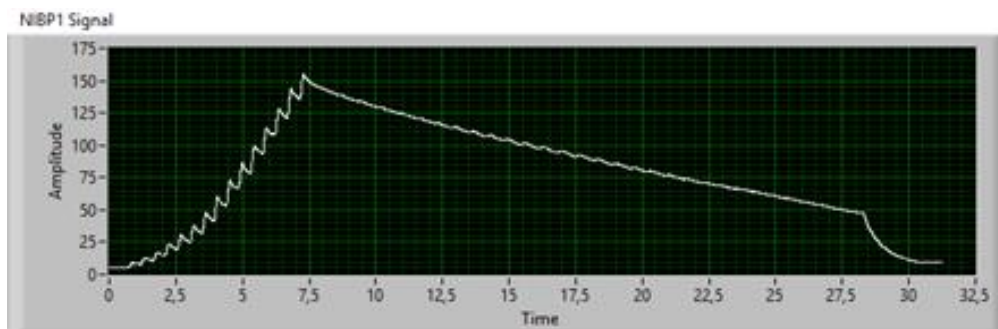


Fig.2 NIBP_Data_1 Signals

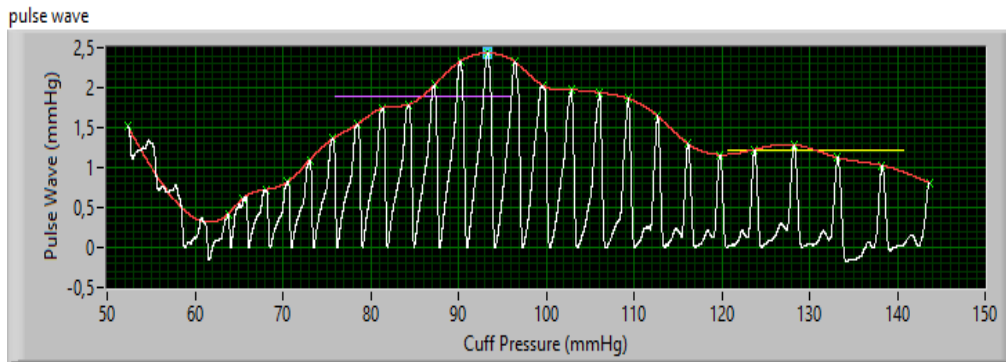


Fig.3 Analyze results of NIBP_Data_1 Signals

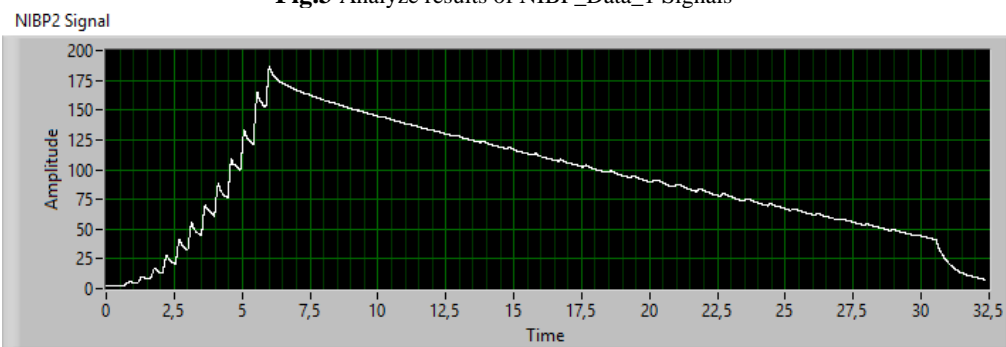


Fig.4 NIBP_Data_2 Signals

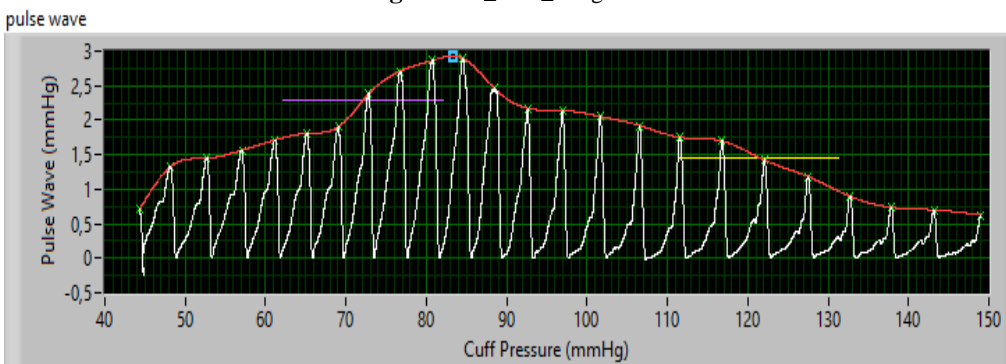


Fig.5 Analyze results of NIBP_Data_2 Signals

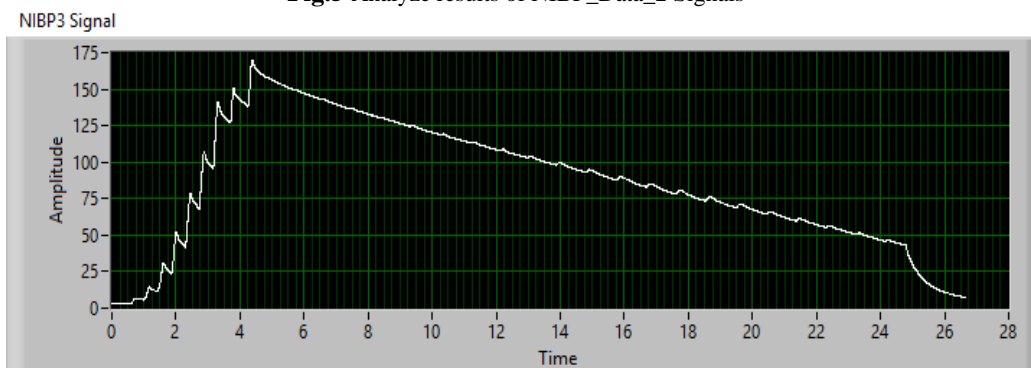


Fig.6 NIBP_Data_3 Signals

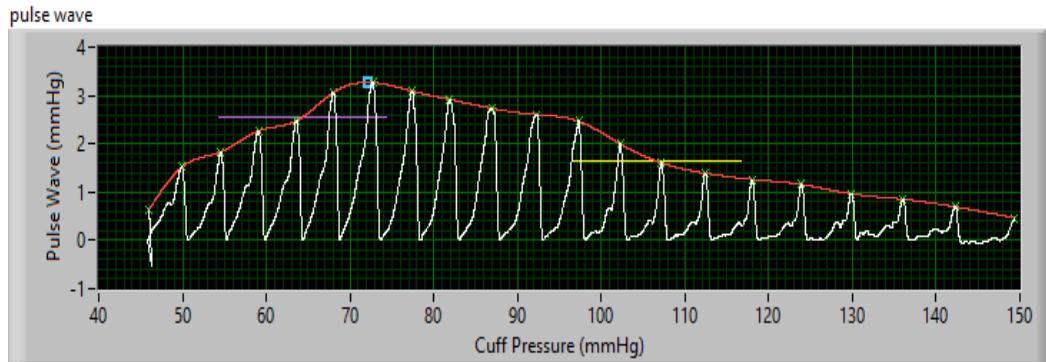


Fig. 7 Analyze results of NIBP_Data_3 Signal

4. Conclusions

Low BP and high BP are important health problems. Especially, hypertension is one of the most important health problems in the world that requires regular checking. Prehypertension is used to describe patients whose BP is elevated but still within normal limits. The optimum BP is below 120/80 mmHg. People with pre-hypertension are more likely to have a risk of myocardial infarction and fallacies than people with normal BP. The normal BP is below 130/85 mmHg. Hypotension is abnormally low BP that is 90/60 mmHg below. It can occur due to many reasons such as sadness, stress, long-term hunger and vitamin deficiency.

So, in this study, it is provided to measure BP level with the developed LabVIEW algorithm. Simple usage of graphical structure allows to observe BP level to the doctor or the patients. In future studies, classification models will be tried to be improved.

5. References

1. Ogedegbe, G., Pickering, T., (2010). Principles and techniques of blood pressure measurement. *Cardiology Clinics*. **28** (4), 571–586.
2. Obrien, E., (2001). Blood pressure measurement is changing *Heart*. **85** (1): 3–5. doi:10.
3. Materson, B.J., Garcia-Estrada, M., Degraff, S.B., Preston, R.A., (2017). Prehypertension is Real and Can be Associated with Target Organ Damage, *Journal of the American Society of Hypertension*, doi.org/10.1016/j.jash.2017.09.005
4. Kehtarnavaz, N, Mahotra, S., *Digital Signal Processing Laboratory: LabVIEW-Based FPGA Implementation*, pp.7.
5. Aydın, S.G., Kaya, T., Güler, H., Wavelet-based study of valence–arousal model of emotions on EEG signals with LabVIEW, *Brain Informatics*, (3), pp.1-9.
6. <http://www.ni.com/white-paper/4752/en/>
7. Deshmukh, A., Gandole, Y., (2015). ECG Feature Extraction Using NI Lab-View Biomedical Workbench. *International Journal of Recent Scientific Research* 6(8), pp.5603-5607.
8. Daniels, R.W., *Approximation Methods for Electronic Filter Design*. New York: McGraw-Hill.

Development of Smart Security System for Remote Control Using Small Computer

Huda AL-SAFFAR¹, Ergun ERÇELEBİ²

^{1,2}Gaziantep University, Electrical and Electronics Engineering, Gaziantep, Turkey

¹msc.computereng89@gmail.com

(Geliş/Received:23.02.2017; Kabul/Accepted:06.04.2017)

Abstract

The aim of this paper is to develop a smart security system for remote control using a small computer. In this paper, it has been proposed a comparatively inexpensive security system which has the capability to automatically initiate capture a picture by Raspberry Pi Camera Module when any movement is detected by PIR sensor and the Raspberry Pi device will send that picture to the user's smartphone device via Wi-Fi using application. Also, the system will light up the light bulb and LEDs when motion is detected. In addition, this system can be counted the number of moving objects located with the help of the infrared PIR sensor and will be sent that number with notification message "Motion Detection" to smartphone alongside the picture. The proposed system is very effective and crucial choice for energy save and security for home or service buildings. Nowadays, in electronic markets, there are many expensive solutions. However, low-cost solutions are very important for spreading between all people. Knowing that the Raspberry Pi 3 device and Telegram application were used in this proposed system.

Keywords: Raspberry Pi 3, PIR Sensor, Raspberry Pi Camera Module, Relay, Smartphone.

Küçük Bilgisayar Kullanarak Uzaktan Kumanda için Akıllı Güvenlik Sisteminin Geliştirilmesi

Özet

Bu makalenin amacı küçük bir bilgisayar kullanarak uzaktan kontrol edilebilir akıllı bir güvenlik sistemi geliştirmektir. Bu yazıda, PAS hareket sensörü PIR hareket tespit ettiğinde Raspberry Pi Kamera Modülü tarafından otomatik olarak fotoğraf çekebilen ve bu fotoğrafı Wi-Fi üzerinden bir uygulama vasıtasıyla kullanıcının akıllı telefonuna gönderen entelektüel güvenlik sistemi önerilmiştir. Ayrıca, sistem PIR hareket tespit ettiğinde ışık ampulünü ve LED'leri aydınlatır. Buna ek olarak, bu sistem, kızılötesi PIR sensörü vasıtasıyla hareket eden nesnelere tespit ettikten sonra, sayısını ve görüntülerini "Hareket Algılama" bildirim mesajıyla birlikte akıllı telefona gönderir. Önerilen sistem, ev ya da hizmet binalarında enerji tasarrufu ve güvenlik için etkili ve önemli bir seçimdir. Günümüzde elektronik pazarlardaki güvenlik çözümleri çok pahalıdır. Fakat, düşük maliyetli çözümler bu sistemlerin tüm insanlar arasında yaygınlaşması için çok önemlidir. Önerilen sistemde Raspberry Pi 3 cihazı ve Telegram uygulaması kullanılmıştır.

Anahtar Kelimeler: Raspberry Pi 3, PIR Sensörü, Ahududu Pi Kamera Modülü, Röle, Smartphone.

1. Introduction

Security is the first attention in everywhere, every time and for everyone. Each person who wishes to be his home and service buildings in safety [1]. The microcontroller in this system is the small computer is Raspberry Pi 3. Obviously, Raspberry Pi 3 is a single board which, when it is interfaced with the screen, keyboard, mouse and installed the operating system to be able to achieve the functions for any computer. The Operating System (OS) is the collection of

programs and instructions that make the Raspberry Pi 3 run. In addition, the operating system whose works in Raspberry Pi 3 based only on Linux operating systems such as Raspbian OS and NOOBS [2]. It is worth to mention that, in this system, Raspbian OS version Jessie with PIXEL is installed in the Raspberry Pi 3 and the python programming language was used to programming the project program.

This project describes a smart security system for all homes and service buildings that can monitor any place in it. The system has been able to detect any object movement, turn ON/OFF light bulb and LEDs when an object moving in light day or darkness, take a picture, count the object moving number and automatically send the data to a smartphone via Wi-Fi using Telegram application. The data include the picture and notification message "Motion Detection" with moving object number located.

The advantage of using this system is that, it is a very crucial choice for energy save and home security. Also, another advantage is that it is a simple circuit and able to work at any time in the light day or darkness [3]. The other major advantage is that it is very economic system and it can be placed anywhere [4].

2. Design and Implementation of Proposed System

The design and implementation of a low-cost system monitoring based on Raspberry Pi 3, a single board computer which interfaced with PIR Sensor, Raspberry Pi Camera Module, LEDs and relay and controlling them by implementing program written in python language in software implementation. The block diagram of this system is illustrated in Figure 1 below.

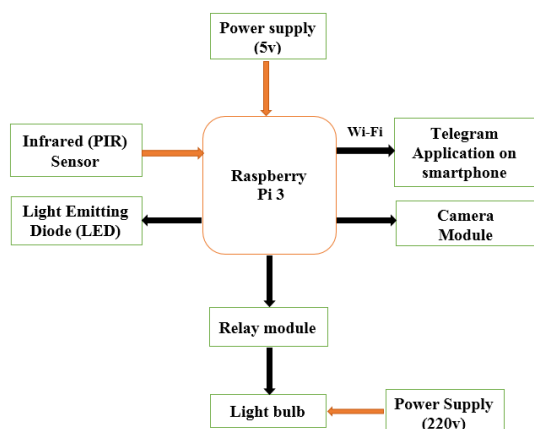


Figure 1. Block Diagram for the proposed system

To improve and facility the algorithm for the proposed system, the algorithm is separate into two parts which are motion detection part and lighting part. The system implementation begins when connecting the Raspberry Pi 3 and relay to

the power supply. Knowing that the starting number for image counter is 1.

Firstly, if there is no motion detected by the PIR sensor, the program will turn OFF the LEDs and suspends the program for 1 second and directly return back to check the motion detection.

Secondly, if the motion is detected by PIR sensor the program will turn ON the lighting part and then the camera module will capture the picture and stores it in micro SD card. After that, the program will send the picture taken and notification message "Motion Detection" with the object number located directly to smartphone by Telegram application every time a motion is detected to alert the owner which having a smartphone and then the program will increment the counter image by 1 and subsequently turn OFF light bulb to energy save after that the program will suspend for 10 seconds before return one more time to check the object movement. The lighting part consists of LEDs and light bulb.

Besides that, the security system will stop when separating the power supply. The flowchart for the proposed system is shown in the Figure 2 and the block diagram of the lighting part is shown in Figure 3.

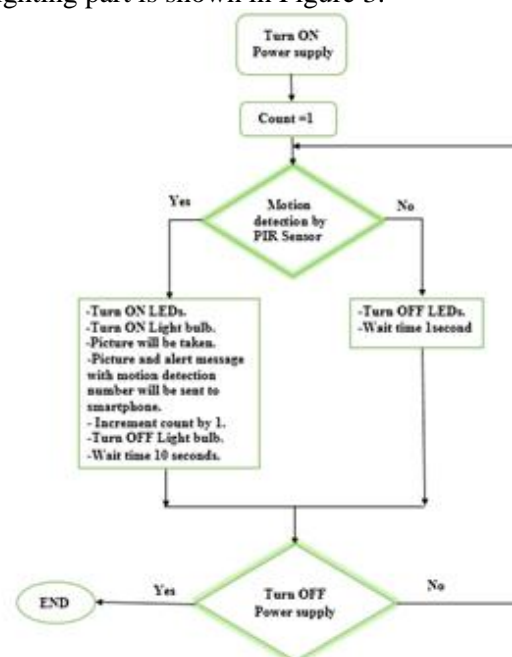


Figure 2. Flow Chart of proposed system

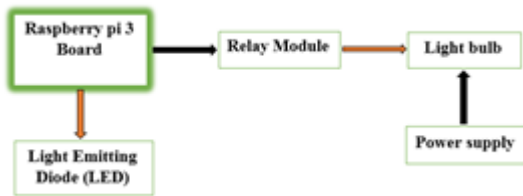


Figure 3. Lighting system

3. System components description

The major components of the proposed system are Raspberry Pi 3 Model B, Passive Infrared (PIR) Sensor, Raspberry Pi Camera Module, Relay, Power supply, LED (Light Emitted Diode), Telegram Application on smartphone and GPIO pins configuration. The block diagram for the proposed system illustrated in Figure 1.

3.1. Raspberry pi 3 Model B

Raspberry Pi is a small credit card sized, single-board computer. It was more useful for projects which require very low power and used for computer science education. The amazing new version of Raspberry Pi is Raspberry Pi 3 Model B. This third generation model developed by the Raspberry Pi Foundation Company in the UK [5].

Table 1. Specification of Raspberry Pi3 Model B.

Specification	Description
SoC (System on Chip)	Broadcom BCM2837
CPU	64-bit, ARMv7, Quad cortex A53 @ 1.2GHz
GPU	400 MHz video Core IV 3D graphics Core
RAM	1GB SDRAM
SD Card Slot	Micro SD Card Slot (Push-Pull)
GPIO	40 Pin
USB 2.0	4 Ports
Bluetooth	Bluetooth 4.1, BLE(Bluetooth Low Energy)
Wireless LAN	802.11n Wi-Fi
Ethernet Port	10/100 LAN Port
HDMI Output	Full-size HDMI Video Output

Power Supply	5V and Up to 2.5 Amps
Audio Output	3.5 mm, 4-track composite video and audio output jack
Dimensions	85.6mm x56mm x21mm
Price	35\$

The proposed system used Raspberry Pi 3 Model B that consists of the key specifications as illustrated in Table 1 and Raspberry Pi 3 board in Figure 4.

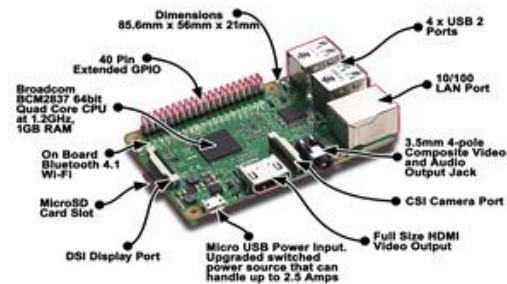


Figure 4. Raspberry Pi 3 Model B board

3.2. Passive Infrared (PIR) Sensor

PIR sensor is an essential part of this proposed system. The object will emit infrared (IR) radiation through his movement. PIR is an electronic sensor that used to detect the object motion by receiving the infrared (IR) radiates light from the external environment. Hence, the sensor compares the intensity of the infrared radiation from time to time. If there is an object movement in the room, then the intensity changes, it causes detecting the object movement. Knowing that the range for PIR sensor can up to 5-7 meters[3]. The PIR Sensor is small in size, inexpensive in price, used low-power, easy in use and connectivity. They are often referred to as PIR, Passive Infrared, Pyroelectric, or IR motion sensors[6]. In this proposed system the HC-SR501 PIR Sensor Module is used.



Figure 5. PIR Sensor

3.3. Raspberry pi Camera Module

The Camera Module Rev 1.3 is a camera that created specifically for Raspberry Pi model A and B. It is manufactured by the Sunny company. It provides high sensitivity, very small PCB design, price almost 25\$, lightweight design and 5-megapixel resolution image. The camera module connects to Raspberry Pi 3 by CSI (Camera Serial Interface) connector using a 15cm ribbon cable to the 15 pin CSI connector [7].



Figure 6. Camera Module

3.4. Relay Card

A relay is an electrical switch that is used to control high voltage by using very low voltage and as an input (GPIO pins). It is used to control several circuits by one signal [8]. The relay card consists of two parts. The first part of the right side in Figure 7 below, it consists of a ground, a control pin to switch ON/OFF depending on the state and a 5V power pin for the relay card itself. The second part on the left side, will be connected to the load device, it contains 3 cards:

- NC means (Normally Closed): this indicate to that when the relay card has 0 on the control pin (no input signal), the connected circuit active. COM is connected to this thing when the relay coil is off .
- NO means (Normally Open): this indicate to that, on the reverse, when the relay card has 1 on the control pin (value of 5V applied to the relay card) will switch off the circuit and vice versa. COM is connected to this thing when the relay coil is on.
- COM means (Common): always connected, it is the moving point of the switch.

Besides that, only two relay plugs will be used in accordance with the selected operating mode. The Raspberry Pi sends a low current on its GPIO pins whether at 0 or 1. This a weak current is enough to excite the relay. In this proposed system the SRD-05VDC-SL-C sainsmart 2 relay module is used and the light bulb is load used for relay card. The light bulb was worked like the flashlight for the camera module.



Figure 7. Relay Card

3.5. Power supply

The proposed system needs of two power supplies. The first one used for Raspberry Pi3 board is Micro USB connector that supplied at least 5V at up to 2.5Amps is main for the proposed system. It is worth to mention that,many smartphone chargers are appropriate for Raspberry Pi [9]as shown in Figure 8 below. The second one used for the light bulb is 220V.



Figure 8. Power supply adapter for Raspberry Pi

3.6. LED (Light Emitting Diode)

Electronic pieces resemble small lamps work to convert electricity to light and are available in different colors. In this system, the 5MM white

LEDs are used to improve lighting for an image which captured by the camera module.



Figure 9. White LED

3.7. Telegram Application on a Smartphone

The telegram is a cloud-based mobile and computer messaging application with a focus on security and speed. The telegram-cli is a private library for telegram application which provides a possibility to send any file type from Raspberry Pi to smartphone and from the smartphone to the Raspberry Pi.



Figure 10. Telegram Application on Smartphone

3.8. GPIO Pins Configuration

The Raspberry Pi 3 has two rows of pins that called General Purpose Input Output (GPIO) connector which includes 40 pin connector. The Raspberry Pi 3 allows the peripheral devices such as sensors, LEDs...etc to connect directly to GPIO pins. Also, the GPIO pins allow control and interact directly with the Raspberry Pi processor [10].In addition,the Raspberry Pi 3 needs to install the libraries such as Rpi.GPIO that allows access to the GPIO pins using a programming language such as python. Besides that,the Rpi.GPIO library is used to install these pins as an input or output. The GPIO pins which

used in the proposed system are mentioned in Figure 11.



Figure 11. GPIO pins layout for proposed system

4. Results

The security system is developed which result is represented in the Figure 12 and Figure 13.

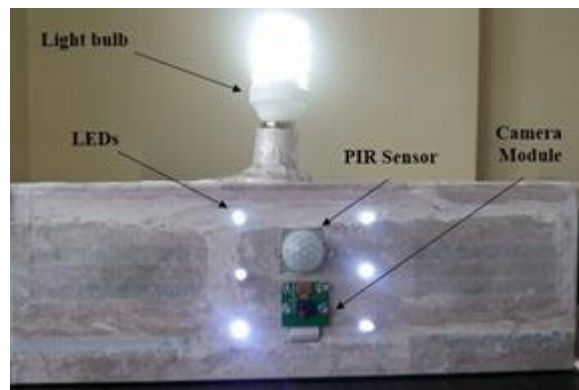


Figure 12. The security system at the moment of take the picture if motion is detected

Transmission of Image, Message and The number of persons located via Wi-Fi internet to a smartphone.



Figure 13. The result of proposed security system in smartphone

5. Conclusion

This paper presents a new smart security system that able to monitor any movement in the room .Besides that, this movement will be detected by using PIR sensor. The smart security system able to give monitoring information (image, a notification message with the numbers of people sites) in real time to alert the user through Telegram Application .Hence, the Raspberry Pi 3 has two basic components interacting with each other: one is the Telegram Application that executes on the smartphone device's browser and server side scripts that run by the Raspberry Pi 3 Hardware tool component. This security system works immediately when turning ON the power supply for the system and no need for the user to execute the smart security system. Additionally, this system is the very effective and the crucial system choice for several reasons belong to inexpensive, consumes low power, simple circuit, and advanced system.

6. References

1. PRIYANKA, Vp. and REDDY, D. R. K. S. (2015) 'PIR Based Security Home Automation System with Exclusive Video Transmission', international journal of Scientific Engineering and Technology Research, 4(18).
2. Narkhede, Y. V. and Khadke, S. G. (2016) 'Application of Raspberry Pi and PIR Sensor for Monitoring of Smart Surveillance System', International Journal of Electronics, Electrical and Computational System IJEECS, 5(5), pp. 145–148.
3. Ahmad, T., Studiawan, H. and Ramadhan, T. T. (2014) 'Developing a Raspberry Pi-based Monitoring System for Detecting and Securing an Object', International Electronics Symposium (IES).
4. Zafar, S. and Carranza, A. (no date) 'Motion Detecting Camera Security System with Email Notifications and Live Streaming Using Raspberry Pi', in Conference of the American Society for Engineering Education, pp. 1–5.
5. Chandana, R., Jilani, S. and Javeed Hussain, S. (2015) 'Smart Surveillance system using Think Speak and Raspberry Pi', International Journal of Advanced Research in Computer and Communication Engineering, 4(7), pp. 214–218.
6. Patel, P. B., Bhatt, K. R., Choksi, V. M. and Potdar, M. B. (2016) 'Smart Surveillance and Monitoring System using Raspberry Pi And Android', International Journal of Enhanced Research in Science, Technology & Engineering, 5(5).
7. Million, R. P. S. P. F. (2013) 'The MagPi Magazine', Edition, 31(14), p. 6.
8. Vigneswari, P., Indhu, V., Narmatha, R. R., Sathinisha, A. and Subashini, J. M. (2015) 'Automated security system using surveillance', International journal of current engineering and technology, 5(2), pp. 882–884.
9. Pi, R. (2012) 'Quick start guide'.
10. Antony, A. and Gidveer, G. R. (no date) 'LIVE STREAMING MOTION DETECTION CAMERA SECURITY SYSTEM WITH EMAIL NOTIFICATION USING RASPBERRY PI', IOSR Journal of Electronics and Communication Engineering (IOSR-JECE), (AETM'16), pp. 142–147.

FPGA Implementation of a Chaotic Quadratic Map for Cryptographic Applications

Hidayet OĞRAŞ, Mustafa TÜRK

Technical Education Faculty, Batman University, Batman, Turkey
Electrical and Electronics Engineering, Firat University, Elazig, Turkey
hidayet.ogras@batman.edu.tr

(Geliş/Received:23.02.2017; Kabul/Accepted:06.04.2017)

Abstract

A hardware implementation of a quadratic map through FPGA platform is proposed in this paper. Firstly, a chaotic quadratic map is modeled by using Matlab/Simulink programming and then implemented into the FPGA (Field Programmable Gate Array) to be used for key generation for cryptographic applications. When the quadratic map is in chaotic mode, its output is unpredictable and aperiodic. Besides this, the map has a uniform output distribution and sufficient randomness. These characteristics make the chaotic quadratic map a suitable key generator for cryptography. This paper also reveals the successful real-time implementation of the quadratic map using FPGA for practical applications. Experimental results confirm that the feasibility of the quadratic map is verified under a digital hardware environment.

Keywords: Chaos; Quadratic Map; Implementation; FPGA

Kriptografik Uygulamalar için Kaotik Kuadratik bir Haritanın FPGA Gerçekleştirilmesi

Özet

Bu çalışmada, kuadratik bir haritanın FPGA üzerinden donanımsal gerçekleştirilmesi sunulmuştur. İlk olarak, kaotik kuadratik haritası Matlab/Simulink yazılımı kullanılarak modellenmiş ve daha sonra kriptografik uygulamalar için FPGA (Sahada Programlanabilir Kapı Dizileri) ortamında anahtar üretici olarak gerçekleştirilmiştir. Kuadratik harita kaotik durumda iken sistem çıkışı tahmin edilemez ve düzensizdir. Ayrıca harita, düzgün bir çıkış dağılımına ve yeterli seviyede rastgeleliğe sahiptir. Bu karakteristik özellikler kaotik kuadratik haritasını kriptografi için uygun bir anahtar üretici yapmaktadır. Bu çalışma aynı zamanda pratik uygulamalara yönelik olarak kuadratik haritasının FPGA ortamındaki başarılı gerçek zamanlı uygulamasını ortaya koymaktadır. Deneysel sonuçlar kuadratik haritanın uygulanabilirliğini sayısal donanım ortamında göstermiştir.

Anahtar Kelimeler: Kaos; Kuadratik Harita; Gerçekleştirme; FPGA

1. Introduction

Chaos theory in complex systems has been cited increasingly in several different scientific areas especially in engineering science such as secure communication and cryptography. For example, chaos is used for analog and digital communication systems in [1-6]; for image cryptosystems in [7-12] and is applied in electrical power systems in [13-16]. Chaotic systems have similar properties such as sensitivity to initial conditions and control parameters, pseudo-random behavior and mixing with modern cryptography. These fundamentals characteristics can make the chaotic systems a

good candidate for the key generation in data encryption algorithms. Many cryptosystems based on the generation of pseudo-random sequences using chaos have been proposed recently for mixing clear messages in information security [17].

Chaos generation in discrete time systems is very easy and simple due to the low complexity, but having high efficiency comparing with analog chaos generators [18]. In fact, analogue chaotic systems typically exhibit some practical difficulties since the component conditions are varying with age, temperature, etc. Furthermore, analog circuit implementations generally require a large chip area for realization. Hence, hardware

implementations of the discrete chaotic systems can be a solution to overcome these problems. Many digital realizations of chaotic systems have been reported to be used as key generators in cryptographic applications. For instance, in [19], Henon map as a chaotic generator is implemented in real-time on a FPGA to obtain high frequency at output for chaotic communication. In other study [20], a chaotic map is used as a bit generator and its FPGA implementation is performed successfully for cryptographic applications. Generally, chaotic system is used to generate pseudo-random sequences as key streams to mask information. using Xilinx blocks in MATLAB/Simulink and then Xilinx system generator (XSG) performs the compilation of the design.

The rest of the paper is structured as follows: Section 2 briefly introduces the Quadratic map with its dynamical behaviors and some statistical analyses of the map are performed. In Section 3, we realize the digital implementation and hardware-co simulation of the Quadratic map on FPGA. Finally, Section 4 concludes the whole paper.

2. Chaotic Quadratic System

A. Quadratic Map

Quadratic map is a simple discrete system exhibiting chaos and defined by [22],

$$x_{n+1} = r - x_n^2 \quad (1)$$

where $0 < r \leq 2$ is called control parameter and $x_n \in (-2, 2)$ is the state variable of the system. Quadratic map can show rich dynamic behaviors from a stationary system to a chaotic state. When $r \in (0, 0.74)$, the map behaves in steady state and if $r \in [0.74, 1.5)$, then the map has periodic behavior. When $r \in [1.5, 2]$, the Quadratic map is capable of very complicated behavior which means that the output of the map is aperiodic, non-convergent and very sensitive to initial conditions. Hence, the value of the control parameter specifies the dynamical behavior of the system.

B. Lyapunov and Bifurcation Analyses

Lyapunov exponent checks a sensitivity criterion of the initial condition for a nonlinear dynamical system [23]. In discrete systems,

Key streams should be generated randomly and contain enough entropy in order to prevent the key from being guessed. Key sensitivity is also required by secure cryptosystems [21].

In this paper, we consider a quadratic map and present direct real-time implementation into the FPGA as well as hardware co-simulation structure in Simulink. Xilinx ISE (Integrated Synthesis Environment) design software including system generator tool is one of the efficient software technologies, is used to design and implement the chaotic Quadratic map. Firstly, the map equation is modeled by

Lyapunov values are given by the following equation.

$$\lambda = \lim_{n \rightarrow \infty} \frac{1}{n} \sum_{i=0}^{n-1} \ln |f'(x_i)| \quad (2)$$

A positive Lyapunov exponent indicates that the orbit of a dynamical system is unstable and chaotic. The dynamical behaviors of a system from a fixed point to a chaos as a function of its control parameter are shown by a bifurcation diagram. Fig. 1 shows the Lyapunov spectrum and the bifurcation diagram of the Quadratic map.

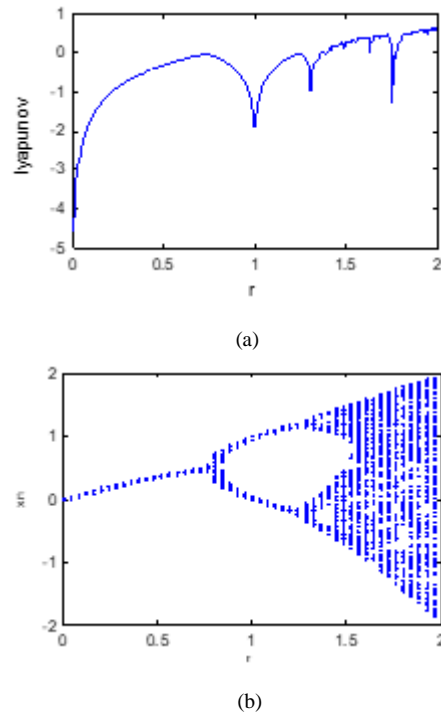


Figure 1 (a) Lyapunov spectrum of the Quadratic map (b) Bifurcation diagram of the Quadratic map

As it is easily observed that when the control parameter is close to 2, then the Lyapunov values are positive and the bifurcation diagram displays complex behavior resulting chaos.

C. Histogram Analysis

Histogram is a graphical display for the frequency distribution of a set of data. A distribution having constant probability for each data is known as uniform distribution. Fig. 2 shows the histogram distribution of the x_n series generated from the Quadratic map with different control parameters. From the graphical results, Fig. 2(a), Fig. 2(b) and Fig. 2(c) demonstrate steady, periodic and chaotic behavior of the Quadratic map, respectively. It is obvious that the histogram has an excellent symmetric property and better uniform distribution when the map behaves chaotically as in Fig. 2(c).

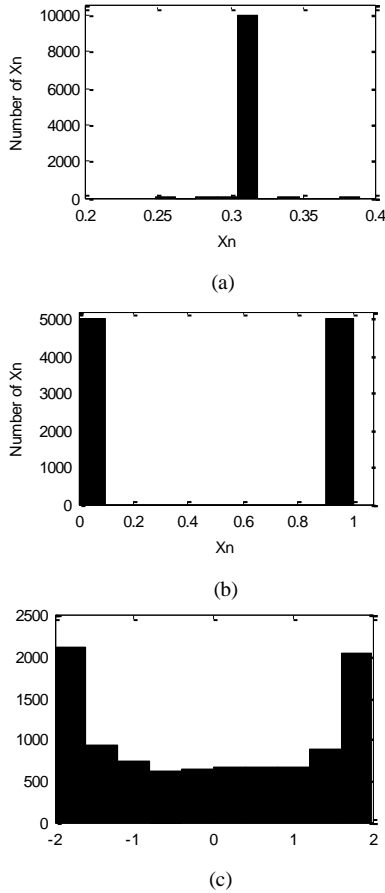


Figure 2. Histogram of x_n series with different control parameter (a) $r=0.4$ (b) $r=1$ (c) $r=2$

D. Checking Chaotic Output

When the Quadratic map is in chaos state, it exhibits complex behavior and generates chaotic sequences at output. Firstly, chaotic output will be checked for homogeneity through central tendency analysis and then the randomness of these sequences will be evaluated by using NIST test. Finally, the entropy of the Quadratic map as a number generator will be determined to measure its uncertainty. If a key generator is used in a cryptosystem, these properties need to be confirmed. In this paper, we chose as $r=2$ to make the system chaotic and perform the following statistical analyses by using Matlab programming.

1) Homogeneity Analysis

In order to check the chaotic output of the Quadratic map, the following two propositions are considered. First of all, the mean value of the output sequences spreading between $(-2,2)$ should be

$$x_{mean} = \lim_{N \rightarrow \infty} \frac{1}{N} \sum_{k=1}^N x_k = 0 \quad (3)$$

and second, the self-correlation of these sequences should be zero as given in the following equation.

$$s(\beta) = \lim_{N \rightarrow \infty} \frac{1}{N} \sum_{k=1}^{\infty} (x_k - x_{mean}) \cdot (x_{k+\beta} - x_{mean}) = 0 \quad (4)$$

According to the above equations, based on 50 simulations with different initial conditions, we have performed 10^6 iterations to get sufficient number of chaotic sequences from the Quadratic map. Then, we got the average mean value 0.000174 and the self-correlation is calculated to be 0.001598. These results are quite good, because both are very close to zero.

2) Randomness Analysis

Randomness means unpredictability and does not follow an intelligible pattern in a sequence of symbols [24]. NIST test is used to determine the degree of randomness of the Quadratic map outputs. NIST includes fifteen tests [25] and each test produces a real p -value in $[0,1]$. If the p -value is greater than a significance predefined level such as $\alpha=0.01$, then the test is passed successfully. When the all statistical tests are passed, then the map is considered as random

generator with 99% confidence. NIST uses binary series to test the randomness, but the output of the chaotic Quadratic map is floating-point value. Therefore, the following transformation is used for the output of the map in order to get sequential bit streams.

$$b_n = \begin{cases} 1, & x_n \geq 0 \\ 0, & x_n < 0 \end{cases} \quad (5)$$

Here, a threshold level of 0 is selected to produce a bit value “1” or “0” from x_n . We preferred the initial value as $x_0 = 0.123$ to obtain 1,000,000 bits to proceed NIST suite. The results are listed in Table 1.

Table 1 Results of the NIST test

Test Name	p-value	Result
Frequency	0.8524	Passed
Block frequency	0.3093	Passed
Runs	0.4939	Passed
Long runs of ones	0.7852	Passed
Rank	0.9912	Passed
Spectral DFT	0.7204	Passed
Non-overlapping templates (m=9; B=000000001)	0.7659	Passed
Overlapping templates (m=9)	0.7819	Passed
Universal (L=7; Q=1280)	0.1201	Passed
Liner complexity	0.9138	Passed
Serial-1 (m=5)	0.5875	Passed
Serial-2 (m=5)	0.6469	Passed
Approximate entropy (m=5)	0.4142	Passed
Cumulative sums forward	0.4086	Passed
Cumulative sums reverse	0.5553	Passed
Random excursions (x=+1)	0.3511	Passed
Random excursions variant (x=-1)	0.8741	Passed

It is concluded that the chaotic Quadratic map is very stochastic that represents random process and generates output sequences having enough randomness according to the NIST results.

3) Uncertainty Analysis

We use information entropy to determine the uncertainty or disorder of the Quadratic map.

Entropy is a measure of uncertainty related to a random event [24, 26]. If $H(X)$ is a random source with N length, then its entropy is

$$H(X) = -\sum_{i=1}^N p(x_i) \cdot \log_2 p(x_i) \quad (6)$$

where $p(x_i)$ represents the probability of x_i . For instance, in a uniform bit stream having equal probability ‘0’ and ‘1’, the entropy will be 1 which is a theoretical result. When the output is certain, then the entropy is zero. The entropy of an practical information source is smaller than the ideal one. Generally, the more uncertain or random the event is, the more entropy it will contain [11].

We have used different initial values and number of iterations in order to generate bit streams using the Eqn. (5) from the chaotic Quadratic map. The entropy results for different conditions of the map are listed in Table 2.

Table 2 Entropy results

Initial value	n	# of ‘0’	# of ‘1’	p(0)	p(1)	Entropy
0.2	100	52	48	0.52	0.48	0.998845
-0.315	1000	490	510	0.49	0.51	0.999711
1.27	10,000	4,967	5,033	0.4967	0.5033	0.999968
-0.88354	100,000	49,829	50,171	0.4982	0.5017	0.999991

From the results, when the number of iteration is increased, then the entropy value closes to 1 which means that the uncertainty of the map is becoming greater. Generated for all bit streams, number of zeros and ones are very close to each other resulting uniform distribution in the sequences.

4) Sensitivity Analysis

Quadratic map is highly sensitive to initial value. Thus, arbitrarily small change in the initial value will cause significantly different future output. This property is also acceptable while the map is used as a bit generator. To perform the sensitivity analysis, firstly, we randomly choose an initial value $x_0 = 0.123456788$ and iteration of $n = 50$ to generate a bit sequence (b_1) from the map. Then, a very slight change of 10^{-9} is applied to the first initial value, such as $x_0 = 0.123456789$ to generate another bit sequence (b_2). The last ten elements for both sequences are shown in Fig. 3.

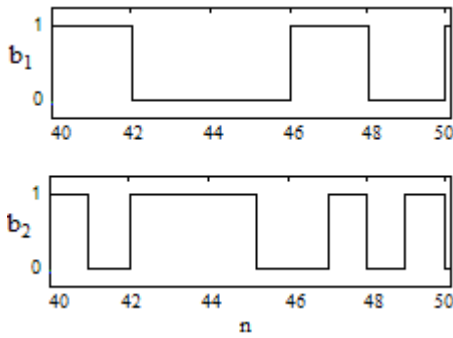


Figure 3 Generated different bit sequences with a slight change of initial value

Fig. 3 states that when a tiny change occurs in the initial value of the chaotic Quadratic map, generated bit sequences are completely different.

3. Digital Implementation

This section describes an approach to the real-time implementation as well as hardware simulation of the chaotic Quadratic map on FPGA. FPGA is a type of programmable chip that can be completely reconfigured for various field applications. Using prebuilt logic blocks and programmable routing resources, FPGAs can be reprogrammed to the required functionality and customized by loading the related configuration data into its internal memory cells. The stored data in these cells determine the logic blocks and reconfigurable interconnects in FPGA. We have used Spartan 3E-XC3S1600E family from Xilinx for the hardware simulation and implementation of the Quadratic map.

Xilinx System Generator (XSG) is a high-level design tool and fully integrated in MATLAB/Simulink that enables the use of the model-based Simulink environment for FPGA design. It allows compilation of the design that is captured using Xilinx blocks and generates synthesizable VHDL (Very High speed integrated circuit Hardware Description Language) codes for FPGA programming. All of the downstream implementation steps including synthesis, place and route processes are automatically performed to generate the programming file via XSG. The Quadratic map model has been designed by Matlab/Simulink with XSG which offers the library of fixed-point arithmetic blocks that can be directly implemented into the FPGA. Fig. 4 shows the

Quadratic map model created by Xilinx blocks under the Simulink.

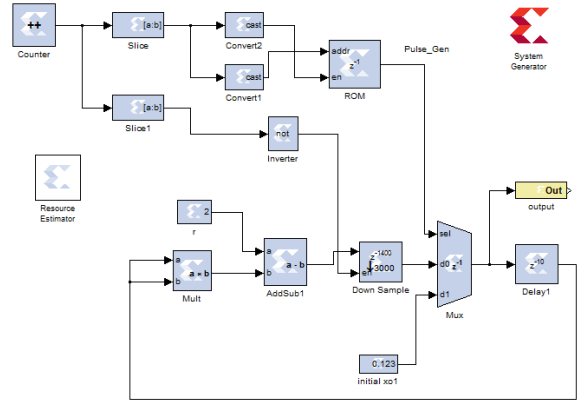


Figure 4 Chaotic Quadratic map model using Xilinx blocks

XSG enables hardware into a simulation, called hardware co-simulation structure that allows incorporating a design running in an FPGA directly into a simulation. Hardware co-simulation compilation targets automatically generate a bit streams and associate it to a block. When this block is simulated in Simulink, then the results for the compiled part are calculated in the hardware. Hence, hardware co-simulation is used to verify that the design actually works in FPGA platform.

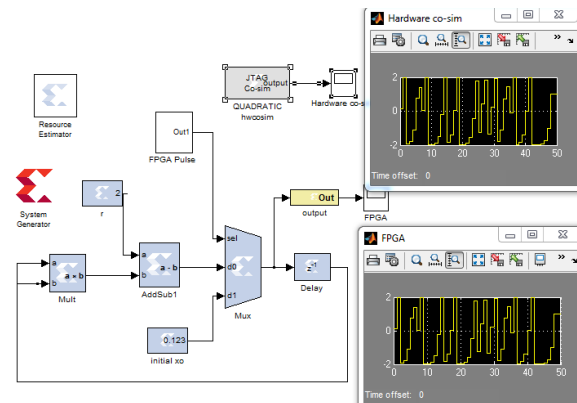


Figure 5 Hardware co-simulation of the Quadratic map

The bitstream download step is performed by using a JTAG cable. We performed the real-time implementation with a fixed-point data type and the real data are represented on 128 bits. Fig. 5 shows the simulation results of the chaotic Quadratic map design with hardware and

software in Simulink. It is observed that the hardware-co simulation result is same to the Simulink simulation which means that the realization of the map is performed successfully and the map design actually works in FPGA.

The generated output depends on the initial value of the map that can be directly entered into the design model before the generator starts. We randomly chose the initial value as $x_0 = 0.123$ for the real-time FPGA implementation.

XSG tool automatically generates a synthesizable VHDL codes associated with the design and the created file can be opened with the Xilinx ISE software. PlanAhead tool in ISE is used to assign input and output pin locations in the design. After assigning pins for input and output, then the design is ready to be synthesized in ISE. Successful synthesis creates the programming file of the design. IMPACT tool is used to load the programming file into the FPGA. For real-time implementation of our design, we use the chaotic Quadratic map as an 8-bit number generator to observe the numbers at LED output of the FPGA. First, the output of the map needs to be converted to 8-bit decimal number between 0 and 255. Hence, the following equation is applied to the output of the map.

$$number = \text{mod}(\text{round}(x_n \times 10^9), 256) \quad (7)$$

Here, *round* operation is used to get the nearest integer value and *mod* limits the output between 0 and 255. We assigned 8-bit number for the implementation because our FPGA has eight LEDs at output. Transformation module is also added to the Quadratic map design. For example, if the initial value of the map is 0.123, then the second number generated from the Eqn. (7) will be 88 in decimal or 01011000 in binary. Fig. 6 shows this value at LED output of the FPGA.



Figure 6 Display of 88 in binary at LED output of the FPGA

Table 3 shows the numbers generated from the chaotic Quadratic system by using MATLAB and FPGA with the same initial value of the map.

Table 3 Generated 8-bit numbers from MATLAB and FPGA

<i>MATLAB (Software)</i>	<i>FPGA (Hardware)</i>
192	192
88	88
137	137
189	189
57	57
133	133
12	12
220	220

The amount of FPGA resources and the required by the Quadratic map can be determined by using Resource Estimator block. They are listed in Table 4.

Table 4 Mapping report of the Quadratic map design

Device	Spartan3E-XC3S1600E				
	<i>Slices</i>	<i>Flip-Flops</i>	<i>RAMB 16S</i>	<i>LUTs</i>	<i>IOBS</i>
Available	14,752	29,504	36	29,504	250
Used	10,160	10,922	1	18,843	9

4. Conclusion

This paper presents a chaotic Quadratic map and its implementation on a digital hardware. The results of the statistical analyses confirm that the output of Quadratic map can be used as cryptographic keys when the map behaves chaotically. In practice, chaotic Quadratic map can be used as a generator in all scientific fields where the pseudo-randomness and chaos are required. The design of the map as well as hardware co-simulation and real-time implementation are successfully applied to the FPGA platform that encourages its usage for practical applications. This paper can be used as a good guide for anyone who wants to implement digital designs on FPGA without knowing VHDL codes.

5. References

1. Kang, Z., Sun, J., Ma, L., Qi, Y. and Jian, S., (2014). Multimode synchronization of chaotic semiconductor ring laser and its potential in chaos communication. IEEE journal of Quantum Electronics, vol. 50, pp. 148-157.

2. Yang, J., Chen, Y. and Zhu, F., (2015) .Associated observer-based synchronization for uncertain chaotic systems subject to channel noise and chaos-based secure communication. *Neurocomputing*, vol. 167, pp. 587-595.
3. Eisencraft, M., et al., (2012). Chaos-based communication systems in non-ideal channels. *Communications in Nonlinear Science and Numerical Simulation*, vol. 17, pp. 4707-4718.
4. Kaddoum, G., Coulon, M., Roviras, D. and Charge, P., (2010). Theoretical performance for asynchronous multi-user chaos-based communication systems on fading channels. *Signal Processing*, vol. 90, pp. 2923-2933.
5. Zaher, A. A. and Abu-Rezq, A., (2011). On the design of chaos-based secure communication systems, *Communications in Nonlinear Science and Numerical Simulation*, vol. 16, pp. 3721-3737.
6. Turk, M. and Ogras, H., (2011). Classification of chaos-based digital modulation techniques using wavelet neural networks and performance comparison of wavelet families. *Expert Systems with Applications*, vol. 38, pp. 2557-2565.
7. Zhu, Z. L., Zhang, W., Wong, K. W., Yu, H., (2011). A Chaos-based symmetric image encryption scheme using a bit-level permutation. *Information Sciences*, vol. 181, pp. 1171-1186.
8. Patidar, V., Pareek, N. K., Purohit, G. and Sud, K. K., (2011). A Robust and secure chaotic standard map based pseudorandom permutation-substitution scheme for image encryption. *Optics Communications*, vol. 284, pp. 4331-4339.
9. Murillo-Escobar, M. A. et al., (2015). A RGB image encryption algorithm based on total plain image characteristics and chaos. *Signal Processing*, vol. 109, pp. 119-131.
10. Ye, R., and Guo, W., (2014). An image encryption scheme Multimode synchronization of chaotic semicon based on chaotic systems with changeable parameters," *I. J. Computer Network and Information Security*, vol. 4, pp. 37-45.
11. Zhu, H., Zhao, C. and Zhang, X., (2013). A Novel image encryption-compression scheme using hyper-chaos and Chinese remainder theorem. *Signal Processing: Image Communication*, vol. 28, pp. 670-680.
12. Ogras, H. and Turk, M., (2017). A Robust chaos-based image cryptosystem with an improved key generator and plain image sensitivity mechanism. *Journal of Information Security*, vol. 8, pp. 23-41.
13. Yibei, W., Man, L., Yanting, X. and Hougui, C., (2011). Research on chaos phenomena in power systems. *Power engineering and automation conference*, vol. 2, pp. 453-456.
14. Yau, H. T., Wang, M. H., Wang, T. Y. and Chen, G., (2015). Signal clustering of power disturbance by using chaos synchronization. *Int. J. Electr. Power Energy System*, vol. 64, pp. 112-120.
15. Ghasemi, M., Ghavidel, S., Aghaei, J., Gitizadeh, M. and Falah, H., (2014). Application of chaos-based chaotic invasive weed optimization techniques for environmental OPF problems in the power systems. *Chaos, Solitons Fract.*, vol. 69, pp. 271-284.
16. Chen, Q., Ren, X. and Na, J., (2015). Robust finite-time chaos synchronization of uncertain permanent magnet synchronous motors. *ISA Trans.*, vol. 58, pp. 262-269.
17. Merah, L., Ali-Pacha, A., Said, N. H. and Mamat, M., (2013). Design and FPGA implementation of Lorenz chaotic system for information security issues. *Applied Mathematical Sciences*, vol. 7, pp. 237-246.
18. Xue, H., Wang S. and Meng, X., (2013). Study on one modified chaotic system based on Logistic map. *Res. J. Appl. Sci. Eng. Technol.*, vol. 5, pp. 898-904.
19. Aseeri, M. A. and Sobhy, M. I., (2002). A New approach to implement Chaotic generators based on Field Programmable Gate Array (FPGA). *Proc. 3rd. Int. Conf. Discrete Chaotic Dynam. Nature Soc.*, September.
20. Mao, Y., Cao, L. and Liu, W., (2006). Design and FPGA implementation of a pseudo-random bit sequence generator using spatiotemporal chaos. *IEEE Proceedings of International Conference on Communications, Circuits and Systems*, pp. 2114-2118.
21. Lian, S., Sun, J. and Wang, Z., (2005). Security analysis of a chaos-based image encryption algorithm. *Physica A: Statistical Mechanics and its Applications*, vol. 351, pp. 645-661.
22. Ramadan, N., Ahmed, H. E., Elkhamy H S. E., and Abd El-Samie, F. E., (2016). Chaos-based image encryption using an improved quadratic chaotic map. *American Journal of Signal Processing*, vol. 6, pp. 1-13.
23. Hathal, H. M., Abdulhussein, R. A. and Ibrahim, S. K., (2014). Lyapunov exponent testing for AWGN generator system. *Communications and Network*, vol. 6, pp. 201-208.
24. Marton, K., Suci, A., Sacarea, C. and Cret, O., (2012). Generation and testing of random numbers for cryptographic applications. *Proceedings of the Romanian Academy*, vol. 13, pp. 368-377.
25. Rukhin, A., Soto, J., Nechvatal, J. and Smid, M., (2010). A Statistical Test for random and pseudorandom number generators for cryptographic applications. *NIST Special Publication 800-22 rev1*, pp. 2-40.
26. Chen, J. X., Zhu, Z. L., Fu, C., Yu, H. and Zhang, L.B (2015). A Fast chaos-based image encryption scheme with a dynamic state variables selection mechanism. *Communications in Nonlinear Science and Numerical Simulation*, vol. 20, pp. 846-860.

TURKISH JOURNAL OF SCIENCE & TECHNOLOGY (TJST)

INSTRUCTIONS FOR AUTHORS

Turkish Journal of Science & Technology is an international journal covering all aspects relating to science, engineering and technology.

The following types of article will be considered:

1. Research Articles: Original research in various fields of science, engineering and technology will be evaluated as research articles. Papers must include an English abstract and if possible a Turkish abstract.

2. Research Notes: These include articles such as preliminary notes on a study, manuscripts.

3. Reviews: Reviews of recent developments, improvements, discoveries and ideas in various fields of selected subjects will be requested by the editor or advisory board.

4. Letters to the Editor: These include opinions, comments relating to the publishing policy of Turkish J. of Sci. & Tech., news and suggestions. Letters are not to exceed a single page.

All manuscripts will be subject to multiple **peer review** before publication. Submitted manuscripts must not be under consideration for publication elsewhere or have already been published. The editor reserves the right to decide that a paper may be treated as a Research Note.

Manuscripts should be sent to below address:

Firat University, Fen Bilimleri Enstitüsü,
Turkish Journal of Sci. & Tech. Editörlüğü,
23119 Elazığ- TURKEY

There are **no page charges**.

SUBMISSION OF MANUSCRIPTS

1. Manuscripts must be submitted in typewritten on one side of the page in a legible font, double-spaced with ample margins. All manuscripts must be accompanied by the **Copyright Release Form**, which can be found following the Instructions. This form must be completed and signed by all the authors before processing of the manuscript can begin. If the manuscript is submitted by e-mail a high quality scan of the Copyright Release Form is acceptable.

Manuscripts must be written in **English**. Contributors who are not native English speakers are strongly advised to ensure that a colleague fluent in the English language, if none of the authors is so, has reviewed their manuscript. Concise English without jargon should be used. Repetitive use of long sentences and passive tense should be avoided. All abbreviations and acronyms should be defined at first mention. To facilitate reader comprehension, abbreviations should be used sparingly. After the manuscript has been accepted for publication, i.e. after referee-recommended revisions are complete, the authors will not be permitted to make any additions. Before publication, the **galley proof** is always sent to the authors for correction. Mistakes or omissions that occur due to some negligence on our part during the final printing will be rectified in an errata section of a later issue. However, this does not include those errors left uncorrected by the authors in the galley proofs.

All due care will be taken with material submitted, but the Advisory Board and the publisher cannot be held responsible for any loss or damage.

2. Manuscripts should have the following **format**: title, name(s) of author(s), key words (3-6), abstract, text, references.

3. The abstract must be brief and informative and must not exceed 200 words. It should include all new names, combinations and rank transfers.

4. The text may be divided into reasonable subdivisions by the authors with numbered (1, 2,...), but the aim of the article, results and discussion must be included. An Introduction and Materials and Methods section may also be included if appropriate.

Within the main text, **author citations** should follow:

Brummitt and Powell, [1]For three or more authors use 'et. al.' for example Özcan et. al. [1]

References in the text should be numbered in square brackets as [1]. Multiple references should be arranged chronologically.

5. In the reference list, references should be numbered in the order of appearance in the text and should appear in the following style:

Journal articles: (i) Surname(s) and initial(s) of author(s), (ii) Year of publication (in parentheses), (iii) Title of article (in lower case), (iv) Title of journal (in italics), (v) Volume number, (vi) Page numbers.

For example, Emiroglu, M. E., and Baylar, A. (2003). Study of the Influence of Air Holes along Length of Convergent-Divergent Passage of a Venturi Device on Aeration. *Journal of Hydraulic Research*, **41** (5), 513-520.

Chapters in books: (i) Surname(s) and initial(s) of author(s), (ii) Year of publication (in parentheses), (iii) Title of chapter (in lower case), (iv) Name of editor (if applicable), (v) Title of book (in upper case and italics), (vi) Page numbers,

(vii) Place of publication, (viii) Name of publisher.

For example, Endler JA (1982). Pleistocene forest refuges: Fact or fancy? In: Prance GT (ed.) Biological Diversification in the Tropics, pp. 641-657. New York: Plenum Press.

Books: (i) Surname(s) and initial(s) of author(s), (ii) Year of publication (in parentheses), (iii) Title of book (in upper case and italics), (iv) Place of publication, (v) Name of publisher.

For example, Mabberley DJ (1987). The Plant-Book. A Portable Dictionary of the Higher Plants. Cambridge: Cambridge University Press.

Ahmed, A. (1974). Aeration by Plunging Liquid Jet. Ph.D. thesis, Loughborough University of Technology, Leicestershire, UK. References to web sites, computer programs, and unpublished theses or reports are unacceptable.

6. All scientific names cited in the running text, irrespective of rank, **must be italicised**. In headings, scientific names must be in bold and not italicised. **Authors of genera and lower taxa** must be cited at the first mention of the taxa in both the abstract and the text.

7. Figures and Tables

All illustrations (photographs, line drawings, graphs, maps, etc.), not including tables, must be labelled "Figure".

The **correct position** of each table and figure must be clearly **indicated** in the paper

All tables and figures must have a number (Table 1, Figure 1) and a caption or legend. All tables and figures must be numbered consecutively. All captions and legends must also appear on a separate sheet, double-spaced and labelled according to the relevant table or figure.

Tables and figures, including caption, title, and column heads, **must not exceed** 16 x 20 cm and should be no smaller than 8 cm in width. Tables must be clearly typed, each on a separate sheet, and double-spaced. Tables may be continued on another sheet if necessary, but the dimensions stated above still apply.

Figures must be the originals. Reduced photocopies are not acceptable. **Photographs** must be clear, black and white, and on glossy paper. **Three sets of photographs** must be submitted.

Before submitting your manuscript, ensure that all the following requirements have been met:

- The **Copyright Release** Form, appearing on the following page, has been completed and **signed by all the authors**
- Spell check and grammar check have been performed
- **Paper** is submitted in **triplicate** (one original, two copies)
- **Entire paper** is **double-spaced** including abstract, tables, captions/legends, and references (NOT 1.5)
- Margins are c. 3 cm each side
- Font size is 12 pt or 3 mm
- There are **no word breaks** at the ends of lines
- **Decimals** are shown by a **decimal point** (e.g., 10.24) and **not by a comma** (e.g., NOT 10,24)
- The percent sign appears after the number (e.g., 53%) and not before (e.g., NOT %53)
- **Names of authors** are written in full (not abbreviated)
- English address is given
- Turkish address (if applicable) is given
- English title is given
- Turkish title is given (if possible)
- English abstract is given
- Turkish abstract is given (if possible)
- English key words are given
- Turkish key words are given (if possible)
- **Authors of genera and lower taxa** are cited at first appearance in both the abstract and the text
- **Unpublished references** (theses, project reports, etc.) are not referred to or cited
- Three sets of **photographs** are enclosed
- **Original figures** are enclosed
- **Figures** are prepared according to the instructions
- Figures are max 16 x 20 cm; min 8 x 20 cm wide
- Figures are referred to consecutively in the paper
- **Tables** are max 16 x 20 cm; min 8 x 20 cm wide
- Tables are referred to consecutively in the paper
- Table and figure legends/captions are typed on a separate sheet
- **References** are listed in alphabetical order in the style shown in the instructions
- All pages are numbered

Further details can be found on our web site. <http://www.firat.edu.tr>

COPYRIGHT RELEASE FORM

TURKISH JOURNAL OF SCIENCE AND TECHNOLOGY (TJST) Published by Firat University

Firat University, Fen Bilimleri Enstitüsü Müdürlüğü
Turkish Journal of Science & Technology Editörlüğü
Elazığ-TURKEY,
Manuscript title:

Full names of all authors (in order to appear on manuscript):

Name, address etc. of corresponding author:

ID Number: Telephone:

E-mail: Mobile phone:

The author(s) warrant(s) that:

- a) the manuscript submitted is his/her/their own original work;
- b) all authors participated in the work in a substantive way and are prepared to take public responsibility for the work;
- c) all authors have seen and approved the manuscript as submitted;
- d) the manuscript has not been published and is not being submitted or considered for publication elsewhere;
- e) the text, illustrations, and any other materials included in the manuscript do not infringe upon any existing copyright or other rights of anyone. Notwithstanding the above, the Contributor(s) or, if applicable the Contributor's Employer, retain(s) all proprietary rights other than copyright, such as

- a) patent rights;
- b) to use, free of charge, all parts of this article for the author's future works in books, lectures, classroom teaching or oral presentations;
- c) the right to reproduce the article for their own purposes provided the copies are not offered for sale.

However, reproduction, posting, transmission or other distribution or use of the article or any material contained therein, in any medium as permitted hereunder, requires a citation to the Journal and appropriate credit to Firat University as publisher, suitable in form and content as follows:

Title of article, author(s), journal title and volume/issue, Copyright© year.

All materials related to manuscripts, accepted or rejected, including photographs, original figures etc., will be kept by Turkish Journal of Science and Technology editority for one year following the editor's decision. These materials will then be destroyed. I/We indemnify Firat University and the Editors of the Journals, and hold them harmless from any loss, expense or damage occasioned by a claim or suit by a third party for copyright infringement, or any suit arising out of any breach of the foregoing warranties as a result of publication of my/our article. I/We also warrant that the article contains no libelous or unlawful statements and does not contain material or instructions that might cause harm or injury.

This copyright form must be signed by all authors. Separate copies of the form (completed in full) may be submitted by authors located at different institutions; however, all signatures must be original.

ID number: ID number:

Full name (block letters) Full name (block letters)

Signature Date Signature Date

ID number: ID number:

Full name (block letters) Full name (block letters)

Signature Date Signature Date

ID number: ID number:

Turkish authors must supply their ID card number; foreign authors must supply their passport number (if possible)

